POLITECNICO DI TORINO

Master's Degree Course
in Civil Engineering

Master's Degree Thesis

Nonlinear Analysis of Longitudinal Shear – Transverse Bending Interaction in Prestressed Concrete Box Girder Bridges

REVIEWERS:

Prof. Giordano Luca

Prof. Gino Diego

AUTHOR:

Lacin Murat

July 2025

TABLE OF CONTENTS

LIST OF FIGURES

LIST OF TABLES

VIII

LIST OF GRAPHS

Abstract

This thesis investigates the nonlinear interaction between transverse bending moment and longitudinal shear in prestressed concrete box girder bridges, with particular attention to the influence of axial prestress, reinforcement ratio, and material strength assumptions. Using the ATENA finite element software, a series of detailed simulations were performed on a web panel modeled with 2D layered shell elements.

Key parameters were systematically varied, including prestressing level (0 to 10 MPa), reinforcement diameter ($\phi20$ and $\phi24$), and concrete strength class (C25/30 and C40/50). Additionally, mean, characteristic, and design-level material properties were implemented to explore the impact of safety-oriented design assumptions. For each configuration, pure shear and pure moment capacities were first evaluated, and then combined to construct dimensionless M–V interaction domains (μ/μ_{rd} vs τ/τ_{rd}).

Results showed that at low prestress and reduced reinforcement, the interaction domains closely resembled the classical triangular or parabolic shapes proposed by Christian Menn. However, at higher prestressing levels, especially when mean material properties were used, the domain contours deviated significantly, exhibiting more rounded and ductile behavior. Superposed diagrams confirmed a transition in failure mechanisms: from brittle, shear-dominated behavior to a prestress-enhanced flexural regime. The interaction domains generated through nonlinear FEM were also compared with Eurocode 2 and fib Model Code predictions. Among them, fib Level of Approximation IIb provided the closest match to FEM results, while Eurocode often yielded overly optimistic estimates under high prestress.

The study highlights the critical role of reinforcement detailing and material assumptions in shaping the interaction response, and emphasizes the importance of nonlinear verification tools in bridge design—especially where shear–moment interaction governs capacity.

1. Introduction

The continuous evolution of bridge design has brought a demand for deeper understanding of structural interaction effects, especially in prestressed concrete box girder bridges. These structures, while commonly designed using simplified interaction checks, are subject to complex combined actions such as longitudinal shear and transverse bending moments.

The aim of this thesis is to investigate the interaction between longitudinal shear and transverse bending moment in concrete web panels, using a non-linear finite element analysis approach. A series of simulations were carried out using ATENA software, where layered shell elements were used to represent the structural behaviour of reinforced concrete walls under different loading conditions and prestressing levels.
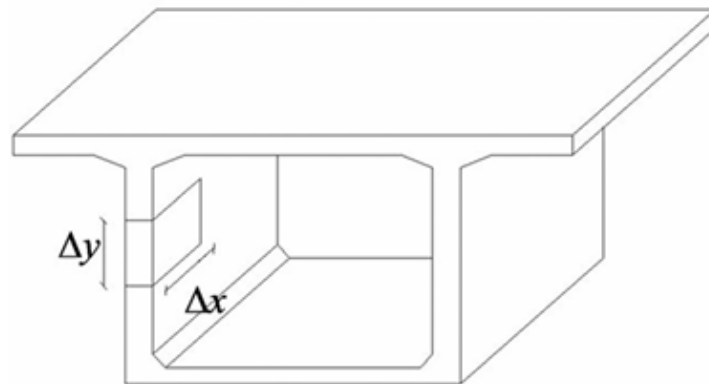
Figure 1. Web segment of concrete box girder

One of the most well-known approaches to address the combined effect of shear and moment in prestressed concrete bridges was developed by Christian Menn. In his book *Prestressed Concrete Bridges*, he proposed simplified interaction domains based on theoretical assumptions and design experience. These interaction curves provide practical guidance for engineers, but they do not fully reflect the non-linear behaviour of concrete and reinforcement under combined actions.

In this study, non-linear simulations were used to develop interaction domains based on actual structural behaviour rather than simplified assumptions. Several models were created to evaluate different prestressing levels, reinforcement diameters, and material properties. First, the shear and moment resistance of a reinforced concrete wall was evaluated separately. Then, combined loading was applied to generate shear–moment interaction domains. These results were compared with the simplified curves proposed by Christian Menn, aiming to highlight the differences and better understand the structural response.

This thesis is structured as follows. Chapter 2 provides a brief overview of relevant literature and theoretical background, including Eurocode 2 provisions. Chapter 3 explains the numerical modelling process in ATENA, covering geometry, materials, boundary conditions, and loading protocols. Chapter 4 presents the simulation results for shear, moment, and their interaction under different conditions. In Chapter 5, the results are compared with Menn's simplified domains. Chapter 6 includes the extension of the study to a full-scale box girder bridge model, where the developed interaction curves are applied and evaluated. Finally, Chapter 7 summarizes the main findings and suggests future directions.

2. Literature Review

In recent decades, many studies have focused on the structural behaviour of reinforced and prestressed concrete elements under combined loading. Among these, the interaction between shear force and bending moment has received particular attention due to its critical role in the design and safety of concrete bridge webs. Researchers have proposed both analytical and experimental methods to evaluate this interaction, often aiming to develop simplified models that are practical for design use.

An important contribution to the understanding of shear–moment interactions in prestressed concrete structures is presented by Recupero et al. (2016). Their study focuses on box girder bridges and emphasizes how internal force interactions—particularly between longitudinal shear and transverse bending—play a crucial role in determining the necessary reinforcement layouts. (Recupero, 2016)

$$\sigma_x = \frac{N_x}{A}$$

$$\sigma_x = \frac{M_z}{I_z} y$$

$$\tau_{xy} = \frac{V_{y,R} S_z}{t I_z}$$

$$\tau = \frac{M_t}{2\Omega t}$$
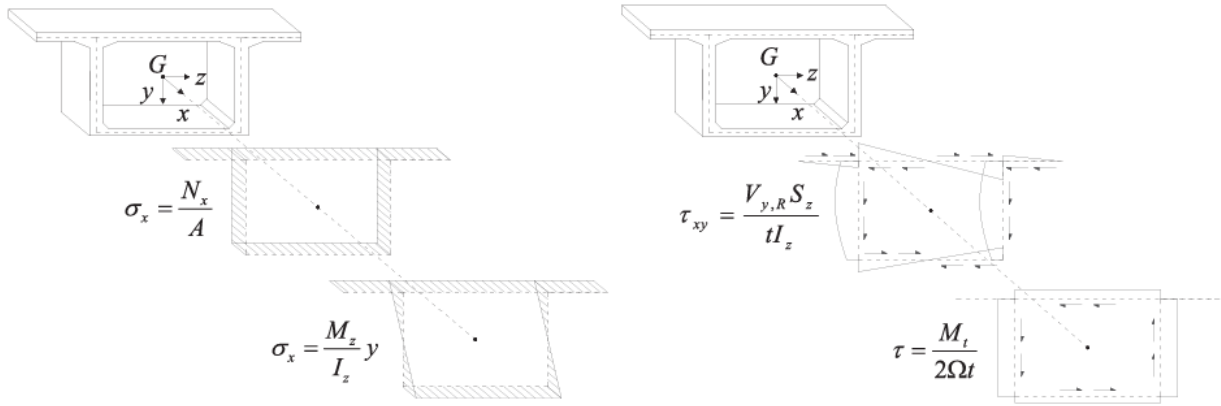
Figure 2. Typical stress state for Saint-Venant's theory (Recupero, 2016)

The authors build upon earlier theories, including those developed by Kaufmann and Menn, by proposing an analytical model rooted in stress field theory and the static theorem of plasticity. This model allows for the development of **dimensionless interaction domains**, offering a practical tool for engineers. Notably, the study highlights how prestressing alters the inclination of the principal stress field, affecting the interaction domain and ultimately the reinforcement requirements.
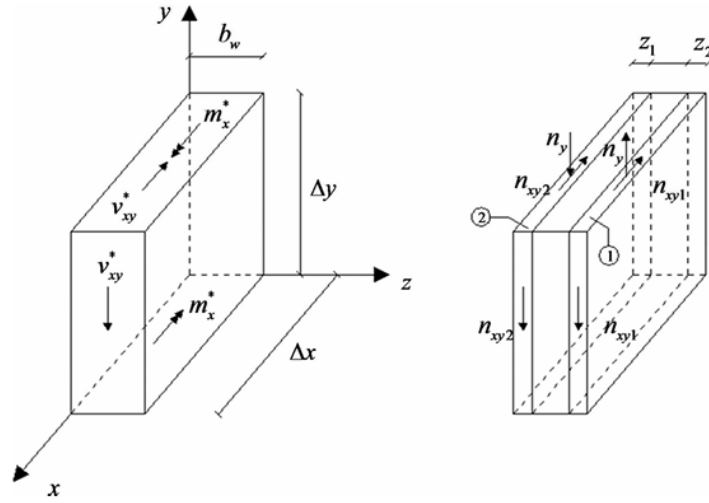
Figure 3. Distribution of internal forces in the sandwich layers

Shear and moment interaction is often visualized through dimensionless interaction domains, where the normalized shear (v) and moment (μ) are calculated as:

$$\mu_x = \frac{M}{(b \cdot d^2 \cdot f_{cd})}$$

$$v_{xy} = \frac{V}{(b \cdot d \cdot f_{cd})}$$
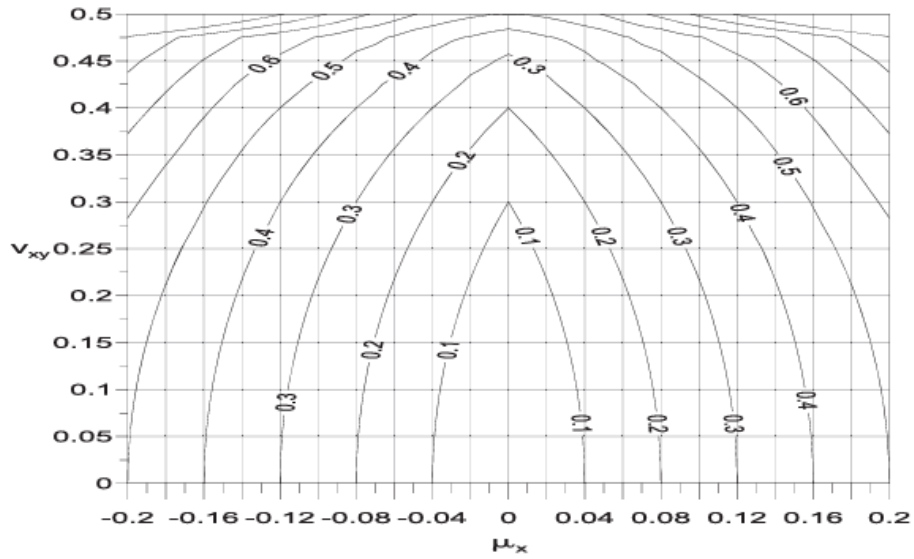
Graph 1. Interaction domains for equal reinforcement on both directions (Recupero, 2016)

5

In recent years, several researchers have employed non-linear finite element analysis (NLFEA) to study the behaviour of concrete bridge elements under combined loading. These methods allow for more accurate simulation of cracking, tension stiffening, and concrete softening, which are not captured by simplified design approaches. Unlike traditional linear models, NLFEA provides the ability to track the redistribution of stresses and strains after cracking occurs. This makes it especially useful in understanding interaction effects in web panels of box girders, where both longitudinal shear and bending moment act simultaneously. The approach used in this thesis follows a similar path, aiming to capture these complex behaviours with a high level of detail.

Furthermore, the paper confirms its findings with experimental data and applies the model to a case study involving a prestressed concrete box girder bridge. This approach is closely related to the methodology employed in this thesis, which uses nonlinear finite element analysis (FEA) to generate interaction domains under varying prestressing levels.

2.1.   Christian Menn's Studies

Christian Menn, in his book *Prestressed Concrete Bridges (pp. 259–264)*, introduced one of the earliest simplified methods to evaluate the interaction between shear and bending in box girder bridge webs. His approach assumes that a reinforced concrete web panel subjected to longitudinal shear and transverse bending behaves according to a linear interaction rule. Using design charts and stress resultants, Menn defined dimensionless interaction domains that engineers can use to quickly check whether a certain combination of shear and moment falls within a safe region. Although practical and widely used, this method does not fully capture the nonlinear behaviour of cracked concrete, nor the contribution of varying prestressing levels.

Christian Menn's conceptual framework for shear–moment interaction in prestressed box girder webs builds upon a fundamental mechanical balance:

- When the section reaches its **shear capacity**, it can no longer sustain bending, (when $V_0/V_{rd}=1$, M_0/M_{rd} must be null.)
- When it reaches its **moment capacity**, it cannot sustain the shear. (When $M_0/M_{rd}=1$, V_0/V_{rd} must be null.)

However, a real web panel must carry both forces simultaneously. Menn proposes that the minimum required web width to resist a given design shear force is:

$$b_w^{req} = \frac{\gamma_R \cdot \gamma_S \cdot V}{f_{c,red} \cdot z \cdot (cos\alpha + cot\beta \cdot sin\alpha) \cdot sin\alpha} \qquad \text{(Menn, 1990)}$$

If the actual web width b_w exceeds this required value, the remaining portion of the web can be utilized to resist the transverse bending moment. This leads to an intuitive interaction between shear and moment — where the available capacity for one reduces as the demand in the other increases.

Figure 4. Equilibrium of a segment (Menn, 1990)

Based on this idea, Menn distinguishes two critical states:
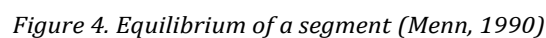
a) Shear predominates (Menn, 1990)

In this condition, the web is fully mobilized to resist shear. The bending moment that the remaining "residual" portion of the section can carry is calculated as:

$$\frac{V_R}{z \cdot cot\alpha} - B_t - B_r = 0 \qquad \text{(Menn, 1990)}$$

$$B_r \cdot b_0 - \frac{V_R}{z \cdot cot\alpha} - m_R = 0 \qquad \text{(Menn, 1990)}$$

b) Transverse bending predominates (Menn, 1990)

Conversely, when the section primarily resists bending, the shear resistance is reduced accordingly. The available shear force is calculated from the portion of the web not engaged by bending stress:

$$\frac{V_R}{z \cdot cot\alpha} + F_{cw} - B_r = 0 \qquad \text{(Menn, 1990)}$$

$$\frac{V_R}{z \cdot cot\alpha} \cdot \left(\frac{b_w^{req} + b_1}{2}\right) + m_R - B_r \cdot \left(b_w - b' - \frac{b_1}{2}\right) = 0 \qquad \text{(Menn, 1990)}$$

where V_R is resisted shear, m_R is resisted moment, *z is internal lever arm,* α is inclination angle of the compression strut, β is inclination angle of the stirrups, B_t is tensile force, B_r is unknown stirrup force, F_{cw} is concrete compressive strength, b' is reinforcement location, b_1 is unknown width and b_w is actual width.

These formulations, although simplified, establish the basis for Menn's dimensionless interaction curves. He defines:

- V_{R0} is shear resistance under pure shear (no bending),
  $$V_{R0} = f_{c,red} \cdot b_w \cdot cos\alpha \cdot sin\alpha \qquad \text{[Menn, 1990]}$$

- m_{R0} is moment resistance under pure bending (no shear),

$$m_{R0} = \omega_0 \cdot (b_0 + b')^2 \cdot f_c \cdot (1 - 0.5 \cdot \omega_0) \qquad \text{[Menn, 1990]}$$

where $\boldsymbol{\omega_0}$ is the mechanical reinforcement ratio.
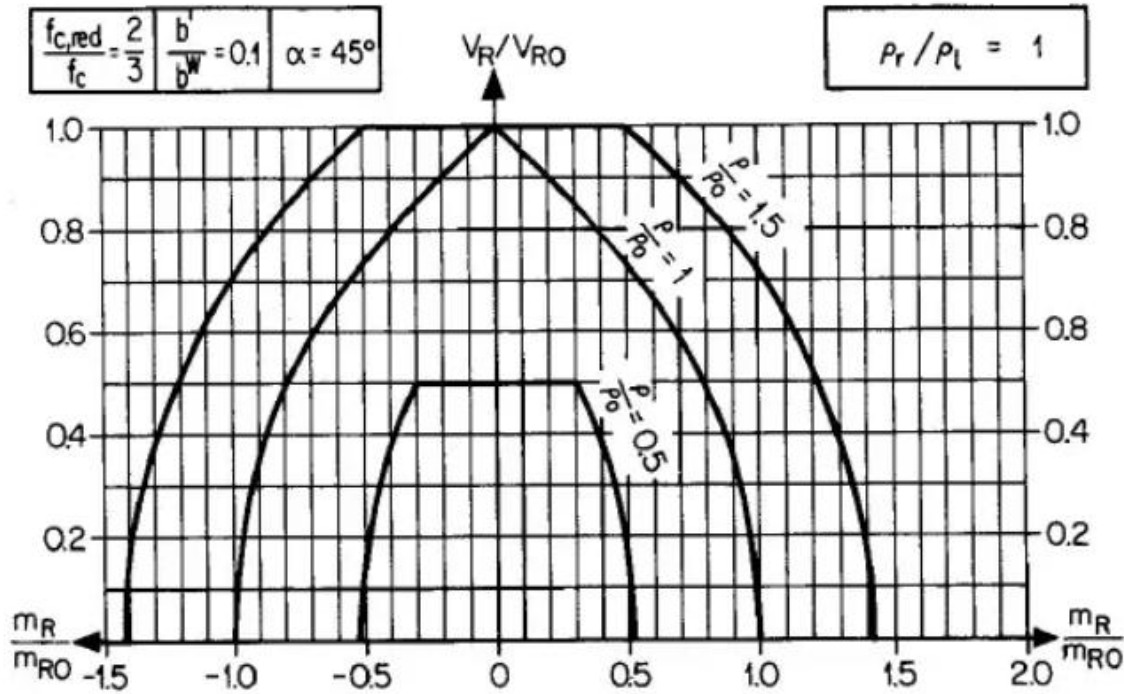
Figure 5. Shear – transverse bending interaction diagram (Menn, 1990)

Menn obtained a point in the interaction diagram by dividing the required sectional resistance $(V_R = \gamma_R \cdot \gamma_S \cdot V, m_R = \gamma_R \cdot \gamma_S \cdot m)$ by the resistances $(V_R/V_{R0}, m_R/m_{R0})$. Linear interpolation can be utilized between the curves plotted on a given diagram and between any two diagrams. (Menn, 1990)

Christian Menn's simplified interaction method, although not based on modern nonlinear computational mechanics, offers a remarkably intuitive and practical design approach. Developed in an era when finite element software and advanced numerical modeling tools were not yet available, Menn's methodology relied heavily on engineering judgment, years of design experience, and observational insight gained through built structures and testing. By introducing relationships between required web width and the available stress capacity, he translated

complex structural behavior into accessible expressions and charts. These diagrams, though approximately, proved highly valuable in the preliminary and even detailed design stages of box girder bridges, and they continue to be referenced in structural design literature.

In this thesis, Menn's interaction diagrams are revisited with the help of nonlinear finite element models. The comparison aims to assess how well his simplified assumptions reflect actual structural behavior under combined shear and moment, and how they hold up against more rigorous computational approaches. This dual perspective bridges the gap between traditional design intuition and modern simulation capabilities.

2.2.   Eurocode Background: Shear Design

When designing reinforced concrete beams under shear, Eurocode 2 provides a comprehensive framework to ensure safety by checking both concrete and shear reinforcement contributions. The total shear capacity, V_{Rd}, is determined as the minimum between the concrete contribution V_{Rcd} and the shear reinforcement contribution V_{Rsd}:

$$V_{Rd} = min(V_{Rcd}, V_{Rsd})$$

1. Shear Capacity of Reinforcement: V_{Rsd} (Eurocode 2, 2004)

If transverse reinforcement is provided (such as stirrups), the following expression is used to compute the shear resistance due to steel:

$$V_{Rsd} = \left(\frac{A_{sw}}{s}\right) \cdot f_{yd} \cdot 0.9d \cdot cot(\theta)$$

- Asw: Area of shear reinforcement (per spacing)
- s: Spacing between stirrups
- fyd: Design yield strength of steel
- d: Effective depth of section
- θ: Inclination of the concrete struts (usually 21.8° to 45°)

2. Shear Capacity of Concrete: V_{Rcd} (Eurocode 2, 2004)

The resistance of concrete to shear is calculated using:

$$V_{Rcd} = 0.9 \cdot d \cdot b_w \cdot \alpha_c \cdot v \cdot f_{cd} \cdot \left[\frac{cot(\theta)}{(1 + cot^2(\theta))} \right]$$

- b_w: Width of the web
- α_c: Coefficient accounting for prestressing (usually $\alpha_c = 1$ if $\sigma_{cp} = 0$)
- v: Reduction factor (commonly taken as 0.5)
- f_{cd}: Design compressive strength of concrete
- θ: Inclination angle of concrete strut
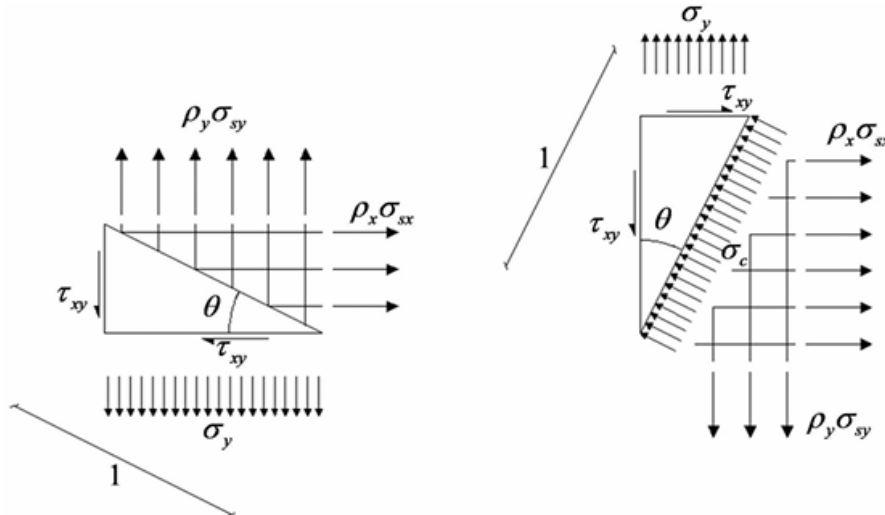
Figure 6. Inclination angle of concrete strut
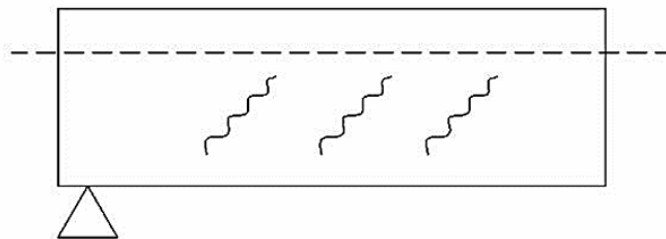
Figure 7. Cracking in a partial section

3. Evaluation Process

Depending on the value of cot(θ), one of three failure mechanisms is assumed:

- If cot(θ) < 1 → failure of concrete strut → use V_{Rcd} with θ = 45°

Graph 2. τ_rd – θ relation when cot(θ) < 1
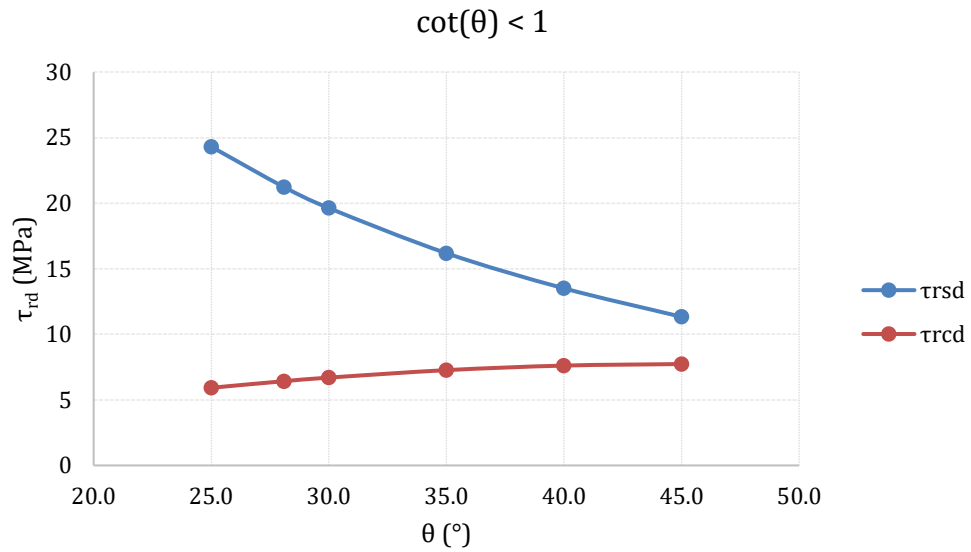
- If cot(θ) > 2.5 → failure of shear reinforcement → use V_{Rsd} with θ = 21.8°
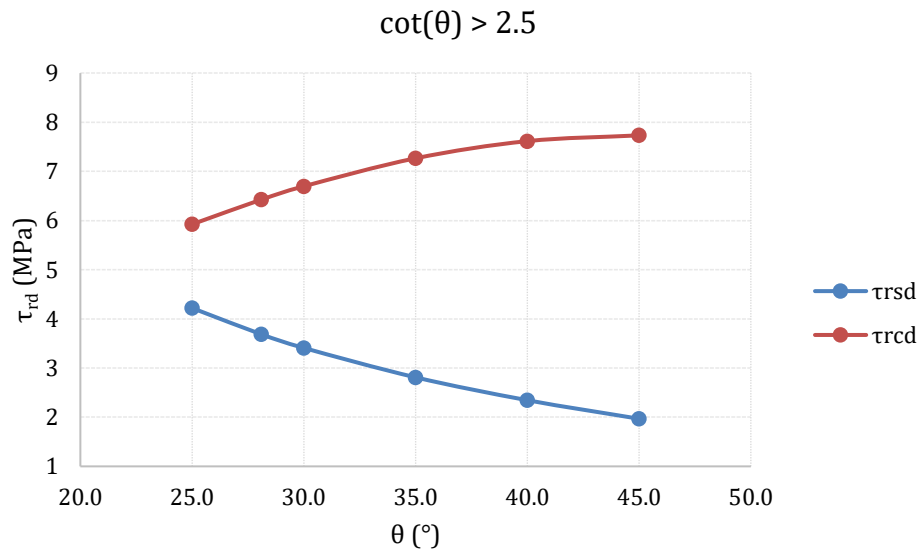
Graph 3. τ_rd – θ relation when cot(θ) > 2.5

- If $1 \leq \cot(\theta) \leq 2.5 \rightarrow$ simultaneous failure $\rightarrow$ solve $V_{Rsd} = V_{Rcd}$ to find θ

$$1 \leq \cot(\theta) \leq 2.5$$
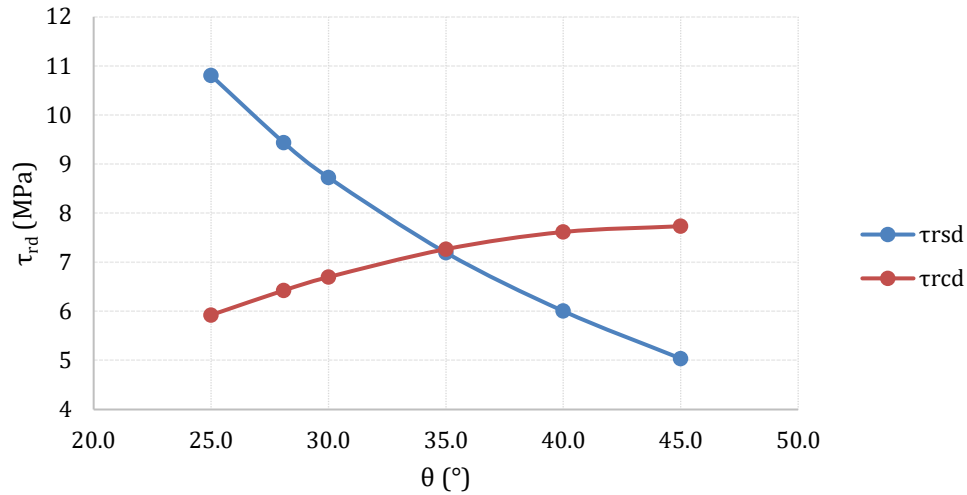
Graph 4. $\tau_{rd} - \theta$ relation for $1 \leq \cot(\theta) \leq 2.5$

This approach avoids the need for graphical iteration by calculating θ using the mechanical reinforcement ratio:

$$\omega_{sw} = \frac{(A_{sw} \cdot f_{yd})}{(s \cdot b_w \cdot f_{cd})} \rightarrow \cot(\theta) = \sqrt{\left(\frac{v \cdot \alpha_c}{\omega_{sw}}\right) - 1}$$

These equations and procedures are illustrated in the Politecnico di Torino course material on "Shear in RC Cross-Sections" (2023) and reflect standard Eurocode 2 practice.
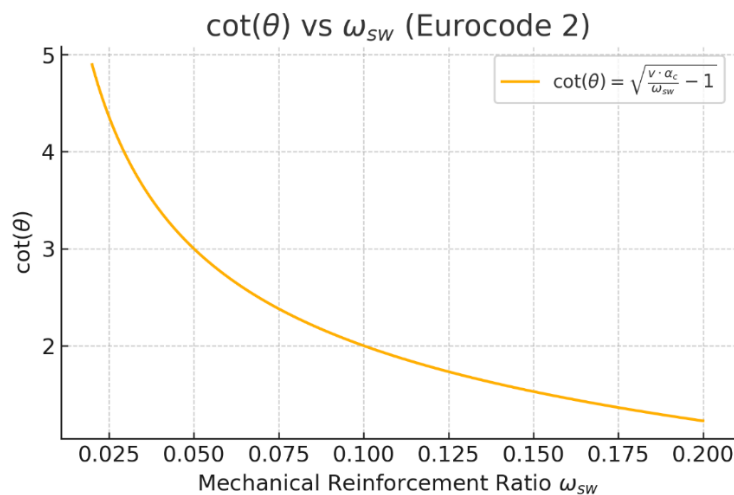
Graph 5. Relation between $\cot(\theta)$ and ω_{sw}

13

2.3.   fib Model Code Background: Shear Design

The Fédération Internationale du Béton (fib) is a global technical organization based in Switzerland, formed through the merger of the CEB (Comité Euro-International du Béton) and FIP (Fédération Internationale de la Précontrainte). It plays a key role in advancing the knowledge and standards of structural concrete, particularly through its Model Codes (e.g., fib Model Code 1990, 2010, and the ongoing development of fib Model Code 2020).

fib is highly regarded in the international engineering community for proposing scientifically grounded and experimentally verified formulations for concrete behavior. Its provisions are often more detailed and flexible compared to traditional codes like Eurocode 2, allowing different **Levels of Approximation (LoA)** based on the desired accuracy and available data.

The design shear resistance can be determined by using:

$$V_{rd} = V_{rd,c} + V_{rd,s} \leq V_{rd,max}$$

Design shear resistance attributed to the concrete:

$$V_{rd,c} = k_v \cdot \frac{\sqrt{f_{ck}}}{\gamma_c} \cdot b_w \cdot z_v$$

where:
- k_v: Empirical factor,
- f_{ck}: Characteristic compressive strength of concrete,
- γ_c: Partial safety factor for concrete,
- b_w: Web width,
- z_v: Internal lever arm (effective depth, generally $z \approx 0.9$).

Design shear resistance provided by shear reinforcement:

$$V_{rd,s} = \frac{A_{sw}}{s_w} \cdot z_v \cdot f_{ywd} \cdot \cot(\theta)$$

where:

- A_{sw}: Area of shear reinforcement within spacing s_w,
- s_w: Spacing of shear reinforcement,
- f_{ywd}: Design yield strength of shear reinforcement,
- θ: inclination angle of the compressive stress field which depends on the LoA.

$$1 \leq \cot(\theta) = \sqrt{\frac{k_\varepsilon \cdot f_{cd}}{\rho_w \cdot f_{ywd}} - 1} \leq \cot(\theta)_{min}$$

Maximum shear resistance related to crushing of concrete carrying the compression field:

$$V_{rd,max} = \frac{k_\varepsilon \cdot f_{cd} \cdot b_w \cdot z_v}{\cot(\theta) + \tan(\theta)}$$

where;

- k_ε: Reduction factor depending on strain state in longitudinal reinforcement; accounts for ductility limitations.
- f_{cd}: Design compressive strength of concrete

The fib Model Code 2010 proposes a multi-level design strategy for shear verification in reinforced concrete members, classified into:

1) Level I approximation   (fib, 2020)

Design shear resistance in LoA-I is given by:

$$V_{rd} = V_{rd,s} \leq V_{rd,max}$$

The minimum inclination of the compressive stress field is:

$cot(\theta)_{min} = 2.2$ for members with subjected to axial compression,
$cot(\theta)_{min} = 1.7$ for reinforced concrete member,
$cot(\theta)_{min} = 1.2$ for members with subjected to axial tension.

The reduction factor should be taken as:

$$k_\varepsilon = 0.55$$

2) Level IIa approximation   (fib, 2020)

Design shear resistance in LoA-IIa is given by:

$$V_{rd} = V_{rd,s} \leq V_{rd,max}$$

The minimum inclination of the compressive stress field is:

$$cot(\theta)_{min} = cot(20° + 4000 \cdot \varepsilon_x)$$

where ε_x represents the longitudinal strain at the mid-depth of the effective shear depth as shown in figure given below:
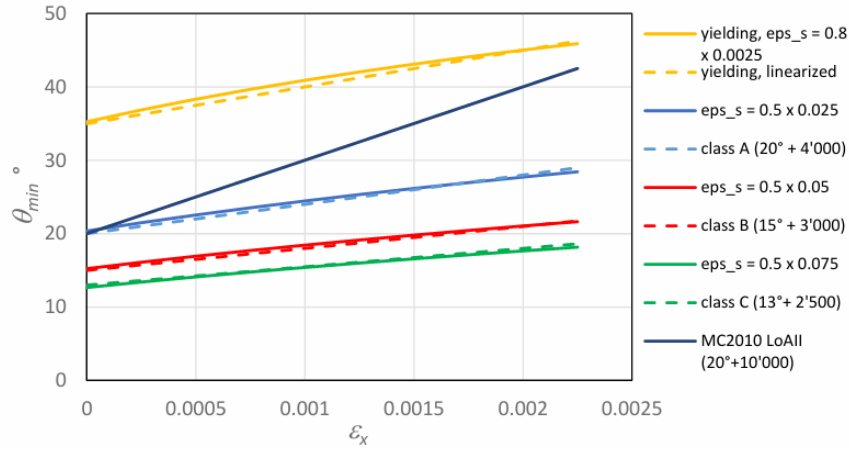
Figure 8. Relation between $\theta_{min} - \varepsilon_x$ (fib 2020 Model Code pp.680)

For shear reinforcement more ductile than class A, the minimum inclination of the compressive stress field is:

$$cot(\theta)_{min} = cot(15° + 3000 \cdot \varepsilon_x) \qquad \text{for ductility class B}$$
$$cot(\theta)_{min} = cot(13° + 2500 \cdot \varepsilon_x) \qquad \text{for ductility class C and D}$$

The contribution of concrete to the design shear resistance is neglected. The reduction factor can be calculated:

$$k_\varepsilon = \frac{1}{1 + 1.10 \cdot \varepsilon_1} \leq 1.0$$

where:

$$\varepsilon_1 = \varepsilon_x + (\varepsilon_x + 0.001) \cdot cot^2(\theta)$$

The longitudinal strain ε_x at mid-depth of the effective shear depths is calculated based on:

$$\varepsilon_x = \frac{1}{2 \cdot E_s \cdot A_s} \cdot \left(\frac{M_{Ed}}{z_v} + \frac{V_{Ed}}{s} \cdot cot(\theta) + N_{Ed} \cdot \left(\frac{1}{2} - \frac{\Delta e}{z_v} \right) \right) \geq 0$$

where, as a first approximation, $cot(\theta) = 2.0$ may be assumed.

17

- M_{Ed} and V_{Ed} shall be taken as positive quantities and N_{Ed} as positive for tension and negative for compression.
- The strain ε_x can exceed half of yield strain $\varepsilon_{sy}/2$ but must not exceed 0.003. Detailed section analysis is required if this limit is approached.
- If ε_x is negative, replace $E_s \cdot A_s$ with $(E_c \cdot A_{c,ten} + E_s \cdot A_s)$, where $A_{c,ten}$ is the tensioned concrete area due to bending.
- A_s includes only main tensile longitudinal bars; any web reinforcement is ignored.

3) Level IIb approximation   (fib, 2020)

Design shear resistance in LoA-IIb is given by:

$$V_{rd} = V_{rd,c} + V_{rd,s} \leq V_{rd,max}$$

The inclination of the compressive stress field for $V_{rd,c} + V_{rd,s}$ can be calculated:

$$cot(\theta) = cot(29° + 7000 \cdot \varepsilon_x)$$

while for $V_{rd,max}$, $cot(\theta)$ can be selected within the ranges used in LoA-IIa.
To determine the design shear resistance $V_{rd,c}$ attributed to the concrete the given expression should be used:

$$k_v = \frac{0.4}{(1 + 1500 \cdot \varepsilon_x)}$$

Table 1. Overview of design equations for different levels of approximation

LoA	Concrete Contribution	Min. compressive stress field inclination	Strength reduction factor for $V_{rd,max}$
I	$V_{Rd,c} = 0$	$cot(\theta)_{min} = fixed$	$k_\varepsilon = fixed$
IIa	$V_{Rd,c} = 0$	$cot(\theta)_{min} = f(\varepsilon_x)$	$k_\varepsilon = f(\varepsilon_x, \theta)$
IIb	$V_{Rd,c} = f(\varepsilon_x)$	$cot(\theta) = f(\varepsilon_x)$	$k_\varepsilon = f(\varepsilon_x, \theta)$

In summary, the fib Model Code's multi-level approach to shear design enables engineers to select the appropriate level of approximation based on the complexity of the structure, the available data, and the required level of accuracy. While Level I provides a practical and conservative solution for standard design cases, Levels IIa and IIb offer more refined models accounting for strain conditions, ductility classes, and stress field optimization. These methods form the theoretical basis for advanced FEM verification and allow consistent comparison with simulation-based interaction domains, such as those developed in this thesis.

3. Numerical Modelling with ATENA

ATENA is a nonlinear finite element analysis software specifically developed for simulating the behavior of reinforced concrete structures. It allows for accurate modeling of cracking, tension stiffening, and post-peak softening, which are essential in evaluating the failure mechanisms in concrete elements. In this study, ATENA 3D Engineering was used to investigate the interaction between longitudinal shear and transverse bending in concrete web panels.

The analysis began with a simplified 2D wall model to focus on the local behavior of the bridge web before extending the study to a full box girder model. The wall panel, sized 3 meters by 5 meters with 0.4 meters thickness, was designed to represent a typical web portion of a box girder bridge. Using a simplified sub-model enables faster simulations, easier parameter control, and a clearer understanding of the fundamental interaction mechanisms.

In the numerical model, a **layered shell element** was used to accurately represent the geometry and reinforcement distribution within the wall. This type of element allows the definition of multiple reinforcement layers at different depths without the need for a full 3D solid mesh, which reduces computational time while preserving the accuracy in capturing shear and bending interactions.

3.1. Geometry and Element Type

The numerical model is based on a reinforced concrete wall panel that represents a typical web segment of a box girder bridge. Its geometric and layering properties are defined as follows:

a) **Panel dimensions:**
- Length (X-direction): 5.0 meters
- Height (Z-direction): 3.0 meters
- Total thickness (Y-direction): 0.4 meters
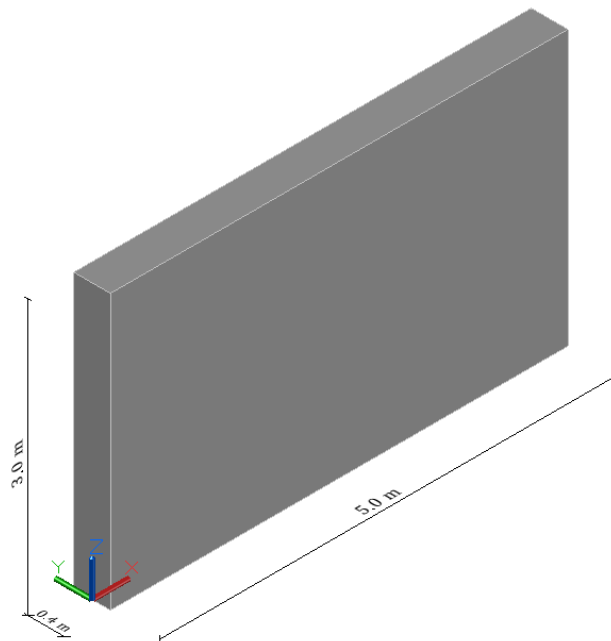
Figure 9. Panel sketch with dimensions

b) **Element type:**
- 2D Layered Shell Element was used in ATENA.
- This element type allows for defining reinforcement layers across the thickness, reducing computational effort while capturing shear–bending interaction effectively.

c) Layer configuration:

The total thickness was subdivided into 4 equal concrete layers, each with 0.1 m thickness.

- **Layer 1 (top)**: Concrete cover with vertical reinforcement placed at a depth of 37 mm from the top surface, horizontal reinforcement placed at a depth of 61 mm from the top surface.

- **Layer 2**: Concrete only (no reinforcement).

- **Layer 3**: Concrete only (no reinforcement).

- **Layer 4 (bottom)**: Concrete cover with same reinforcement configuration with Layer 1.
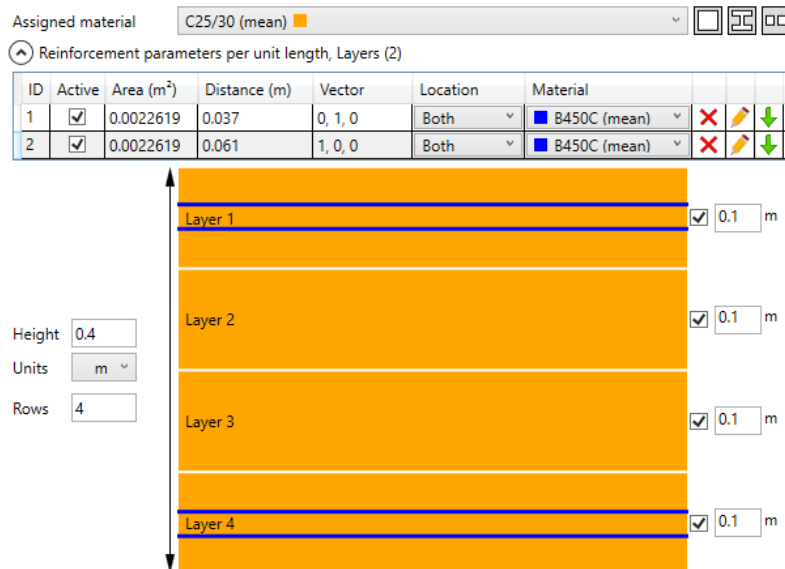
Figure 10. 2D Layered shell properties in ATENA

d) Concrete cover:

- 25 mm cover assumed from both outer surfaces.

- The reinforcement bars are placed within the shell using ATENA's internal reinforcement layer system, not as separate bar elements.

e) Reinforcement details:

- Bar diameter: 24 mm (ϕ24) and 20 mm (ϕ20)

- Spacing: 200 mm

3.2.   Material Properties

According to Eurocode 2 and commonly accepted engineering practice, the material strength values used in design and simulation can be categorized as:

Table 2. Material properties with safety design values

	Concrete:	Reinforcement:
Mean Strength	$f_{cm} = f_{ck} + 8$	$f_{ym} = 1.10 \cdot f_{yk}$
Characteristic	f_{ck}	f_{yk}
Design strength	$f_{cd} = f_{ck}/\gamma_c$	$f_{yd} = f_{yk}/\gamma_s$
Safety Factor	$\gamma_c = 1.5$	$\gamma_s = 1.15$

In this study, different material strengths were defined depending on the type of analysis. Concrete and reinforcement properties were assigned using strength parameters consistent with Eurocode 2 terminology. Both **mean**, **characteristic**, and **design values** were used based on the objective of each simulation.

3.2.1. Concrete

- Material model in ATENA: CC3DNonLinCementitious2
- Poisson's ratio: $\mu = 0.2$

  C25/30 (used in most simulations)
- Mean compressive strength: $f_{cm} = 33\ MPa$
- Characteristic strength: $f_{ck}\ = 25\ MPa$
- Design compressive strength: $f_{cd}\ = 16.67\ MPa$
- Tensile strength : $f_t = 2.6\ MPa$
- Young modulus : $E_c = 31\ GPa$
- Fracture energy : $G_F = 65\ N/m$
- Used in: nonlinear FE simulations and Eurocode-based calculations
- Hardening parameter : k $\approx$ 1 (elastic – perfectly plastic behaviour)

C40/50 (used for comparative purposes)

- Mean compressive strength: $f_{cm} = 48\ MPa$
- Tensile strength : $f_t = 3.5\ MPa$
- Young modulus : $E_c = 35\ GPa$
- Fracture energy : $G_F = 87.5\ N/m$
- Other parameters were not used; only mean value considered
- Used in: selected simulations to observe material influence on behavior
- Hardening parameter : k = 1.15 (elastic – plastic with strain hardening)

3.2.2. Steel Reinforcement

- Type: B450C (used in all models)
- Bar diameters: ϕ24 mm and ϕ20 mm used in different simulations.
- Mean strength: $f_{ym} = 495\ MPa$
- Characteristic strength: $f_{yk} = 450\ MPa$
- Design strength: $f_{yd} = 391\ MPa$
- Modulus of Elasticity : $E_s = 210\ GPa$
- Ultimate strain : $\varepsilon_u = 0{,}075$
- Density : $\rho = 7850\ kg/m^3$

Reinforcement was defined using embedded reinforcement layers in the shell element.
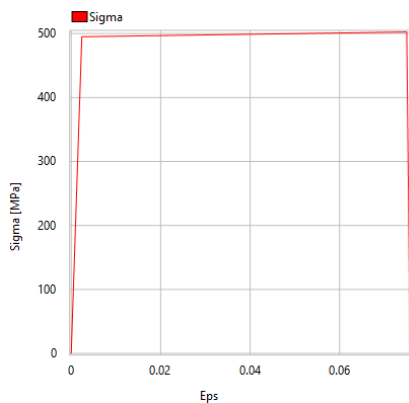
Graph 6. σ – ε diagram of elastic – perfectly plastic behaviour (k ≈ 1)
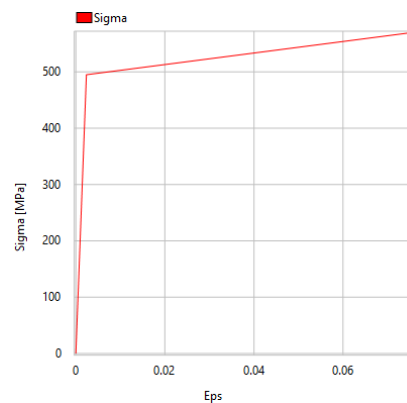
Graph 7. σ – ε diagram of elastic – plastic with strain hardening (k = 1.15)

3.3.   Reinforcement Detailing

The reinforcement was symmetrically placed on both faces of the wall panel, reflecting realistic detailing in box girder webs. Two different bar diameters were studied: $\phi24$ mm and $\phi20$ mm, both conforming to B450C high-ductility steel. All reinforcement was arranged with a constant spacing of 200 mm in both vertical and horizontal directions.

The reinforcement configuration consists of both vertical and horizontal bars placed on the inner and outer faces of the wall. Starting from the exterior toward the interior, the layer sequence is as follows:

	Concrete cover 25 mm
Layer 1 →	Vertical reinforcement
	Horizontal reinforcement
Layer 2 →	Core concrete
Layer 3 →	Core concrete
	Horizontal reinforcement
Layer 4 →	Vertical reinforcement
	Concrete cover 25 mm

This configuration ensures symmetrical stiffness and strength, especially under combined bending and shear effects. The vertical bars are located slightly closer to the outer surface, while horizontal bars are placed just inside, enabling proper anchorage and interaction. Reinforcement was implemented using layered reinforcement definitions within the 2D shell element in ATENA, without explicitly meshing individual bars.

In a secondary test series, both the vertical and horizontal reinforcement diameters were reduced from $\phi24$ mm to $\phi20$ mm, while keeping the spacing constant at 200 mm. This variation was implemented to investigate the effect of overall reinforcement ratio on the structural capacity, especially regarding the interaction between shear and bending. All other material and geometrical parameters remained unchanged to isolate the influence of bar diameter.

3.4.   Boundary Conditions

The boundary conditions were defined to realistically simulate the panel behaviour under combined axial, shear, and bending loads while maintaining global equilibrium and avoiding rigid body motion. Four support points were used to ensure statical determinacy and geometric stability:
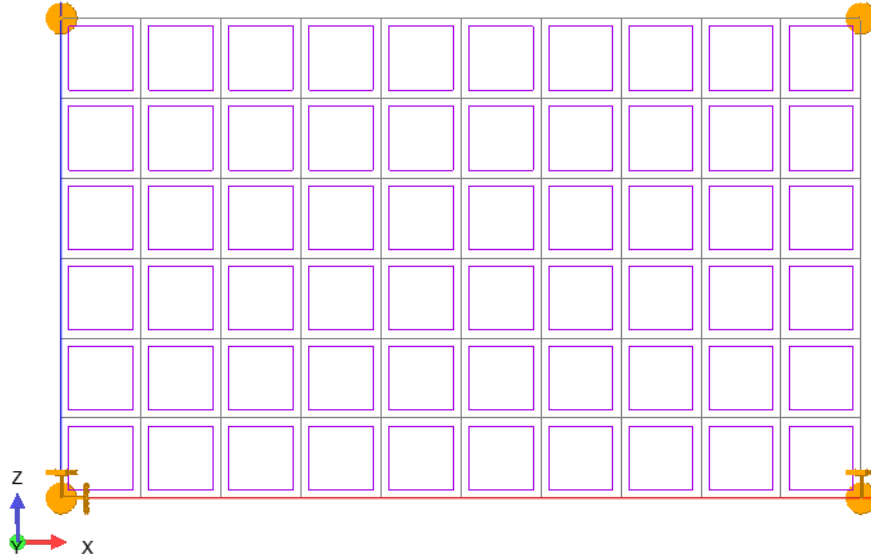
Figure 11. Boundary conditions representation in ATENA model

Table 3. Boundary conditions

Point	Coordinate	U_x	U_y	U_z	
A	(0, 0, 0)	fixed	fixed	fixed	fully pinned
B	(5, 0, 0)	free	fixed	fixed	roller support
C	(5, 0, 3)	free	fixed	free	prevents rigid body motion
D	(0, 0, 3)	free	fixed	free	prevents rigid body motion

All rotations are left free to allow natural shell behaviour. This configuration ensures stability while avoiding over constraint.

3.5.   Mesh Definition

A structured mesh consisting of 50 × 50 cm quadrilateral shell elements was used to discretize the wall panel. This resulted in 10 elements along the horizontal (X) direction and 6 elements along the vertical (Z) direction, totaling 60 elements. Manual meshing was preferred to ensure uniformity and compatibility with load application points, as nodal coordinates aligned with both edge and center loading locations.

The mesh was fine enough to capture crack patterns and nonlinear stress distribution accurately, while still being computationally efficient for multiple simulations. Additionally, the element size was selected to maintain consistency with the reinforcement spacing and to allow proper definition of reinforcement layers within the shell structure.

3.6.   Loading Scenarios

The loads in this study were not applied as distributed line loads, but rather as concentrated nodal forces. Given the mesh size of 50 × 50 cm, the panel was divided into 6 vertical (Z-direction) and 10 horizontal (X-direction) elements, forming a total of 60 shell elements. The mesh node locations and element centres were used as load application points in order to distribute the forces realistically and maintain control over load increment behaviour.

In order to investigate the structural behaviour of the wall panel under different loading conditions, a series of loading scenarios were designed and applied within ATENA. These scenarios were created to individually assess the effects of axial load (prestressing), shear, and bending moment, as well as their combinations.

3.6.1. Axial Load – Prestressing Simulation

Axial compression was applied to represent prestressing effects and was simulated by placing 12-point loads on each of the left and right vertical edges of the panel. The total prestressing force was incrementally applied over 10 equal steps, ensuring no immediate cracking while allowing the axial stress to develop gradually.
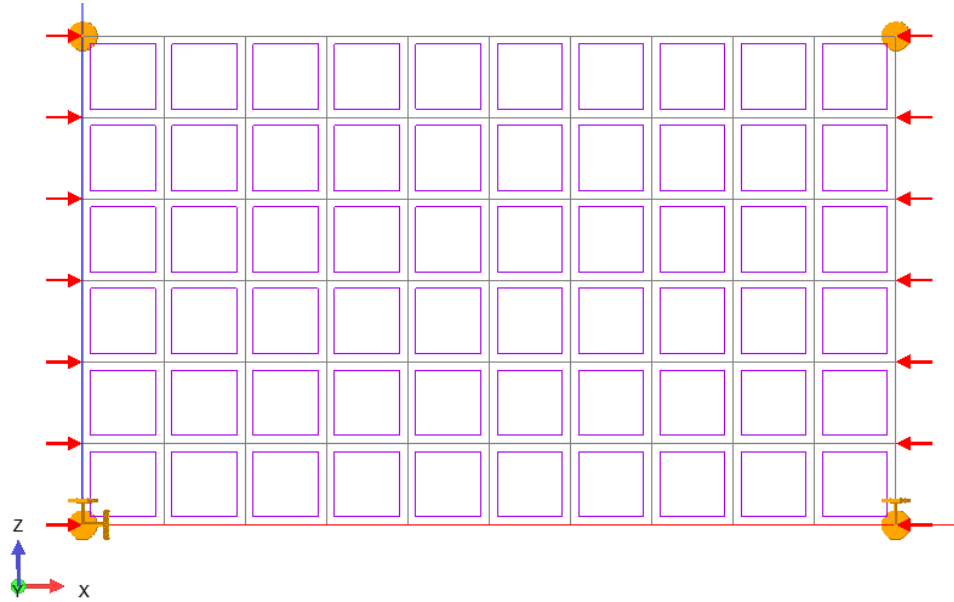
Figure 12. Axial loading – prestressing simulation

For each level, the resulting axial stress on the panel was calculated using:

$$N_{tot} = 12 \cdot n \cdot m$$

where **n** is the interrupted step and **m** is the step multiplier

$$\sigma_{cp} = \frac{N_{tot}}{A_c}$$

where A_c is the gross area of the panel. Prestressing levels were defined as:

$$\sigma_{cp} = 0, 2.5, 5.0, 7.5, 10.0 \ MPa$$

The purpose of this stage was not to induce cracking, but to examine how varying levels of axial compression influence shear and bending resistance.

3.6.2. Shear-Only Simulation (Determination of V$_{rd}$)

Shear forces were applied in a self-equilibrated pattern along both the top and bottom (horizontal) and left and right (vertical) edges of the panel.
- 20-point loads were applied at the top and bottom edges
- 12-point loads were applied at the left and right edges

The directions were chosen to induce positive and negative shear components along X and Z axes, simulating an internal shear flow consistent with panel behavior. Again, each point load was 1 kN, and total shear was scaled using the step multiplier. The total applied shear at top edge was calculated as:

$$V_{rd} = 20 \cdot n \cdot m$$

where $\boldsymbol{n}$ is the interrupted step and $\boldsymbol{m}$ is the step multiplier.
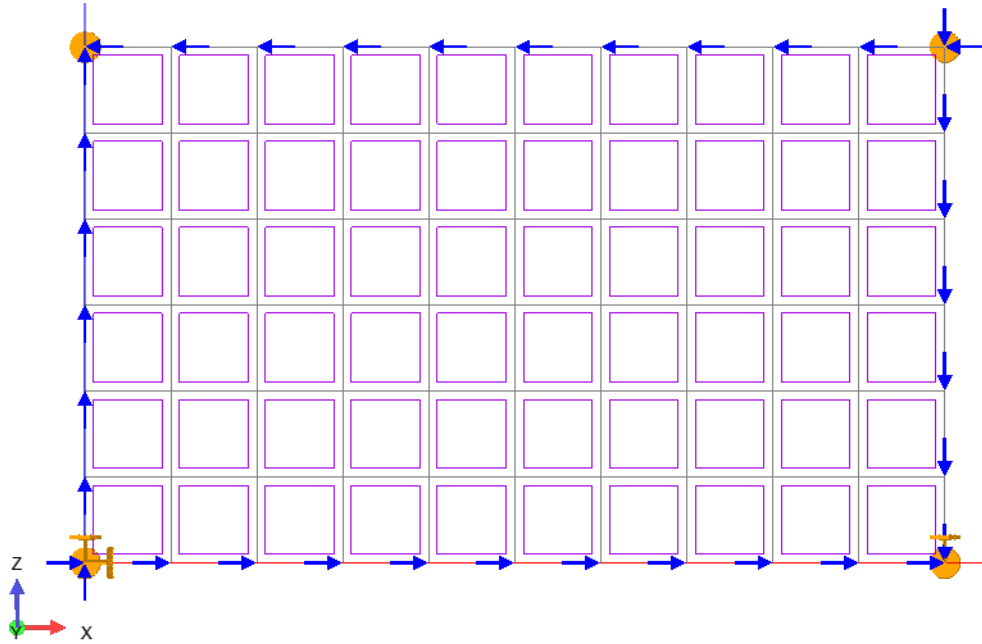
Figure 13. Shear loading – pure shear simulation

3.6.3. Moment-Only Simulation (Determination of M_{rd})

To simulate bending, 20-point loads were applied on the top edge and 20 on the bottom edge in opposite directions, forming a moment-inducing force couple. Each point carried a unit load, scaled using the multiplier. The total applied moment at each step was calculated as:

$$M_{rd} = 20 \cdot n \cdot m$$

where n is the interrupted step and m is the step multiplier.
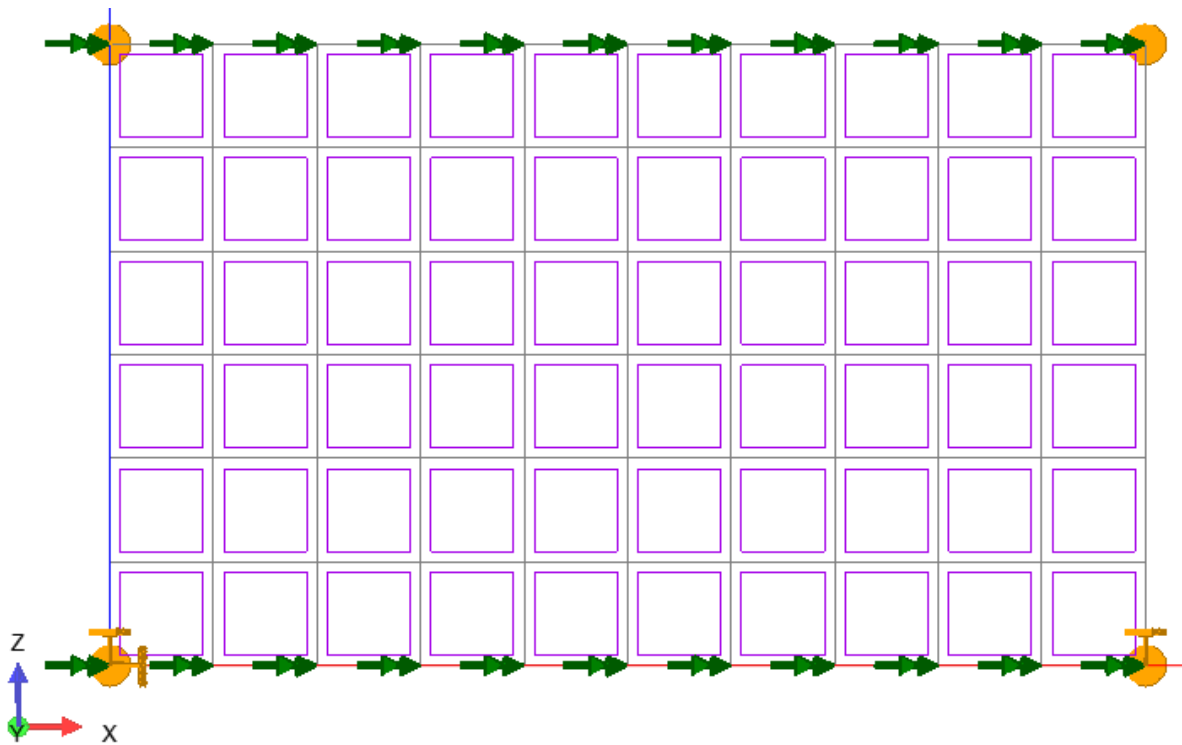
Figure 14. Moment force loading – pure bending simulation.

3.6.4. M–V Interaction (Combined Loading)

After the individual capacities for pure shear and pure moment (Vrd and Mrd) were identified under different prestressing levels, a series of combined loading simulations were carried out to define the interaction domain between these two actions. In each simulation, a selected level of prestress was first applied and held constant. Then, a shear load corresponding to a defined percentage of the previously determined Vrd value (ranging from 90% down to 20%) was imposed on the model. Once the shear was in place, a bending moment was gradually introduced through opposing force couples until failure occurred. The corresponding moment at failure was recorded for each shear level.
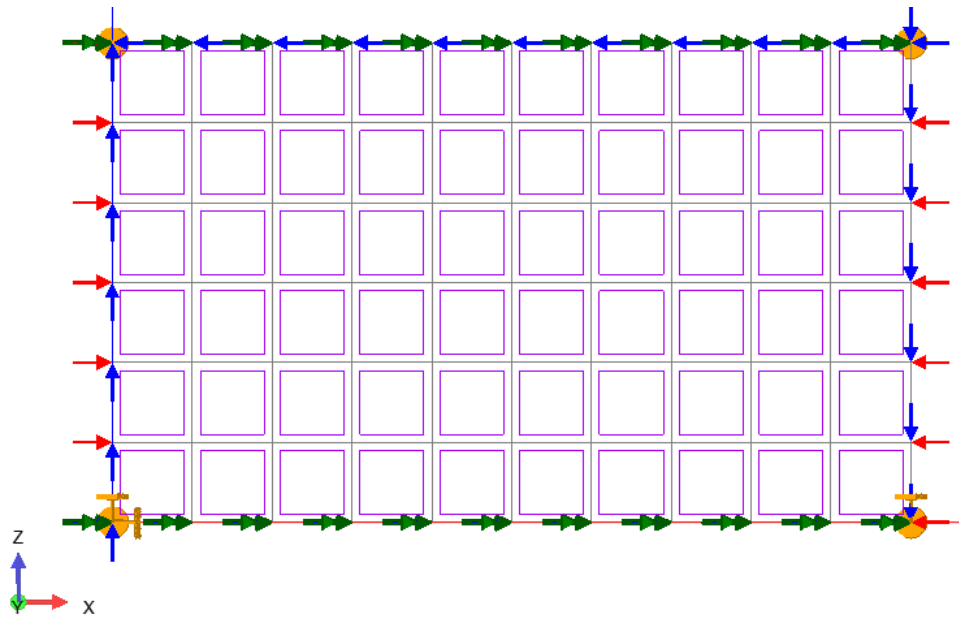
Figure 15. Combined load configuration

To allow for dimensionless comparison and consistent plotting, the resulting shear and moment capacities were normalized using the following expressions:

$$\tau = \frac{V_{rd}}{b \cdot l} \qquad\qquad \mu = \frac{M_{rd}}{b \cdot h^2 \cdot f_{cd}}$$

where **b** is the panel thickness, **l** and **h** are the length and height of the wall respectively, and **f$_{cd}$** is the design compressive strength of concrete.

These normalized values (τ and μ) were used to build the shear–moment interaction domains, providing a clear framework for comparing numerical results with analytical models available in the literature.

4. Post-Processing and Results Evaluation

This chapter presents the results obtained from the nonlinear finite element analyses conducted using ATENA. The aim is to evaluate the shear and moment resistance of the modeled wall element under various prestressing levels and reinforcement configurations. The post-processing phase includes the extraction of failure loads, crack development, stress distributions, and support reactions.

All numerical simulations were performed using the ATENA Engineering environment, and results were visualized and evaluated through the ATENA Studio Post-Processor. The failure criteria were based on the inability of the model to converge under increasing load steps, and the corresponding step at which the analysis was interrupted was considered the critical capacity point.

In addition to numerical outputs, the structural response of the panel during each simulation was carefully monitored. This included observing the deformation patterns, crack initiation and propagation, and stress redistribution throughout the loading steps. These qualitative evaluations helped verify the realism of the model and supported the interpretation of final resistance values.

In the following sections, results are first categorized based on individual loading cases — pure axial, shear-only, and moment-only — followed by combined shear-moment loading cases used to build the interaction domains. The influence of prestressing and reinforcement diameter is also explored in detail through normalized resistance comparisons.

4.1.   Result Extraction and Observation in ATENA Studio

The evaluation of structural performance and failure mechanisms was conducted through ATENA Studio's post-processing environment. Several output windows and visual tools were utilized to extract relevant data from each simulation and to interpret the behaviour of the panel under different loading conditions. The following key result types were considered:

a) Reaction Forces (Support Reactions)

This output was used to verify the accuracy of boundary conditions and the equilibrium of the model. For example, when applying self-equilibrated axial loads, the reactions at the supports were expected to be nearly zero. Any unexpected values in this window indicated potential issues with constraint definitions.
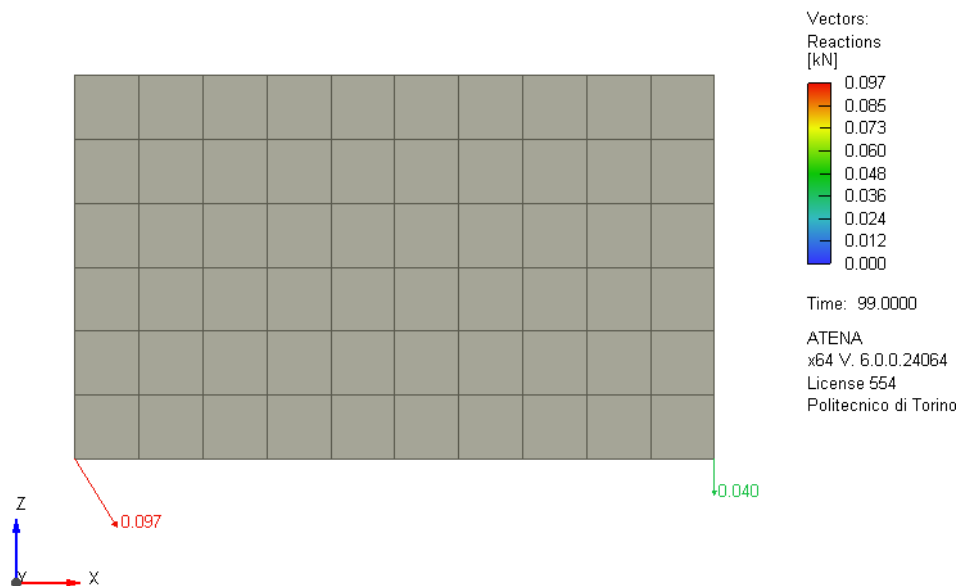
Figure 16. Post-processor – support reactions

b) Crack Pattern and Width Visualization

One of the most essential outputs in nonlinear concrete modeling, this feature allowed the identification of crack initiation, propagation, and orientation. The crack width and distribution were directly correlated with structural damage and used to visually confirm the mode of failure (shear-dominant or flexural-dominant).
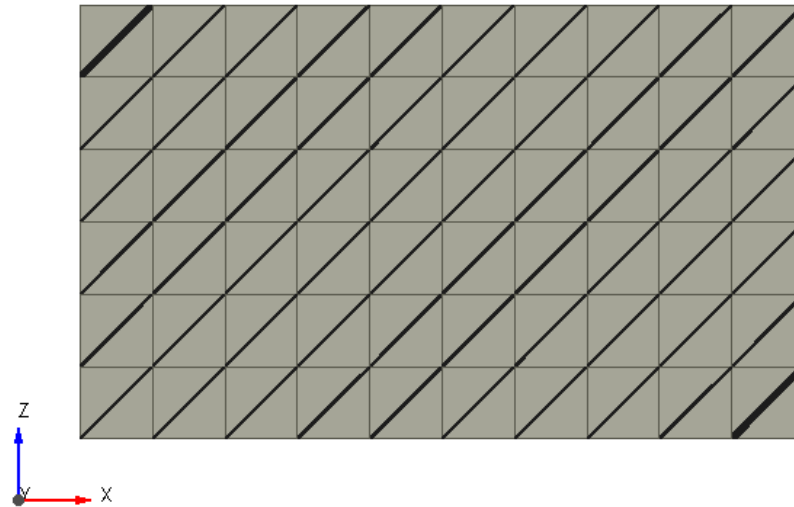
Figure 17. Post-processor – crack propagation and crack width

c) Principal Stress and Strain Fields

Contour plots showing the principal stresses (especially tensile) helped identify stress concentrations and potential failure zones before cracking occurred. These fields also revealed the directionality of internal forces, aiding in the interpretation of crack directions and reinforcement effectiveness.
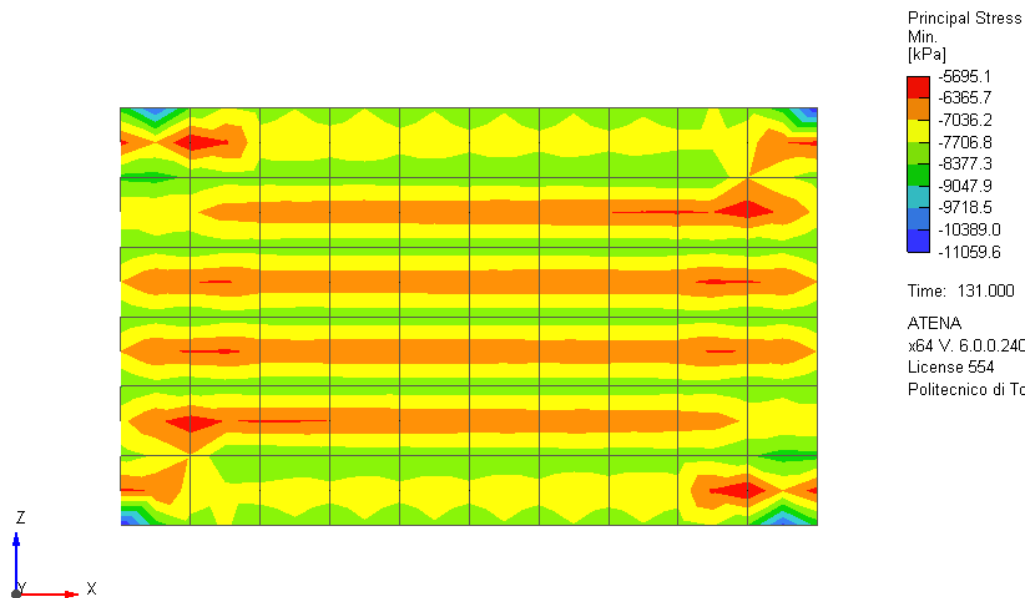
Figure 18. Post-processor – Principal min. stress distribution

d) Displacement and Deformed Shape

The deformed geometry at various steps provided insight into the overall structural behavior, including lateral drift, panel curvature, and instability tendencies. Especially under combined loading, these outputs helped visualize the contribution of axial compression, shear deformation, and bending rotation.
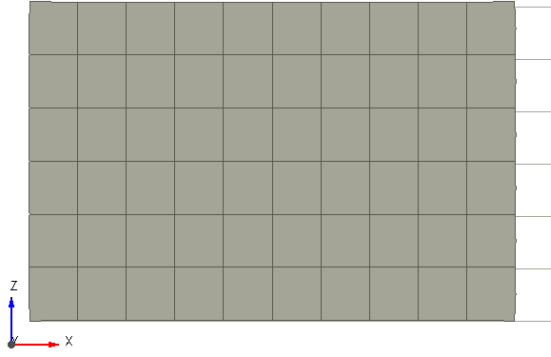
Figure 19. Deformed shape under axial compression
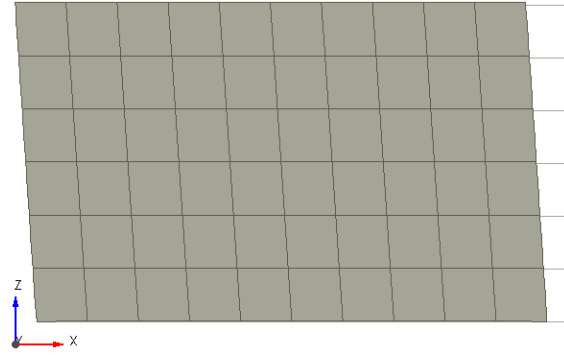
Figure 20. Deformed shape under shear deformation
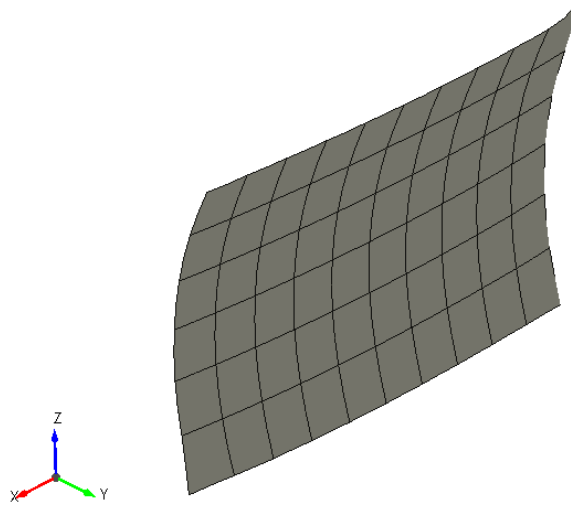
Figure 21. Deformed shape under combination of axial compression, shear and bending

e) Load Step Information and Convergence Status

Each simulation step was incrementally loaded using predefined multipliers. The interrupted step—at which the model failed to converge—was considered the failure point. Recording the load multiplier and step number at this stage enabled the calculation of V_{rd} and M_{rd} values.

These visual and numerical tools provided a comprehensive understanding of how the panel responded throughout the loading process. By combining both quantitative values (reactions, load steps) and qualitative observations (crack formation, deformation modes), the results could be evaluated with greater confidence and engineering judgment.
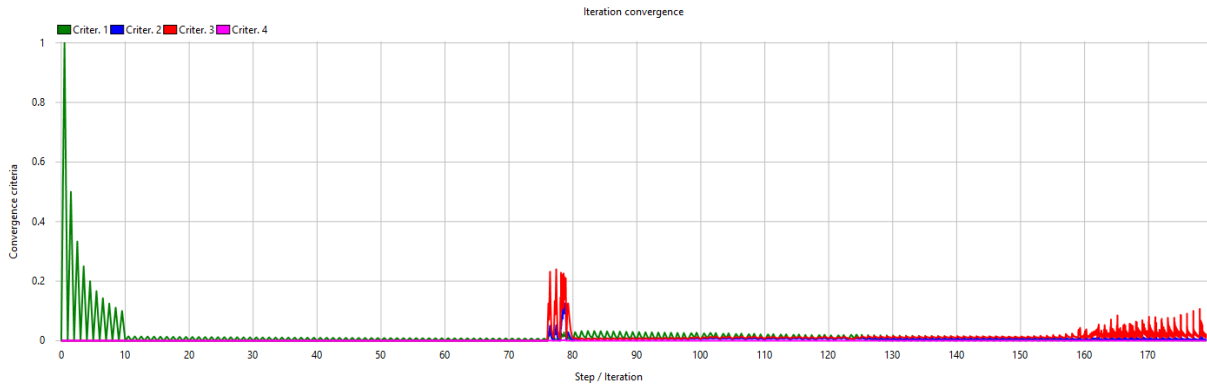
Figure 22. Iteration convergence progress

4.2.   Shear Resistance Results

In order to determine the shear resistance of the panel, a series of simulations were performed using a constant prestressing level and gradually increasing shear forces applied along the top and bottom edges. These forces were defined as concentrated point loads distributed across nodes at element intersections, representing a self-equilibrated shear loading condition. The analysis continued incrementally, with the load scaled through a predefined multiplier at each step, until the model could no longer converge due to excessive deformation or crack development. The step at which the simulation was interrupted was considered the failure point, and the corresponding total shear load was recorded as the shear capacity V_{rd} .

For each simulation, the total applied shear force was calculated based on the number of nodal loads and the step multiplier:

$$V_{rd} = 20 \cdot n \cdot m$$

where n is the interrupted step and m is the step multiplier

To enable a dimensionless comparison of shear resistance across different prestressing levels and reinforcement configurations, the shear force was normalized using the following expression:

$$\tau = \frac{V_{rd}}{b \cdot l}$$

where b is the panel thickness and l is the length of the wall. This value, expressed in MPa, represents the average shear stress resisted by the structure at failure. Throughout the loading process, the panel behaviour was carefully monitored using ATENA Studio's post-processing tools. Prior to cracking, the structure showed negligible support reactions, validating the effectiveness of the self-equilibrated loading setup. However, after the onset of cracks, internal force redistribution resulted in increased reactions at the supports, especially near the failure step. Crack development, principal stress distribution, and displacement contours were also observed to confirm that the failure mode was primarily shear-driven.

4.2.1. Influence of Prestressing Level

To investigate the effect of prestressing on shear resistance, simulations were performed for two different reinforcement configurations: ϕ24 mm and ϕ20 mm bars. In both cases, only the mean material properties were used. Axial compression (prestressing) was applied at levels from 0 MPa to 20 MPa, in 2.5 MPa increments.

For each prestress level:

- A constant axial force was first applied.
- Then, incremental shear forces were added until the model failed to converge.

Two values were extracted for each simulation:

1. The crack initiation load, where visible diagonal cracks developed across the panel.
2. The shear capacity at failure, defined by the interrupted step in the analysis.

Table 4. Results for ϕ24

σ$_{cp}$ (MPa)	Crack Load	V$_{rd}$ (kN/m)	τ$_{rd}$ (MPa)	α$_c$	Failure Type
0.0	820.00	2480.00	6.20	1.000	Diagonal Shear
2.5	1200.00	2880.00	7.20	1.076	Diagonal Shear
5.0	1380.00	3220.00	8.05	1.152	Diagonal Shear
7.5	1560.00	3460.00	8.65	1.227	Inclined + flexural
10.0	1820.00	3420.00	8.55	1.250	Inclined + ductile
12.5	2120.00	3200.00	8.00	1.250	Compression-driven
15.0	2300.00	3120.00	7.80	1.250	Compressive softening
17.5	2540.00	3060.00	7.65	1.174	Compressive softening
20.0	2720.00	2680.00	7.60	0.985	Post-peak failure
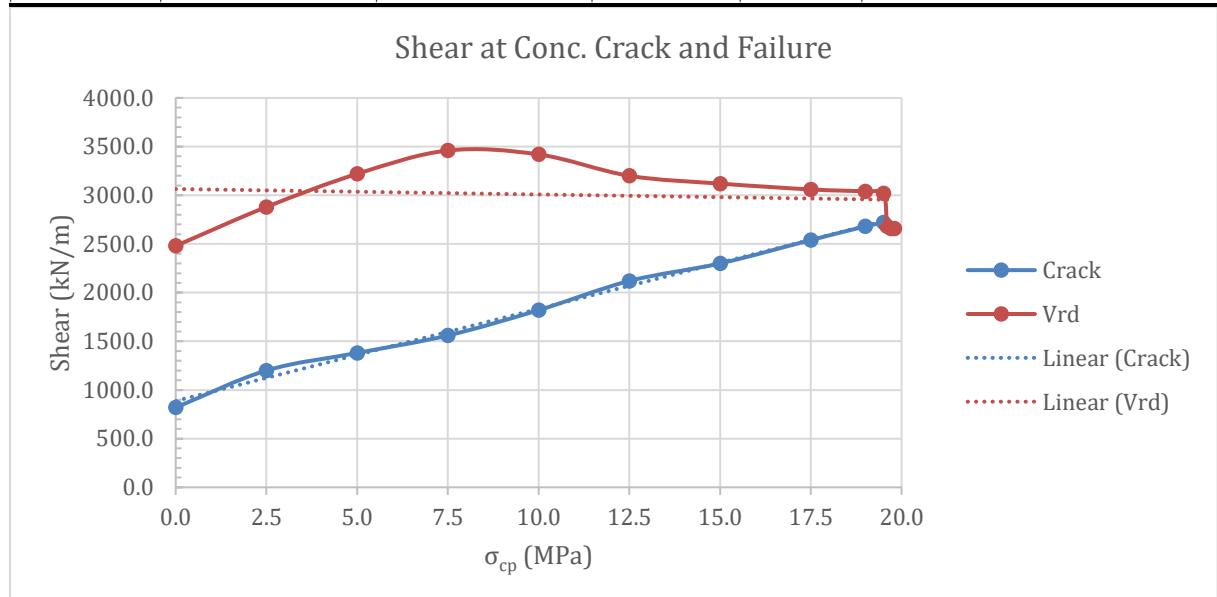
Graph 8. Shear Crack Load and Shear Capacity for ϕ24 vs. Prestressing Level

The crack threshold increases continuously with prestressing, while the shear capacity rises until ~10 MPa and then declines. The peak resistance occurs near the maximum α_c value.

Table 5. Results for φ20

$\sigma_{cp\,(MPa)}$	Crack Load	V_{rd} (kN/m)	$\tau_{rd\,(MPa)}$	α_c	Failure Type
0.0	820.00	1840.00	4.60	1.000	Diagonal Shear
2.5	1200.00	2240.00	5.60	1.076	Diagonal Shear
5.0	1340.00	2560.00	6.40	1.152	Diagonal Shear
7.5	1540.00	2840.00	7.10	1.227	Inclined + flexural
10.0	1780.00	2940.00	7.35	1.250	Inclined + ductile
12.5	2000.00	2940.00	7.35	1.250	Compression-driven
15.0	2200.00	2820.00	7.05	1.250	Compressive softening
17.5	2480.00	2780.00	6.95	1.174	Compressive softening
20.0	2660.00	2700.00	6.75	0.985	Post-peak failure
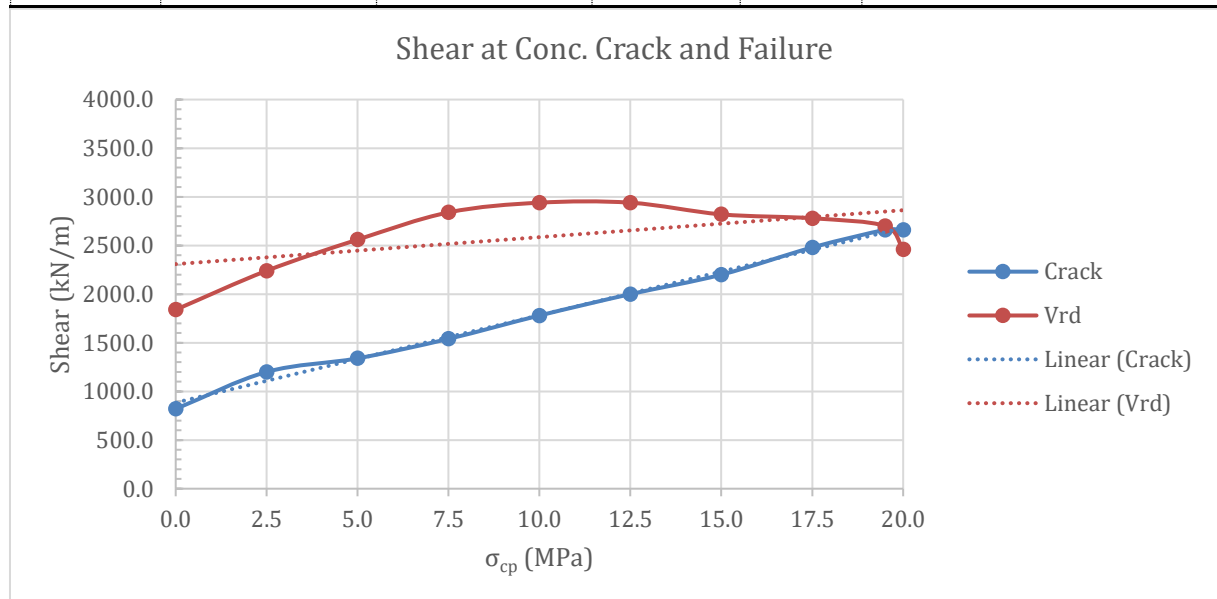
Graph 9. Shear Crack Load and Shear Capacity for φ20 vs. Prestressing Level

Similar to the φ24 case, the shear capacity initially improves with prestressing but drops after 10 MPa. Lower reinforcement ratio results in reduced overall shear resistance.

This seemingly counterintuitive behavior can be attributed to the influence of **the α_c coefficient**, which adjusts the contribution of concrete under sustained or high

axial compression. According to Eurocode 2, this factor decreases as the compressive stress $\boldsymbol{\sigma_{cp}}$ increases, which means that although prestressing initially strengthens the member by delaying cracking, excessive prestress may actually reduce the effective shear resistance due to material softening or loss of ductility.
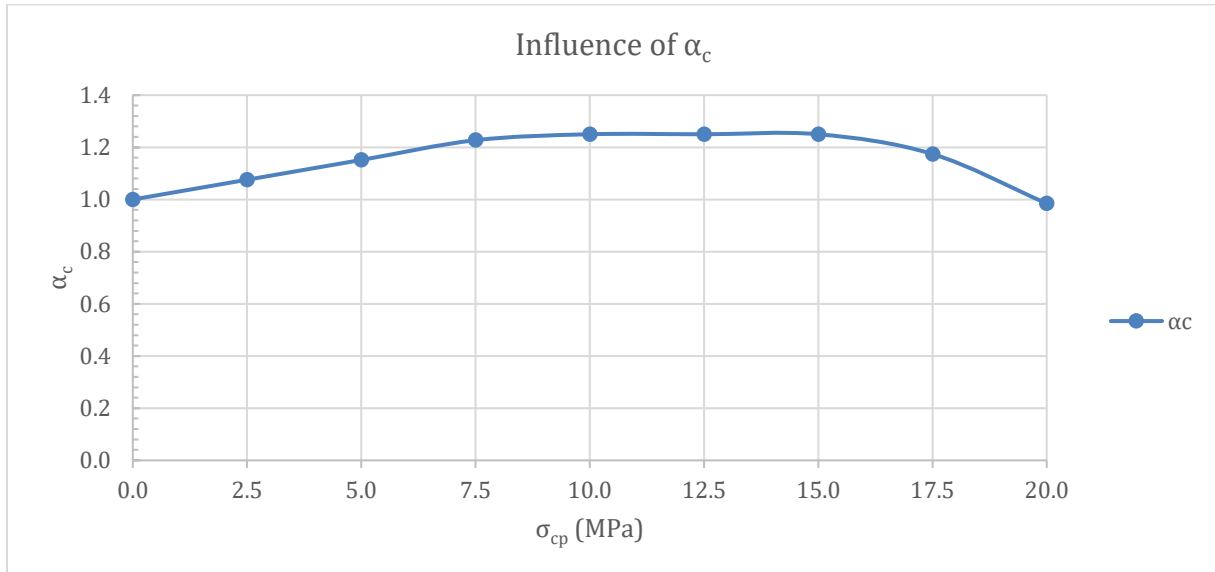
Graph 10. Variation of α_c with σ_{cp}

The theoretical α_c trend from Eurocode 2 explains the non-linear shear resistance behaviour observed in FEM results.

This trend closely mirrors the behaviour of the α_c coefficient defined in Eurocode 2, which increases with moderate compressive stress and decreases beyond a certain limit. The strong correlation between τ_{rd} and α_c observed in the simulations suggests that the shear resistance of prestressed concrete is directly governed by this coefficient.
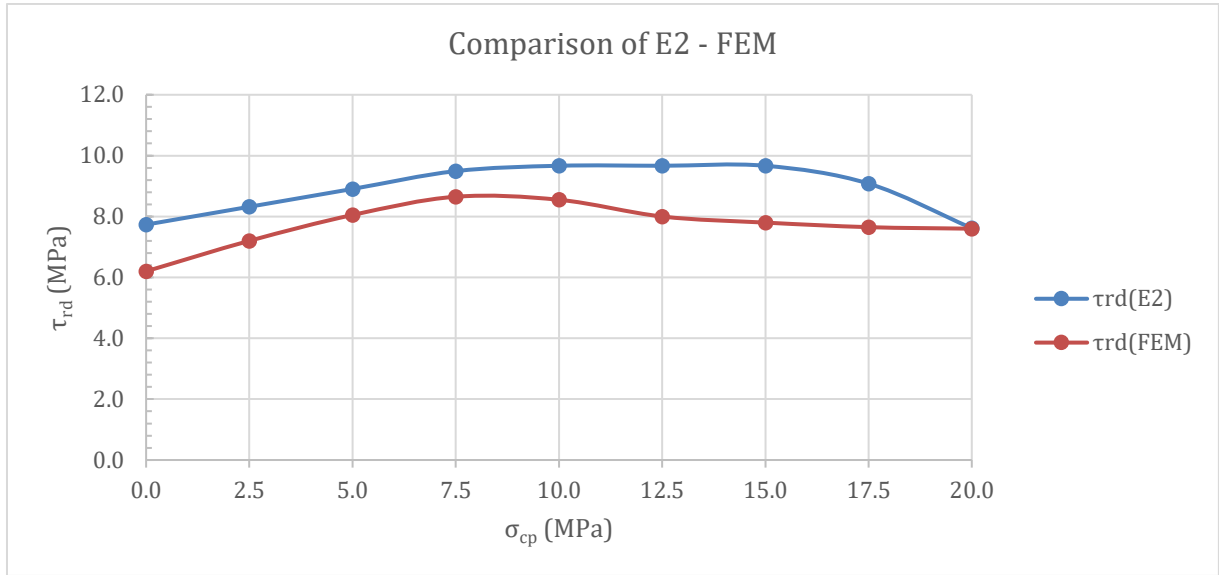
Graph 11. τ_{rd} - σ_{cp} diagrams obtained by FEM and E2

As observed in both reinforcement layouts, the shear capacity initially increases with prestressing due to the delay in crack formation. This is attributed to the clamping effect of axial compression, which improves the tensile strength of concrete across potential crack planes.

However, beyond a certain point (approximately 10 MPa of σ_{cp}), the capacity plateaus and even begins to decline. This reversal is linked to the behavior of the α_c coefficient, which reflects the effective contribution of concrete under compressive stress.

4.2.2. Effect of Reinforcement Ratio on Shear Resistance

In this comparison, the concrete strength was kept constant (C25/30), while the reinforcement diameter was reduced from ϕ24 mm to ϕ20 mm, corresponding to a decrease in reinforcement ratio. For each configuration, three material property sets were considered: mean, characteristic, and design values. The purpose of this comparison was to observe how shear capacity responds to changes in reinforcement content under the same concrete behavior.

The graphs number 12 and 13 show the variation of shear resistance V_{rd} with increasing prestress levels for both reinforcement configurations.

As expected, increasing the reinforcement ratio leads to a noticeable improvement in shear capacity. The φ24 mm bars provided significantly higher resistance at every prestress level compared to φ20 mm, across all material strength assumptions.

Moreover, all graphs show a consistent trend:

- The shear resistance increases with axial compression (σ_{cp}) up to a certain level,
- Followed by a plateau or slight reduction, especially noticeable in design values.

This decline at higher prestressing levels aligns with the earlier discussed influence of the α_c coefficient, which decreases after a threshold due to over-compression in the concrete section.

Table 6. Shear Capacity vs. Prestress for φ24 mm

σ_{cp} (MPa)	$V_{rd(mean)}$ (kN/m)	$\tau_{rd(mean)}$ (MPa)	$V_{rd(char.)}$ (kN/m)	$\tau_{rd(char.)}$ (MPa)	$V_{rd(design)}$ (kN/m)	$\tau_{rd(design)}$ (MPa)
0.0	2480.00	6.20	2160.00	5.40	1820.00	4.55
2.5	2880.00	7.20	2560.00	6.40	2080.00	5.20
5.0	3220.00	8.05	2840.00	7.10	1920.00	4.80
7.5	3460.00	8.65	2700.00	6.75	1900.00	4.75
10.0	3420.00	8.55	2560.00	6.40	1860.00	4.65
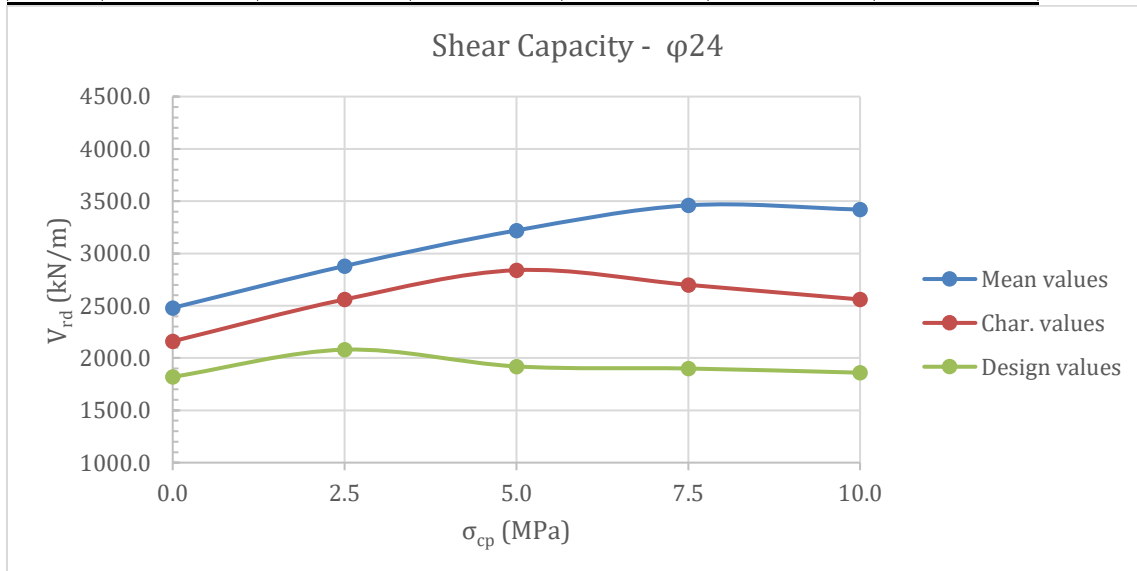
Graph 12. Shear Capacity vs. Prestress for φ24 mm

Comparison of mean, characteristic, and design values. Higher reinforcement results in greater overall shear resistance. A plateau is observed around 10 MPa of prestressing.

Table 7. Shear Capacity vs. Prestress for ϕ20 mm

σ_{cp} (MPa)	$V_{rd(mean)}$ (kN/m)	$\tau_{rd(mean)}$ (MPa)	$V_{rd(char.)}$ (kN/m)	$\tau_{rd(char.)}$ (MPa)	$V_{rd(design)}$ (kN/m)	$\tau_{rd(design)}$ (MPa)
0.0	1840.00	4.60	1600.00	4.00	1320.00	3.30
2.5	2240.00	5.60	1980.00	4.95	1700.00	4.25
5.0	2560.00	6.40	2280.00	5.70	1780.00	4.45
7.5	2840.00	7.10	2420.00	6.05	1720.00	4.30
10.0	2940.00	7.35	2320.00	5.80	1640.00	4.10
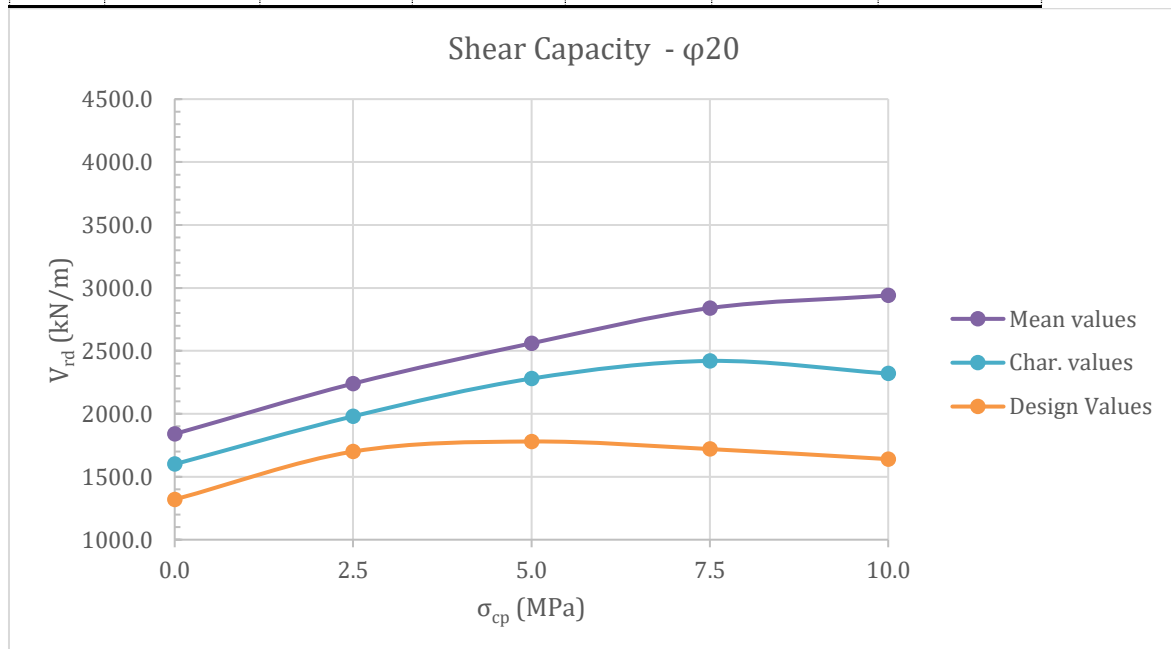
Graph 13. Shear Capacity vs. Prestress for ϕ20 mm

Shear resistance is significantly lower compared to ϕ24. While mean and characteristic values rise steadily, design values peak earlier and decrease beyond 7.5 MPa.

4.2.3. Effect of Concrete Strength on Shear Resistance

This subsection investigates the influence of concrete compressive strength on shear resistance by comparing simulations with C25/30 and C40/50 concrete classes. Two reinforcement configurations were analyzed for each case: $\phi24$ mm and $\phi20$ mm, while maintaining a constant spacing and layout. All material properties are based on mean values.

The results presented in Graph 14 show a clear and consistent trend:

- Higher concrete strength leads to higher shear capacity, regardless of reinforcement size,
- For both $\phi24$ and $\phi20$ mm layouts, the V_{rd} curves for C40/50 stay above those of C25/30 across all prestress levels,
- The difference becomes more pronounced at higher prestressing levels (σ_{cp} > 5 MPa), where cracking is delayed and concrete contribution dominates.

This outcome aligns with theoretical expectations: stronger concrete resists diagonal cracking more effectively and contributes more significantly to the V_{Rcd} portion of the shear capacity. It also highlights the synergistic effect between prestress and concrete class — higher compressive strength better sustains the prestress-induced confinement.

Table 8. Effect of Concrete Strength on Shear Resistance

σ_cp (MPa)	V_rd(mean) (kN/m)	τ_rd(mean) (MPa)	V_rd(mean) (kN/m)	τ_rd(mean) (MPa)	V_rd(mean) (kN/m)	τ_rd(mean) (MPa)	V_rd(mean) (kN/m)	τ_rd(mean) (MPa)
	C25/30 - φ24		C40/50 - φ24		C25/30 - φ20		C40/50 - φ20	
0.0	2480.00	6.20	2640.00	6.60	1840.00	4.60	1960.00	4.90
2.5	2880.00	7.20	3080.00	7.70	2240.00	5.60	2420.00	6.05
5.0	3220.00	8.05	3460.00	8.65	2560.00	6.40	2760.00	6.90
7.5	3460.00	8.65	3740.00	9.35	2840.00	7.10	3040.00	7.60
10.0	3420.00	8.55	4000.00	10.00	2940.00	7.35	3300.00	8.25
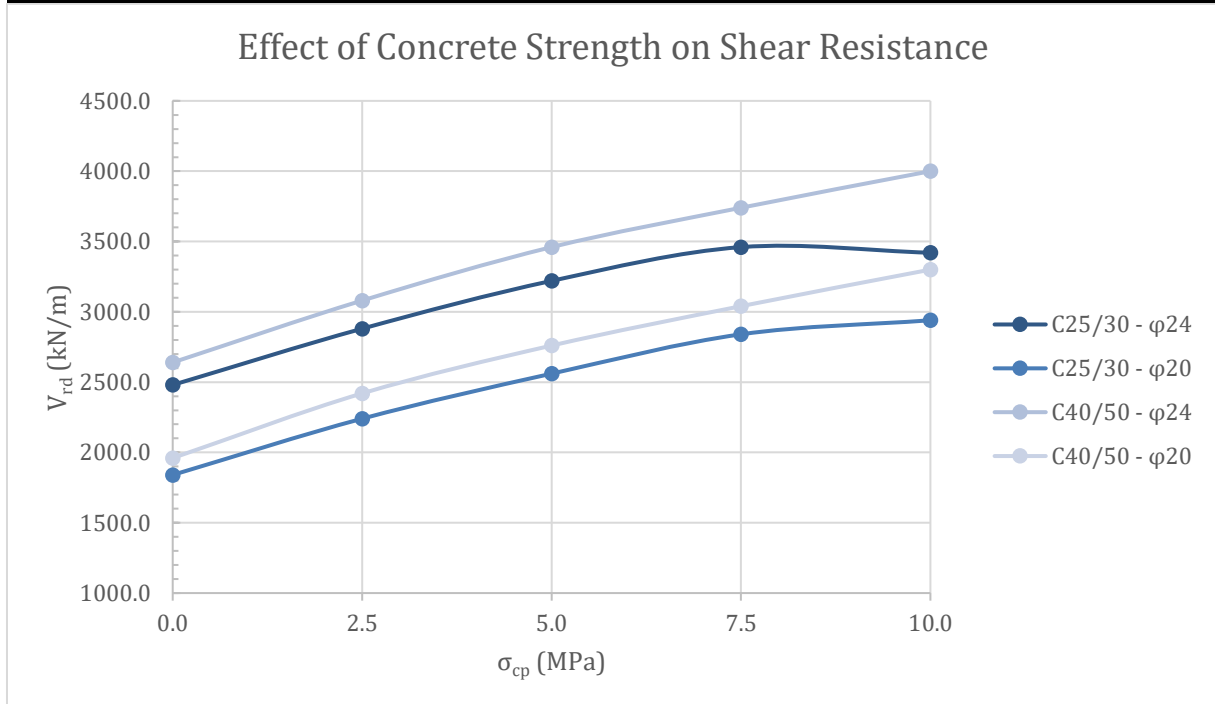
Graph 14. Effect of Concrete Strength on Shear Resistance

Shear capacity comparison between C25/30 and C40/50 concrete for both φ24 and φ20 reinforcement. C40/50 provides consistently higher V_{rd} values at all prestress levels.

4.2.4. FEM vs Eurocode Comparison

a) Methodology

To provide a consistent comparison between the Eurocode 2 design framework and the finite element results obtained from ATENA, shear capacity was evaluated using dimensionless shear stress, τ_{rd}, rather than the total force V_{rd}. This allows all results to be normalized with respect to geometry and interpreted independently of wall dimensions.

According to Eurocode 2 (EN 1992-1-1), the design shear resistance of a reinforced concrete section is governed by the minimum of the shear contribution of the concrete and the transverse reinforcement:

$$V_{rd} = min(V_{rd,s}, V_{rd,c})$$

Where:

- $V_{rd,s} = f_{yd} \cdot \frac{A_{sw}}{s} \cdot 0.9 \cdot d \cdot cot(\theta)$
- $V_{rd,c} = \alpha_c \cdot \nu \cdot \sigma_{cd} \cdot b_w \cdot 0.9 \cdot d \cdot \frac{cot(\theta)}{1+cot^2(\theta)}$

The parameters in the above equations were selected in accordance with the design assumptions and Eurocode guidelines:

- **ν = 0.5** (coefficient for concrete strength reduction)
- **α_c** depends on axial stress and was computed using the Eurocode provisions
- **θ** was taken between **21.8° and 45°**, depending on the reinforcement layout
- **A_{sw}/s** was calculated from the bar diameter and spacing (ϕ = 24 mm or 20 mm, s = 200 mm)
- **$\tau_{rd} = V_{rd}/ (b \cdot d)$** was used to normalize the results and match FEM outputs

To enable comparisons across multiple concrete grades, α_c was computed for different design compressive strengths (f_{cd}). A single table summarizing α_c values as a function of σ_{cp} is provided, while only key graphical trends are shown in the figures.

To capture the influence of prestressing on the α_c coefficient used in the Eurocode formulation of shear resistance, a parametric analysis was performed for different concrete strengths. The table and graph below summarize α_c values for compressive stress levels up to 10 MPa and for four different design compressive strengths (f_{cd}):

Table 9. Evolution of α_c with σ_{cp} for Different Concrete Strengths

σ_{cp} (MPa)	α_c (fc=16.67 MPa)	α_c (fc=25 MPa)	α_c (fc=33 MPa)	α_c (fc=48 MPa)
0.0	1.000	1.000	1.000	1.000
2.5	1.150	1.100	1.076	1.052
5.0	1.250	1.200	1.152	1.104
7.5	1.250	1.250	1.227	1.156
10.0	1.000	1.250	1.250	1.208
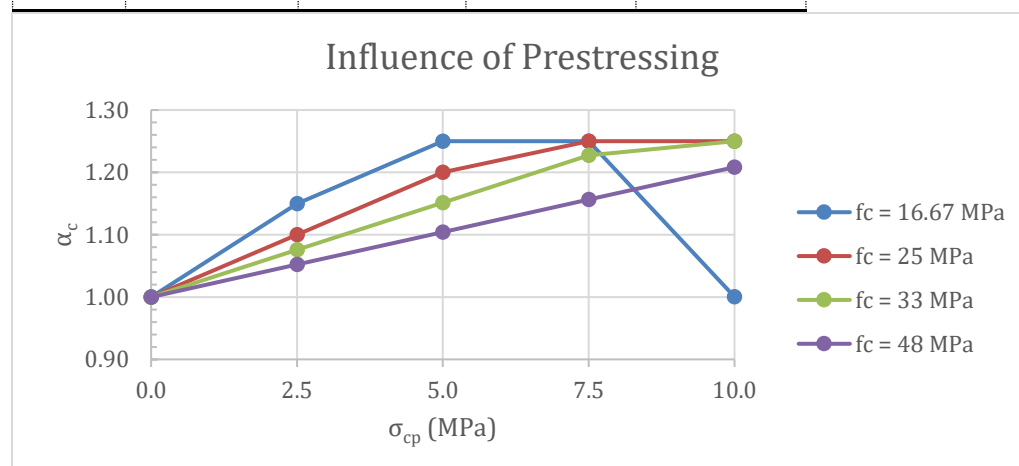
Graph 15. Evolution of α_c with σ_{cp} for Different Concrete Strengths

For lower strength concrete (e.g., f_{cd}= 16.7 MPa), α_c reaches a peak earlier and drops rapidly. In contrast, higher strength concrete maintains a gradual increase or plateau, supporting more prestress before α_c reduction begins.

b) Comparison Tables and Graphs

In this section, the dimensionless shear strength values (τ_{rd}) obtained through Eurocode 2 formulations (denoted as E2) are compared against the non-linear FEM analysis results (denoted as FEM). The comparisons cover different configurations in terms of reinforcement diameter ($\phi20$ vs. $\phi24$), concrete strength class (C25/30 vs. C40/50), and design assumption (mean, characteristic, and design values). Each configuration is evaluated under varying levels of axial precompression ($\sigma_{cp} = 0-10$ MPa), which allows a detailed investigation into how τ_{rd} evolves under prestress and material class variation.

Using dimensionless shear strength (τ_{rd}) enables a normalized comparison between theoretical and numerical results, independent of cross-sectional geometry. This approach eliminates the influence of width (b) and effective depth (d), focusing the evaluation purely on material properties, reinforcement configuration, and the effect of prestress. It ensures consistency when comparing varying concrete strengths and reinforcement diameters across different analysis setups.

The plotted graphs highlight both numerical agreement and discrepancy between theoretical (E2) and numerical (FEM) models. While Eurocode estimations mostly predict conservative values in low-prestress regions, FEM results exhibit nonlinear growth and greater sensitivity to reinforcement ratio. These variations will be discussed through the graphical trends below.

Table 10. τrd(E2) and τrd(FEM) values with θ estimations for C25/30 – mean values

σ_{cp} (MPa)	$\theta_{(\phi 24)}$ (°)	$\tau_{rd(E2)}$ (MPa)	$\tau_{rd(FEM)}$ (MPa)	$\theta_{(\phi 20)}$ (°)	$\tau_{rd(E2)}$ (MPa)	$\tau_{rd(FEM)}$ (MPa)
	C25/30 – φ24 (mean)			C25/30 – φ20 (mean)		
0.0	34.8	6.52	6.20	28.4	5.82	4.60
2.5	33.4	6.88	7.20	27.3	6.10	5.60
5.0	32.1	7.22	8.05	26.3	6.37	6.40
7.5	31.0	7.54	8.65	25.4	6.62	7.10
10.0	30.7	7.64	8.55	25.2	6.70	7.35
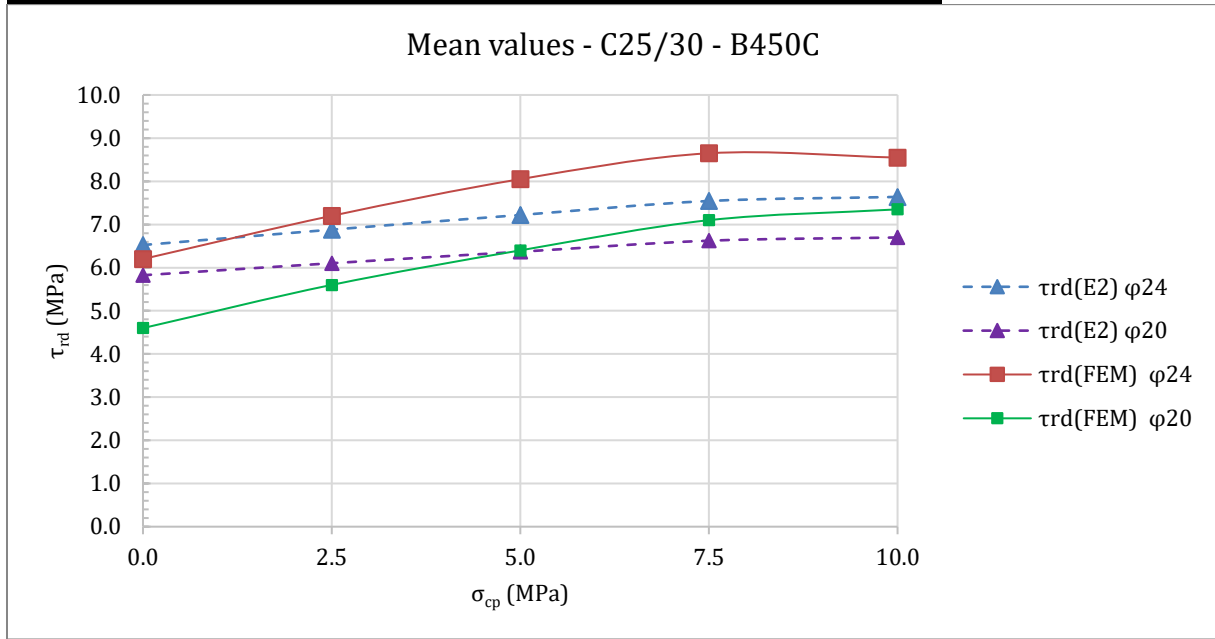
Graph 16. τrd(E2) and τrd(FEM) comparison for C25/30 – mean values

In this configuration, the calculations are based on mean material properties for both concrete and reinforcement. The updated results indicate that the FEM predictions exceed the Eurocode (E2) estimations, particularly for the φ24 reinforcement. This deviation becomes more significant at higher prestressing levels, demonstrating the sensitivity of the non-linear FEM approach to both reinforcement amount and axial precompression. For φ20, the FEM values start below the E2 estimations but eventually surpass them as σcp increases. These trends suggest that while the Eurocode provides conservative and stable predictions, the FEM model captures the nonlinear gains in shear resistance due to increased confinement and reinforcement efficiency. Moreover, the reduction

in θ angles reflects an evolution towards a more efficient internal truss mechanism under increasing axial load.

Table 11. τ$_{rd(E2)}$ and τ$_{rd(FEM)}$ values with θ estimations for C25/30 – characteristic values

σ$_{cp}$ (MPa)	θ$_{(φ24)}$ (°)	τ$_{rd(E2)}$ (MPa)	τ$_{rd(FEM)}$ (MPa)	θ$_{(φ20)}$ (°)	τ$_{rd(E2)}$ (MPa)	τ$_{rd(FEM)}$ (MPa)
	C25/30 - φ24 (char.)			C25/30 - φ24 (char.)		
0.0	37.9	5.30	5.40	30.8	4.81	4.00
2.5	35.8	5.71	6.40	29.2	5.12	4.95
5.0	34.1	6.09	7.10	27.8	5.42	5.70
7.5	33.3	6.27	6.75	27.2	5.56	6.05
10.0	33.3	6.27	6.40	27.2	5.56	5.80
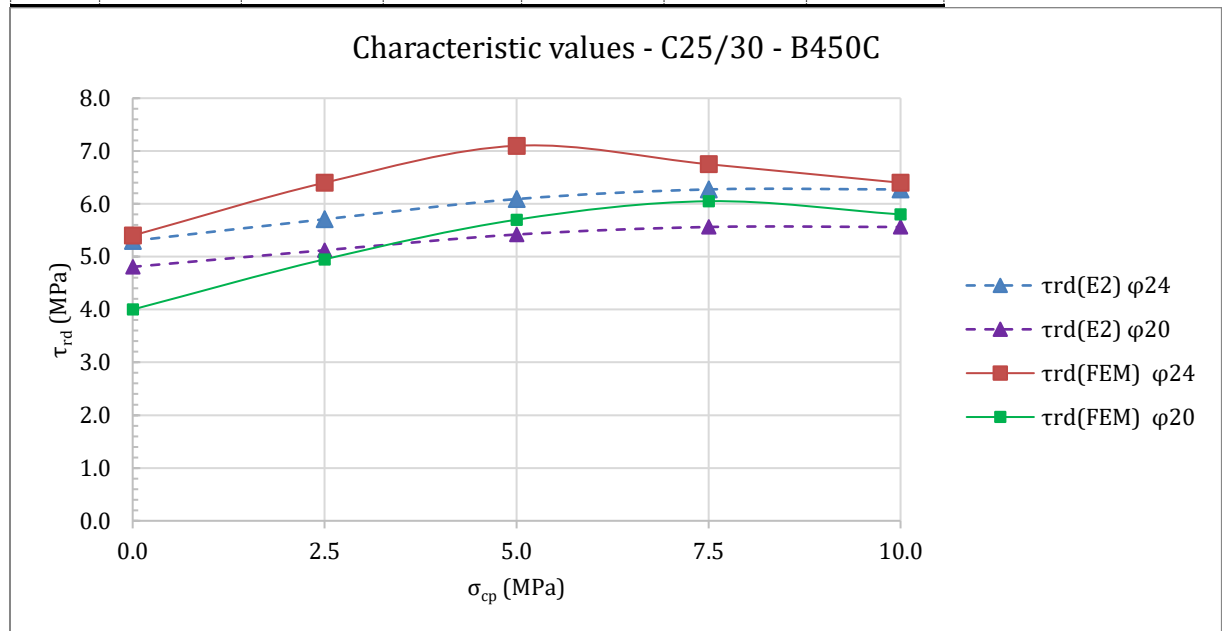
Graph 17. τ$_{rd(E2)}$ and τ$_{rd(FEM)}$ comparison for C25/30 – characteristic values

For the characteristic material configuration, the updated results highlight a pronounced difference between FEM and Eurocode (E2) estimations, especially for the φ24 reinforcement. Unlike the previous trend where E2 values for φ24 and φ20 converged, the current data reveals that larger reinforcement continues to enhance shear resistance even under characteristic assumptions. The τrd(FEM) values for both diameters consistently exceed their E2 counterparts across all σcp levels, indicating a more realistic capture of reinforcement contribution by the FEM analysis. This suggests that the concrete capacity alone does not govern shear failure in this case; instead, reinforcement layout and axial

49

compression remain influential. The persistence of θ reduction further supports the development of a more effective internal force path as prestress increases.

Table 12. $\tau_{rd(E2)}$ and $\tau_{rd(FEM)}$ values with θ estimations for C25/30 – design values

σ_{cp} (MPa)	$\theta_{(\phi24)}$ (°)	$\tau_{rd(E2)}$ (MPa)	$\tau_{rd(FEM)}$ (MPa)	$\theta_{(\phi20)}$ (°)	$\tau_{rd(E2)}$ (MPa)	$\tau_{rd(FEM)}$ (MPa)
	C25/30 - φ24 (design)			C25/30 - φ20 (design)		
0.0	43.5	3.78	4.55	35.0	3.55	3.30
2.5	39.9	4.28	5.20	32.3	3.93	4.25
5.0	38.0	4.59	4.80	30.9	4.16	4.45
7.5	38.0	4.59	4.75	30.9	4.16	4.30
10.0	43.5	3.78	4.65	35.0	3.55	4.10
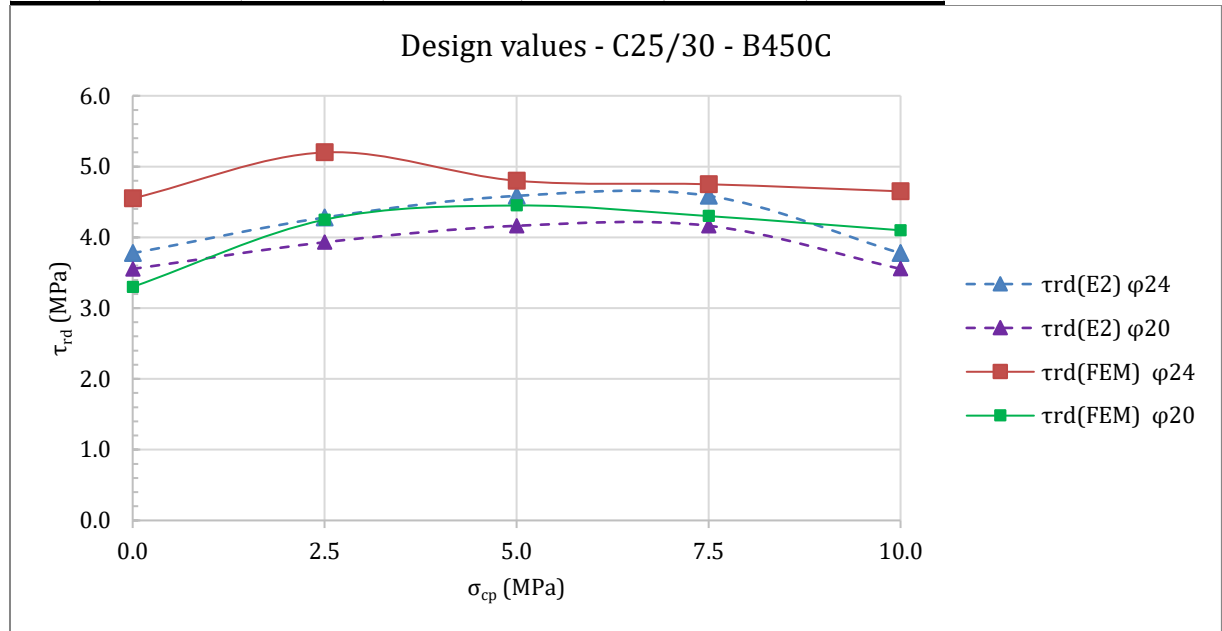
Graph 18. $\tau_{rd(E2)}$ and $\tau_{rd(FEM)}$ comparison for C25/30 – design values

In the design value configuration, the difference between FEM and Eurocode (E2) estimations becomes more explicit. The E2 values remain nearly identical for both reinforcement diameters, indicating that the model is governed almost entirely by the reduced concrete design strength, disregarding the reinforcement's contribution. In contrast, the FEM results exhibit a notable increase in τrd with larger reinforcement (φ24), reaffirming the importance of reinforcement even under conservative material assumptions. As σcp increases, the FEM curves maintain their upward trend, while the E2 predictions stay flat and conservative.

This reflects the Eurocode's limitation in representing reinforcement efficiency under design-level constraints and highlights FEM's ability to better capture shear behaviour under realistic boundary conditions.

Table 13. $\tau_{rd(E2)}$ and $\tau_{rd(FEM)}$ values with θ estimations for C40/50 – mean values

σ_{cp} (MPa)	$\theta_{(\phi 24)}$ (°)	$\tau_{rd(E2)}$ (MPa)	$\tau_{rd(FEM)}$ (MPa)	$\theta_{(\phi 20)}$ (°)	$\tau_{rd(E2)}$ (MPa)	$\tau_{rd(FEM)}$ (MPa)
	C40/50 - φ24 (mean)			C40/50 - φ20 (mean)		
0.0	29.4	8.06	6.60	24.1	7.03	4.90
2.5	28.6	8.33	7.70	23.5	7.25	6.05
5.0	27.8	8.59	8.65	22.9	7.46	6.90
7.5	27.1	8.85	9.35	22.3	7.66	7.60
10.0	26.5	9.09	10.00	21.8	7.86	8.25
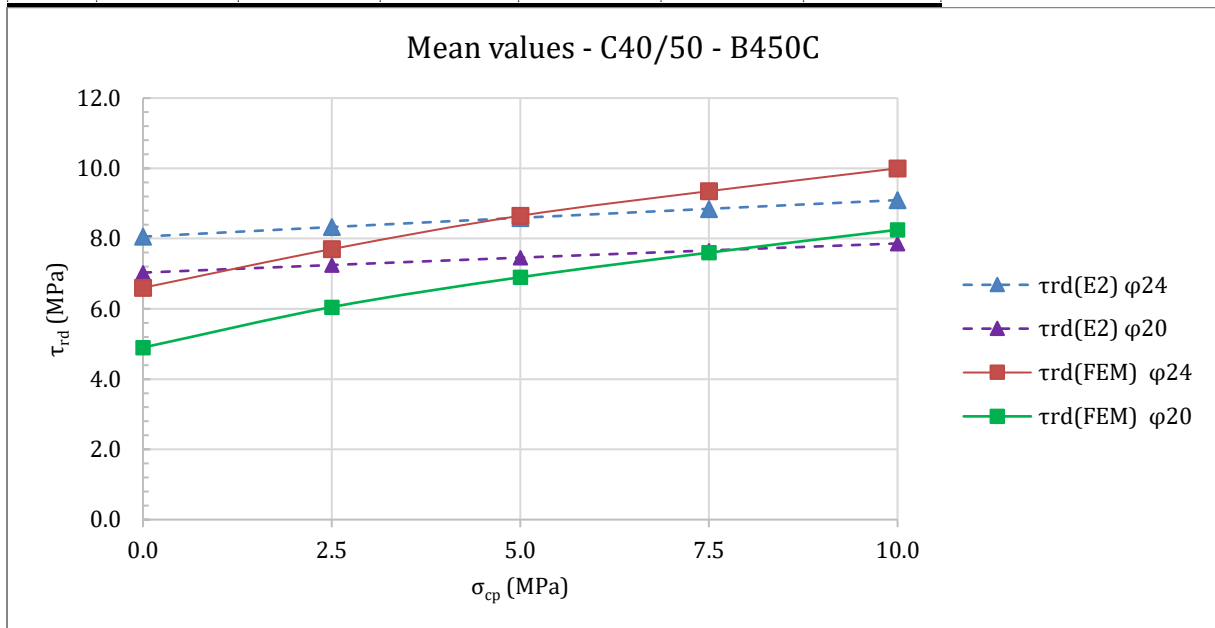
Graph 19. $\tau_{rd(E2)}$ and $\tau_{rd(FEM)}$ comparison for C40/50 – mean values

When the concrete strength class is increased to C40/50, both E2 and FEM estimations show a clear rise in τrd values. However, the FEM results demonstrate a significantly steeper increase, especially for the φ24 reinforcement, surpassing the Eurocode predictions across all prestress levels. The influence of reinforcement diameter becomes markedly pronounced in the FEM analysis, whereas the E2 model displays a more uniform growth pattern, relatively insensitive to reinforcement variation. This behaviour highlights the

regained efficiency of reinforcement under higher concrete strengths in nonlinear simulations. The decreasing θ values further confirm the enhanced internal stress transfer mechanisms activated under increased axial compression and material quality, reinforcing the superiority of FEM in capturing realistic shear behaviour in high-strength concrete panels.

4.2.5. FEM vs fib model comparison

In this section, the nonlinear finite element method (FEM) predictions for shear resistance are systematically compared with the theoretical values prescribed by the fib Model Code 2010. The objective is to critically evaluate the accuracy, conservatism, and consistency of fib-based analytical models—namely Level of Approximation 1, Level 2a, and Level 2b—in predicting the longitudinal shear behaviour of prestressed concrete web panels under combined loading. This comparison provides a complementary perspective to the previously discussed Eurocode 2 benchmarks and allows for a deeper validation of the FEM outcomes using more detailed, strain-based code formulations, as introduced in Section 2.3.

The analysis covers a total of eight parametric configurations, varying in concrete strength (C25/30 and C40/50), reinforcement diameter (ϕ20 and ϕ24), and axial prestress level (σ_{cp} = 0–10 MPa). For each configuration, the shear stress design values (τ_{rd}) are calculated based on:

- $\tau_{rd}^{(FEM)}$: Shear resistance obtained from nonlinear FEM simulation,
- $\tau_{rd}^{(LoAI)}$, $\tau_{rd}^{(LoAIIa)}$, $\tau_{rd}^{(LoAIIb)}$: Shear resistance values calculated using fib formulations at each LoA,
- $\tau_{rd}^{(E2)}$: Eurocode 2-based shear resistance (for reference).

To ensure consistency in the comparison, all design shear resistance values obtained from analytical methods (Eurocode 2 and fib Model Code) were converted into shear stress form (τ_{rd}) using the effective web width and internal lever arm:

$$\tau_{rd} = \frac{V_{rd}}{b_w \cdot z}$$

52

The results are presented in tabular and graphical format, and the comparison focuses on trend alignment, absolute deviations, and the conservatism margins of each code-based prediction with respect to the FEM baseline. Particular emphasis is placed on the ability of LoA2b to capture nonlinear stress redistribution and axial-prestress sensitivity, thus bridging the gap between simplified code design and advanced numerical modelling.

Table 14. Overview recall of design equations for different levels of approximation

LoA	Concrete Contribution	Min. compressive stress field inclination	Strength reduction factor for $V_{rd,max}$
I	$V_{Rd,c} = 0$	$cot(\theta)_{min} = fixed$	$k_\varepsilon = fixed$
IIa	$V_{Rd,c} = 0$	$cot(\theta)_{min} = f(\varepsilon_x)$	$k_\varepsilon = f(\varepsilon_x, \theta)$
IIb	$V_{Rd,c} = f(\varepsilon_x)$	$cot(\theta) = f(\varepsilon_x)$	$k_\varepsilon = f(\varepsilon_x, \theta)$

Before delving into the detailed comparison results, it is useful to revisit the fundamental analytical distinctions between the three Levels of Approximation (LoA) defined in the fib Model Code. The table below summarizes how each level treats the main parameters influencing shear design, namely the concrete contribution to shear resistance ($V_{Rd,c}$), the assumed inclination of the compressive stress field (θ), and the strength reduction factor (k_ε) used in determining the crushing limit $V_{Rd,max}$.

This structured distinction is particularly important in interpreting the results that follow, as LoA2b is expected to exhibit better alignment with the FEM outcomes due to its closer theoretical proximity to nonlinear material behaviour.

Table 15. Comparison of τ_rd values (Mean values - C25/30 - B450C - φ24)

σ_{cp} (MPa)	$\tau_{rd}^{(LoAI)}$ (MPa)	$\tau_{rd}^{(LoAIIa)}$ (MPa)	$\tau_{rd}^{(LoAIIb)}$ (MPa)	$\tau_{rd}^{(E2)}$ (MPa)	$\tau_{rd}^{(FEM)}$ (MPa)
0.0	7.54	7.34	9.17	6.52	6.20
2.5	7.54	7.39	9.24	6.88	7.20
5.0	7.54	7.44	9.31	7.22	8.05
7.5	7.54	7.50	9.37	7.54	8.65
10.0	7.54	7.55	9.44	7.64	8.55
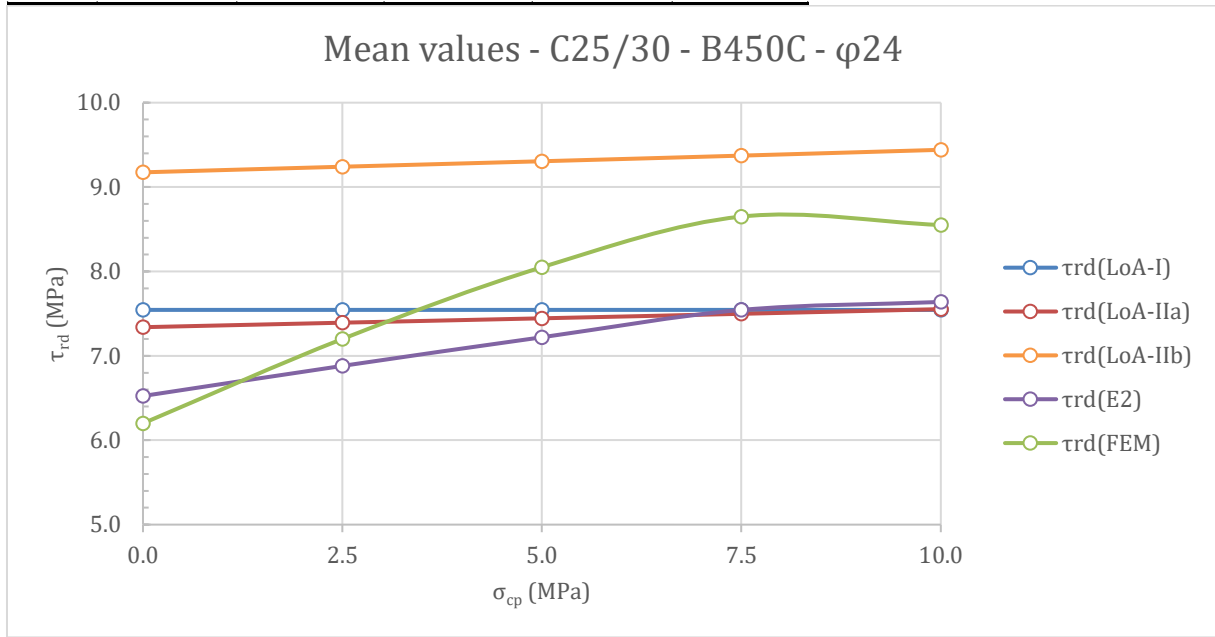
Graph 20. Comparison of τ_rd values (Mean values - C25/30 - B450C - φ24)

In this configuration, LoA1 predictions remain constant across the entire prestress range, reflecting the fixed-angle assumption and lack of prestress sensitivity. LoA2a shows a modest increase with σ_{cp}, while LoA2b demonstrates the highest and most consistent correlation with the FEM results. The FEM values show a nonlinear increase, especially after σ_{cp} = 5 MPa, highlighting the growing influence of axial compression on shear resistance. Compared to Eurocode 2, both LoA2a and LoA2b provide significantly closer estimations, confirming the added accuracy of strain-based fib formulations in capturing stress redistribution.

Table 16. Comparison of τ$_{rd}$ values (Characteristic values - C25/30 - B450C - φ24)

σ$_{cp}$ (MPa)	τ$_{rd}$$^{(LoAI)}$ (MPa)	τ$_{rd}$$^{(LoAIIa)}$ (MPa)	τ$_{rd}$$^{(LoAIIb)}$ (MPa)	τ$_{rd}$$^{(E2)}$ (MPa)	τ$_{rd}$$^{(FEM)}$ (MPa)
0.0	5.98	6.09	7.62	5.30	5.40
2.5	5.98	6.14	7.67	5.71	6.40
5.0	5.98	6.18	7.72	6.09	7.10
7.5	5.98	6.22	7.78	6.27	6.75
10.0	5.98	6.26	7.83	6.27	6.40

Graph 21. Comparison of τ$_{rd}$ values (Characteristic values - C25/30 - B450C - φ24)

Compared to the mean values, the characteristic τ$_{rd}$ results exhibit a slightly more conservative profile across all approaches. LoA1 remains constant again, while LoA2a and especially LoA2b follow the nonlinear growth trend observed in the FEM data. LoA2b closely tracks the FEM curve, particularly in the σ$_{cp}$ = 5–10 MPa range, reinforcing its validity for capturing prestress-sensitive behaviour. Eurocode 2 once again underestimates the resistance, especially at higher prestress levels, making fib formulations—especially LoA2b—more reliable for characteristic design evaluation.

Table 17. Comparison of τ$_{rd}$ values (Design values - C25/30 - B450C - φ24)

σ$_{cp}$ (MPa)	τ$_{rd}$(LoAI) (MPa)	τ$_{rd}$(LoAIIa) (MPa)	τ$_{rd}$(LoAIIb) (MPa)	τ$_{rd}$(E2) (MPa)	τ$_{rd}$(FEM) (MPa)
0.0	4.12	4.58	5.73	3.78	4.55
2.5	4.12	4.61	5.77	4.28	5.20
5.0	4.12	4.64	5.80	4.59	4.80
7.5	4.12	4.67	5.84	4.59	4.75
10.0	4.12	4.71	5.88	3.78	4.65

Graph 22. Comparison of τ$_{rd}$ values (Design values - C25/30 - B450C - φ24)

At the design level, all τ$_{rd}$ values decrease due to the application of partial safety factors, but relative trends remain consistent. LoA2b again aligns most closely with the FEM predictions, especially between σ$_{cp}$ = 2.5–7.5 MPa. While LoA1 remains constant and conservative, it becomes less accurate at higher prestress levels. LoA2a moderately improves upon LoA1 but still underestimates compared to FEM. Eurocode 2 shows significant deviation beyond σ$_{cp}$ = 5 MPa, highlighting the limited adaptability of its fixed-angle approach under prestress. This confirms LoA2b's superior accuracy even under safety-adjusted design conditions.

Table 18. Comparison of τ$_{rd}$ values (Mean values - C25/30 - B450C - φ20)

σ$_{cp}$ (MPa)	τ$_{rd}$(LoAI) (MPa)	τ$_{rd}$(LoAIIa) (MPa)	τ$_{rd}$(LoAIIb) (MPa)	τ$_{rd}$(E2) (MPa)	τ$_{rd}$(FEM) (MPa)
0.0	5.95	6.02	7.11	5.82	4.60
2.5	6.70	6.06	7.31	6.10	5.60
5.0	6.70	6.11	7.52	6.37	6.40
7.5	6.70	6.16	7.70	6.62	7.10
10.0	6.70	6.20	7.76	6.70	7.35

Graph 23. Comparison of τ$_{rd}$ values (Mean values - C25/30 - B450C - φ20)

Reducing the reinforcement diameter to ɸ20 leads to visibly lower shear resistance in all approaches, especially in the FEM results, which are more sensitive to reinforcement ratio than the analytical models. While LoA1 and LoA2a again show limited growth with increasing σ$_{cp}$, LoA2b continues to match the nonlinear FEM trend more effectively, particularly from 5 MPa upward. The discrepancy between Eurocode 2 and FEM becomes more pronounced under reduced reinforcement, emphasizing the need for strain-dependent formulations like LoA2b when assessing shear behaviour in lightly reinforced sections.

Table 19. Comparison of τrd values (Characteristic values - C25/30 - B450C - φ20)

σ_{cp} (MPa)	$\tau_{rd}^{(LoAI)}$ (MPa)	$\tau_{rd}^{(LoAIIa)}$ (MPa)	$\tau_{rd}^{(LoAIIb)}$ (MPa)	$\tau_{rd}^{(E2)}$ (MPa)	$\tau_{rd}^{(FEM)}$ (MPa)
0.0	5.41	5.05	6.31	4.81	4.00
2.5	5.41	5.08	6.36	5.12	4.95
5.0	5.41	5.12	6.40	5.42	5.70
7.5	5.41	5.16	6.45	5.56	6.05
10.0	5.41	5.20	6.50	5.56	5.80

Graph 24. Comparison of τrd values (Characteristic values - C25/30 - B450C - φ20)

Under characteristic loading conditions, the reduction in reinforcement continues to influence shear capacity across all methods, with FEM showing the strongest sensitivity. LoA1 and LoA2a produce relatively flat or linear trends, while LoA2b again captures the upward curvature of the FEM results. As in previous cases, Eurocode 2 underestimates the shear resistance, especially at higher prestress levels. This reinforces the conclusion that only LoA2b reliably reflects the nonlinear enhancement provided by axial compression in sections with lower reinforcement ratios.

Table 20. Comparison of τ_rd values (Design values - C25/30 - B450C - φ20)

σ_{cp} (MPa)	$\tau_{rd}^{(LoAI)}$ (MPa)	$\tau_{rd}^{(LoAIIa)}$ (MPa)	$\tau_{rd}^{(LoAIIb)}$ (MPa)	$\tau_{rd}^{(E2)}$ (MPa)	$\tau_{rd}^{(FEM)}$ (MPa)
0.0	3.90	3.87	4.84	3.55	3.30
2.5	3.90	3.90	4.87	3.93	4.25
5.0	3.90	3.92	4.90	4.16	4.45
7.5	3.90	3.95	4.94	4.16	4.30
10.0	3.90	3.98	4.98	3.55	4.10

Graph 25. Comparison of τ_rd values (Design values - C25/30 - B450C - φ20)

At the design level with reduced reinforcement, all τ_{rd} values drop further due to safety factors, but the influence of prestress remains evident. FEM values continue to rise with σ_{cp}, while LoA1 and LoA2a either plateau or slightly increase. LoA2b again follows the FEM trend most closely, especially between 2.5–7.5 MPa. The divergence between Eurocode 2 and FEM becomes more critical in this case, showing that EC2's fixed-angle method may not provide sufficient reliability for design in lightly reinforced, prestressed panels. LoA2b stands out as the most consistent and accurate across the entire range.

Table 21. Comparison of τrd values (Mean values – C40/50 - B450C - φ24)

σ_{cp} (MPa)	$\tau_{rd}^{(LoAI)}$ (MPa)	$\tau_{rd}^{(LoAIIa)}$ (MPa)	$\tau_{rd}^{(LoAIIb)}$ (MPa)	$\tau_{rd}^{(E2)}$ (MPa)	$\tau_{rd}^{(FEM)}$ (MPa)
0.0	8.57	8.70	9.75	8.06	6.60
2.5	9.71	8.77	10.01	8.33	7.70
5.0	9.71	8.83	10.28	8.59	8.65
7.5	9.71	8.90	10.57	8.85	9.35
10.0	9.71	8.97	10.90	9.09	10.00

Graph 26. Comparison of τrd values (Mean values – C40/50 - B450C - φ24)

With higher concrete strength, all methods predict increased shear capacity; however, the growth trend differs. LoA1 shows a step increase due to fixed input parameters, while LoA2a captures modest strain effects. LoA2b continues to exhibit the best alignment with FEM results, especially at higher σ_{cp} levels. FEM shows a steep and nonlinear increase in τ_{rd}, benefiting from both axial prestress and improved material performance. Eurocode 2 again underpredicts the shear strength, indicating limited sensitivity to material upgrades. This case demonstrates how LoA2b adapts more effectively to strength-driven gains in shear resistance.

Table 22. Comparison of τ_{rd} values (Mean values – C40/50 - B450C - φ20)

σ_{cp} (MPa)	$\tau_{rd}^{(LoAI)}$ (MPa)	$\tau_{rd}^{(LoAIIa)}$ (MPa)	$\tau_{rd}^{(LoAIIb)}$ (MPa)	$\tau_{rd}^{(E2)}$ (MPa)	$\tau_{rd}^{(FEM)}$ (MPa)
0.0	5.95	7.02	7.53	7.03	4.90
2.5	7.70	7.08	7.76	7.25	6.05
5.0	7.70	7.13	8.01	7.46	6.90
7.5	7.70	7.19	8.28	7.66	7.60
10.0	7.70	7.25	8.59	7.86	8.25

Graph 27. Comparison of τ_{rd} values (Mean values – C40/50 - B450C - φ20)

In this final configuration combining high concrete strength with reduced reinforcement, the divergence between FEM and code-based predictions becomes even more pronounced. The FEM results show a sharp nonlinear increase in τ_{rd} with rising σ_{cp}, reflecting enhanced confinement and stress transfer capabilities in high-strength concrete. LoA1 and LoA2a show more restrained growth, while LoA2b again provides the closest approximation—particularly from 5 MPa onward. Eurocode 2 remains significantly below the FEM results, especially under high prestress, underscoring its limited capacity to reflect real material behaviour in such configurations. LoA2b emerges as the only fib model adequately capturing both prestress and material class effects.

The comparative analysis between FEM-based shear resistance and fib Model Code predictions reveals a clear trend across all configurations. While LoA1 and LoA2a offer conservative and simplified estimates, their ability to reflect prestress effects and reinforcement variations remains limited. In contrast, LoA2b consistently shows strong alignment with FEM results, especially under increasing axial compression and higher concrete strength. The inclusion of strain-dependent formulations and concrete contribution in LoA2b enables it to replicate the nonlinear behaviour observed in simulations more accurately. Overall, among the fib approximations, LoA2b emerges as the most reliable approach for predicting shear resistance in prestressed concrete panels, closely approximating the detailed insights provided by advanced nonlinear FEM.

4.3.   Moment Resistance Results

In this section, the moment capacities of selected specimens are compared using two different methods: Eurocode 2-based analytical formulation and nonlinear finite element analysis (FEM) results obtained from ATENA. The design moment resistance was calculated using the simplified expression:

$$M_{rd} = 0.9 \cdot d \cdot f_{yd} \cdot A_s$$

where:
- d is the effective depth,
- f_{yd} is the design yield strength of reinforcement,
- A_s is the cross-sectional area of tensile reinforcement.

This simplified expression assumes that the bending failure is governed by reinforcement yielding and that the internal lever arm is approximately $0.9 \cdot d$. It is a common approximation used for singly reinforced, ductile sections, particularly when axial effects are negligible.

A total of eight different configurations were evaluated, each differing in terms of safety assumptions (mean, characteristic, design), reinforcement ratio (ϕ20 and

φ24), and concrete class (C25/30 and C40/50). The results are summarized in the following table and bar chart:

- Analyses 1–3 represent the same section under varying material safety assumptions.
- Analyses 4–6 investigate the effect of reinforcement reduction with again under varying material safety assumptions.
- Analyses 7–8 reflect an increase in concrete strength and hardening coefficient k=1.15

The results indicate that the simplified analytical method (Eurocode-based) yields conservative predictions in most cases, especially under mean and characteristic assumptions. However, in configurations with increased concrete strength and steel hardening (Analyses 7 and 8), FEM predictions exceed the analytical estimates, highlighting the limitations of simplified methods in capturing material nonlinearity and redistribution effects.

Although some deviations exist—up to ±12–19%—the general agreement between the methods confirms the validity of using the simplified expression for preliminary design and comparative evaluation.

$$Relative\ Error\ (\%) = \frac{M_{rd}(FEM) - M_{rd}(E2)}{M_{rd}(E2)} \times 100$$

Table 23. Comparison of moment resistance —$M_{rd}(E2)$ - $M_{rd}(FEM)$— values.

No.	Safety fac.	Concrete	Steel	φ (mm)	$M_{rd(E2)}$ (kNm/m)	$M_{rd\ (FEM)}$ (kNm/m)	Error %
1	mean	C25/30	B450C	24	441.37	412.00	7%
2	char.	C25/30	B450C	24	401.25	368.00	-8%
3	design	C25/30	B450C	24	348.91	308.00	-12%
4	mean	C25/30	B450C	20	306.51	308.00	0%
5	char.	C25/30	B450C	20	278.64	268.00	-4%
6	design	C25/30	B450C	20	242.30	220.00	-9%
7	mean	C40/50	B450C	24	441.37	496.00	12%
8	mean	C40/50	B450C	20	306.51	364.00	19%

	1	2	3	4	5	6	7	8
■ Mrd(E2)	441.37	401.25	348.91	306.51	278.64	242.30	441.37	306.51
■ Mrd(FEM)	412.00	368.00	308.00	308.00	268.00	220.00	496.00	364.00

Graph 28. Comparison of moment resistance —M$_{rd}$(E2) - M$_{rd}$(FEM)— values.

In most configurations, the moment capacity calculated using Eurocode 2 slightly overestimates the FEM-based value due to the simplifications involved in the analytical formula. However, in Analyses 7 and 8, where the reinforcement hardening parameter k is increased to 1.15 (reflecting the use of higher-grade concrete C40/50), the FEM results surpass the Eurocode estimations. This discrepancy can be attributed to the fact that Eurocode assumes an elastic–perfectly plastic behavior for reinforcement, ignoring any strain-hardening effects. In contrast, ATENA incorporates post-yield behaviour based on the defined k-factor, allowing the reinforcement to carry additional stress beyond the yield point, which results in a higher moment resistance. This highlights the sensitivity of moment capacity to material modelling assumptions in non-linear finite element analysis.

This confirms that simplified code-based formulas may underestimate the capacity when advanced material models with hardening behaviour are considered.

4.4.   Shear – Moment Interaction Curves

To examine the interaction between shear and bending moment, a total of 8 nonlinear analyses were performed using various configurations of concrete strength, reinforcement diameter, and material safety assumptions. For each configuration, a pair of moment and shear resistance values (M_{rd} and V_{rd} were first calculated individually. Then, interaction domain analyses were conducted by applying combinations of shear and moment in inverse proportional increments—gradually reducing the shear load while increasing the applied moment, keeping the axial prestress constant in each simulation.

In all simulations, applied loads were represented in a dimensionless form by normalizing with respect to their respective resistance values. That is, moment and shear values were plotted using the ratios:

$$\frac{M_0}{M_{rd}} \qquad\qquad\qquad \frac{V_0}{V_{rd}}$$

which are numerically equivalent to the dimensionless moment (μ) and shear (τ) values, since:

$$\frac{M_0}{M_{rd}} = \frac{\mu_0}{\mu_{rd}} \qquad\qquad\qquad \frac{V_0}{V_{rd}} = \frac{\tau_0}{\tau_{rd}}$$

As a result, the interaction diagrams naturally take a dimensionless form, allowing different material and reinforcement configurations to be compared on a common basis.

4.4.1. Domain – C25/30 – B450C – ϕ24 – *Mean Values*

Table 24. M - V interaction domain curve for prestressing level σ$_{cp}$=2.5MPa (mean values - ϕ24)

V$_{rd}$ (kN/m)	M$_{rd}$ (kNm/m)	$\dfrac{V_0}{V_{rd}}$	$\dfrac{M_0}{M_{rd}}$	Mean Values – σ$_{cp}$ = 2.5 MPa	
2880	0	1.00	0.00		
2600	108	0.90	0.26		
2300	172	0.80	0.42		
2020	232	0.70	0.56		
1720	280	0.60	0.68		
1440	324	0.50	0.79		
1160	364	0.40	0.88		
860	392	0.30	0.95		
580	404	0.20	0.98		
0	412	0.00	1.00		
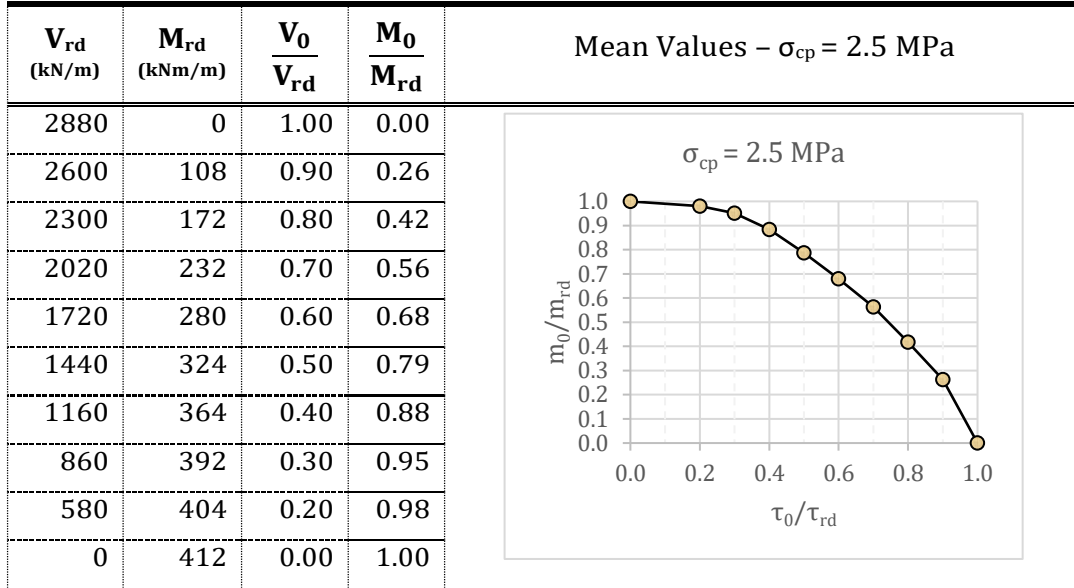
Graph 29. M - V interaction domain curve for prestressing level σ$_{cp}$=2.5MPa (mean values - ϕ24)

At low prestress, moment capacity remains limited while shear plays a significant role in failure.

Table 25. M - V interaction domain curve for prestressing level σ$_{cp}$=5.0MPa (mean values - ϕ24)

V$_{rd}$ (kN/m)	M$_{rd}$ (kNm/m)	$\dfrac{V_0}{V_{rd}}$	$\dfrac{M_0}{M_{rd}}$	Mean Values – σ$_{cp}$ = 5.0 MPa	
3220	0	1.00	0.00		
2900	104	0.90	0.25		
2580	164	0.80	0.40		
2260	224	0.70	0.54		
1940	284	0.60	0.69		
1620	332	0.50	0.81		
1280	368	0.40	0.89		
960	392	0.30	0.95		
640	408	0.20	0.99		
0	412	0.00	1.00		
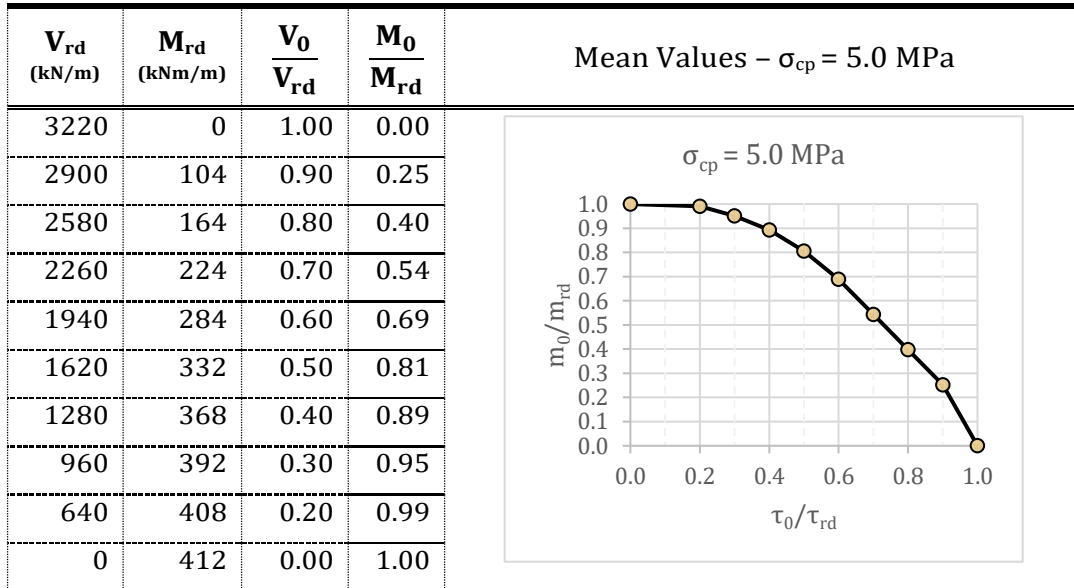
Graph 30. M - V interaction domain curve for prestressing level σ$_{cp}$=5.0MPa (mean values - ϕ24)

Prestress contributes to increased moment capacity, shifting the domain slightly upward.

Table 26. M - V interaction domain curve for prestressing level σcp=7.5MPa (mean values - ϕ24)

V_{rd} (kN/m)	M_{rd} (kNm/m)	$\dfrac{V_0}{V_{rd}}$	$\dfrac{M_0}{M_{rd}}$	Mean Values – σ_{cp} = 7.5 MPa
3460	0	1.00	0.00	
3120	104	0.90	0.25	
2760	180	0.80	0.44	
2420	240	0.70	0.58	
2080	288	0.60	0.70	
1740	328	0.50	0.80	
1380	368	0.40	0.89	
1040	392	0.30	0.95	
700	408	0.20	0.99	
0	412	0.00	1.00	
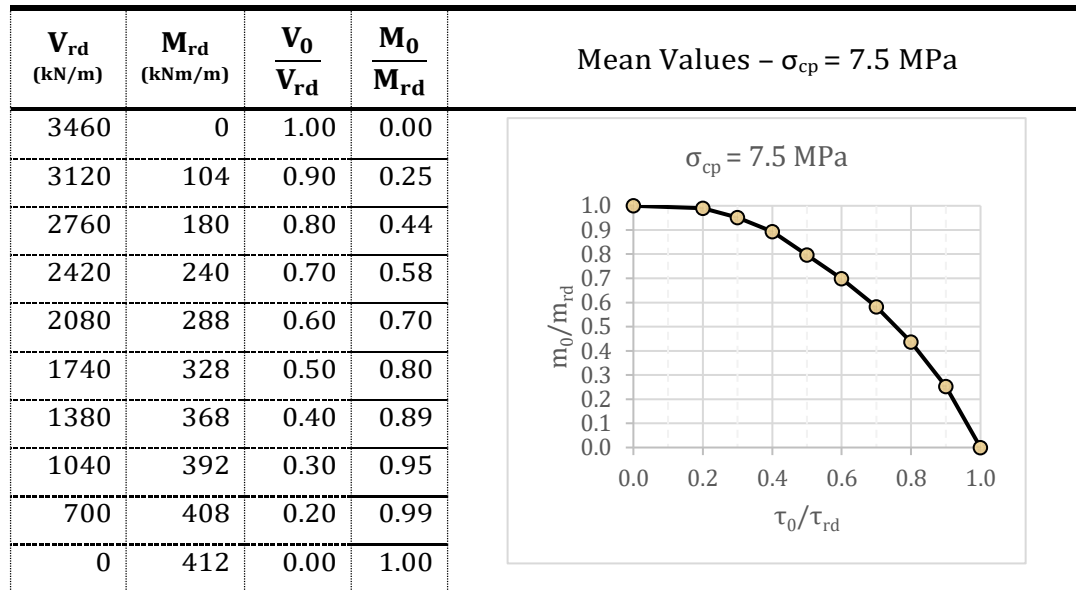
Graph 31. M - V interaction domain curve for prestressing level σcp=7.5 MPa (mean values - ϕ24)

Interaction curve becomes noticeably more rounded as prestress enhances overall resistance.

Table 27. M - V interaction domain curve for prestressing level σcp=10.0MPa (mean values - ϕ24)

V_{rd} (kN/m)	M_{rd} (kNm/m)	$\dfrac{V_0}{V_{rd}}$	$\dfrac{M_0}{M_{rd}}$	Mean Values – σ_{cp} = 10.0 MPa
3420	0	1.00	0.00	
3080	140	0.90	0.34	
2740	196	0.80	0.48	
2400	244	0.70	0.59	
2060	288	0.60	0.70	
1720	336	0.50	0.82	
1360	376	0.40	0.91	
1020	396	0.30	0.96	
680	408	0.20	0.99	
0	412	0.00	1.00	
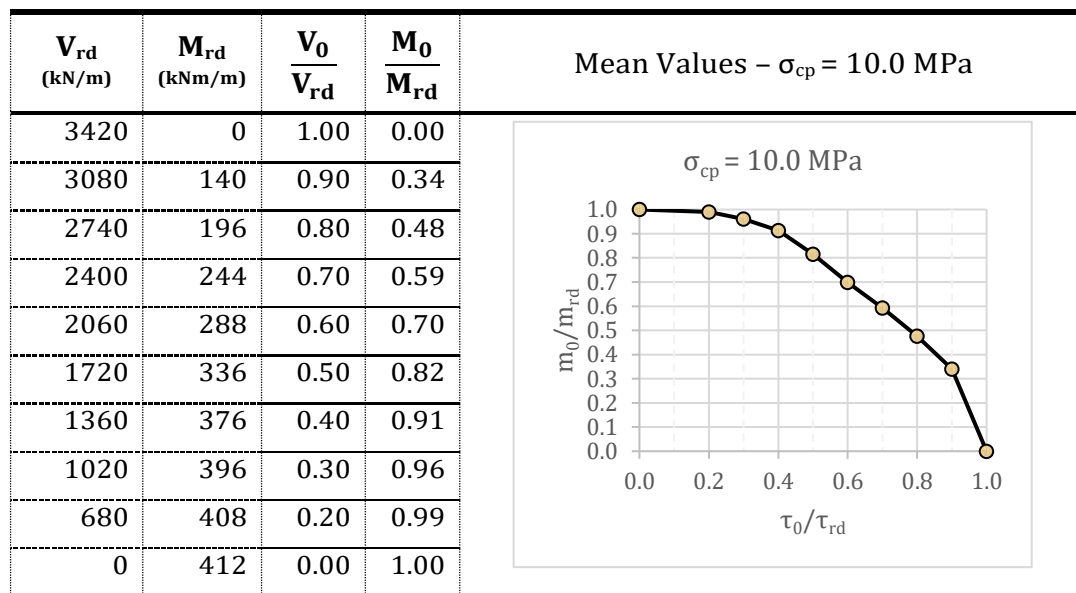
Graph 32. M - V interaction domain curve for prestressing level σcp=10.0MPa (mean values - ϕ24)

Highest prestress level leads to improved moment performance under low shear conditions.
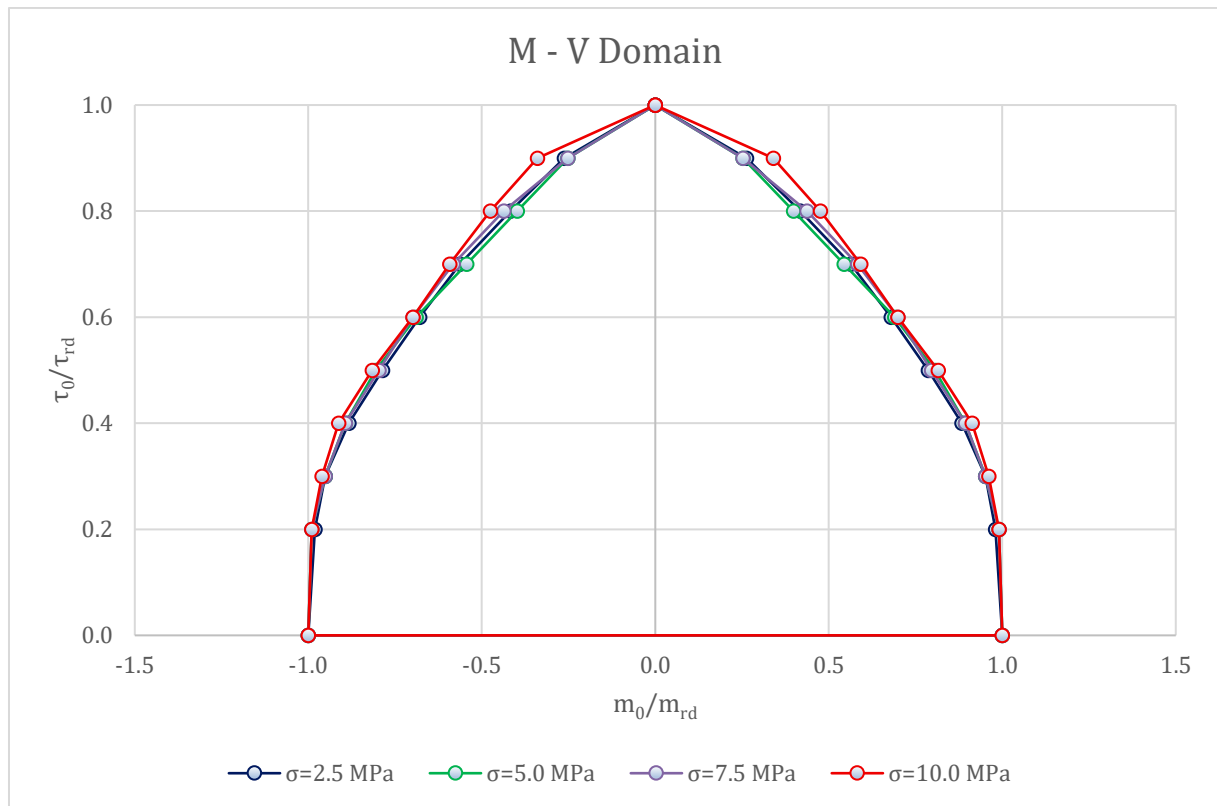
Graph 33. M–V interaction domain comparison for all prestressing levels. (mean values - C25 - ϕ24)

As prestressing increases from 2.5 MPa to 10 MPa, the interaction domain exhibits a clear and progressive expansion. At low prestress (2.5 MPa), the panel displays a relatively balanced but limited capacity, with shear effects playing a dominant role especially at higher shear levels. When the prestress increases to 5 MPa, the domain begins to shift upward, indicating enhanced moment capacity, particularly in scenarios where shear demand is low. At 7.5 MPa, the effect of prestressing becomes more visible in terms of curvature, as the domain gradually becomes more rounded showing that the panel starts to behave more ductile under combined actions. Finally, at 10 MPa, the interaction domain reaches its widest form, where the moment resistance under reduced shear levels significantly improves. This confirms that axial compression not only delays cracking but also allows the panel to redistribute stresses more efficiently. Overall, in this configuration (C25/30, ϕ24, mean values), prestress clearly contributes to improving the global performance by enhancing moment resistance without severely compromising shear behaviour.

4.4.2. Domain – C25/30 – B450C – ϕ24 – Characteristic Values

Table 28. M - V interaction domain curve for prestressing level σ$_{cp}$=2.5MPa (characteristic values - ϕ24)

V$_{rd}$ (kN/m)	M$_{rd}$ (kNm/m)	$\frac{V_0}{V_{rd}}$	$\frac{M_0}{M_{rd}}$	Characteristic Values – σ$_{cp}$ = 2.5 MPa
2560	0	1.00	0.00	
2300	80	0.90	0.22	
2040	144	0.80	0.39	
1800	188	0.70	0.51	
1540	236	0.60	0.64	
1280	280	0.50	0.76	
1020	312	0.40	0.85	
760	336	0.30	0.91	
520	352	0.20	0.96	
0	368	0.00	1.00	
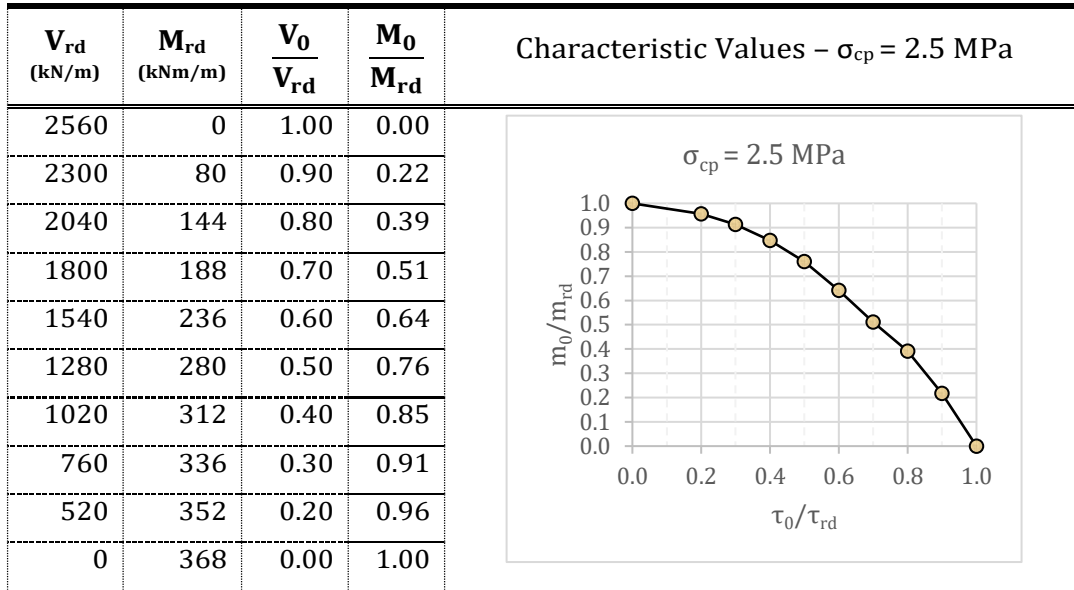
Graph 34. M - V interaction domain curve for prestressing level σ$_{cp}$=2.5MPa (characteristic values - ϕ24)

Lower material strengths result in reduced capacity in both moment and shear.

Table 29. M - V interaction domain curve for prestressing level σ$_{cp}$=5.0MPa (characteristic values - ϕ24)

V$_{rd}$ (kN/m)	M$_{rd}$ (kNm/m)	$\frac{V_0}{V_{rd}}$	$\frac{M_0}{M_{rd}}$	Characteristic Values – σ$_{cp}$ = 5.0 MPa
2840	0	1.00	0.00	
2560	88	0.90	0.24	
2280	144	0.80	0.39	
1980	204	0.70	0.55	
1700	244	0.60	0.66	
1420	284	0.50	0.77	
1140	316	0.40	0.86	
860	340	0.30	0.92	
560	356	0.20	0.97	
0	368	0.00	1.00	
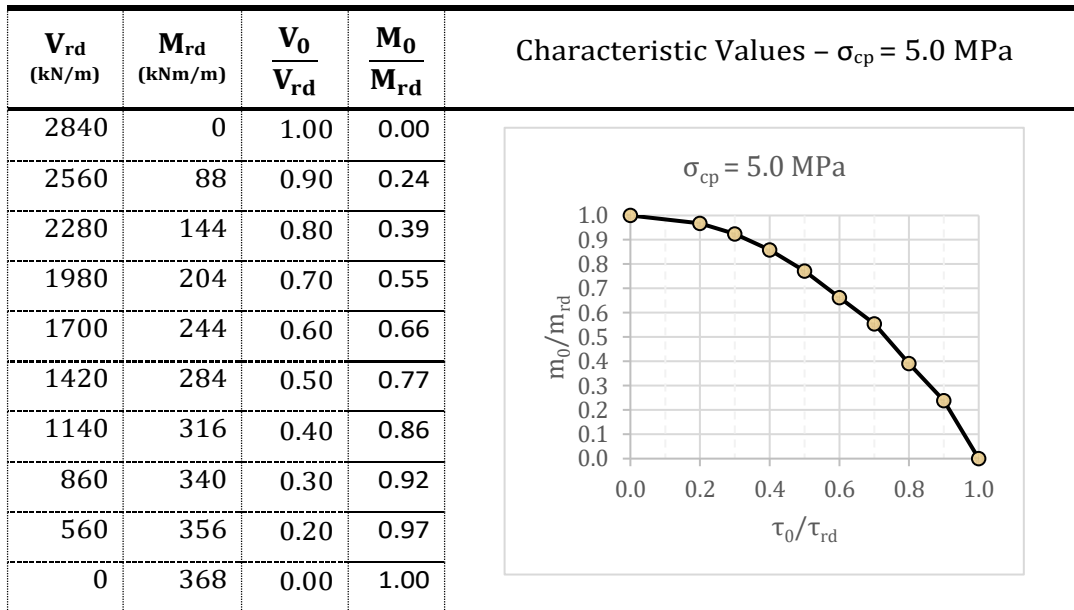
Graph 35. M - V interaction domain curve for prestressing level σ$_{cp}$=5.0MPa (characteristic values - ϕ24)

Prestress improves moment behaviour slightly, but interaction remains limited.

Table 30. M - V interaction domain curve for prestressing level σ_cp=7.5MPa (characteristic values - φ24)

V_{rd} (kN/m)	M_{rd} (kNm/m)	$\dfrac{V_0}{V_{rd}}$	$\dfrac{M_0}{M_{rd}}$	Characteristic Values – σ_cp = 7.5 MPa
2700	0	1.00	0.00	
2440	136	0.90	0.37	
2160	184	0.80	0.50	
1900	220	0.70	0.60	
1620	256	0.60	0.70	
1360	296	0.50	0.80	
1080	332	0.40	0.90	
820	348	0.30	0.95	
540	356	0.20	0.97	
0	368	0.00	1.00	
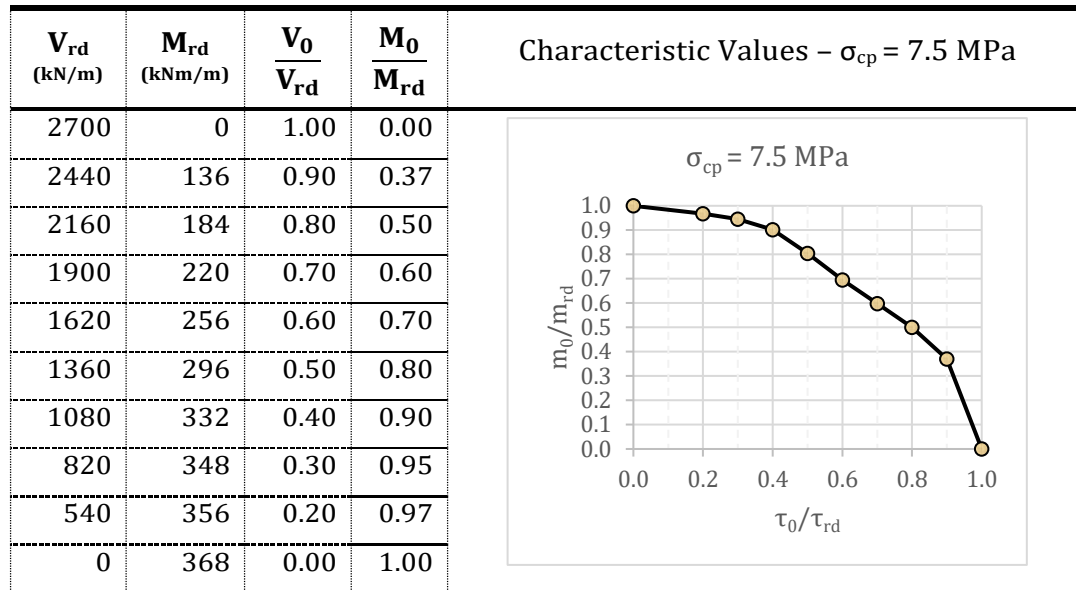
Graph 36. M - V interaction domain curve for prestressing level σ_cp=7.5MPa (characteristic values - φ24)

Notable increase in moment resistance, though the curve still remains below mean-value results.

Table 31 M - V interaction domain curve for prestressing level σ_cp=10.0MPa (characteristic values - φ24)

V_{rd} (kN/m)	M_{rd} (kNm/m)	$\dfrac{V_0}{V_{rd}}$	$\dfrac{M_0}{M_{rd}}$	Characteristic Values – σ_cp = 10.0 MPa
2560	0	1.00	0.00	
2300	168	0.90	0.46	
2040	200	0.80	0.54	
1800	228	0.70	0.62	
1540	272	0.60	0.74	
1280	316	0.50	0.86	
1020	340	0.40	0.92	
760	352	0.30	0.96	
520	360	0.20	0.98	
0	368	0.00	1.00	
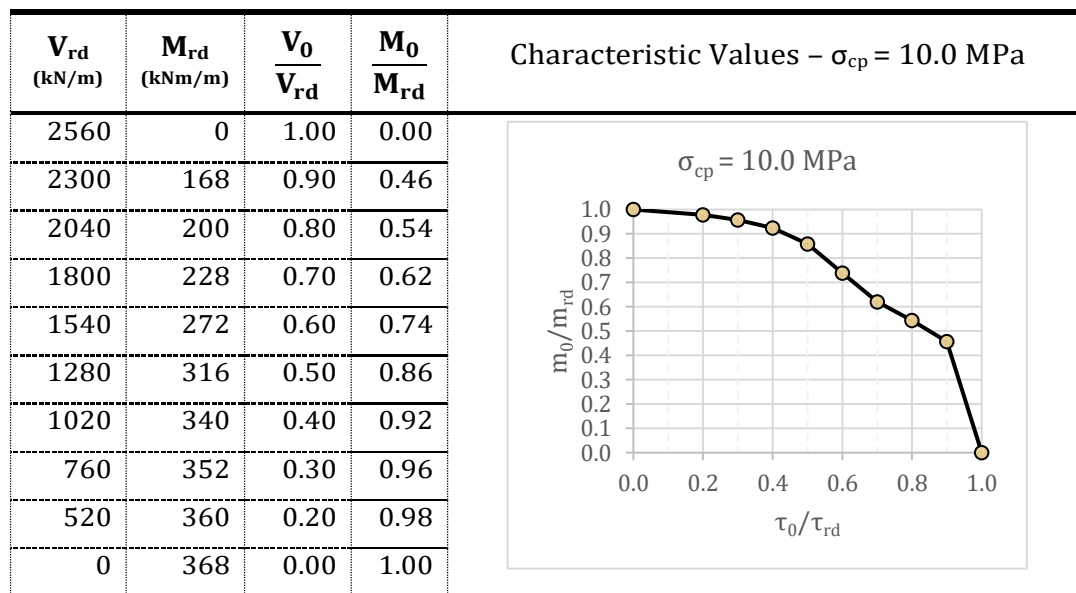
Graph 37. M - V interaction domain curve for prestressing level σ_cp=10.0MPa (characteristic values - φ24)

Curve becomes more stable, indicating increased crack control with high prestress.
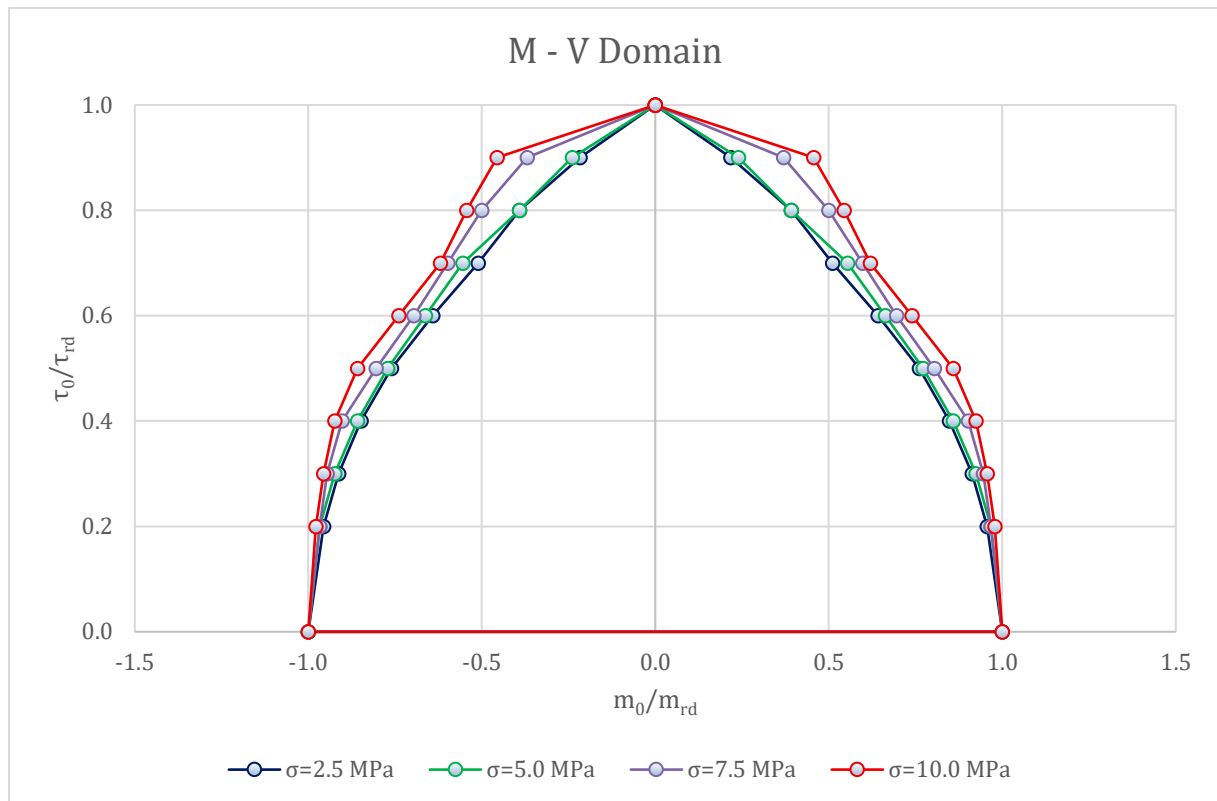
Graph 38. M–V interaction domain comparison for all prestressing levels. (characteristic values - C25 - ϕ24)

In the case of characteristic material values, the interaction domains retain the same general shape but appear narrower and more conservative compared to the mean value simulations. The initial case with 2.5 MPa prestress shows that the panel performs adequately, though the capacity is reduced due to lower characteristic strengths. With increased prestressing (5 MPa and 7.5 MPa), the interaction domain gradually expands, but the rate of increase is slower than in the mean scenario. At 10 MPa, the domain stabilizes at a higher level, indicating a modest gain in moment capacity, yet it remains consistently below the mean-value counterpart. The shear resistance seems relatively unaffected by the change in material strength, reinforcing the idea that moment is more sensitive to prestress and reinforcement assumptions. This set of results highlights the conservative nature of characteristic design and emphasizes the importance of accurate material evaluation in assessing ultimate capacity.

4.4.3. Domain – C25/30 – B450C – φ24 – Design Values

Table 32. M - V interaction domain curve for prestressing level σ_{cp}=2.5MPa (design values - φ24)

V_{rd} (kN/m)	M_{rd} (kNm/m)	$\dfrac{V_0}{V_{rd}}$	$\dfrac{M_0}{M_{rd}}$	Design Values – σ_{cp} = 2.5 MPa
2080	0	1.00	0.00	
1880	80	0.90	0.26	
1660	128	0.80	0.42	
1460	172	0.70	0.56	
1240	204	0.60	0.66	
1040	232	0.50	0.75	
840	260	0.40	0.84	
620	284	0.30	0.92	
420	300	0.20	0.97	
0	308	0.00	1.00	
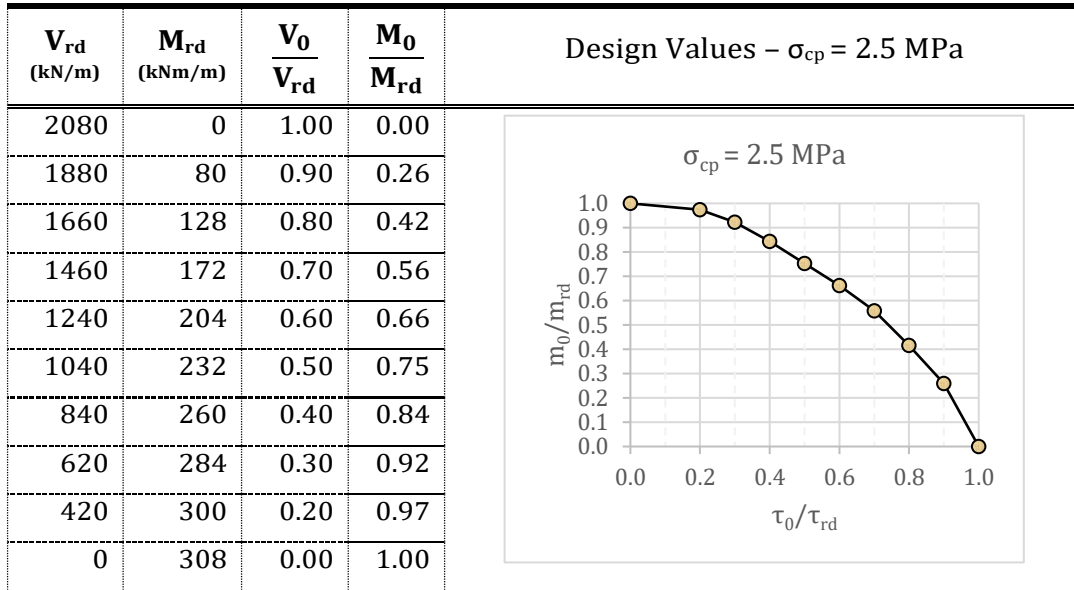
Graph 39. M - V interaction domain curve for prestressing level σ_{cp}=2.5MPa (design values - φ24)

Design strengths heavily limit capacity, with shear failure governing behaviour.
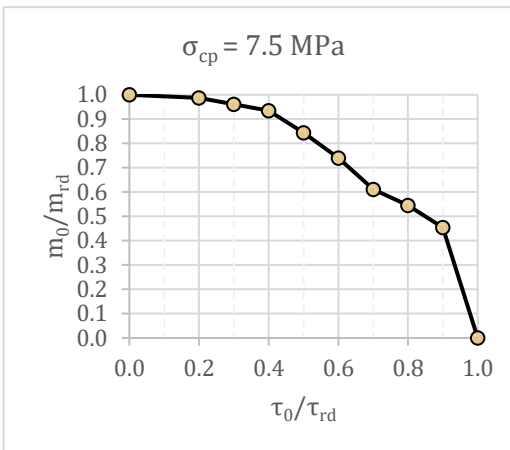
Table 33. M - V interaction domain curve for prestressing level σ_{cp}=5.0MPa (design values - φ24)

V_{rd} (kN/m)	M_{rd} (kNm/m)	$\dfrac{V_0}{V_{rd}}$	$\dfrac{M_0}{M_{rd}}$	Design Values – σ_{cp} = 5.0 MPa
1920	0	1.00	0.00	
1720	144	0.90	0.47	
1540	172	0.80	0.56	
1340	200	0.70	0.65	
1160	224	0.60	0.73	
960	252	0.50	0.82	
760	280	0.40	0.91	
580	296	0.30	0.96	
380	304	0.20	0.99	
0	308	0.00	1.00	
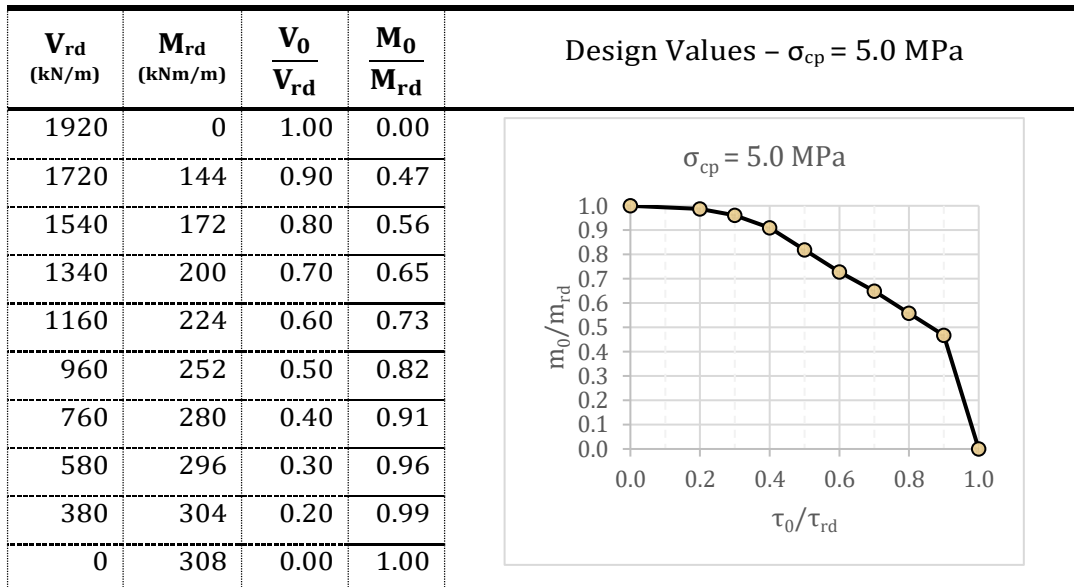
Graph 40 M - V interaction domain curve for prestressing level σ_{cp}=5.0MPa (design values - φ24)

Moment capacity remains weak; prestress has minor impact due to material conservatism.
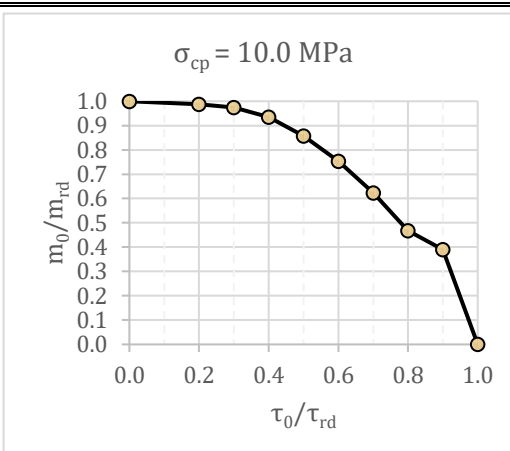
Table 34. M - V interaction domain curve for prestressing level σ_cp=7.5MPa (design values - ϕ24)

V_{rd} (kN/m)	M_{rd} (kNm/m)	$\dfrac{V_0}{V_{rd}}$	$\dfrac{M_0}{M_{rd}}$	Design Values – σ_{cp} = 7.5 MPa
1900	0	1.00	0.00	
1720	140	0.90	0.45	
1520	168	0.80	0.55	
1340	188	0.70	0.61	
1140	228	0.60	0.74	
960	260	0.50	0.84	
760	288	0.40	0.94	
580	296	0.30	0.96	
380	304	0.20	0.99	
0	308	0.00	1.00	

Graph 41. M – V interaction domain curve for prestressing level σ_cp=7.5Mpa (design values – ϕ24)

Slight improvement in moment, but still below characteristic domain.

Table 35. M - V interaction domain curve for prestressing level σ_cp=10.0MPa (design values – ϕ24)

V_{rd} (kN/m)	M_{rd} (kNm/m)	$\dfrac{V_0}{V_{rd}}$	$\dfrac{M_0}{M_{rd}}$	Design Values – σ_{cp} = 10.0 MPa
1860	0	1.00	0.00	
1680	120	0.90	0.39	
1480	144	0.80	0.47	
1300	192	0.70	0.62	
1120	232	0.60	0.75	
940	264	0.50	0.86	
740	288	0.40	0.94	
560	300	0.30	0.97	
380	304	0.20	0.99	
0	308	0.00	1.00	

Graph 42. M - V interaction domain curve for prestressing level σ_cp=10.0MPa (design values - ϕ24)

Prestress contributes minimally; overall curve is highly restricted.
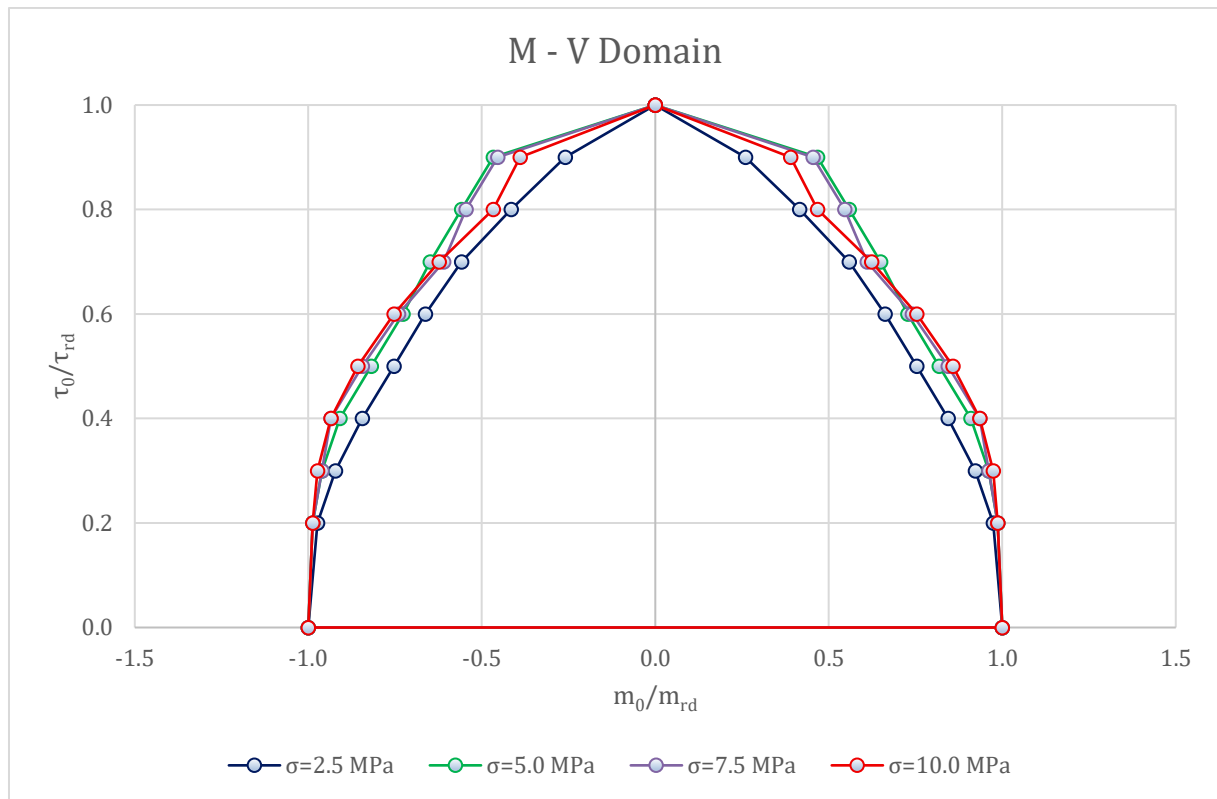
Graph 43. M–V interaction domain comparison for all prestressing levels. (design values - C25 - $\phi24$)

When design values are used, the interaction domains become the most restrictive among all material configurations. At 2.5 MPa prestress, the panel shows limited performance, with failure dominated by shear even at low moment levels. As prestress increases (5–10 MPa), the domain grows slightly, but the increase in moment resistance is marginal due to the very conservative material parameters (f_{cd} , f_{yd}). Shear capacity appears to govern most of the combined failure modes, indicating that increasing prestress alone is not sufficient to offset the strength reduction imposed by design safety factors. This leads to an interaction domain with sharp corners and steep edges, representing a brittle behaviour with little room for redistribution. These simulations demonstrate how design-level assumptions, while safe, may significantly underestimate the available capacity—especially for members subjected to combined actions. Nonetheless, the methodology remains consistent and provides a valuable envelope for limit state design verifications.

4.4.4. Domain – C25/30 – B450C – ϕ20 – Mean Values

Table 36. M - V interaction domain curve for prestressing level σ$_{cp}$=2.5MPa (mean values - ϕ20)

V$_{rd}$ (kN/m)	M$_{rd}$ (kNm/m)	$\frac{V_0}{V_{rd}}$	$\frac{M_0}{M_{rd}}$	Mean Values – σ$_{cp}$ = 2.5 MPa
2240	0	1.00	0.00	
2020	84	0.90	0.27	
1800	132	0.80	0.43	
1560	172	0.70	0.56	
1340	216	0.60	0.70	
1120	252	0.50	0.82	
900	276	0.40	0.90	
680	296	0.30	0.96	
440	304	0.20	0.99	
0	308	0.00	1.00	
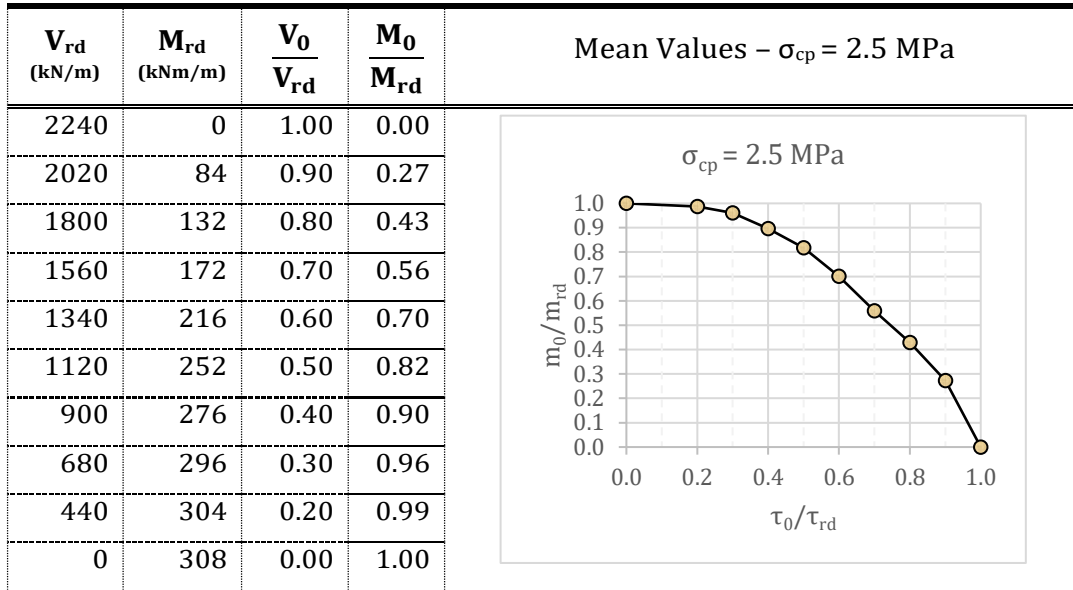
Graph 44. M - V interaction domain curve for prestressing level σ$_{cp}$=2.5MPa (mean values - ϕ20)

Lower reinforcement ratio limits moment capacity, mostly at higher shear levels.

Table 37. M - V interaction domain curve for prestressing level σ$_{cp}$=5.0MPa (mean values - ϕ20)

V$_{rd}$ (kN/m)	M$_{rd}$ (kNm/m)	$\frac{V_0}{V_{rd}}$	$\frac{M_0}{M_{rd}}$	Mean Values – σ$_{cp}$ = 5.0 MPa
2560	0	1.00	0.00	
2300	80	0.90	0.26	
2040	136	0.80	0.44	
1800	176	0.70	0.57	
1540	220	0.60	0.71	
1280	252	0.50	0.82	
1020	284	0.40	0.92	
760	296	0.30	0.96	
520	304	0.20	0.99	
0	308	0.00	1.00	
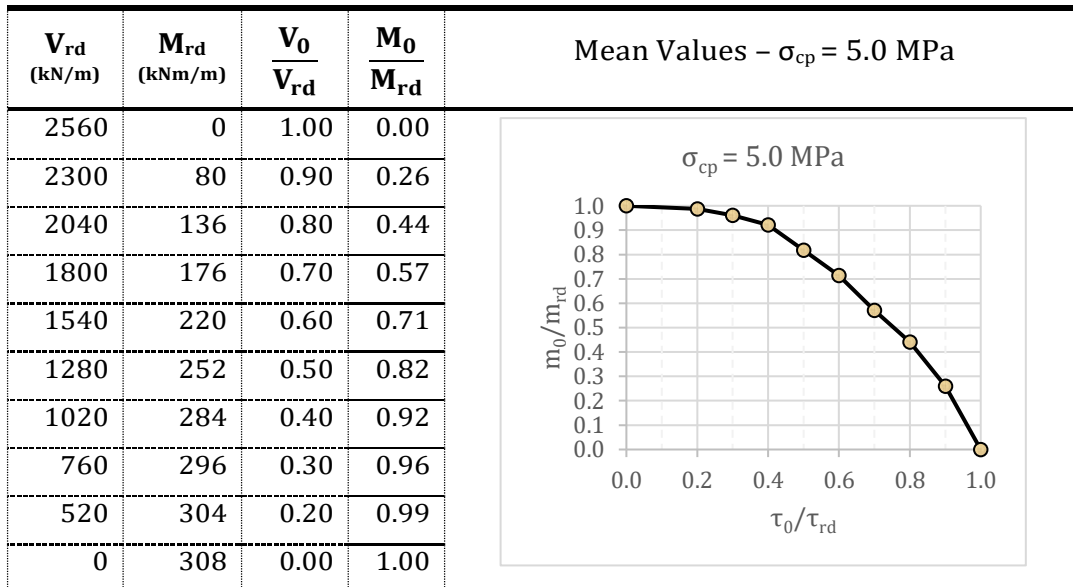
Graph 45. M - V interaction domain curve for prestressing level σ$_{cp}$=5.0MPa (mean values - ϕ20)

Prestress slightly improves moment resistance, but the influence is less than with ϕ24.

Table 38. M - V interaction domain curve for prestressing level σ$_{cp}$=7.5MPa (mean values – φ20)

V_{rd} (kN/m)	M_{rd} (kNm/m)	$\dfrac{V_0}{V_{rd}}$	$\dfrac{M_0}{M_{rd}}$	Mean Values – σ$_{cp}$ = 7.5 MPa		
2840	0	1.00	0.00			
2560	76	0.90	0.25			
2280	136	0.80	0.44			
1980	188	0.70	0.61			
1700	224	0.60	0.73			
1420	256	0.50	0.83			
1140	280	0.40	0.91			
860	296	0.30	0.96			
560	304	0.20	0.99			
0	308	0.00	1.00			
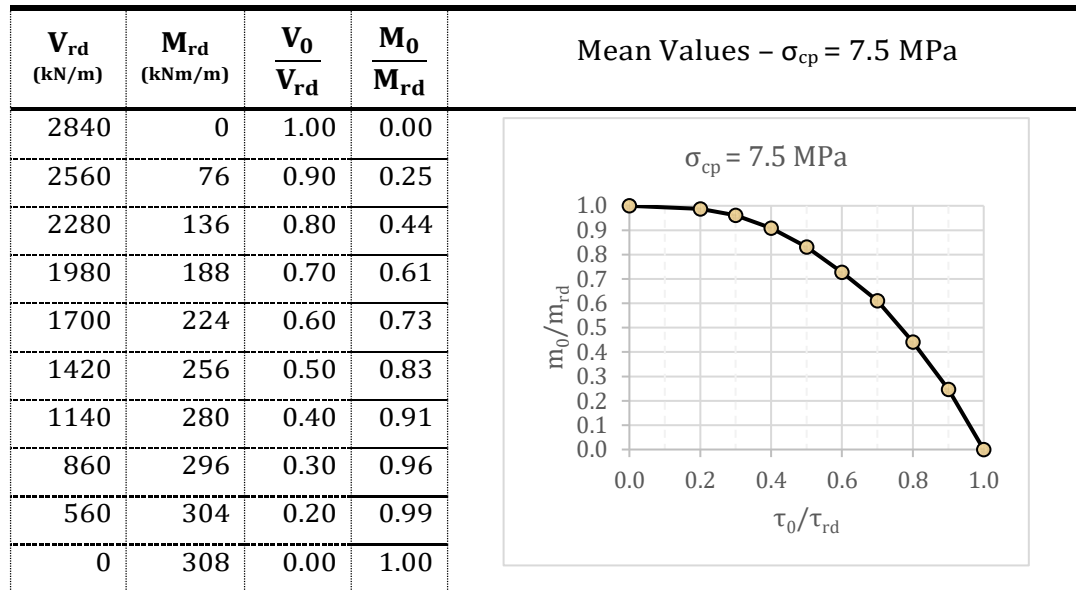
Graph 46. M - V interaction domain curve for prestressing level σ$_{cp}$=7.5MPa (mean values - φ20)

Domain curvature increases: panel begins to exhibit improved ductility.

Table 39. M - V interaction domain curve for prestressing level σ$_{cp}$=10.0MPa (mean values - φ20)

V_{rd} (kN/m)	M_{rd} (kNm/m)	$\dfrac{V_0}{V_{rd}}$	$\dfrac{M_0}{M_{rd}}$	Mean Values – σ$_{cp}$ = 10.0 MPa		
2940	0	1.00	0.00			
2640	104	0.90	0.34			
2360	148	0.80	0.48			
2060	192	0.70	0.62			
1760	224	0.60	0.73			
1480	260	0.50	0.84			
1180	284	0.40	0.92			
880	296	0.30	0.96			
580	304	0.20	0.99			
0	308	0.00	1.00			
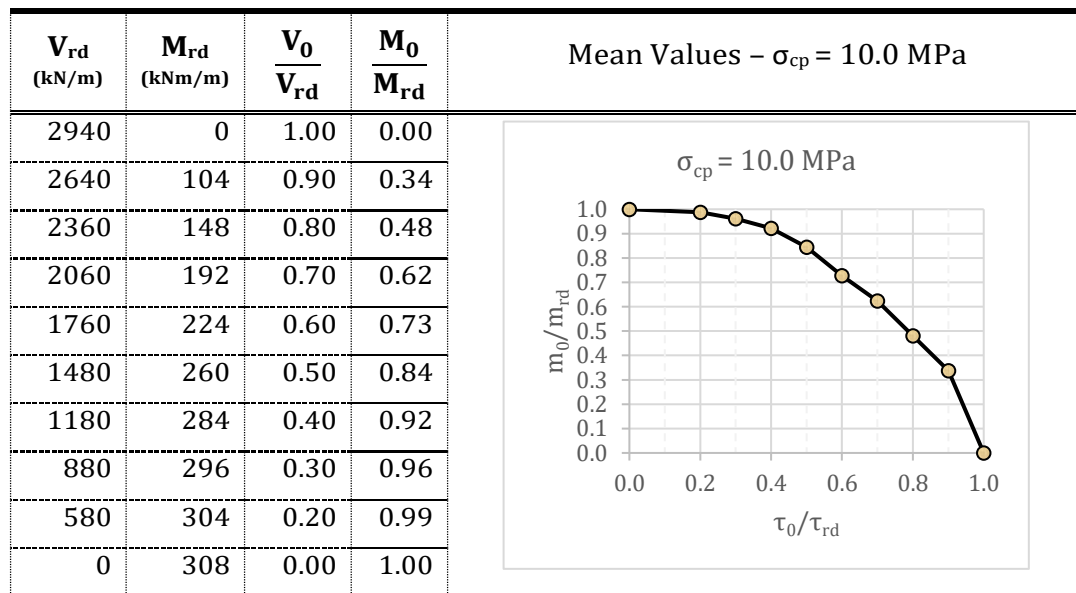
Graph 47. M - V interaction domain curve for prestressing level σ$_{cp}$=10.0MPa (mean values - φ20)

Prestressing compensates for reduced reinforcement to some extent, enhancing moment.
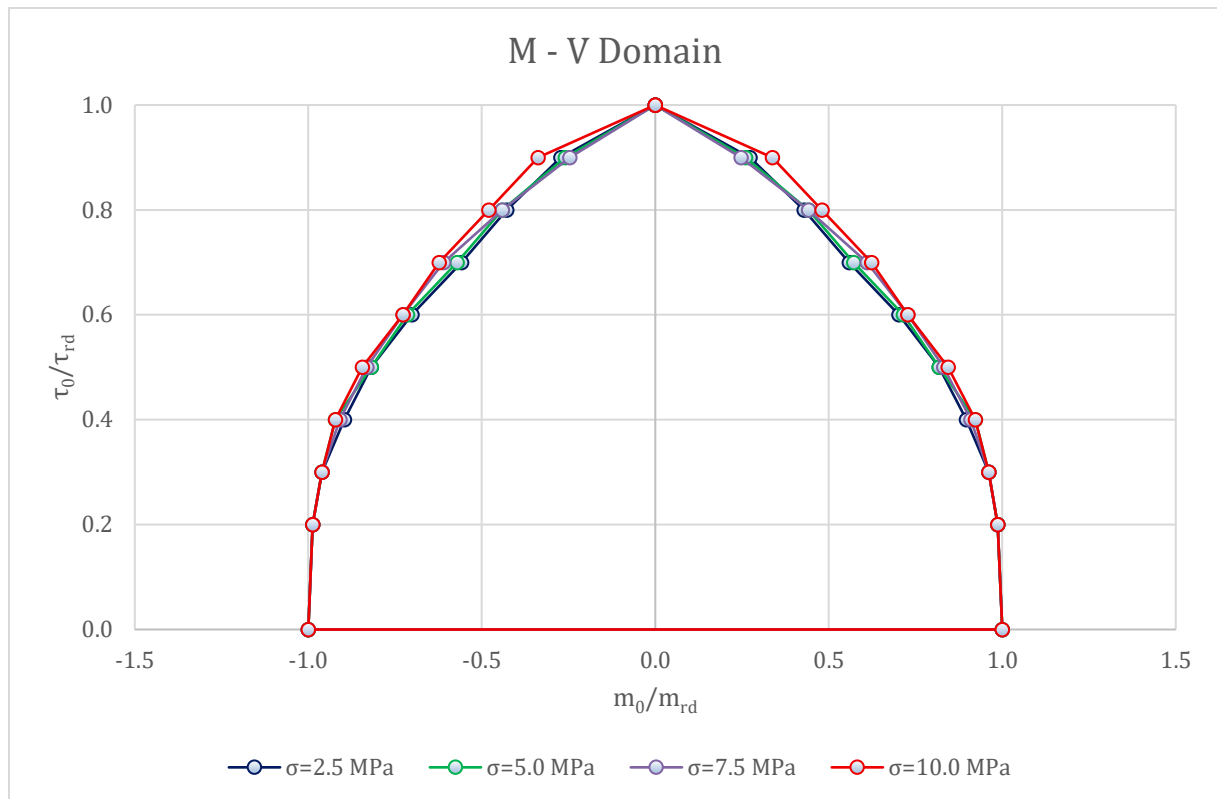
Graph 48. M–V interaction domain comparison for all prestressing levels. (mean values - C25 - ϕ20)

The results clearly reflect the influence of reinforcement ratio on interaction behavior. Compared to ϕ24, the domain is narrower across all prestress levels. While increasing axial compression improves moment capacity, the thinner bars result in cracking earlier and lower overall strength. The domain expansion from 2.5 MPa to 10 MPa is consistent, though more modest than in the higher reinforcement case. These results highlight that reinforcement ratio plays a more dominant role than prestress when both moment and shear act together.

4.4.5. Domain – C25/30 – B450C – φ20 – Characteristic Values

Table 40. M - V interaction domain curve for prestressing level σ$_{cp}$=2.5MPa (characteristic values – φ20)

V$_{rd}$ (kN/m)	M$_{rd}$ (kNm/m)	$\dfrac{V_0}{V_{rd}}$	$\dfrac{M_0}{M_{rd}}$	Characteristic Values – σ$_{cp}$ = 2.5 MPa
1980	0	1.00	0.00	
1780	64	0.90	0.24	
1580	104	0.80	0.39	
1380	144	0.70	0.54	
1180	184	0.60	0.69	
1000	212	0.50	0.79	
800	236	0.40	0.88	
600	252	0.30	0.94	
400	264	0.20	0.99	
0	268	0.00	1.00	
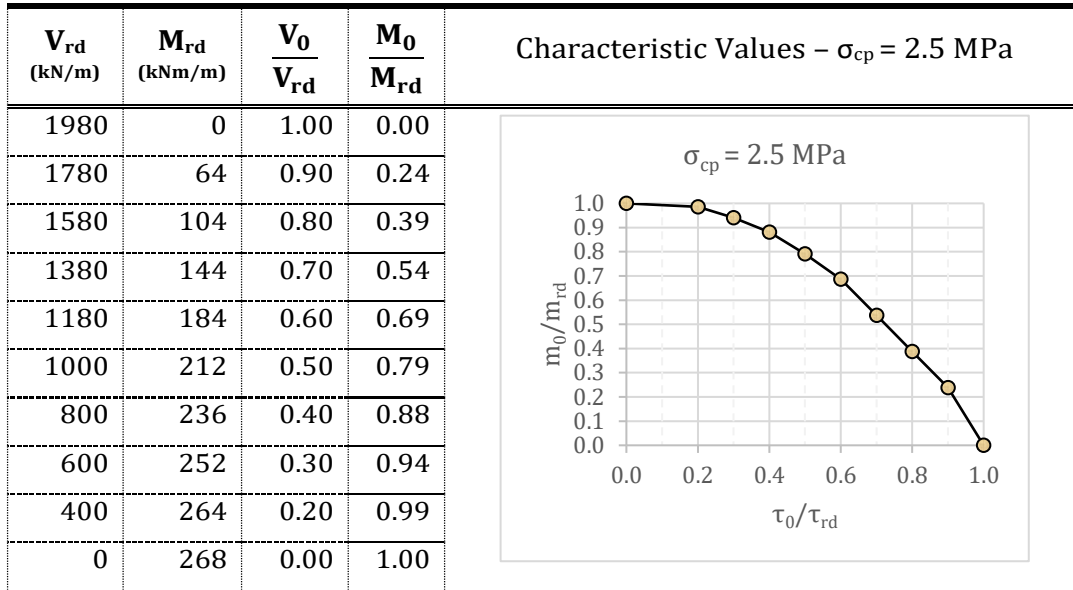
Graph 49. M – V interaction domain curve for prestressing level σ$_{cp}$=2.5Mpa (characteristic values – φ20)

Panel fails early due to low reinforcement and reduced material strengths.

Table 41. M - V interaction domain curve for prestressing level σ$_{cp}$=5.0MPa (characteristic values – φ20)

V$_{rd}$ (kN/m)	M$_{rd}$ (kNm/m)	$\dfrac{V_0}{V_{rd}}$	$\dfrac{M_0}{M_{rd}}$	Characteristic Values – σ$_{cp}$ = 5.0 MPa
2280	0	1.00	0.00	
2060	60	0.90	0.22	
1820	108	0.80	0.40	
1600	152	0.70	0.57	
1360	188	0.60	0.70	
1140	216	0.50	0.81	
920	240	0.40	0.90	
680	256	0.30	0.96	
460	264	0.20	0.99	
0	268	0.00	1.00	
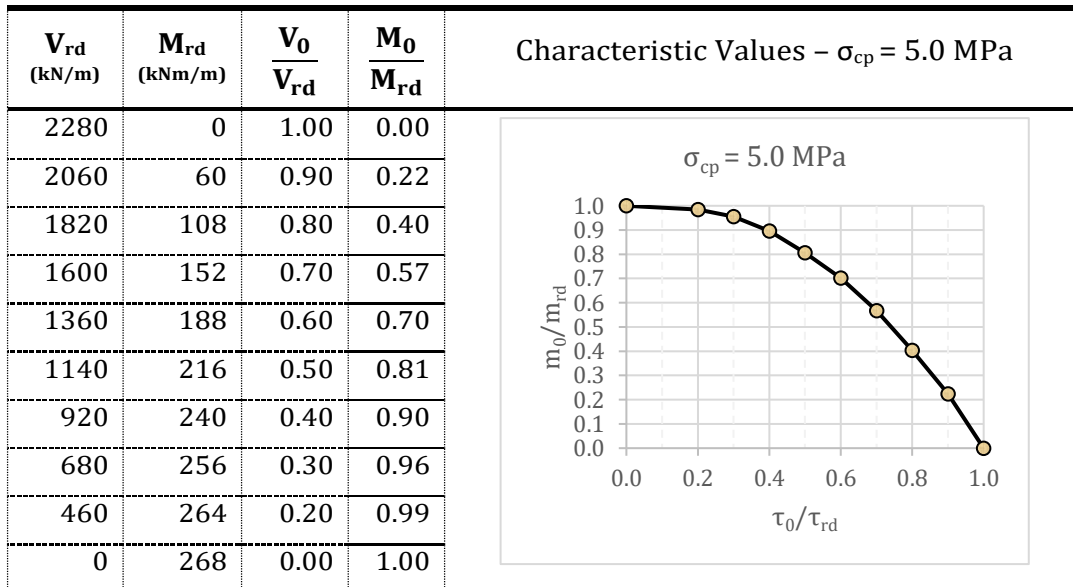
Graph 50. M - V interaction domain curve for prestressing level σ$_{cp}$=5.0MPa (characteristic values - φ20)

Prestress effect becomes visible, but interaction remains significantly limited.

Table 42. M - V interaction domain curve for prestressing level σcp=7.5MPa (characteristic values – φ20)

V_{rd} (kN/m)	M_{rd} (kNm/m)	$\dfrac{V_0}{V_{rd}}$	$\dfrac{M_0}{M_{rd}}$	Characteristic Values – σcp = 7.5 MPa
2420	0	1.00	0.00	
2180	84	0.90	0.31	
1940	120	0.80	0.45	
1700	160	0.70	0.60	
1460	188	0.60	0.70	
1220	220	0.50	0.82	
960	244	0.40	0.91	
720	256	0.30	0.96	
480	264	0.20	0.99	
0	268	0.00	1.00	
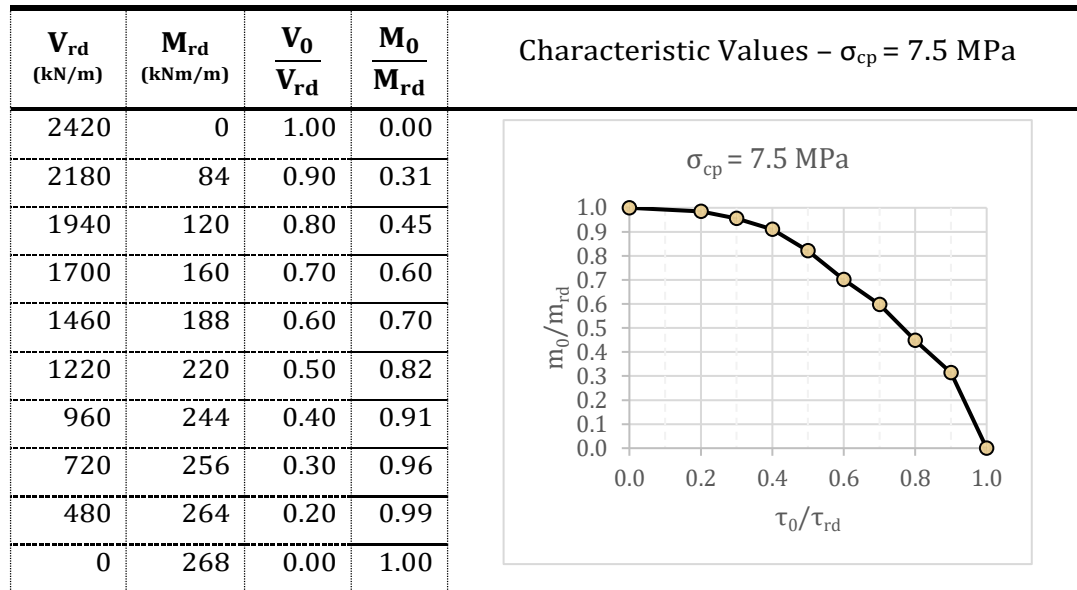
Graph 51. M - V interaction domain curve for prestressing level σcp=7.5MPa (characteristic values – φ20)

Slight upward shift in moment capacity with increased axial compression.

Table 43. M - V interaction domain curve for prestressing level σcp=10.0MPa (characteristic values – φ20)

V_{rd} (kN/m)	M_{rd} (kNm/m)	$\dfrac{V_0}{V_{rd}}$	$\dfrac{M_0}{M_{rd}}$	Characteristic Values – σcp = 10.0 MPa
2320	0	1.00	0.00	
2080	112	0.90	0.42	
1860	140	0.80	0.52	
1620	168	0.70	0.63	
1400	196	0.60	0.73	
1160	232	0.50	0.87	
920	248	0.40	0.93	
700	260	0.30	0.97	
460	264	0.20	0.99	
0	268	0.00	1.00	
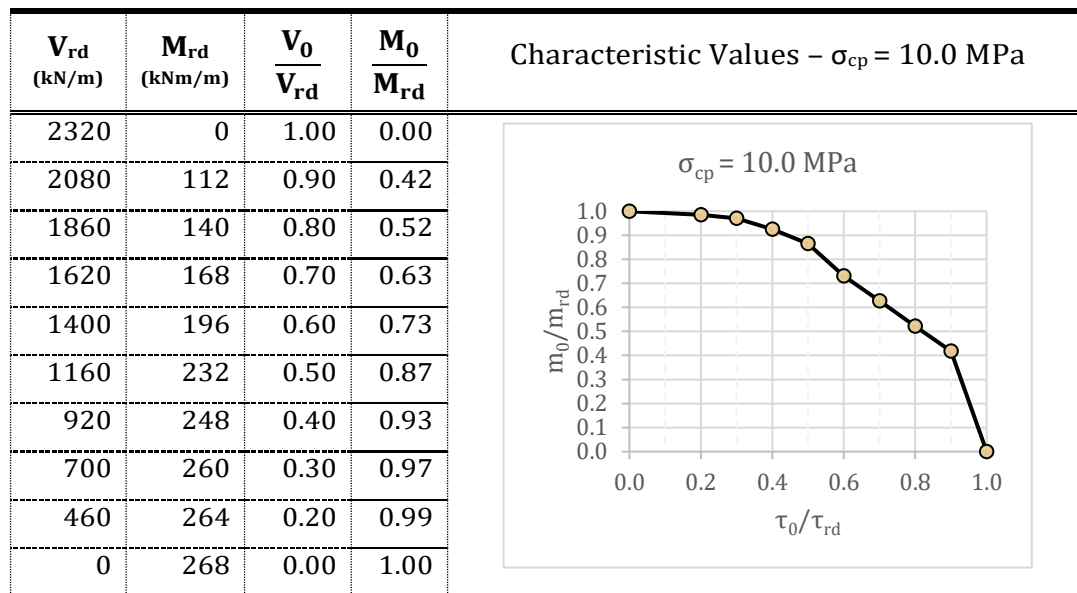
Graph 52. M - V interaction domain curve for prestressing level σcp=10.0MPa (characteristic values - φ20)

Shear still governs failure; moment improvement is marginal.
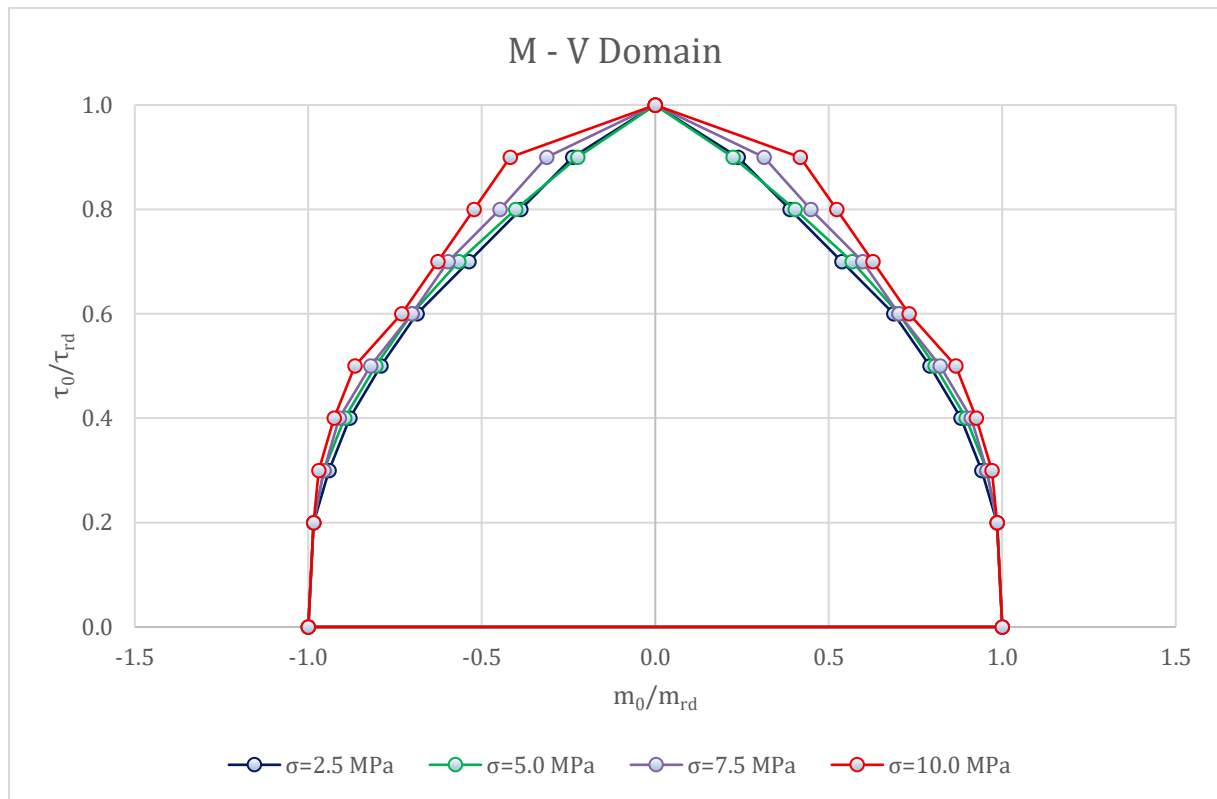
Graph 53. M–V interaction domain comparison for all prestressing levels. (characteristic values - C25 - ϕ20)

Compared to the mean case, the interaction domains are compressed and flatter. The characteristic material assumptions combined with the lower reinforcement result in limited gains from prestressing. Moment resistance stays low, and most curves show steep drops in capacity once shear is introduced. Nonetheless, the trend across prestress levels is still consistent. This scenario represents a more conservative estimate, aligning with expected characteristic-level safety margins.

4.4.6. Domain – C25/30 – B450C – ϕ20 – *Design Values*

Table 44. M - V interaction domain curve for prestressing level σ$_{cp}$=2.5MPa (design values – ϕ20)

V$_{rd}$ (kN/m)	M$_{rd}$ (kNm/m)	$\frac{V_0}{V_{rd}}$	$\frac{M_0}{M_{rd}}$	Design Values – σ$_{cp}$ = 2.5 MPa
1700	0	1.00	0.00	
1540	44	0.90	0.20	
1360	84	0.80	0.38	
1200	116	0.70	0.53	
1020	152	0.60	0.69	
860	172	0.50	0.78	
680	192	0.40	0.87	
520	208	0.30	0.95	
340	216	0.20	0.98	
0	220	0.00	1.00	
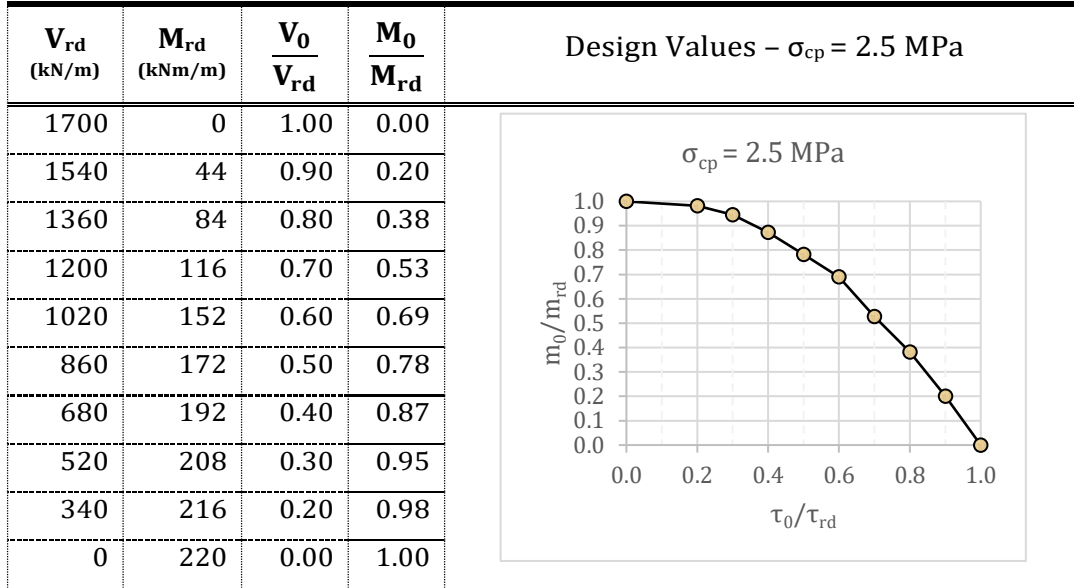
Graph 54. M - V interaction domain curve for prestressing level σ$_{cp}$=2.5MPa (design values - ϕ20)

Failure is shear-dominated with very low moment capacity.

Table 45. M - V interaction domain curve for prestressing level σ$_{cp}$=5.0MPa (design values – ϕ20)

V$_{rd}$ (kN/m)	M$_{rd}$ (kNm/m)	$\frac{V_0}{V_{rd}}$	$\frac{M_0}{M_{rd}}$	Design Values – σ$_{cp}$ = 5.0 MPa
1780	0	1.00	0.00	
1600	56	0.90	0.25	
1420	112	0.80	0.51	
1240	140	0.70	0.64	
1060	164	0.60	0.75	
900	184	0.50	0.84	
720	204	0.40	0.93	
540	212	0.30	0.96	
360	216	0.20	0.98	
0	220	0.00	1.00	
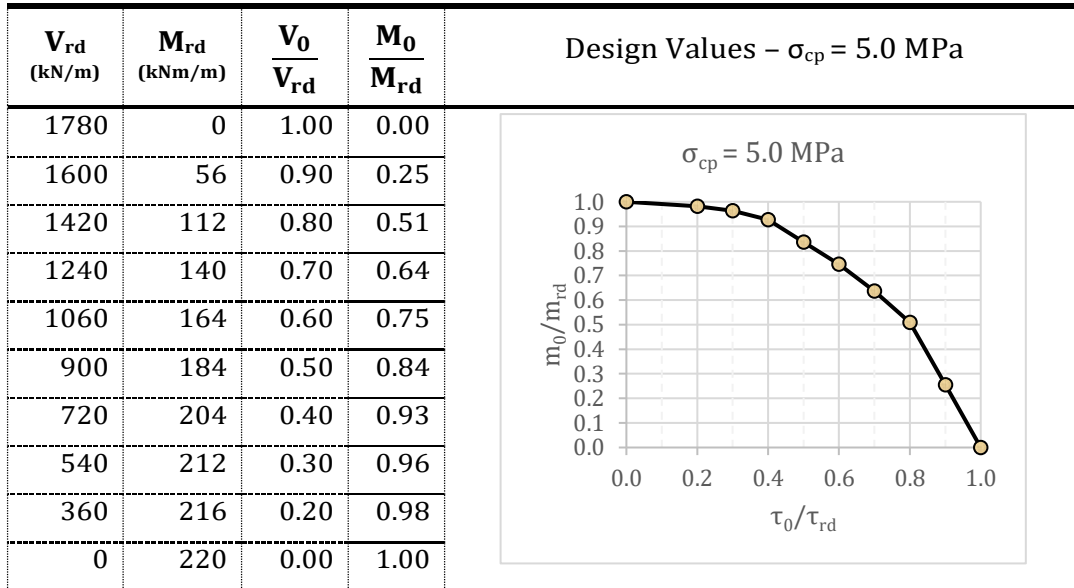
Graph. 55. M - V interaction domain curve for prestressing level σ$_{cp}$=5.0MPa (design values - ϕ20)

Prestress effect is almost negligible under design assumptions.

Table. 46. M - V interaction domain curve for prestressing level σ_{cp}=7.5MPa (design values - φ20)

V_{rd} (kN/m)	M_{rd} (kNm/m)	$\dfrac{V_0}{V_{rd}}$	$\dfrac{M_0}{M_{rd}}$	Design Values – σ_{cp} = 7.5 MPa
1720	0	1.00	0.00	
1540	96	0.90	0.44	
1380	116	0.80	0.53	
1200	136	0.70	0.62	
1040	168	0.60	0.76	
860	192	0.50	0.87	
680	208	0.40	0.95	
520	212	0.30	0.96	
340	216	0.20	0.98	
0	220	0.00	1.00	
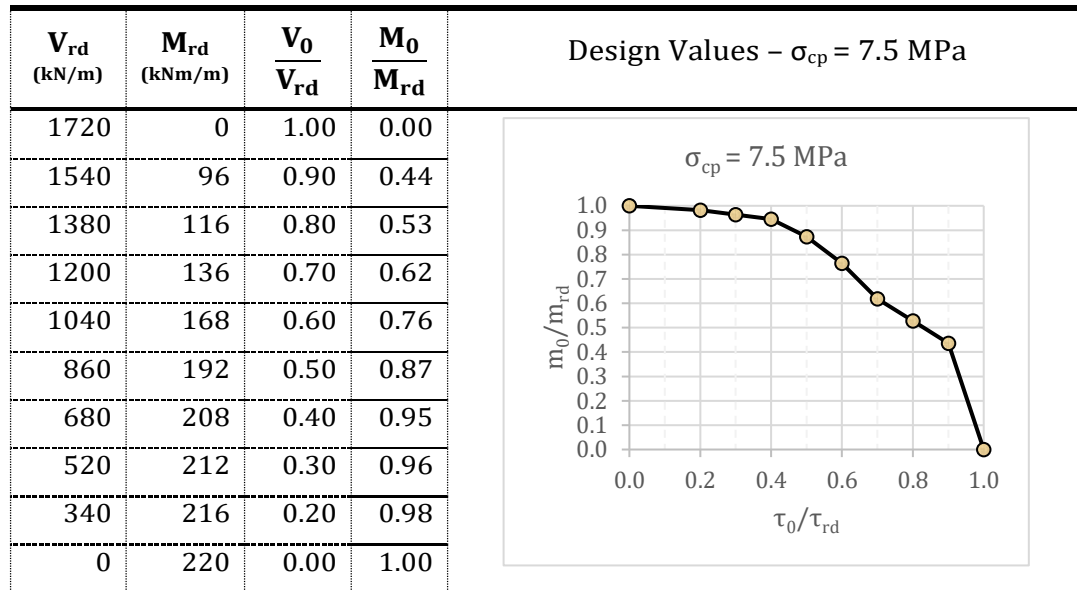
Graph 56. M - V interaction domain curve for prestressing level σ_{cp}=7.5MPa (design values - φ20)

Slight increase in curve area, but brittle behaviour remains.

Table 47. M - V interaction domain curve for prestressing level σ_{cp}=10.0MPa (design values - φ20)

V_{rd} (kN/m)	M_{rd} (kNm/m)	$\dfrac{V_0}{V_{rd}}$	$\dfrac{M_0}{M_{rd}}$	Design Values – σ_{cp} = 10.0 MPa
1640	0	1.00	0.00	
1480	92	0.90	0.42	
1320	100	0.80	0.45	
1140	132	0.70	0.60	
980	164	0.60	0.75	
820	192	0.50	0.87	
660	204	0.40	0.93	
500	212	0.30	0.96	
320	216	0.20	0.98	
0	220	0.00	1.00	
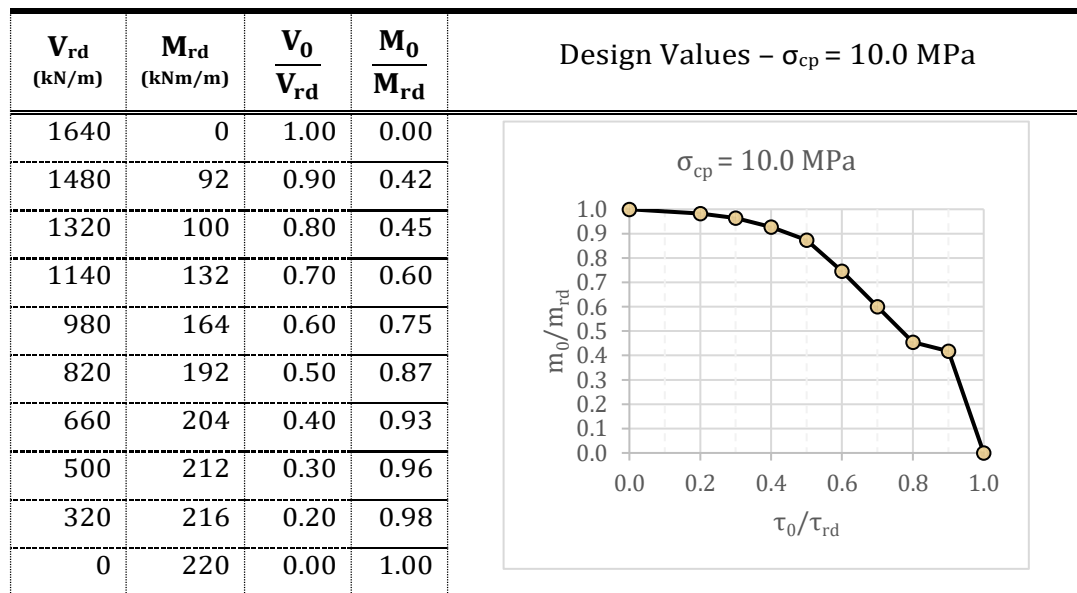
Graph 57. M - V interaction domain curve for prestressing level σ_{cp}=10.0MPa (design values - φ20)

Domain reaches maximum extent, yet still significantly limited.
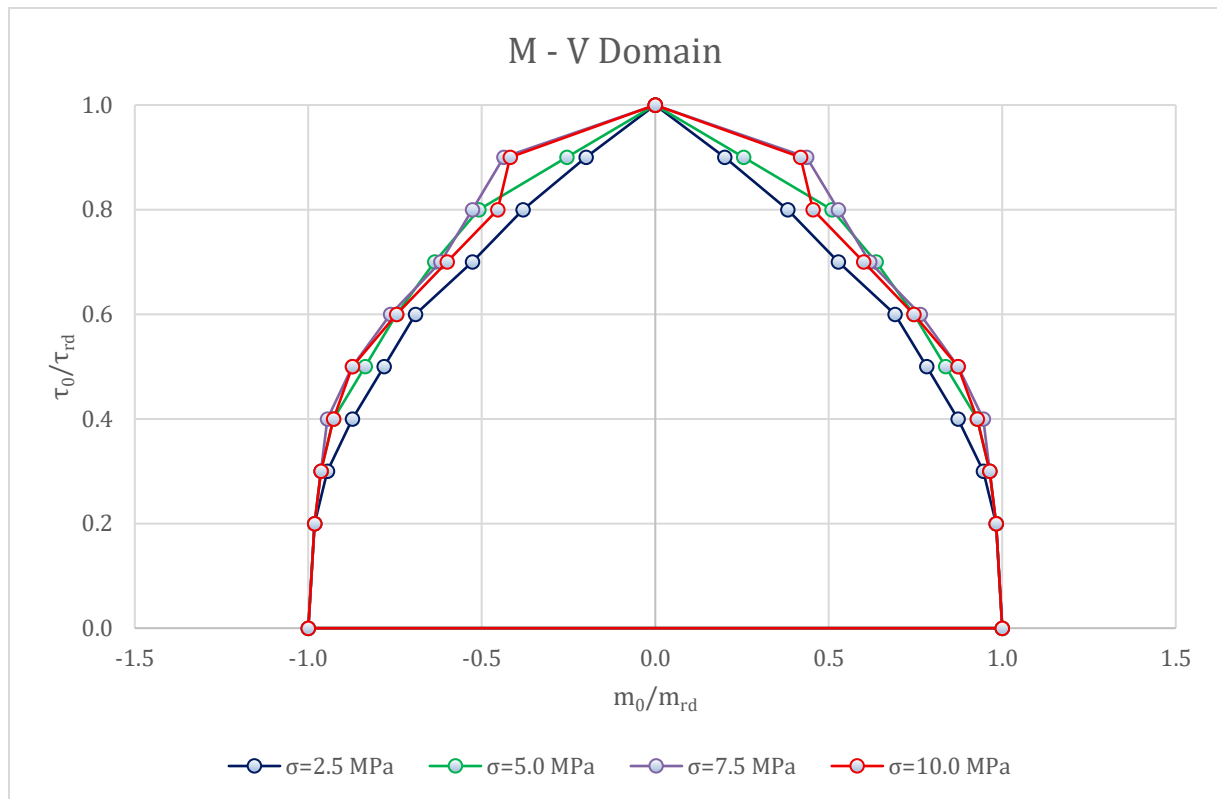
Graph 58. M–V interaction domain comparison for all prestressing levels. (design values - C25 - ϕ20)

This is the most restricted set of results among all ϕ20 configurations. Prestressing has very limited influence, and the combination of conservative design values and reduced reinforcement produces sharp, brittle interaction domains. Cracking occurs early, and redistribution is minimal. While this yields safe design envelopes, it also shows that design-based predictions may significantly underestimate real capacity, especially under biaxial stress conditions.

4.4.7. Domain – C40/50 – B450C – ϕ24 – Mean Values

Table 48. M - V interaction domain curve for prestressing level σ_cp=2.5MPa (mean values - ϕ24 - C40)

V_{rd} (kN/m)	M_{rd} (kNm/m)	$\dfrac{V_0}{V_{rd}}$	$\dfrac{M_0}{M_{rd}}$	Mean Values – σ_{cp} = 2.5 MPa
3080	0	1.00	0.00	
2780	116	0.90	0.23	
2460	192	0.80	0.39	
2160	248	0.70	0.50	
1840	312	0.60	0.63	
1540	360	0.50	0.73	
1240	396	0.40	0.80	
920	420	0.30	0.85	
620	432	0.20	0.87	
0	496	0.00	1.00	
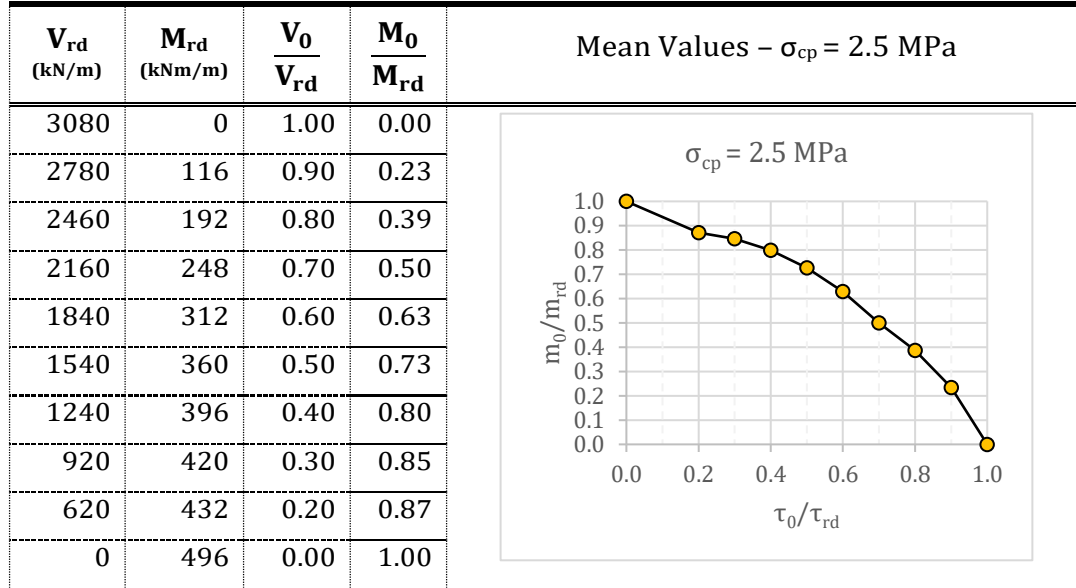
Graph 59. M - V interaction domain curve for prestressing level σ_cp=2.5MPa (mean values - ϕ24 - C40)

Higher concrete strength slightly enhances shear performance under low prestress.

Table 49. M - V interaction domain curve for prestressing level σ_cp=5.0MPa (mean values – ϕ24 – C40)

V_{rd} (kN/m)	M_{rd} (kNm/m)	$\dfrac{V_0}{V_{rd}}$	$\dfrac{M_0}{M_{rd}}$	Mean Values – σ_{cp} = 5.0 MPa
3460	0	1.00	0.00	
3120	104	0.90	0.21	
2760	192	0.80	0.39	
2420	264	0.70	0.53	
2080	304	0.60	0.61	
1740	360	0.50	0.73	
1380	400	0.40	0.81	
1040	424	0.30	0.85	
700	444	0.20	0.90	
0	496	0.00	1.00	
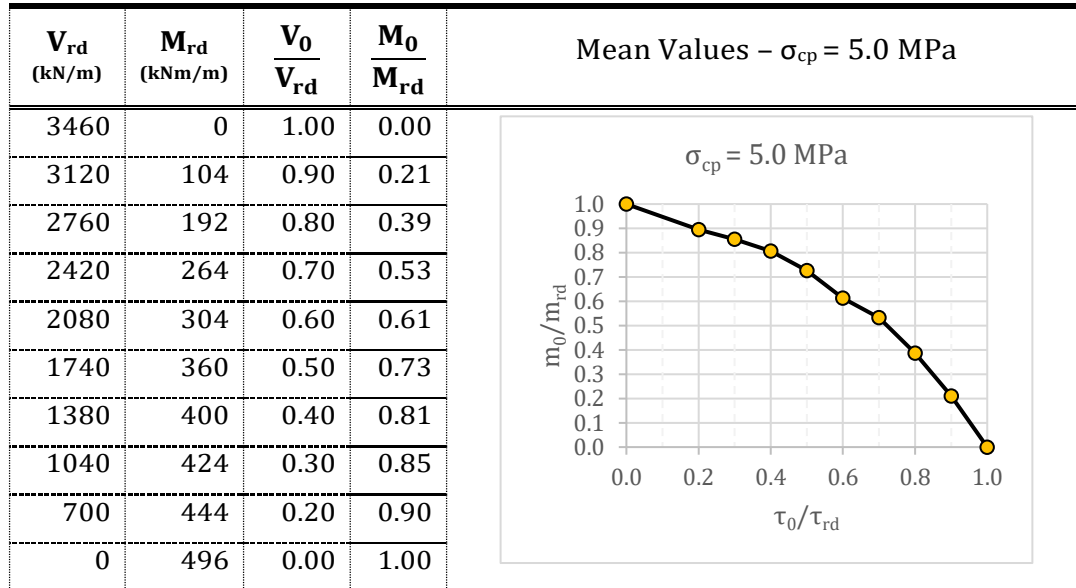
Graph 60. M - V interaction domain curve for prestressing level σ_cp=5.0MPa (mean values - ϕ24 - C40)

Moment resistance begins to improve significantly, domain area expands.

Table 50. M - V interaction domain curve for prestressing level σcp=7.5MPa (mean values - ϕ24 - C40)

V_{rd} (kN/m)	M_{rd} (kNm/m)	$\dfrac{V_0}{V_{rd}}$	$\dfrac{M_0}{M_{rd}}$	Mean Values – σcp = 7.5 MPa
3740	0	1.00	0.00	
3360	124	0.90	0.25	
3000	184	0.80	0.37	
2620	252	0.70	0.51	
2240	316	0.60	0.64	
1880	372	0.50	0.75	
1500	404	0.40	0.81	
1120	424	0.30	0.85	
740	468	0.20	0.94	
0	496	0.00	1.00	
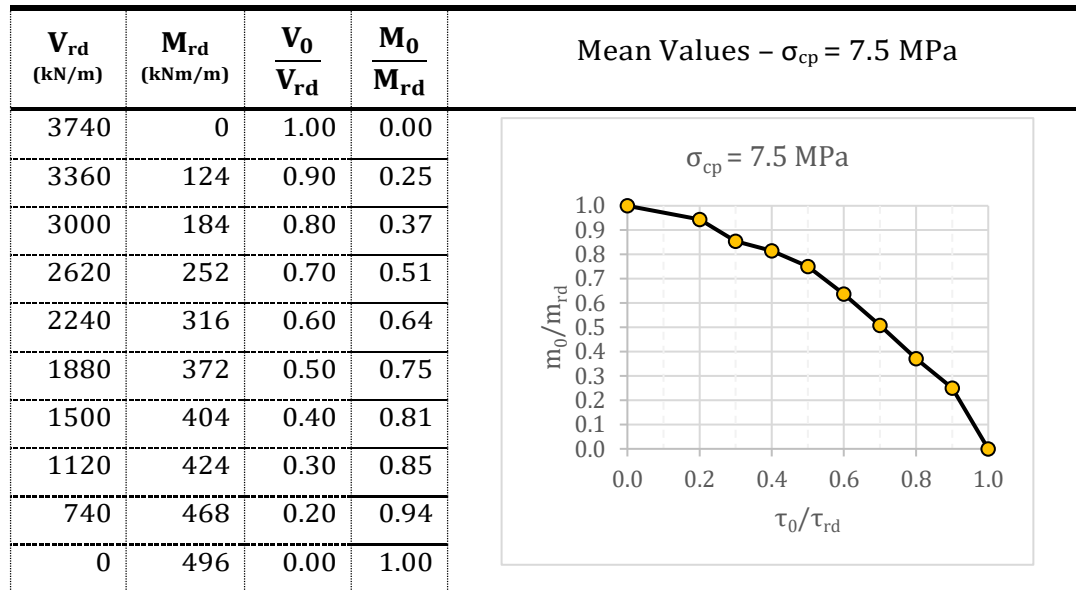
Graph 61. M - V interaction domain curve for prestressing level σcp=7.5MPa (mean values - ϕ24 - C40)

Prestressing effectively increases ductility and moment–shear synergy.

Table 51. M - V interaction domain curve for prestressing level σcp=10.0MPa (mean values – ϕ24 – C40)

V_{rd} (kN/m)	M_{rd} (kNm/m)	$\dfrac{V_0}{V_{rd}}$	$\dfrac{M_0}{M_{rd}}$	Mean Values – σcp = 10.0 MPa
4000	0	1.00	0.00	
3600	120	0.90	0.24	
3200	192	0.80	0.39	
2800	268	0.70	0.54	
2400	324	0.60	0.65	
2000	376	0.50	0.76	
1600	404	0.40	0.81	
1200	428	0.30	0.86	
800	456	0.20	0.92	
0	496	0.00	1.00	
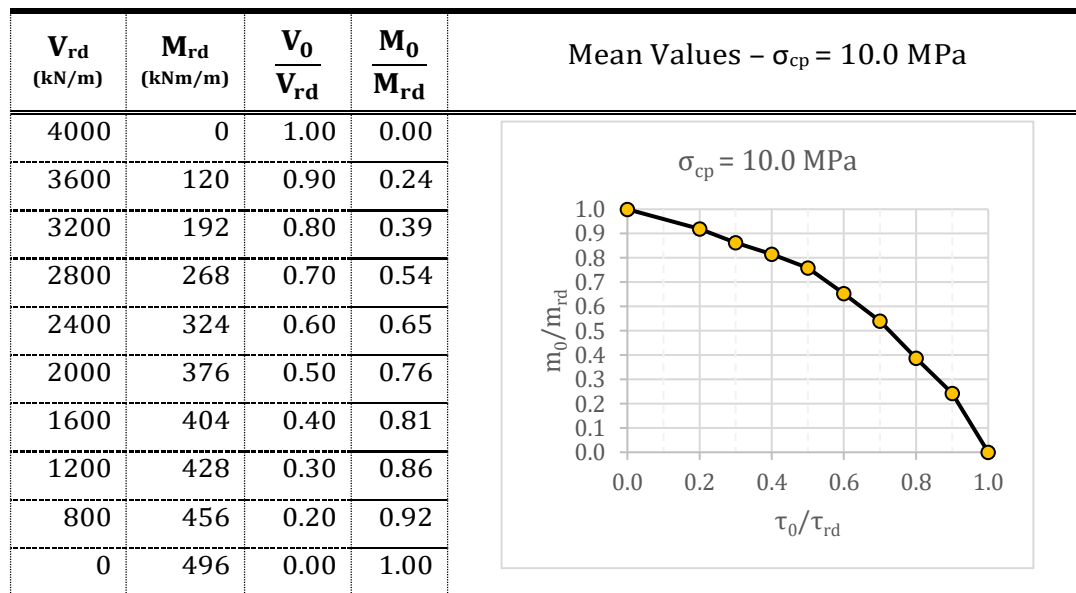
Graph 62. M - V interaction domain curve for prestressing level σcp=10.0MPa (mean values - ϕ24 - C40)

Panel reaches maximum performance with enhanced interaction capacity.
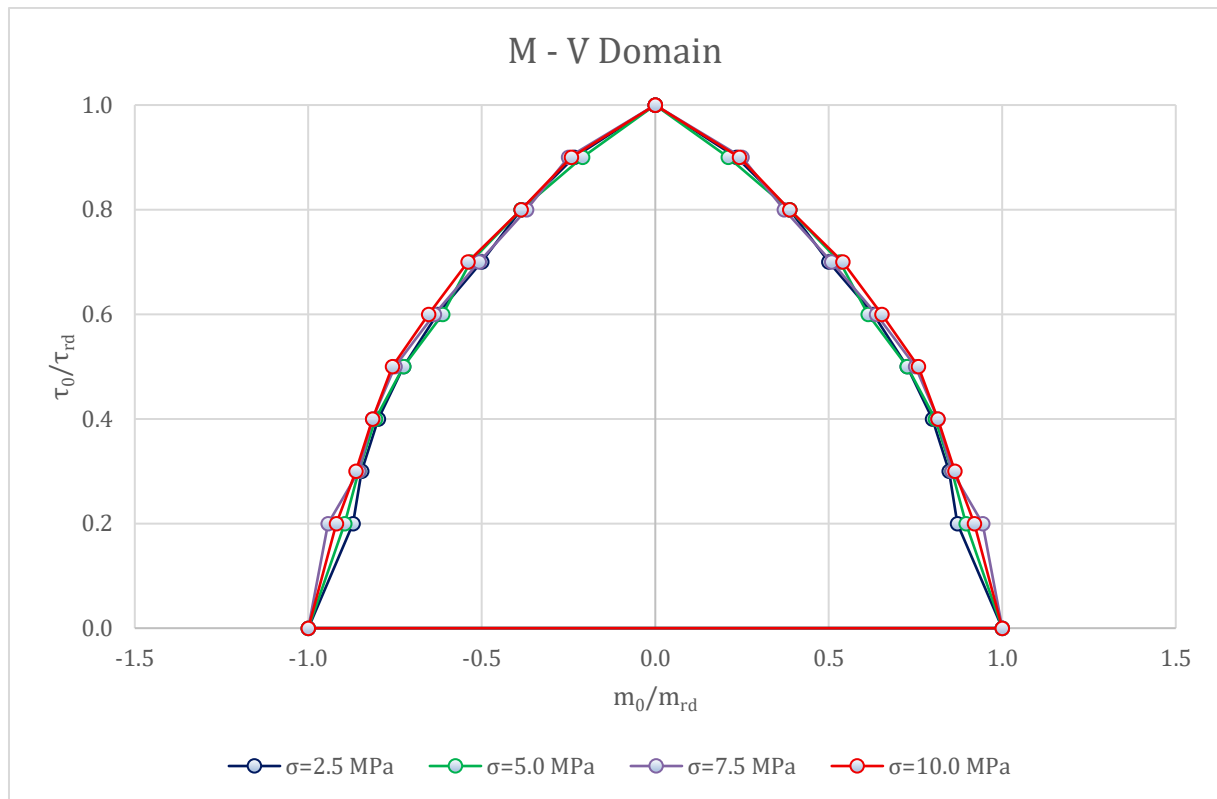
Graph 63. M–V interaction domain comparison for all prestressing levels. (mean values – C40 - φ24)

In comparison to C25/30 results, this set displays superior capacity under all prestress levels. The higher-grade concrete allows greater moment development without early shear cracking, especially when coupled with increased prestress. While the general shape of the interaction domain is similar to previous analyses, its overall size is larger and more rounded. This reflects both the strength gain from the concrete and the increased ductility enabled by prestressing. The φ24 reinforcement further complements this, resulting in the most efficient interaction among all tested configurations.

4.4.8. Domain – C40/50 – B450C – ϕ24 – *Mean Values*

Table 52. M - V interaction domain curve for prestressing level σ$_{cp}$=2.5MPa (mean values - ϕ20 - C40)

V$_{rd}$ (kN/m)	M$_{rd}$ (kNm/m)	$\dfrac{V_0}{V_{rd}}$	$\dfrac{M_0}{M_{rd}}$	Mean Values – σ$_{cp}$ = 2.5 MPa
2420	0	1.00	0.00	
2180	100	0.90	0.27	
1940	152	0.80	0.42	
1700	200	0.70	0.55	
1460	236	0.60	0.65	
1220	280	0.50	0.77	
960	308	0.40	0.85	
720	320	0.30	0.88	
480	344	0.20	0.95	
0	364	0.00	1.00	
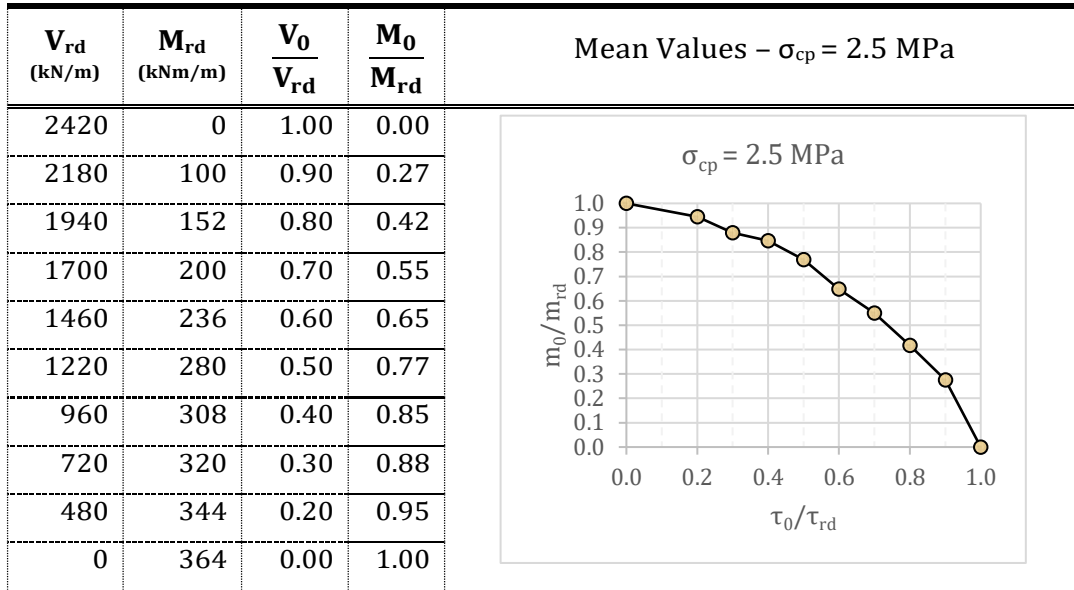
Graph 64. M - V interaction domain curve for prestressing level σ$_{cp}$=2.5MPa (mean values - ϕ20 - C40)

Due to the reduced reinforcement ratio, the interaction domain remains narrow despite the higher concrete strength.

Table 53. M - V interaction domain curve for prestressing level σ$_{cp}$=5.0MPa (mean values – ϕ20 – C40)

V$_{rd}$ (kN/m)	M$_{rd}$ (kNm/m)	$\dfrac{V_0}{V_{rd}}$	$\dfrac{M_0}{M_{rd}}$	Mean Values – σ$_{cp}$ = 5.0 MPa
2760	0	1.00	0.00	
2480	96	0.90	0.26	
2200	152	0.80	0.42	
1940	204	0.70	0.56	
1660	248	0.60	0.68	
1380	284	0.50	0.78	
1100	312	0.40	0.86	
820	324	0.30	0.89	
560	336	0.20	0.92	
0	364	0.00	1.00	
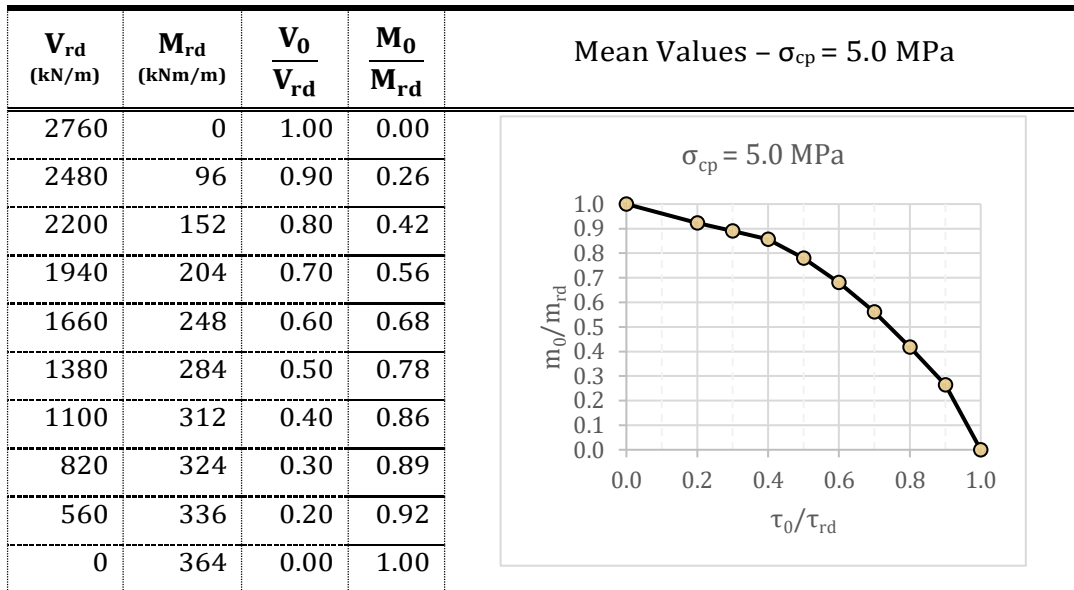
Graph 65. M - V interaction domain curve for prestressing level σ$_{cp}$=5.0MPa (mean values - ϕ20 - C40)

Prestressing begins to improve moment resistance.

Table 54. M - V interaction domain curve for prestressing level σcp=7.5MPa (mean values - ϕ20 - C40)

V_{rd} (kN/m)	M_{rd} (kNm/m)	$\dfrac{V_0}{V_{rd}}$	$\dfrac{M_0}{M_{rd}}$	Mean Values – σ_{cp} = 7.5 MPa
3040	0	1.00	0.00	
2740	96	0.90	0.26	
2440	156	0.80	0.43	
2120	212	0.70	0.58	
1820	256	0.60	0.70	
1520	292	0.50	0.80	
1220	312	0.40	0.86	
920	324	0.30	0.89	
600	340	0.20	0.93	
0	364	0.00	1.00	
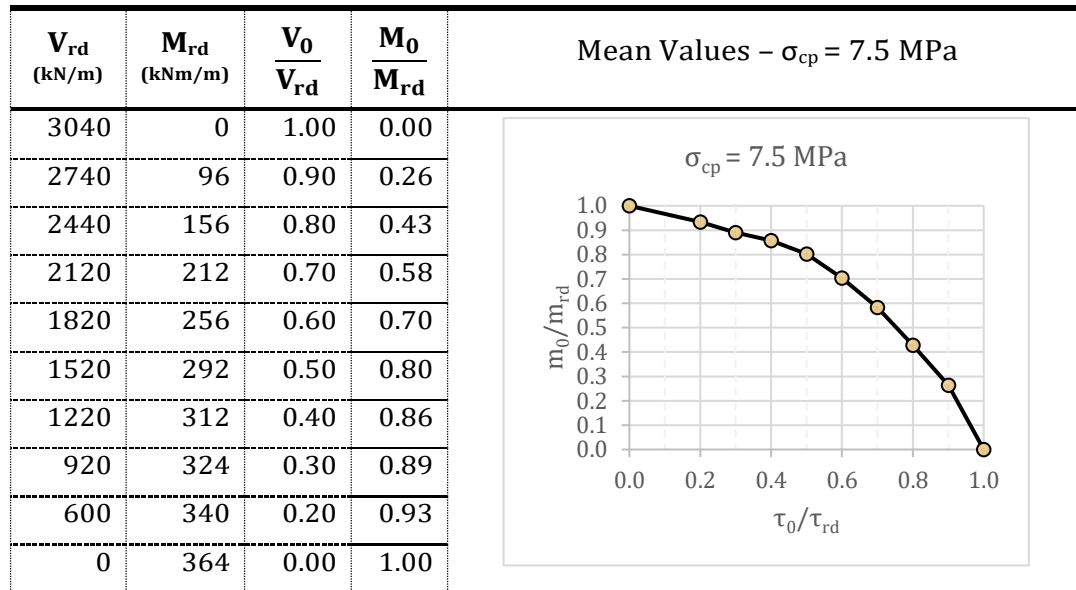
Graph 66. M - V interaction domain curve for prestressing level σcp=7.5MPa (mean values - ϕ20 - C40)

Domain curvature improves noticeably; prestress allows a more balanced interaction response.

Table 55. M - V interaction domain curve for prestressing level σcp=10.0MPa (mean values - ϕ20 - C40)

V_{rd} (kN/m)	M_{rd} (kNm/m)	$\dfrac{V_0}{V_{rd}}$	$\dfrac{M_0}{M_{rd}}$	Mean Values – σ_{cp} = 10.0 MPa
3300	0	1.00	0.00	
2980	100	0.90	0.27	
2640	160	0.80	0.44	
2320	208	0.70	0.57	
1980	256	0.60	0.70	
1660	288	0.50	0.79	
1320	312	0.40	0.86	
1000	324	0.30	0.89	
660	348	0.20	0.96	
0	364	0.00	1.00	
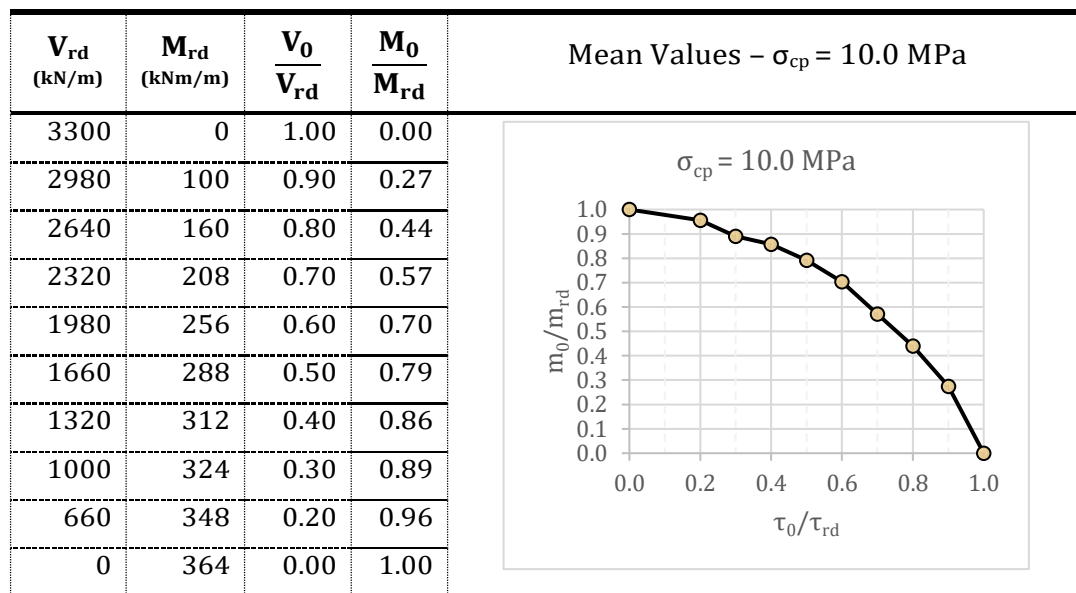
Graph 67. M - V interaction domain curve for prestressing level σcp=10.0MPa (mean values - ϕ20 - C40)

A significant increase in moment capacity is observed; prestress dominates and enhances the system's performance.
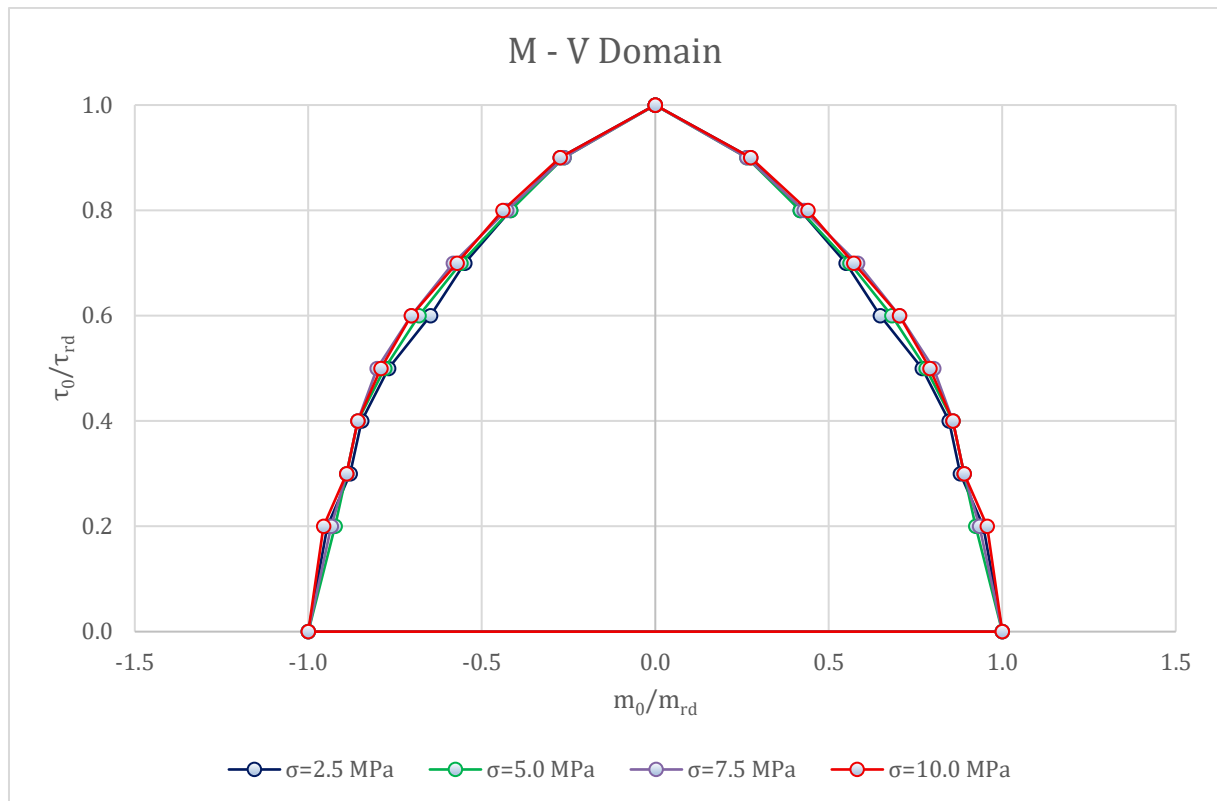
Graph 68. M–V interaction domain comparison for all prestressing levels. (mean values - C40 - ϕ20)

Among all tested configurations, this setup highlights the interaction between limited reinforcement and high-strength concrete under varying prestress levels. Although the concrete grade is high (C40/50), the reduced reinforcement area (ϕ20) leads to a narrower domain, especially at low prestress levels (2.5–5 MPa). However, as prestressing increases, the panel exhibits a strong upward trend in moment resistance. At σ_{cp} = 10 MPa, the domain expands considerably, indicating that prestress has a compensating effect for the lower steel ratio. Still, the overall domain remains smaller than that of the ϕ24 configuration. These findings suggest that while higher concrete strength improves the system's resilience, reinforcement ratio remains a dominant factor in achieving optimal moment–shear interaction.

4.4.9. Conclusion on Interaction Domains

The domain analyses presented in this section demonstrate the complex yet predictable relationship between prestressing level, reinforcement ratio, and concrete strength. While prestressing consistently enhances moment resistance, its influence on shear capacity remains limited unless reinforcement is adequately provided. Configurations with higher bar diameters (ϕ24) and high-strength concrete (C40/50) yield the largest and most ductile interaction domains. Conversely, design-level assumptions or reduced reinforcement result in narrower and more brittle behaviors. These findings validate the effectiveness of the layered shell FEM approach in capturing combined stress responses and provide a robust foundation for further structural evaluations and comparisons in the following sections.

4.5. General Comparison of Interaction Domains

In this section, the interaction domains obtained from the nonlinear FEM simulations are comparatively evaluated to highlight the individual effects of reinforcement ratio, concrete strength, and axial prestressing on combined shear–moment behaviours. The comparison is based on the previously defined dimensionless format (τ_0/τ_{rd} vs. μ_0/μ_{rd}) to ensure that the observed trends are independent of scale, units, and geometry. Each parameter is analysed in isolation by keeping the others constant to assess its unique influence on the overall domain shape, curvature, and strength envelope.

4.5.1. Effect of Reinforcement Ratio

To investigate the effect of reinforcement ratio on the interaction between shear and moment, a comparative study was conducted using two reinforcement configurations: ϕ24 mm and ϕ20 mm, while maintaining the same concrete class (C25/30) and prestressing levels. The normalized interaction domains (μ_0/μ_{rd} vs. τ_0/τ_{rd}) were plotted for each case under identical conditions.

The following figures illustrate the interaction domains for different reinforcement diameters and stress assumptions (mean, characteristic, design):
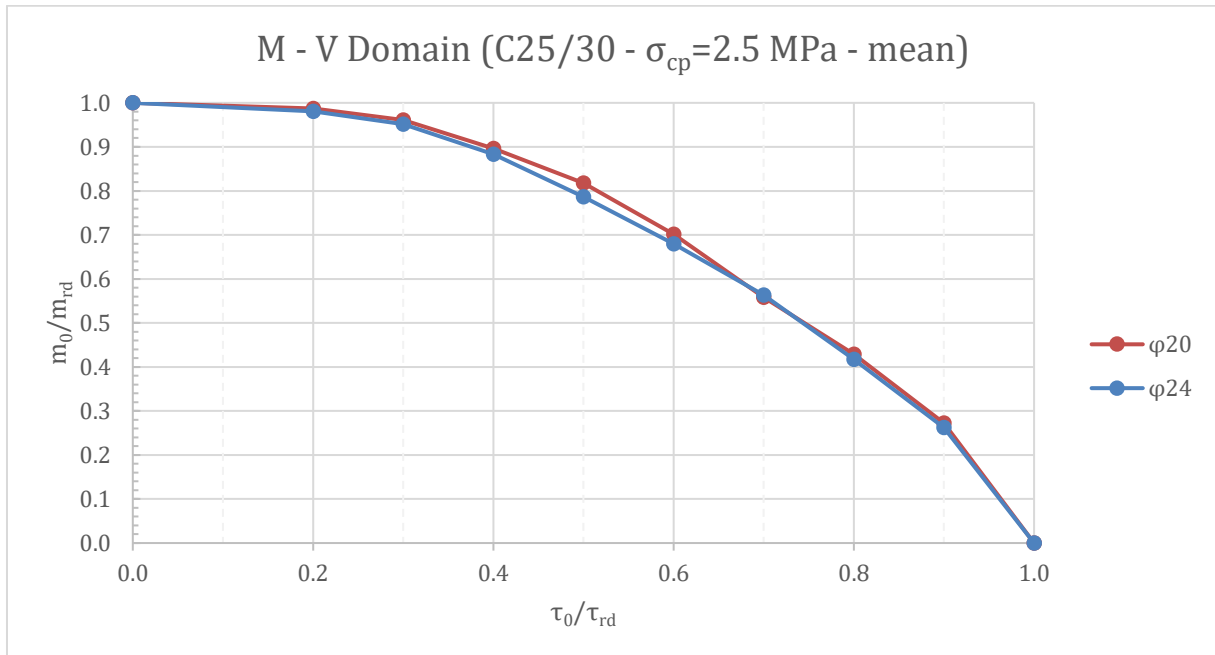
Graph 69. M–V interaction domain for C25/30 concrete under 2.5 MPa prestress, comparing reinforcement diameters ϕ20 and ϕ24 (mean values).

Although a higher reinforcement ratio is expected to improve moment redistribution capacity, this figure shows a nearly identical domain shape for both reinforcement configurations. The ϕ20 curve slightly exceeds ϕ24 throughout most of the domain, especially in the mid-to-high shear zone ($\tau_0/\tau_{rd} \approx 0.4$–$0.8$). This counterintuitive result suggests that, under low prestress conditions (2.5 MPa), the reinforcement effect is minimal, and the concrete capacity dominates. The closeness of the curves highlights that moment capacity is not significantly compromised by the smaller diameter, particularly in low axial stress environments.

M - V Domain (C40/50 - σ_{cp}=2.5 MPa - mean)
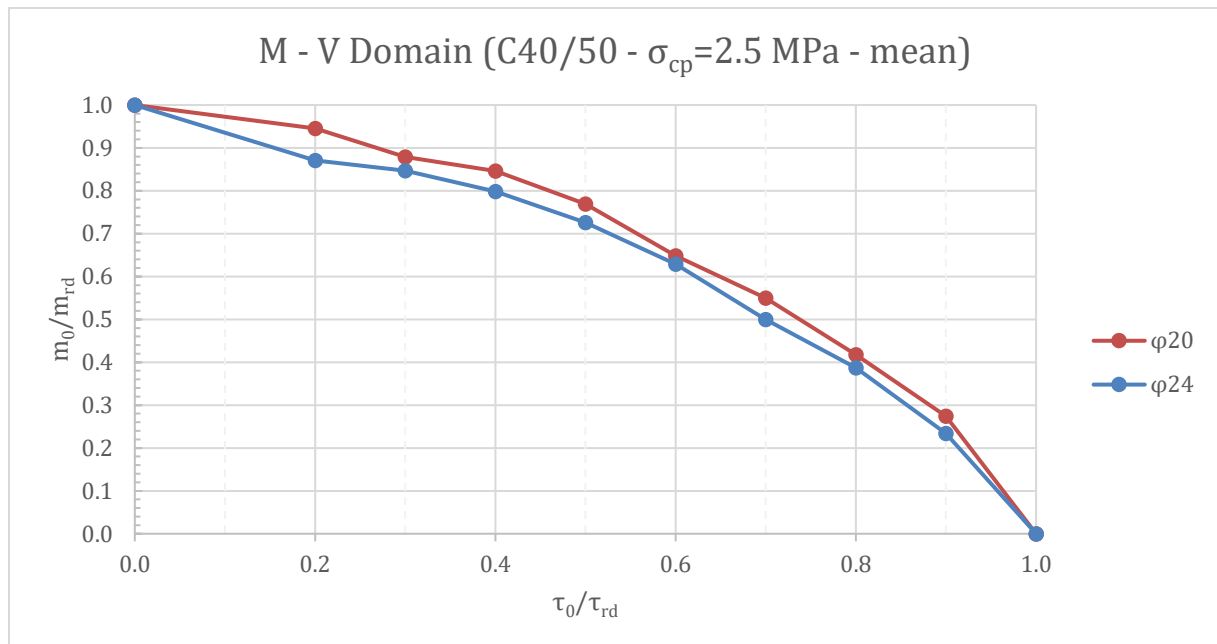
Graph 70. M–V interaction domain for C40/50 concrete under 2.5 MPa prestress, comparing reinforcement diameters ɸ20 and ɸ24 (mean values).

Compared to the C25/30 case, this figure shows a more distinct separation between the reinforcement configurations. The curve for ɸ20 consistently lies above that of ɸ24, indicating better moment preservation across increasing shear demand. This result highlights that when higher concrete strength (C40/50) is used, the reinforcement layout becomes more influential in determining the interaction domain. The sharper drop in moment capacity for the ɸ24 case suggests a more brittle failure trend, whereas the ɸ20 configuration maintains a slightly more favourable redistribution capability under combined loading.
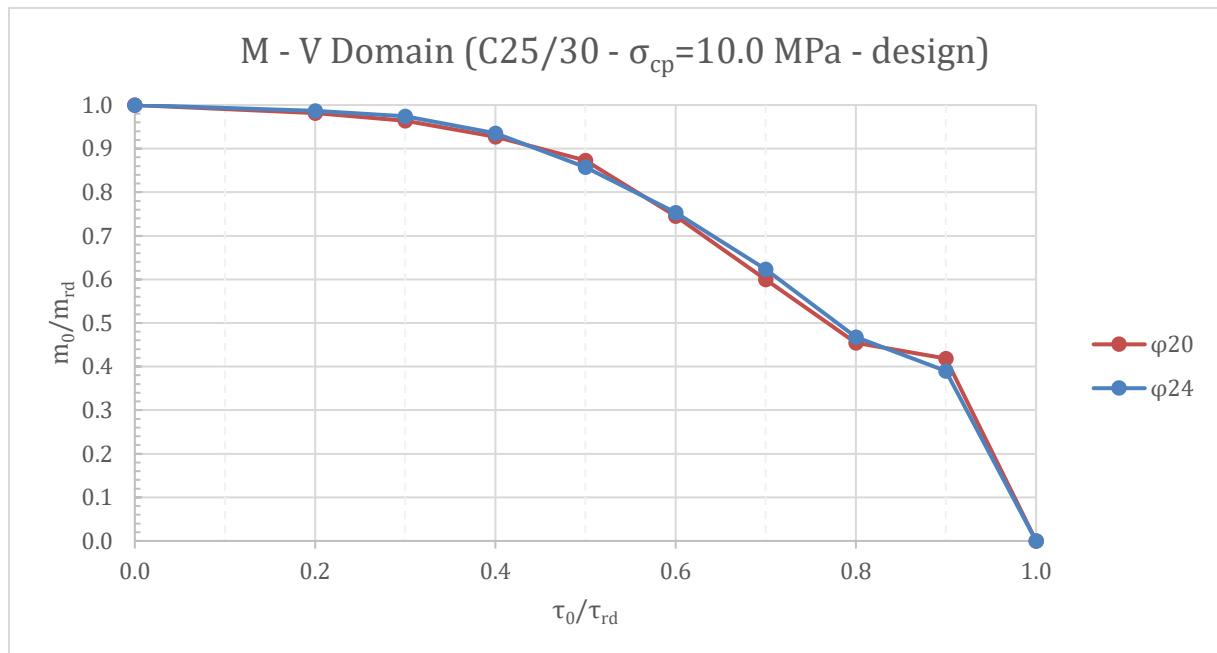
Graph 71. M–V interaction domain for C25/30 concrete under 10.0 MPa prestress, comparing reinforcement diameters ϕ20 and ϕ24 (design values).

This chart reveals an interesting deviation in the domain curve behavior around a shear ratio (τ_0/τ_{rd}) of approximately 0.8. While in most cases the domain follows a smooth and convex path, here the μ_0/μ_{rd} value exhibits a slightly irregular slope, particularly for the ϕ20 curve. The curves remain very close to each other overall, suggesting that under design-level material properties and high prestress levels, the reinforcement ratio has a relatively minor influence on the interaction domain.

However, the slight disturbance observed near $\tau_0/\tau_{rd} \approx 0.8$ is consistently present in similar cases where either the concrete strength or reinforcement capacity is reduced. This pattern may be attributed to a transition in failure mode sensitivity, where shear capacity becomes nearly exhausted while moment capacity has not yet reached its limit. The steepening of the curve beyond this point suggests a reduced ability of the cross-section to redistribute internal forces once shear resistance is critically low, especially under conservative design parameters.

Across the evaluated M–V interaction domains, several trends emerge regarding the influence of reinforcement ratio under varying material assumptions. In all configurations, the effect of changing reinforcement diameter (φ20 vs. φ24) remains relatively modest. Particularly in low prestress scenarios and with higher concrete strength (e.g., C40/50), the domain curves for different reinforcement ratios are nearly overlapping, indicating that the section's ultimate behavior is governed more by the concrete properties than by reinforcement variation.

However, as prestressing increases or as more conservative (design) material values are adopted, subtle divergences begin to appear—especially near the intermediate region of $\tau_0/\tau_{rd} \approx 0.8$. In some cases, a slight distortion in the curve shape emerges, suggesting a transitional behavior between shear-dominant and flexure-dominant failure. This effect is more evident when either concrete strength or reinforcement strength is relatively limited, leading to sharper reductions in moment capacity as shear demand increases.

Overall, the consistency between domain curves reinforces the idea that while reinforcement ratio influences strength values in absolute terms (V_{rd}, M_{rd}), its effect on normalized interaction domains remains limited, especially within the elastic-to-failure transition region.

4.5.2. Effect of Concrete Strength

In this section, the influence of concrete compressive strength on the M–V interaction behaviour is examined. By keeping the reinforcement layout constant (φ24, mean values), two different concrete strength classes—C25/30 and C40/50—are compared under varying levels of prestressing. This comparison helps to understand how concrete stiffness and strength affect the balance between moment and shear capacity, especially under combined loading scenarios.
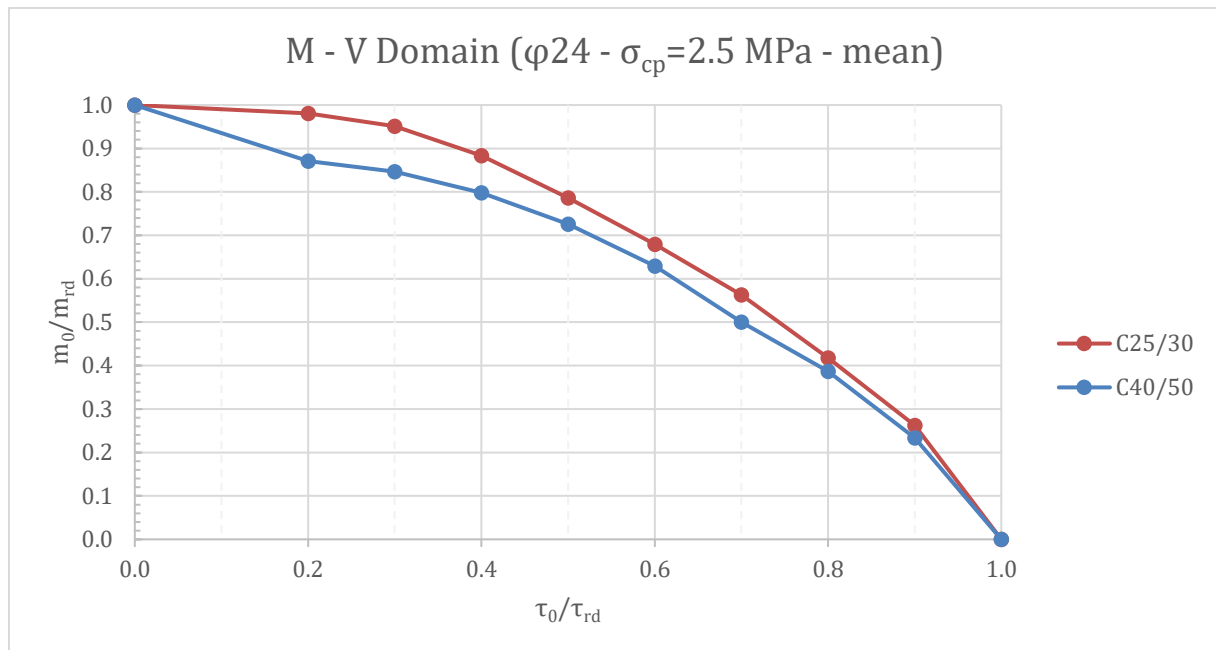
Graph 72. M–V interaction domain for φ24 reinforcement under 2.5 MPa prestress, comparing concrete strength (mean values).

The graph illustrates the moment–shear interaction domains for two concrete classes—C25/30 and C40/50—under the same reinforcement layout (ϕ24, mean values) and axial prestress of 2.5 MPa. Although C40/50 has a higher compressive strength, the dimensionless moment capacity (μ_0/μ_{rd}) appears consistently lower than that of C25/30 for any given shear ratio (τ_0/τ_{rd}). This implies that the higher concrete strength leads to a more shear-dominant failure behaviour, possibly due to a stiffer response and reduced deformability. Additionally, the reduced influence of reinforcement on higher-strength concrete may contribute to earlier moment capacity reduction under increasing shear demand.
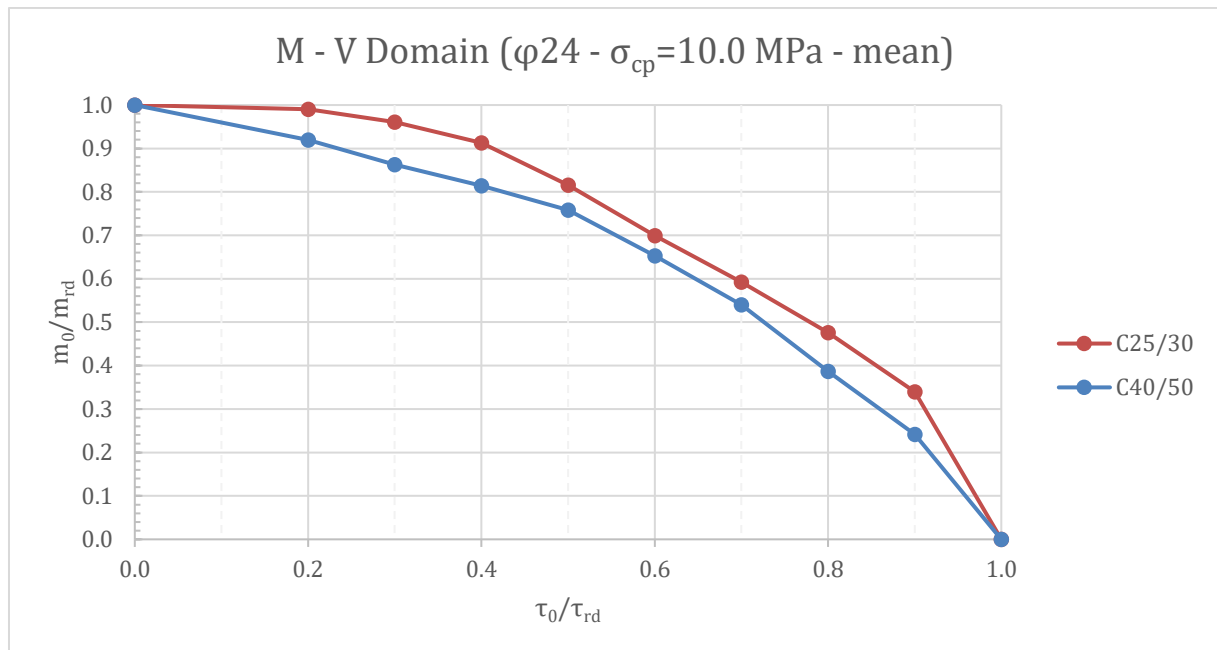
Graph 73. M–V interaction domain for ϕ24 reinforcement under 10.0 MPa prestress, comparing concrete strength (mean values).

This comparison highlights how the increase in prestress level (σ_{cp} = 10 MPa) affects the interaction behaviour between C25/30 and C40/50 concretes. The trend observed in the earlier case (at 2.5 MPa) becomes more pronounced here: the C40/50 curve consistently falls below that of C25/30, indicating lower dimensionless moment capacity under the same shear ratio. The prestressing increases the shear capacity (τ_{rd}) in both cases, but its influence on moment behaviour appears more limited in higher-strength concrete. This suggests that in stiffer, stronger concrete such as C40/50, the system becomes less ductile, and the capacity trade-off between shear and moment becomes sharper under high prestress. Additionally, the separation between the two curves widens as τ_0/τ_{rd} increases, emphasizing that concrete strength has a growing influence on failure mode at higher shear demand.

4.5.3. Effect of Safety Factor

This section investigates how the use of different safety factors—mean, characteristic, and design values—affects the moment-shear interaction response of reinforced concrete elements. These safety assumptions, defined by Eurocode, directly influence the material strengths used in design, and thus alter both the ultimate shear (V_{rd}) and moment (M_{rd}) capacities. By keeping the reinforcement and concrete class constant, the impact of safety factor variation on the M–V domain is visualized. This allows assessment of how conservative assumptions modify the interaction behaviour and load-sharing capacity.
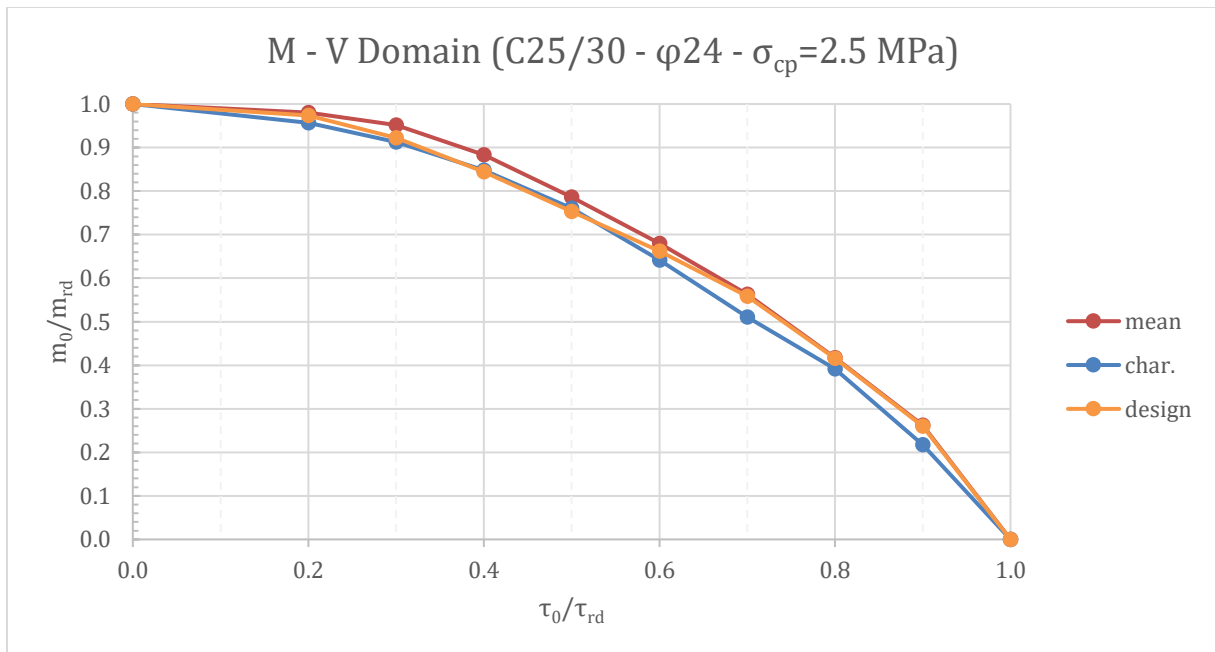
Graph 74. M–V interaction domain for ϕ24 reinforcement and C25/30 concrete under 2.5 MPa prestress, comparing safety values.

In the low-prestressing case, the M–V domain curves derived from mean, characteristic, and design values display similar overall shapes. The three curves remain close to each other throughout the range of τ_0/τ_{rd}, with the mean curve positioned slightly above the characteristic and design ones. The differences between them are mostly limited to vertical shifts, reflecting the varying capacity limits (M_{rd} and V_{rd}) imposed by each safety level.

There is no notable change in the interaction trend, and all curves show a relatively smooth and gradual transition from moment-dominated to shear-dominated behaviour.
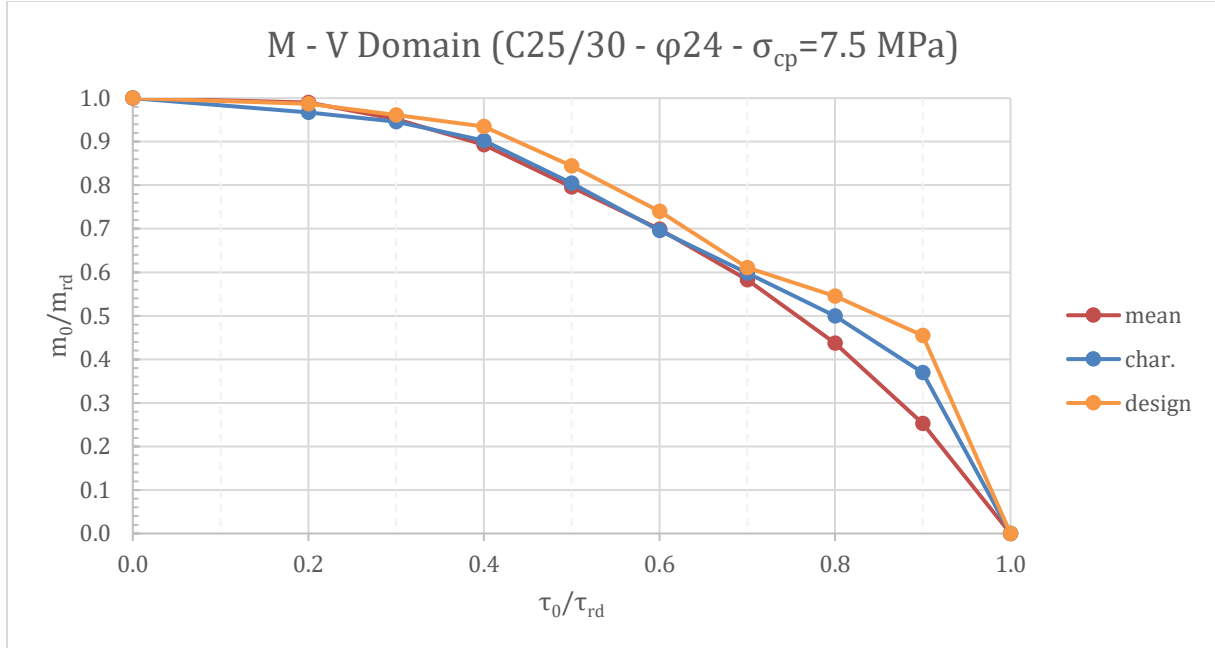
Graph 75. M–V interaction domain for φ24 reinforcement and C25/30 concrete under 7.5 MPa prestress, comparing safety values.

When the prestressing level increases, the separation between the curves becomes more visible. The mean value curve exhibits a more pronounced curvature, particularly in the high-shear region ($\tau_0/\tau_{rd} > 0.7$), while the characteristic and design curves follow a comparatively flatter trajectory. This distinction indicates that higher prestress tends to enhance the effect of safety assumptions on the overall domain shape. The design value curve in particular maintains a more linear decline in μ_0/μ_{rd}, suggesting a more conservative response under combined loading.

5. Comparison with Cristian Menn's Studies

In this chapter, the numerical results obtained through non-linear finite element analyses are compared with the classical interaction domains proposed by Christian Menn, as introduced in Chapter 2.1. Menn's method, developed in an era preceding modern numerical simulation tools, relies on simplified yet insightful design principles and interaction diagrams that represent the balance between transverse bending and longitudinal shear in box girder webs.

In his book *Prestressed Concrete Bridges*, Christian Menn proposed an interaction domain concept that correlates transverse bending and longitudinal shear within web elements of box girders. His formulation relies on the estimation of ultimate moment and shear capacities, denoted as m_{R0} and V_{R0}, which represent the maximum resistance of a panel under pure bending and pure shear, respectively. These capacities are determined using simplified assumptions, including the reduced compressive strength of concrete $fc, red = 2/3 \cdot fc$, and a constant lever arm $z = 0.9 \cdot d$ The nominal shear strength is expressed as:

$$V_{R0} = f_{c,red} \cdot b_w \cdot cos\alpha \cdot sin\alpha$$

and the flexural strength as:

$$m_{R0} = \omega_0 \cdot (b_0 + b')^2 \cdot f_c \cdot (1 - 0.5 \cdot \omega_0)$$

Menn then uses these to construct dimensionless interaction domains, plotting the ratio $\frac{m_R}{m_{R0}}$ on the horizontal axis and $\frac{V_R}{V_{R0}}$ on the vertical, under various reinforcement ratios ρ_r/ρ_l. It is important to note that prestressing is not explicitly modeled in his diagrams, nor is nonlinear material behavior considered. Instead, the diagrams serve as practical tools derived from engineering intuition, structural experience, and conservative assumptions, reflecting the design philosophy of that period.

In contrast to Menn's simplified design-oriented framework, the present study utilizes detailed non-linear finite element analyses (FEM) to evaluate the interaction between shear and bending. Rather than relying on reduced material strengths and fixed geometric assumptions, the capacity limits—namely the ultimate shear resistance V_{rd} and moment resistance M_{rd}—are directly extracted from load steps at which failure occurs in the numerical simulations. Once these capacities are obtained, the dimensionless interaction domain is constructed by normalizing each applied load pair (V_0, M_0) with respect to V_{rd} and M_{rd}, yielding points in the form:

$$\left(\frac{m_0}{m_{rd}} \ , \ \frac{\tau_0}{\tau_{rd}} \right)$$

where:

$$\tau_0 = \frac{V_0}{b \cdot z} \qquad \tau_{rd} = \frac{V_{rd}}{b \cdot z} \qquad \text{and} \qquad m_0 = \frac{M_0}{b \cdot z^2} \qquad m_{rd} = \frac{M_{rd}}{b \cdot z^2}$$

in line with Eurocode formulations.

The resulting domains are mirrored across the vertical axis to produce symmetric diagrams comparable to Menn's original format.

While Menn varies reinforcement ratios independently in each direction to assess their influence, the FEM models here maintain a constant and equal reinforcement in both longitudinal and transverse directions. This allows for a focused investigation of other parameters such as concrete strength class (C25/30 vs. C40/50), bar diameter (ɸ20 vs. ɸ24 mm), safety level (mean, characteristic, and design values), and axial precompression σ_{cp}. Additionally, the effect of prestressing—absent in Menn's method—is incorporated by applying different σ_{cp} levels in the model, enabling a more realistic representation of modern post-tensioned systems.

In summary, Christian Menn's analytical approach serves as a pragmatic, design-oriented tool rooted in simplified mechanics, while the method adopted in this study leverages detailed material modelling and failure-based extraction of capacity from non-linear finite element analyses. By converting both approaches into dimensionless interaction domains, a direct visual and numerical comparison becomes possible. This comparison not only validates the consistency of FEM results within the safety envelope proposed by Menn but also reveals nuanced behaviours such as the influence of prestressing and reinforcement symmetry, which Menn's method does not explicitly address. The following sections present this comparison in greater detail, beginning with the base case configuration.

5.1. Comparison of the Interaction Domains

The interaction domain derived from the non-Linear FEM analysis for the configuration $\sigma_{cp} = 2.5\ MPa$, C25/30 concrete, and $\varphi24$ mm reinforcement (mean values) exhibits a remarkable similarity in shape and symmetry to the central curve of Christian Menn's classical domain diagram, specifically the one associated with $\rho_r/\rho_l = 1$. This agreement is significant, as it confirms that even under modern nonlinear modeling, the web behavior remains consistent with Menn's fundamental assumption: a parabolic or near-bilinear domain that symmetrically distributes moment capacity across the full range of shear utilization.

The FEM-based curve was mirrored across the vertical axis to align with Menn's bidirectional representation of moment capacity. Unlike Menn, who parametrically varies the reinforcement ratio and captures its effect on the domain width, the present FEM model uses equal reinforcement in both directions. Despite this constraint, the curve comfortably resides within Menn's safety envelope, reinforcing the conservative nature of his approach.

Another key difference lies in how capacities are derived. Menn uses design-level simplifications based on effective web width and ultimate shear/moment equilibrium, while this study obtains V_{rd} and M_{rd} directly from failure-based outputs of non-linear FEM simulations. Nonetheless, once normalized, the resultant dimensionless domain confirms that Menn's charts remain valid for preliminary design checks — although they lack the resolution to capture effects such as prestress-induced asymmetry or cracking behavior.
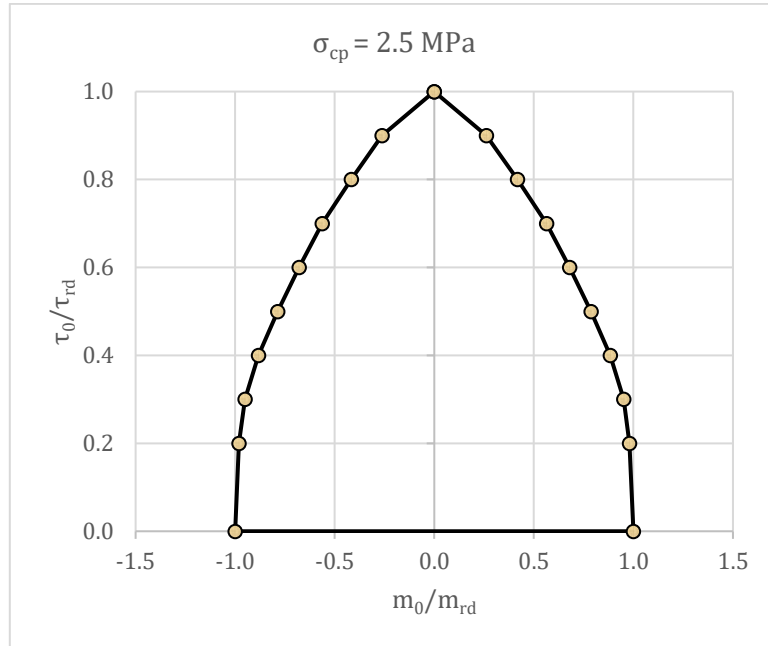
Graph 76. FEM-based interaction domain (σ_cp = 2.5 MPa, φ24 mm, C25/30)
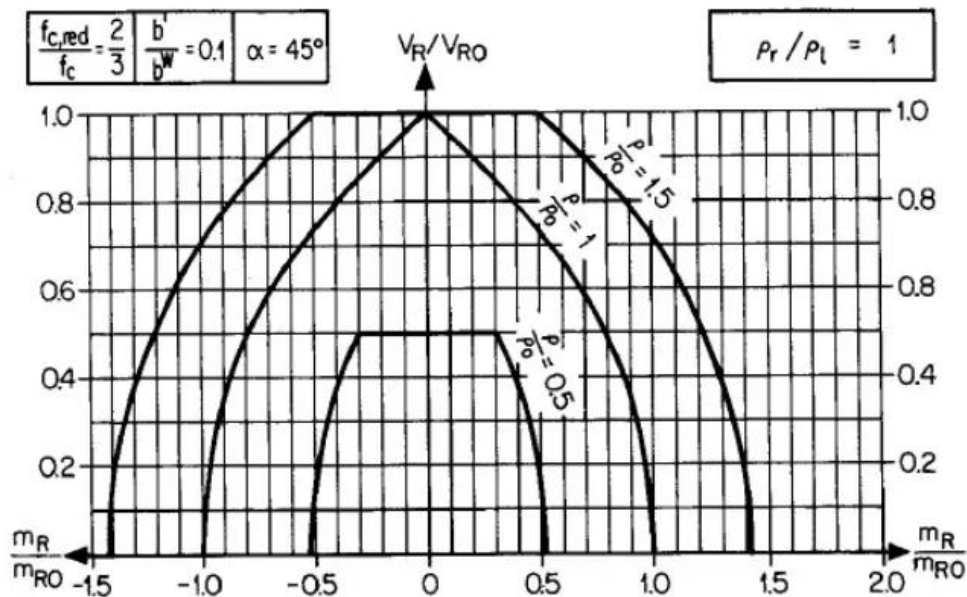
Figure 23. Shear – transverse bending interaction diagram (Menn, 1990, p. 263)

The comparison between the FEM-based interaction domain and Christian Menn's classical chart (as shown in Graph 76 and Figure 23) reveals a notable degree of consistency in terms of domain shape and boundary trends. Despite differences in methodology—Menn's chart being derived from semi-empirical estimations and simplified assumptions, and the current domain based on detailed nonlinear FEM simulations—both approaches produce an approximately parabolic curve symmetric about the bending axis. Particularly, the FEM results obtained for the configuration with φ24 reinforcement, C25/30 concrete, and $\sigma_{cp} = 2.5\ MPa$ align closely with Menn's $\rho_r/\rho_l = 1$ curve, supporting the validity of his design envelope under moderate prestressing and uniform reinforcement conditions.

5.2.   Prestressing Level Effects on the Interaction Domains

To investigate how axial prestressing affects the shape and extent of shear–moment interaction domains, additional normalized τ_0/τ_{rd} vs. m_0/m_{rd} plots were generated for four levels of compressive stress: 2.5, 5.0, 7.5, and 10.0 MPa. These graphs allow a direct evaluation of prestressing influence on the ultimate load-carrying behaviour under combined shear and bending. While Christian Menn's original diagrams do not explicitly incorporate axial prestressing as a variable, the current FEM-based analysis isolates its effect while maintaining symmetric reinforcement ratios and fixed material parameters.
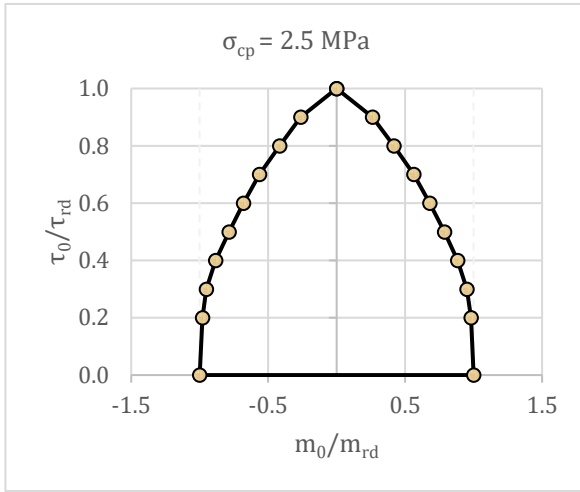
Graph 77. FEM-based interaction domain (σ_{cp} = 2.5)
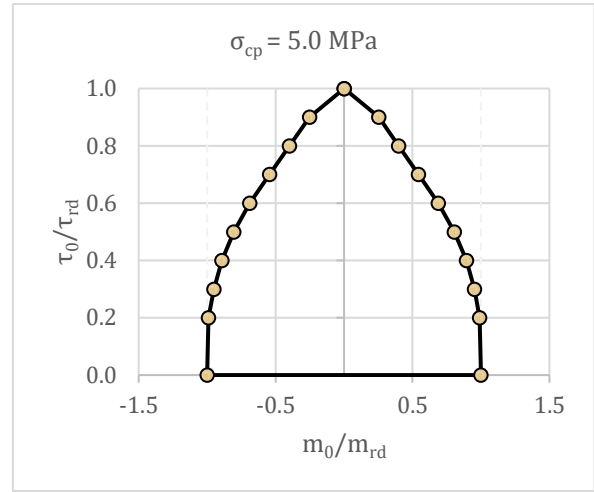
Graph 78. FEM-based interaction domain (σ_{cp} = 5.0)
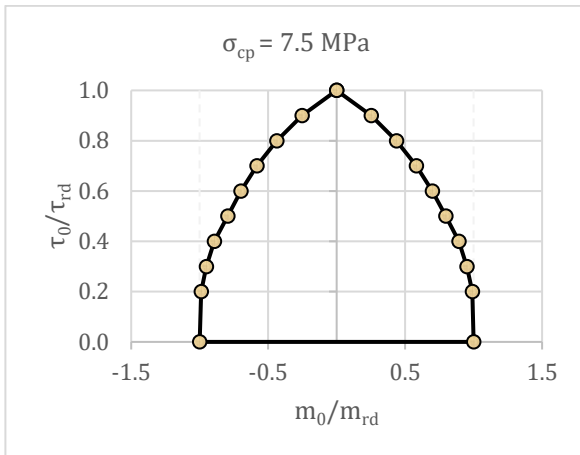
Graph 79. FEM-based interaction domain (σ_{cp} = 7.5)
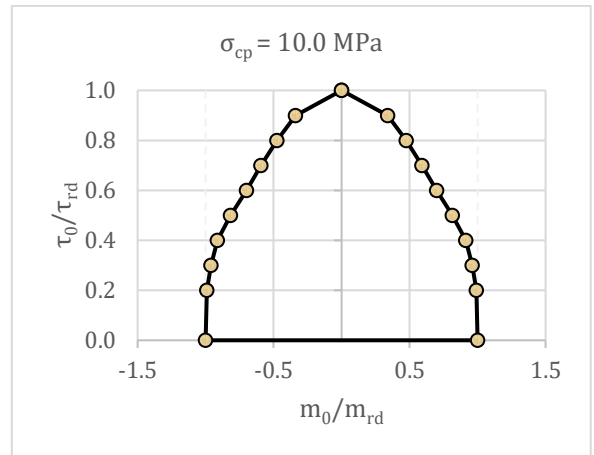
Graph 80. FEM-based interaction domain (σ_{cp} = 10.0)

The plotted diagrams reveal a consistent widening of the upper region of the interaction domains as σ_{cp} increases. This trend suggests that axial compression significantly enhances the web's resistance to shear–bending interaction, especially when shear demand is dominant ($\tau_{rd} > 0.6$). From a mechanical perspective, the confinement effect of prestressing delays cracking and increases the overall stiffness of the web, leading to a higher residual moment capacity even under substantial shear. Notably, while the lower boundary remains nearly vertical due to the symmetric reinforcement layout and fixed geometric conditions, the arch-like domain peak shifts outward, indicating a more forgiving failure envelope. This finding contrasts with Menn's more conservative domains,

which do not reflect such prestress-induced benefits. Thus, prestressing is shown to be a critical factor in optimizing interaction performance—an insight not captured in the original theoretical simplifications.
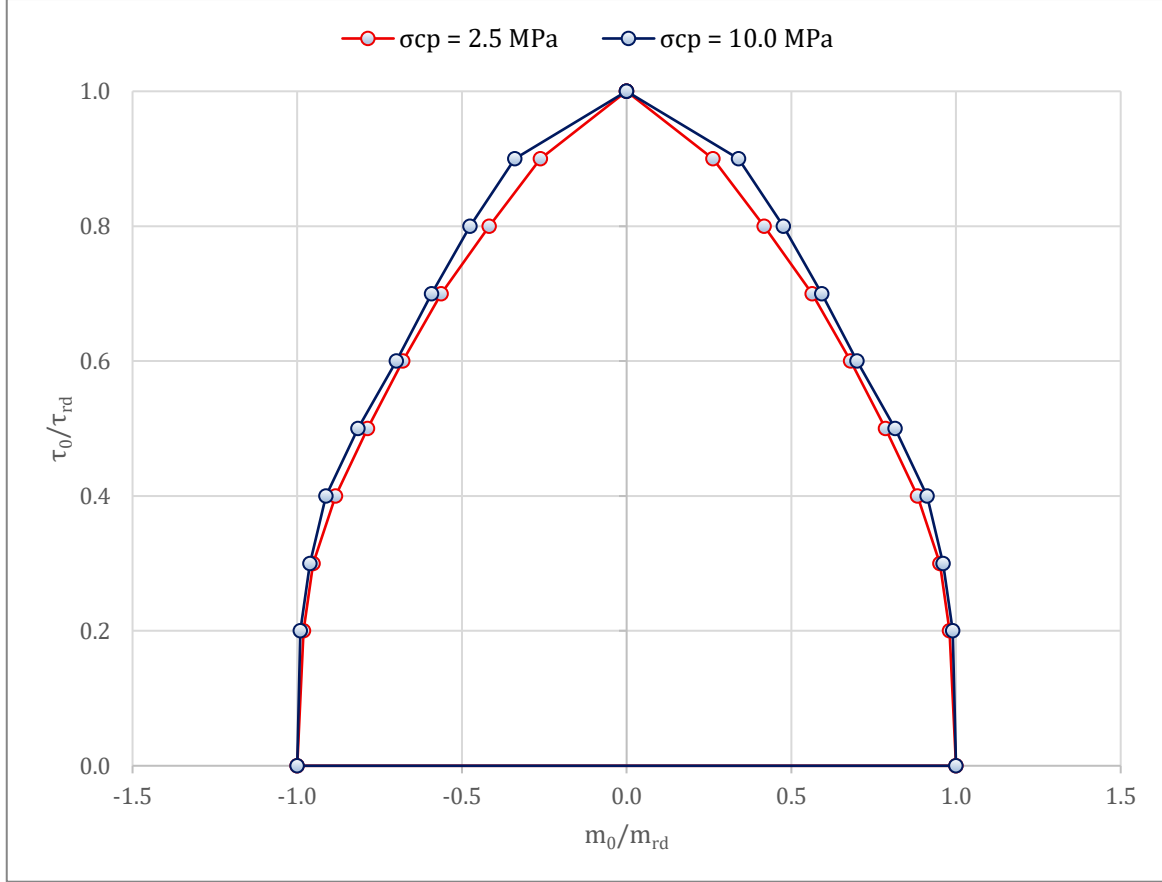
Graph 81. Comparison of FEM-based interaction domain due to different prestressing levels (σ_{cp} = 2.5 - 10.0)

To illustrate the effect of increasing axial prestress on the shear–moment interaction domain, Graph 81 compares the normalized failure envelopes for $\sigma_{cp} = 2.5\ MPa$ and $\sigma_{cp} = 10.0\ MPa$. The superposition of these two curves makes it evident that higher compressive stress causes a lateral expansion in the upper portion of the domain, particularly near the peak region $(\tau_0/\tau_{rd} \approx 0.8 - 1.0)$. This widening indicates that the section can sustain greater bending under high shear demand when sufficient axial compression is applied.

Mechanically, this can be attributed to a prestressing role in enhancing the web's crack resistance and delaying tensile failure. As a result, the structure retains more flexural capacity under high shear levels. It is also worth noting that the lower limbs of the domain (near $m_0/m_{rd} = 1.0$) remain nearly vertical and unaffected, since the interaction is dominated by pure bending in those zones.

In contrast to Christian Menn's original diagrams, which assume no prestress effect and thus predict a more conservative interaction shape, the FEM-based domains capture these prestress-induced benefits. This emphasizes the importance of integrating modern material behavior and precompression effects when assessing structural interaction capacity.

5.3.   Interaction Domain Behaviour under Reduced Reinforcement and Design Safety Factors

To complete and compare the findings presented in Section 5.2, an additional set of simulations was conducted to assess the interaction domains under reduced reinforcement and conservative material assumptions. In other words, less shear resistance capacity in term of reinforcement and concrete. In this parametric study, the reinforcement diameter was reduced from ɸ24 mm to ɸ20 mm, while both concrete and steel strengths were assigned using design values (*f*cd , *f*yd), as defined in Eurocode 2. This configuration aims to investigate how safety-factor driven material reduction and lower reinforcement area affect the overall shear–moment interaction behaviour across varying prestressing levels.
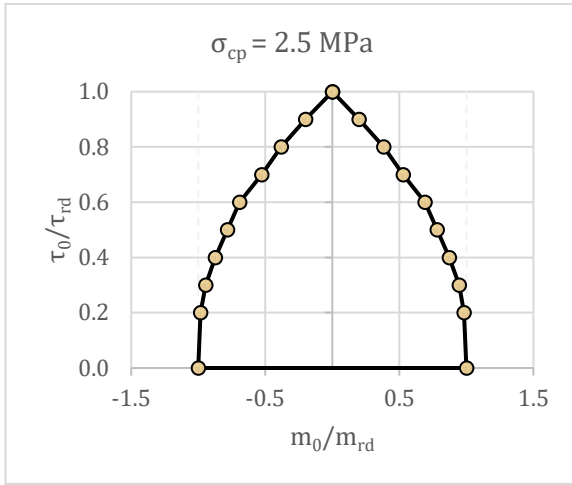
Graph 82. FEM-based interaction domain under design values (σ_{cp} = 2.5 MPa - ϕ20)
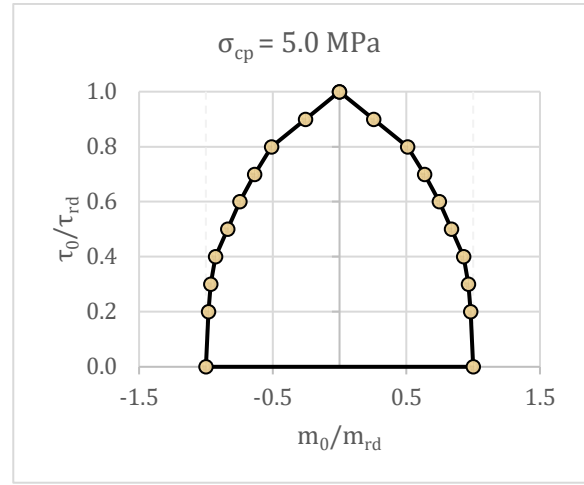
Graph 83. FEM-based interaction domain under design values (σ_{cp} = 5.0 MPa - ϕ20)
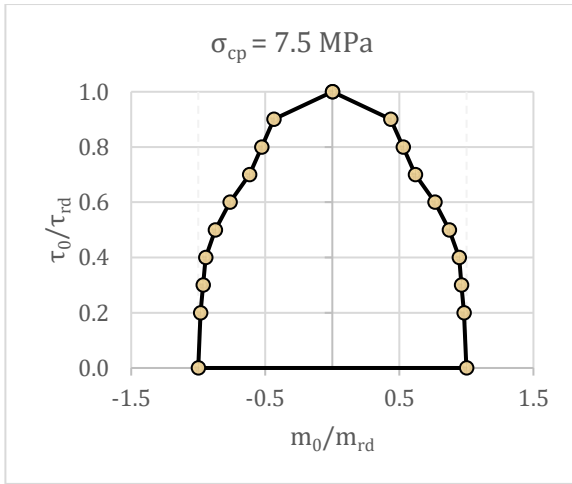
Graph 84. FEM-based interaction domain under design values (σ_{cp} = 7.5 MPa - ϕ20)
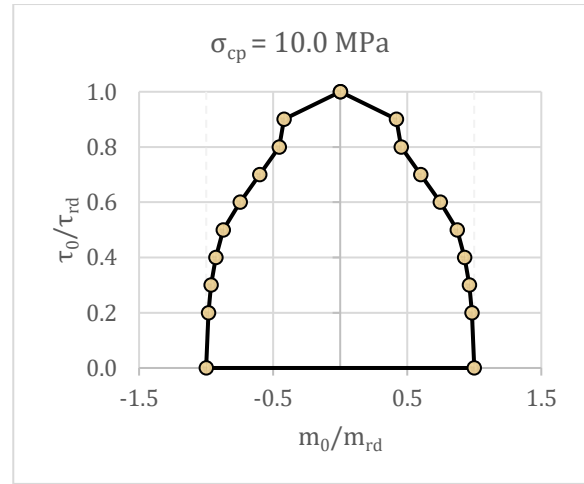
Graph 85. FEM-based interaction domain under design values (σ_{cp} = 10.0 MPa - ϕ20)

As observed in the domain curves, the results for σ_{cp} = 2.5 MPa and 5.0 MPa show strong similarity to Christian Menn's original interaction shapes, indicating that when both material strength and reinforcement ratio are limited, the panel behaviour tends to follow a near-linear or bilinear interaction envelope. However, at higher prestressing levels (σ_{cp} = 7.5 MPa and 10.0 MPa), the interaction curves begin to flatten and round at the peak, diverging from the classical shape. This reflects an increasing capacity for moment redistribution under reduced shear demand, likely enabled by prestress-induced confinement. The transformation

from sharp to smooth curvature suggests a shift from brittle to more ductile failure modes as axial compression increases.
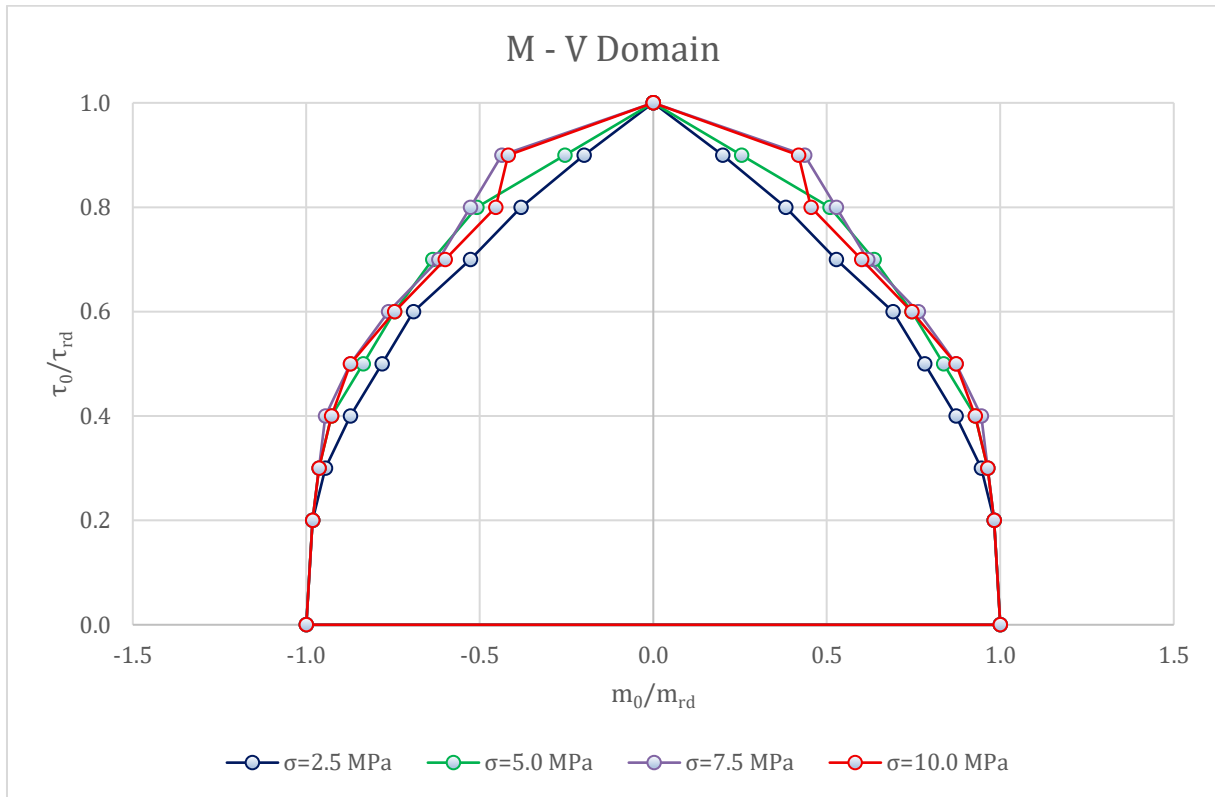
Graph 86. Comparison of FEM-based interaction domain under design values due to different prestressing levels (σ_{cp} = 2.5 - 10.0 MPa - $\phi 20$)

The superposed interaction domains further emphasize the transition in behaviour. While all curves start from a similar base shape, their divergence becomes evident as prestressing increases. The domain corresponding to σ_{cp} = 10.0 MPa exhibits the widest spread, especially in the moment-dominant region, indicating a pronounced increase in flexural contribution despite limited reinforcement. In contrast, the domain for σ_{cp} = 2.5 MPa remains compact and shear-dominant, closely matching the interaction form proposed by Menn. This variation demonstrates that prestressing effects become more pronounced under conservative material and reinforcement assumptions, ultimately shifting the structural response toward a prestress-governed regime.

Compared to the results in Section 5.2, where higher reinforcement (ϕ24 mm) and mean material strengths were used, the current configuration displays narrower and more brittle interaction domains, especially at low prestress. While the increase in axial compression still enhances moment resistance, the overall capacity is reduced due to the lower steel and concrete strength assumptions. The contrast between the two sets highlights the combined role of reinforcement ratio and safety-factor-driven material properties in shaping the interaction behaviour. Ultimately, the comparison illustrates that both reinforcement detailing and material quality must be jointly considered when evaluating shear–moment interactions in prestressed concrete elements.

5.4.   Limitations and Underlying Assumptions

While both the simplified design domains proposed by Christian Menn and the non-linear FEM-based interaction curves serve as valuable tools for evaluating shear–moment interaction, they rest on fundamentally different assumptions. Menn's method, rooted in practical engineering intuition and simplified mechanics, assumes linear interaction and uniform material behaviour, neglecting the influence of crack progression, tension stiffening, and axial precompression. His charts are parameterized primarily by reinforcement ratio and transverse-to-longitudinal reinforcement distribution, making them suitable for rapid design checks under idealized conditions.

Conversely, the FEM-based domains presented in this study incorporate material nonlinearity, tension softening, and the contribution of prestressing, allowing for a more refined representation of concrete behaviour under combined actions. However, this approach is inherently more computationally intensive and sensitive to modelling choices such as mesh quality, boundary conditions, and failure criteria. Additionally, all analyses assumed a symmetric and equal reinforcement layout in both directions, whereas Menn's charts allow for reinforcement anisotropy.

It should also be emphasized that the present study idealizes the cross-section geometry and boundary effects to isolate the behaviour of the web panel. Real-life bridge webs may involve complex interaction with flanges, diaphragms, or prestress eccentricities, which are not captured here. Therefore, while the FEM results offer enhanced accuracy in isolated conditions, Menn's method retains significant pedagogical and practical relevance for preliminary design and quick safety assessments.

6. Conclusion

This thesis investigated the nonlinear interaction between longitudinal shear and transverse bending in the web panels of prestressed concrete box girder bridges. While traditional design approaches often treat these actions separately or assume simplified linear interaction models, this study aimed to explore their combined effects using advanced finite element modelling. By employing layered shell elements within the ATENA simulation environment, a series of parametric analyses were conducted to quantify the influence of prestressing level, reinforcement ratio, and material strength assumptions on the shear–moment interaction domains.

The results clearly demonstrated that the shape and curvature of the interaction domains are significantly affected by both mechanical and material parameters. Specifically, increasing prestressing levels generally enhanced the flexural capacity under low shear conditions, while reduced reinforcement diameter and conservative design values narrowed the interaction domain and led to more brittle failure responses. The normalized domain diagrams revealed a distinct transformation from Menn-like linear behavior at low prestress to more rounded, ductile domains at higher prestress levels—particularly when mean material properties and higher reinforcement were used.

Comparative assessments with Eurocode 2 and fib Model Code formulations confirmed that while code-based predictions are often conservative, they may

overlook the nonlinear interaction effects captured by FEM. Among the fib approaches, Level of Approximation IIb showed the closest agreement with FEM results, especially in configurations involving moderate to high axial compression.

From a structural design perspective, the findings suggest that prestress level alone is not sufficient to ensure ductile interaction behavior; appropriate reinforcement detailing and accurate material modeling are also essential. The study reinforces the importance of adopting nonlinear verification tools in cases where combined shear and moment actions govern the capacity of web elements, particularly in prestressed box girder systems.

While this study focused on isolated wall panel behavior under idealized boundary conditions, several possible extensions can be identified for future research. One potential direction is to extend the developed interaction domains to full-scale bridge simulations, incorporating additional effects such as web–flange interaction or construction-stage prestress loss. Another valuable step would be the experimental validation of selected FEM configurations, particularly for confirming the ductility and cracking mechanisms observed in the nonlinear simulations.

Furthermore, while this thesis assumed equal reinforcement in both vertical and horizontal directions, Christian Menn's work explored asymmetric reinforcement ratios and their influence on the interaction domain shape. A future study may investigate these effects by conducting nonlinear simulations with varying transverse and longitudinal reinforcement ratios, offering a deeper understanding of reinforcement asymmetry in prestressed box girder webs.

7. Appendix

Table 56. Shear and Bending capacity simulation steps and analysis progress (C25/30, ϕ24 mm, mean values)

No	Load Step 1	Step Mult.	Load Step 2	Step Mult.	Load Step 3	Step Mult.	Σ step	Crack Initiate	Final Step	σcp	Vrd	Mrd
	Axial force - N		Shear force - V		Moment - M		Analysis steps			MPa	kN/m	kNm/m
1	0	0	200	5	0	0	200	41	124	0.0	2480	0
2	10	25	200	5	0	0	210	70	154	2.5	2880	0
3	10	50	200	5	0	0	210	79	171	5.0	3220	0
4	10	75	200	5	0	0	210	88	183	7.5	3460	0
5	10	100	200	5	0	0	210	101	181	10.0	3420	0
6	0	0	0	0	150	1	150	-	103	0.0	0	412
7	10	25	0	0	150	1	160	-	113	2.5	0	412
8	10	50	0	0	150	1	160	-	113	5.0	0	412
9	10	75	0	0	150	1	160	-	113	7.5	0	412
10	10	100	0	0	150	1	160	-	113	10.0	0	412

Table 57. Shear and Bending capacity simulation steps and analysis progress (C25/30, ϕ24 mm, char. values)

No	Load Step 1	Step Mult.	Load Step 2	Step Mult.	Load Step 3	Step Mult.	Σ step	Crack Initiate	Final Step	σcp	Vrd	Mrd
	Axial force - N		Shear force - V		Moment - M		Analysis steps			MPa	kN/m	kNm/m
1	0	0	200	5	0	0	200	29	108	0.0	2160	0
2	10	25	200	5	0	0	210	55	138	2.5	2560	0
3	10	50	200	5	0	0	210	64	152	5.0	2840	0
4	10	75	200	5	0	0	210	77	145	7.5	2700	0
5	10	100	200	5	0	0	210	88	138	10.0	2560	0
6	0	0	0	0	150	1	150	-	92	0.0	0	368
7	10	25	0	0	150	1	160	-	102	2.5	0	368
8	10	50	0	0	150	1	160	-	102	5.0	0	368
9	10	75	0	0	150	1	160	-	102	7.5	0	368
10	10	100	0	0	150	1	160	-	102	10.0	0	368

Table 58. Shear and Bending capacity simulation steps and analysis progress (C25/30, ϕ24 mm, design values)

No	Load Step 1	Step Mult.	Load Step 2	Step Mult.	Load Step 3	Step Mult.	Σ step	Crack Initiate	Final Step	σcp	Vrd	Mrd
	Axial force - N		Shear force - V		Moment - M		Analysis steps			MPa	kN/m	kNm/m
1	0	0	200	5	0	0	200	19	91	0.0	1820	0
2	10	25	200	5	0	0	210	43	114	2.5	2080	0
3	10	50	200	5	0	0	210	55	106	5.0	1920	0
4	10	75	200	5	0	0	210	67	105	7.5	1900	0
5	10	100	200	5	0	0	210	82	103	10.0	1860	0
6	0	0	0	0	150	1	150	-	77	0.0	0	308
7	10	25	0	0	150	1	160	-	87	2.5	0	308
8	10	50	0	0	150	1	160	-	87	5.0	0	308
9	10	75	0	0	150	1	160	-	87	7.5	0	308
10	10	100	0	0	150	1	160	-	87	10.0	0	308

Table 59. Shear and Bending capacity simulation steps and analysis progress (C25/30, ϕ20 mm, mean values)

No	Load Step 1	Step Mult.	Load Step 2	Step Mult.	Load Step 3	Step Mult.	Σ step	Crack Initiate	Final Step	σcp	Vrd	Mrd
	Axial force - N		Shear force - V		Moment - M		Analysis steps			MPa	kN/m	kNm/m
1	0	0	200	5	0	0	200	41	92	0.0	1840	0
2	10	25	200	5	0	0	210	70	122	2.5	2240	0
3	10	50	200	5	0	0	210	77	138	5.0	2560	0
4	10	75	200	5	0	0	210	87	152	7.5	2840	0
5	10	100	200	5	0	0	210	99	157	10.0	2940	0
6	0	0	0	0	150	1	150	-	77	0.0	0	308
7	10	25	0	0	150	1	160	-	87	2.5	0	308
8	10	50	0	0	150	1	160	-	87	5.0	0	308
9	10	75	0	0	150	1	160	-	87	7.5	0	308
10	10	100	0	0	150	1	160	-	87	10.0	0	308

Table 60. Shear and Bending capacity simulation steps and analysis progress (C25/30, φ20 mm, char. values)

No	Load Step 1	Step Mult.	Load Step 2	Step Mult.	Load Step 3	Step Mult.	∑ step	Crack Initiate	Final Step	σ_cp	V_rd	M_rd
	Axial force - N		Shear force - V		Moment - M		Analysis steps			MPa	kN/m	kNm/m
1	0	0	200	5	0	0	200	28	80	0.0	1600	0
2	10	25	200	5	0	0	210	55	109	2.5	1980	0
3	10	50	200	5	0	0	210	62	124	5.0	2280	0
4	10	75	200	5	0	0	210	75	131	7.5	2420	0
5	10	100	200	5	0	0	210	86	126	10.0	2320	0
6	0	0	0	0	150	1	150	-	67	0.0	0	268
7	10	25	0	0	150	1	160	-	77	2.5	0	268
8	10	50	0	0	150	1	160	-	77	5.0	0	268
9	10	75	0	0	150	1	160	-	77	7.5	0	268
10	10	100	0	0	150	1	160	-	77	10.0	0	268

Table 61. Shear and Bending capacity simulation steps and analysis progress (C25/30, φ20 mm, design values)

No	Load Step 1	Step Mult.	Load Step 2	Step Mult.	Load Step 3	Step Mult.	∑ step	Crack Initiate	Final Step	σ_cp	V_rd	M_rd
	Axial force - N		Shear force - V		Moment - M		Analysis steps			MPa	kN/m	kNm/m
1	0	0	200	5	0	0	200	19	66	0.0	1320	0
2	10	25	200	5	0	0	210	42	95	2.5	1700	0
3	10	50	200	5	0	0	210	53	99	5.0	1780	0
4	10	75	200	5	0	0	210	66	96	7.5	1720	0
5	10	100	200	5	0	0	210	79	92	10.0	1640	0
6	0	0	0	0	150	1	150	-	55	0.0	0	220
7	10	25	0	0	150	1	160	-	65	2.5	0	220
8	10	50	0	0	150	1	160	-	65	5.0	0	220
9	10	75	0	0	150	1	160	-	65	7.5	0	220
10	10	100	0	0	150	1	160	-	65	10.0	0	220

Table 62. Shear and Bending capacity simulation steps and analysis progress (C40/50, φ24 mm, mean values)

No	Load Step 1	Step Mult.	Load Step 2	Step Mult.	Load Step 3	Step Mult.	∑ step	Crack Initiate	Final Step	σ_cp	V_rd	M_rd
	Axial force - N		Shear force - V		Moment - M		Analysis steps			MPa	kN/m	kNm/m
1	0	0	200	5	0	0	200	55	132	0.0	2640	0
2	10	25	200	5	0	0	210	85	164	2.5	3080	0
3	10	50	200	5	0	0	210	97	183	5.0	3460	0
4	10	75	200	5	0	0	210	105	197	7.5	3740	0
5	10	100	200	5	0	0	210	115	210	10.0	4000	0
6	0	0	0	0	150	1	150	-	124	0.0	0	496
7	10	25	0	0	150	1	160	-	134	2.5	0	496
8	10	50	0	0	150	1	160	-	134	5.0	0	496
9	10	75	0	0	150	1	160	-	134	7.5	0	496
10	10	100	0	0	150	1	160	-	134	10.0	0	496

Table 63. Shear and Bending capacity simulation steps and analysis progress (C40/50, φ20 mm, mean values)

No	Load Step 1	Step Mult.	Load Step 2	Step Mult.	Load Step 3	Step Mult.	∑ step	Crack Initiate	Final Step	σ_cp	V_rd	M_rd
	Axial force - N		Shear force - V		Moment - M		Analysis steps			MPa	kN/m	kNm/m
1	0	0	200	5	0	0	200	55	98	0.0	1960	0
2	10	25	200	5	0	0	210	85	131	2.5	2420	0
3	10	50	200	5	0	0	210	98	148	5.0	2760	0
4	10	75	200	5	0	0	210	104	162	7.5	3040	0
5	10	100	200	5	0	0	210	114	175	10.0	3300	0
6	0	0	0	0	150	1	150	-	91	0.0	0	364
7	10	25	0	0	150	1	160	-	101	2.5	0	364
8	10	50	0	0	150	1	160	-	101	5.0	0	364
9	10	75	0	0	150	1	160	-	101	7.5	0	364
10	10	100	0	0	150	1	160	-	101	10.0	0	364

Table 64. Shear – Bending interaction simulation (C25/30, φ24 mm, mean values, σ$_{cp}$=2.5 MPa)

No	Load Step 1	Step Mult.	Load Step 2	Step Mult.	Load Step 3	Step Mult.	Σ step	Final Step	σ$_{cp}$	V$_{rd}$	M$_{rd}$	$\dfrac{M_0}{M_{rd}}$	$\dfrac{V_0}{V_{rd}}$
	Axial force - N		Shear force - V		Moment - M		Analysis steps		MPa	kN/m	kNm/m		
1	10	25	144	5	0	1	154	154	2.5	2880	0	0.00	1.00
2	10	25	130	5	150	1	290	167	2.5	2600	108	0.26	0.90
3	10	25	115	5	150	1	275	168	2.5	2300	172	0.42	0.80
4	10	25	101	5	150	1	261	169	2.5	2020	232	0.56	0.70
5	10	25	86	5	150	1	246	166	2.5	1720	280	0.68	0.60
6	10	25	72	5	150	1	232	163	2.5	1440	324	0.79	0.50
7	10	25	58	5	150	1	218	159	2.5	1160	364	0.88	0.40
8	10	25	43	5	150	1	203	151	2.5	860	392	0.95	0.30
9	10	25	29	5	150	1	189	140	2.5	580	404	0.98	0.20
10	10	25	0	5	150	1	160	113	2.5	0	412	1.00	0.00

Table 65. Shear – Bending interaction simulation (C25/30, φ24 mm, mean values, σ$_{cp}$=5.0 MPa)

No	Load Step 1	Step Mult.	Load Step 2	Step Mult.	Load Step 3	Step Mult.	Σ step	Final Step	σ$_{cp}$	V$_{rd}$	M$_{rd}$	$\dfrac{M_0}{M_{rd}}$	$\dfrac{V_0}{V_{rd}}$
	Axial force - N		Shear force - V		Moment - M		Analysis steps		MPa	kN/m	kNm/m		
1	10	50	161	5	0	1	171	171	5.0	3220	0	0.00	1.00
2	10	50	145	5	150	1	305	181	5.0	2900	104	0.25	0.90
3	10	50	129	5	150	1	289	180	5.0	2580	164	0.40	0.80
4	10	50	113	5	150	1	273	179	5.0	2260	224	0.54	0.70
5	10	50	97	5	150	1	257	178	5.0	1940	284	0.69	0.60
6	10	50	81	5	150	1	241	174	5.0	1620	332	0.81	0.50
7	10	50	64	5	150	1	224	166	5.0	1280	368	0.89	0.40
8	10	50	48	5	150	1	208	156	5.0	960	392	0.95	0.30
9	10	50	32	5	150	1	192	144	5.0	640	408	0.99	0.20
10	10	50	0	5	150	1	160	113	5.0	0	412	1.00	0.00

Table 66. Shear – Bending interaction simulation (C25/30, φ24 mm, mean values, σ$_{cp}$=7.5 MPa)

No	Load Step 1	Step Mult.	Load Step 2	Step Mult.	Load Step 3	Step Mult.	Σ step	Final Step	σ$_{cp}$	V$_{rd}$	M$_{rd}$	$\dfrac{M_0}{M_{rd}}$	$\dfrac{V_0}{V_{rd}}$
	Axial force - N		Shear force - V		Moment - M		Analysis steps		MPa	kN/m	kNm/m		
1	10	75	173	5	0	1	183	183	7.5	3460	0	0.00	1.00
2	10	75	156	5	150	1	316	192	7.5	3120	104	0.25	0.90
3	10	75	138	5	150	1	298	193	7.5	2760	180	0.44	0.80
4	10	75	121	5	150	1	281	191	7.5	2420	240	0.58	0.70
5	10	75	104	5	150	1	264	186	7.5	2080	288	0.70	0.60
6	10	75	87	5	150	1	247	179	7.5	1740	328	0.80	0.50
7	10	75	69	5	150	1	229	171	7.5	1380	368	0.89	0.40
8	10	75	52	5	150	1	212	160	7.5	1040	392	0.95	0.30
9	10	75	35	5	150	1	195	147	7.5	700	408	0.99	0.20
10	10	75	0	5	150	1	160	113	7.5	0	412	1.00	0.00

Table 67. Shear – Bending interaction simulation (C25/30, φ24 mm, mean values, σ$_{cp}$=10.0 MPa)

No	Load Step 1	Step Mult.	Load Step 2	Step Mult.	Load Step 3	Step Mult.	Σ step	Final Step	σ$_{cp}$	V$_{rd}$	M$_{rd}$	$\dfrac{M_0}{M_{rd}}$	$\dfrac{V_0}{V_{rd}}$
	Axial force - N		Shear force - V		Moment - M		Analysis steps		MPa	kN/m	kNm/m		
1	10	100	171	5	0	1	181	181	10.0	3420	0	0.00	1.00
2	10	100	154	5	150	1	314	199	10.0	3080	140	0.34	0.90
3	10	100	137	5	150	1	297	196	10.0	2740	196	0.48	0.80
4	10	100	120	5	150	1	280	191	10.0	2400	244	0.59	0.70
5	10	100	103	5	150	1	263	185	10.0	2060	288	0.70	0.60
6	10	100	86	5	150	1	246	180	10.0	1720	336	0.82	0.50
7	10	100	68	5	150	1	228	172	10.0	1360	376	0.91	0.40
8	10	100	51	5	150	1	211	160	10.0	1020	396	0.96	0.30
9	10	100	34	5	150	1	194	146	10.0	680	408	0.99	0.20
10	10	100	0	5	150	1	160	113	10.0	0	412	1.00	0.00

Table 68. Shear – Bending interaction simulation (C25/30, φ24 mm, char. values, σ$_{cp}$=2.5 MPa)

No	Load Step 1	Step Mult.	Load Step 2	Step Mult.	Load Step 3	Step Mult.	Σ step	Final Step	σ$_{cp}$	V$_{rd}$	M$_{rd}$	$\frac{M_0}{M_{rd}}$	$\frac{V_0}{V_{rd}}$
	Axial force - N		Shear force - V		Moment - M		Analysis steps		MPa	kN/m	kNm/m		
1	10	25	128	5	0	1	138	138	2.5	2560	0	0.00	1.00
2	10	25	115	5	150	1	275	145	2.5	2300	80	0.22	0.90
3	10	25	102	5	150	1	262	148	2.5	2040	144	0.39	0.80
4	10	25	90	5	150	1	250	147	2.5	1800	188	0.51	0.70
5	10	25	77	5	150	1	237	146	2.5	1540	236	0.64	0.60
6	10	25	64	5	150	1	224	144	2.5	1280	280	0.76	0.50
7	10	25	51	5	150	1	211	139	2.5	1020	312	0.85	0.40
8	10	25	38	5	150	1	198	132	2.5	760	336	0.91	0.30
9	10	25	26	5	150	1	186	124	2.5	520	352	0.96	0.20
10	10	25	0	5	150	1	160	102	2.5	0	368	1.00	0.00

Table 69. Shear – Bending interaction simulation (C25/30, φ24 mm, char. values, σ$_{cp}$=5.0 MPa)

No	Load Step 1	Step Mult.	Load Step 2	Step Mult.	Load Step 3	Step Mult.	Σ step	Final Step	σ$_{cp}$	V$_{rd}$	M$_{rd}$	$\frac{M_0}{M_{rd}}$	$\frac{V_0}{V_{rd}}$
	Axial force - N		Shear force - V		Moment - M		Analysis steps		MPa	kN/m	kNm/m		
1	10	50	142	5	0	1	152	152	5.0	2840	0	0.00	1.00
2	10	50	128	5	150	1	288	160	5.0	2560	88	0.24	0.90
3	10	50	114	5	150	1	274	160	5.0	2280	144	0.39	0.80
4	10	50	99	5	150	1	259	160	5.0	1980	204	0.55	0.70
5	10	50	85	5	150	1	245	156	5.0	1700	244	0.66	0.60
6	10	50	71	5	150	1	231	152	5.0	1420	284	0.77	0.50
7	10	50	57	5	150	1	217	146	5.0	1140	316	0.86	0.40
8	10	50	43	5	150	1	203	138	5.0	860	340	0.92	0.30
9	10	50	28	5	150	1	188	127	5.0	560	356	0.97	0.20
10	10	50	0	5	150	1	160	102	5.0	0	368	1.00	0.00

Table 70. Shear – Bending interaction simulation (C25/30, φ24 mm, char. values, σ$_{cp}$=7.5 MPa)

No	Load Step 1	Step Mult.	Load Step 2	Step Mult.	Load Step 3	Step Mult.	Σ step	Final Step	σ$_{cp}$	V$_{rd}$	M$_{rd}$	$\frac{M_0}{M_{rd}}$	$\frac{V_0}{V_{rd}}$
	Axial force - N		Shear force - V		Moment - M		Analysis steps		MPa	kN/m	kNm/m		
1	10	75	135	5	0	1	145	145	7.5	2700	0	0.00	1.00
2	10	75	122	5	150	1	282	166	7.5	2440	136	0.37	0.90
3	10	75	108	5	150	1	268	164	7.5	2160	184	0.50	0.80
4	10	75	95	5	150	1	255	160	7.5	1900	220	0.60	0.70
5	10	75	81	5	150	1	241	155	7.5	1620	256	0.70	0.60
6	10	75	68	5	150	1	228	152	7.5	1360	296	0.80	0.50
7	10	75	54	5	150	1	214	147	7.5	1080	332	0.90	0.40
8	10	75	41	5	150	1	201	138	7.5	820	348	0.95	0.30
9	10	75	27	5	150	1	187	126	7.5	540	356	0.97	0.20
10	10	75	0	5	150	1	160	102	7.5	0	368	1.00	0.00

Table 71. Shear – Bending interaction simulation (C25/30, φ24 mm, char. values, σ$_{cp}$=10.0 MPa)

No	Load Step 1	Step Mult.	Load Step 2	Step Mult.	Load Step 3	Step Mult.	Σ step	Final Step	σ$_{cp}$	V$_{rd}$	M$_{rd}$	$\frac{M_0}{M_{rd}}$	$\frac{V_0}{V_{rd}}$
	Axial force - N		Shear force - V		Moment - M		Analysis steps		MPa	kN/m	kNm/m		
1	10	100	128	5	0	1	138	138	10.0	2560	0	0.00	1.00
2	10	100	115	5	150	1	275	167	10.0	2300	168	0.46	0.90
3	10	100	102	5	150	1	262	162	10.0	2040	200	0.54	0.80
4	10	100	90	5	150	1	250	157	10.0	1800	228	0.62	0.70
5	10	100	77	5	150	1	237	155	10.0	1540	272	0.74	0.60
6	10	100	64	5	150	1	224	153	10.0	1280	316	0.82	0.50
7	10	100	51	5	150	1	211	146	10.0	1020	340	0.91	0.40
8	10	100	38	5	150	1	198	136	10.0	760	352	0.96	0.30
9	10	100	26	5	150	1	186	126	10.0	520	360	0.99	0.20
10	10	100	0	5	150	1	160	102	10.0	0	368	1.00	0.00

Table 72. Shear – Bending interaction simulation (C25/30, ϕ24 mm, design values, σcp=2.5 MPa)

No	Load Step 1	Step Mult.	Load Step 2	Step Mult.	Load Step 3	Step Mult.	∑ step	Final Step	σcp	Vrd	Mrd	$\frac{M_0}{M_{rd}}$	$\frac{V_0}{V_{rd}}$
	Axial force - N		Shear force - V		Moment - M		Analysis steps		MPa	kN/m	kNm/m		
1	10	25	104	5	0	1	114	114	2.5	2080	0	0.00	1.00
2	10	25	94	5	150	1	254	124	2.5	1880	80	0.26	0.90
3	10	25	83	5	150	1	243	125	2.5	1660	128	0.42	0.80
4	10	25	73	5	150	1	233	126	2.5	1460	172	0.56	0.70
5	10	25	62	5	150	1	222	123	2.5	1240	204	0.66	0.60
6	10	25	52	5	150	1	212	120	2.5	1040	232	0.75	0.50
7	10	25	42	5	150	1	202	117	2.5	840	260	0.84	0.40
8	10	25	31	5	150	1	191	112	2.5	620	284	0.92	0.30
9	10	25	21	5	150	1	181	106	2.5	420	300	0.97	0.20
10	10	25	0	5	150	1	160	87	2.5	0	308	1.00	0.00

Table 73. Shear – Bending interaction simulation (C25/30, ϕ24 mm, design values, σcp=5.0 MPa)

No	Load Step 1	Step Mult.	Load Step 2	Step Mult.	Load Step 3	Step Mult.	∑ step	Final Step	σcp	Vrd	Mrd	$\frac{M_0}{M_{rd}}$	$\frac{V_0}{V_{rd}}$
	Axial force - N		Shear force - V		Moment - M		Analysis steps		MPa	kN/m	kNm/m		
1	10	50	96	5	0	1	106	106	5.0	1920	0	0.00	1.00
2	10	50	86	5	150	1	246	132	5.0	1720	144	0.47	0.90
3	10	50	77	5	150	1	237	130	5.0	1540	172	0.56	0.80
4	10	50	67	5	150	1	227	127	5.0	1340	200	0.65	0.70
5	10	50	58	5	150	1	218	124	5.0	1160	224	0.73	0.60
6	10	50	48	5	150	1	208	121	5.0	960	252	0.82	0.50
7	10	50	38	5	150	1	198	118	5.0	760	280	0.91	0.40
8	10	50	29	5	150	1	189	113	5.0	580	296	0.96	0.30
9	10	50	19	5	150	1	179	105	5.0	380	304	0.99	0.20
10	10	50	0	5	150	1	160	87	5.0	0	308	1.00	0.00

Table 74. Shear – Bending interaction simulation (C25/30, ϕ24 mm, design values, σcp=7.5 MPa)

No	Load Step 1	Step Mult.	Load Step 2	Step Mult.	Load Step 3	Step Mult.	∑ step	Final Step	σcp	Vrd	Mrd	$\frac{M_0}{M_{rd}}$	$\frac{V_0}{V_{rd}}$
	Axial force - N		Shear force - V		Moment - M		Analysis steps		MPa	kN/m	kNm/m		
1	10	75	95	5	0	1	105	105	7.5	1900	0	0.00	1.00
2	10	75	86	5	150	1	246	131	7.5	1720	140	0.45	0.90
3	10	75	76	5	150	1	236	128	7.5	1520	168	0.55	0.80
4	10	75	67	5	150	1	227	124	7.5	1340	188	0.61	0.70
5	10	75	57	5	150	1	217	124	7.5	1140	228	0.74	0.60
6	10	75	48	5	150	1	208	123	7.5	960	260	0.84	0.50
7	10	75	38	5	150	1	198	120	7.5	760	288	0.94	0.40
8	10	75	29	5	150	1	189	113	7.5	580	296	0.96	0.30
9	10	75	19	5	150	1	179	105	7.5	380	304	0.99	0.20
10	10	75	0	5	150	1	160	87	7.5	0	308	1.00	0.00

Table 75 Shear – Bending interaction simulation (C25/30, ϕ24 mm, design values, σcp=10.0 MPa)

No	Load Step 1	Step Mult.	Load Step 2	Step Mult.	Load Step 3	Step Mult.	∑ step	Final Step	σcp	Vrd	Mrd	$\frac{M_0}{M_{rd}}$	$\frac{V_0}{V_{rd}}$
	Axial force - N		Shear force - V		Moment - M		Analysis steps		MPa	kN/m	kNm/m		
1	10	100	93	5	0	1	103	103	10.0	1860	0	0.00	1.00
2	10	100	84	5	150	1	244	124	10.0	1680	120	0.39	0.90
3	10	100	74	5	150	1	234	120	10.0	1480	144	0.47	0.80
4	10	100	65	5	150	1	225	123	10.0	1300	192	0.62	0.70
5	10	100	56	5	150	1	216	124	10.0	1120	232	0.75	0.60
6	10	100	47	5	150	1	207	123	10.0	940	264	0.86	0.50
7	10	100	37	5	150	1	197	119	10.0	740	288	0.94	0.40
8	10	100	28	5	150	1	188	113	10.0	560	300	0.97	0.30
9	10	100	19	5	150	1	179	105	10.0	380	304	0.99	0.20
10	10	100	0	5	150	1	160	87	10.0	0	308	1.00	0.00

Table 76. Shear – Bending interaction simulation (C25/30, φ20 mm, mean values, σcp=2.5 MPa)

No	Load Step 1	Step Mult.	Load Step 2	Step Mult.	Load Step 3	Step Mult.	Σ step	Final Step	σ_{cp}	V_{rd}	M_{rd}	$\dfrac{M_0}{M_{rd}}$	$\dfrac{V_0}{V_{rd}}$
	Axial force - N		Shear force - V		Moment - M		Analysis steps		MPa	kN/m	kNm/m		
1	10	25	112	5	0	1	122	122	2.5	2240	0	0.00	1.00
2	10	25	101	5	150	1	261	132	2.5	2020	84	0.27	0.90
3	10	25	90	5	150	1	250	133	2.5	1800	132	0.43	0.80
4	10	25	78	5	150	1	238	131	2.5	1560	172	0.56	0.70
5	10	25	67	5	150	1	227	131	2.5	1340	216	0.70	0.60
6	10	25	56	5	150	1	216	129	2.5	1120	252	0.82	0.50
7	10	25	45	5	150	1	205	124	2.5	900	276	0.90	0.40
8	10	25	34	5	150	1	194	118	2.5	680	296	0.96	0.30
9	10	25	22	5	150	1	182	108	2.5	440	304	0.99	0.20
10	10	25	0	5	150	1	160	87	2.5	0	308	1.00	0.00

Table 77. Shear – Bending interaction simulation (C25/30, φ20 mm, mean values, σcp=5.0 MPa)

No	Load Step 1	Step Mult.	Load Step 2	Step Mult.	Load Step 3	Step Mult.	Σ step	Final Step	σ_{cp}	V_{rd}	M_{rd}	$\dfrac{M_0}{M_{rd}}$	$\dfrac{V_0}{V_{rd}}$
	Axial force - N		Shear force - V		Moment - M		Analysis steps		MPa	kN/m	kNm/m		
1	10	50	128	5	0	1	138	138	5.0	2560	0	0.00	1.00
2	10	50	115	5	150	1	275	145	5.0	2300	80	0.26	0.90
3	10	50	102	5	150	1	262	146	5.0	2040	136	0.44	0.80
4	10	50	90	5	150	1	250	144	5.0	1800	176	0.57	0.70
5	10	50	77	5	150	1	237	142	5.0	1540	220	0.71	0.60
6	10	50	64	5	150	1	224	137	5.0	1280	252	0.82	0.50
7	10	50	51	5	150	1	211	132	5.0	1020	284	0.92	0.40
8	10	50	38	5	150	1	198	122	5.0	760	296	0.96	0.30
9	10	50	26	5	150	1	186	112	5.0	520	304	0.99	0.20
10	10	50	0	5	150	1	160	87	5.0	0	308	1.00	0.00

Table 78. Shear – Bending interaction simulation (C25/30, φ20 mm, mean values, σcp=7.5 MPa)

No	Load Step 1	Step Mult.	Load Step 2	Step Mult.	Load Step 3	Step Mult.	Σ step	Final Step	σ_{cp}	V_{rd}	M_{rd}	$\dfrac{M_0}{M_{rd}}$	$\dfrac{V_0}{V_{rd}}$
	Axial force - N		Shear force - V		Moment - M		Analysis steps		MPa	kN/m	kNm/m		
1	10	75	142	5	0	1	152	152	7.5	2840	0	0.00	1.00
2	10	75	128	5	150	1	288	157	7.5	2560	76	0.25	0.90
3	10	75	114	5	150	1	274	158	7.5	2280	136	0.44	0.80
4	10	75	99	5	150	1	259	156	7.5	1980	188	0.61	0.70
5	10	75	85	5	150	1	245	151	7.5	1700	224	0.73	0.60
6	10	75	71	5	150	1	231	145	7.5	1420	256	0.83	0.50
7	10	75	57	5	150	1	217	137	7.5	1140	280	0.91	0.40
8	10	75	43	5	150	1	203	127	7.5	860	296	0.96	0.30
9	10	75	28	5	150	1	188	114	7.5	560	304	0.99	0.20
10	10	75	0	5	150	1	160	87	7.5	0	308	1.00	0.00

Table 79. Shear – Bending interaction simulation (C25/30, φ20 mm, mean values, σcp=10.0 MPa)

No	Load Step 1	Step Mult.	Load Step 2	Step Mult.	Load Step 3	Step Mult.	Σ step	Final Step	σ_{cp}	V_{rd}	M_{rd}	$\dfrac{M_0}{M_{rd}}$	$\dfrac{V_0}{V_{rd}}$
	Axial force - N		Shear force - V		Moment - M		Analysis steps		MPa	kN/m	kNm/m		
1	10	100	147	5	0	1	157	157	10.0	2940	0	0.00	1.00
2	10	100	132	5	150	1	292	168	10.0	2640	104	0.34	0.90
3	10	100	118	5	150	1	278	165	10.0	2360	148	0.48	0.80
4	10	100	103	5	150	1	263	161	10.0	2060	192	0.62	0.70
5	10	100	88	5	150	1	248	154	10.0	1760	224	0.73	0.60
6	10	100	74	5	150	1	234	149	10.0	1480	260	0.84	0.50
7	10	100	59	5	150	1	219	140	10.0	1180	284	0.92	0.40
8	10	100	44	5	150	1	204	128	10.0	880	296	0.96	0.30
9	10	100	29	5	150	1	189	115	10.0	580	304	0.99	0.20
10	10	100	0	5	150	1	160	87	10.0	0	308	1.00	0.00

Table 80. Shear – Bending interaction simulation (C25/30, ϕ20 mm, char. values, σ_cp=2.5 MPa)

No	Load Step 1	Step Mult.	Load Step 2	Step Mult.	Load Step 3	Step Mult.	Σ step	Final Step	σ_cp	V_rd	M_rd	$\frac{M_0}{M_{rd}}$	$\frac{V_0}{V_{rd}}$
	Axial force - N		Shear force - V		Moment - M		Analysis steps		MPa	kN/m	kNm/m		
1	10	25	99	5	0	1	109	109	2.5	1980	0	0.00	1.00
2	10	25	89	5	150	1	249	115	2.5	1780	64	0.24	0.90
3	10	25	79	5	150	1	239	115	2.5	1580	104	0.39	0.80
4	10	25	69	5	150	1	229	115	2.5	1380	144	0.54	0.70
5	10	25	59	5	150	1	219	115	2.5	1180	184	0.69	0.60
6	10	25	50	5	150	1	210	113	2.5	1000	212	0.79	0.50
7	10	25	40	5	150	1	200	109	2.5	800	236	0.88	0.40
8	10	25	30	5	150	1	190	103	2.5	600	252	0.94	0.30
9	10	25	20	5	150	1	180	96	2.5	400	264	0.99	0.20
10	10	25	0	5	150	1	160	77	2.5	0	268	1.00	0.00

Table 81. Shear – Bending interaction simulation (C25/30, ϕ20 mm, char. values, σ_cp=5.0 MPa)

No	Load Step 1	Step Mult.	Load Step 2	Step Mult.	Load Step 3	Step Mult.	Σ step	Final Step	σ_cp	V_rd	M_rd	$\frac{M_0}{M_{rd}}$	$\frac{V_0}{V_{rd}}$
	Axial force - N		Shear force - V		Moment - M		Analysis steps		MPa	kN/m	kNm/m		
1	10	50	114	5	0	1	124	124	5.0	2280	0	0.00	1.00
2	10	50	103	5	150	1	263	128	5.0	2060	60	0.22	0.90
3	10	50	91	5	150	1	251	128	5.0	1820	108	0.40	0.80
4	10	50	80	5	150	1	240	128	5.0	1600	152	0.57	0.70
5	10	50	68	5	150	1	228	125	5.0	1360	188	0.70	0.60
6	10	50	57	5	150	1	217	121	5.0	1140	216	0.81	0.50
7	10	50	46	5	150	1	206	116	5.0	920	240	0.90	0.40
8	10	50	34	5	150	1	194	108	5.0	680	256	0.96	0.30
9	10	50	23	5	150	1	183	99	5.0	460	264	0.99	0.20
10	10	50	0	5	150	1	160	77	5.0	0	268	1.00	0.00

Table 82. Shear – Bending interaction simulation (C25/30, ϕ20 mm, char. values, σ_cp=7.5 MPa)

No	Load Step 1	Step Mult.	Load Step 2	Step Mult.	Load Step 3	Step Mult.	Σ step	Final Step	σ_cp	V_rd	M_rd	$\frac{M_0}{M_{rd}}$	$\frac{V_0}{V_{rd}}$
	Axial force - N		Shear force - V		Moment - M		Analysis steps		MPa	kN/m	kNm/m		
1	10	75	121	5	0	1	131	131	7.5	2420	0	0.00	1.00
2	10	75	109	5	150	1	269	140	7.5	2180	84	0.31	0.90
3	10	75	97	5	150	1	257	137	7.5	1940	120	0.45	0.80
4	10	75	85	5	150	1	245	135	7.5	1700	160	0.60	0.70
5	10	75	73	5	150	1	233	130	7.5	1460	188	0.70	0.60
6	10	75	61	5	150	1	221	126	7.5	1220	220	0.82	0.50
7	10	75	48	5	150	1	208	119	7.5	960	244	0.91	0.40
8	10	75	36	5	150	1	196	110	7.5	720	256	0.96	0.30
9	10	75	24	5	150	1	184	100	7.5	480	264	0.99	0.20
10	10	75	0	5	150	1	160	77	7.5	0	268	1.00	0.00

Table 83. Shear – Bending interaction simulation (C25/30, ϕ20 mm, char. values, σ_cp=10.0 MPa)

No	Load Step 1	Step Mult.	Load Step 2	Step Mult.	Load Step 3	Step Mult.	Σ step	Final Step	σ_cp	V_rd	M_rd	$\frac{M_0}{M_{rd}}$	$\frac{V_0}{V_{rd}}$
	Axial force - N		Shear force - V		Moment - M		Analysis steps		MPa	kN/m	kNm/m		
1	10	100	116	5	0	1	126	126	10.0	2320	0	0.00	1.00
2	10	100	104	5	150	1	264	142	10.0	2080	112	0.42	0.90
3	10	100	93	5	150	1	253	138	10.0	1860	140	0.52	0.80
4	10	100	81	5	150	1	241	133	10.0	1620	168	0.63	0.70
5	10	100	70	5	150	1	230	129	10.0	1400	196	0.73	0.60
6	10	100	58	5	150	1	218	126	10.0	1160	232	0.87	0.50
7	10	100	46	5	150	1	206	118	10.0	920	248	0.93	0.40
8	10	100	35	5	150	1	195	110	10.0	700	260	0.97	0.30
9	10	100	23	5	150	1	183	99	10.0	460	264	0.99	0.20
10	10	100	0	5	150	1	160	77	10.0	0	268	1.00	0.00

Table 84. Shear – Bending interaction simulation (C25/30, φ20 mm, design values, σcp=2.5 MPa)

No	Load Step 1	Step Mult.	Load Step 2	Step Mult.	Load Step 3	Step Mult.	∑ step	Final Step	σcp	Vrd	Mrd	$\dfrac{M_0}{M_{rd}}$	$\dfrac{V_0}{V_{rd}}$
	Axial force - N		Shear force - V		Moment - M		Analysis steps		MPa	kN/m	kNm/m		
1	10	25	85	5	0	1	95	95	2.5	1700	0	0.00	1.00
2	10	25	77	5	150	1	237	98	2.5	1540	44	0.20	0.90
3	10	25	68	5	150	1	228	99	2.5	1360	84	0.38	0.80
4	10	25	60	5	150	1	220	99	2.5	1200	116	0.53	0.70
5	10	25	51	5	150	1	211	99	2.5	1020	152	0.69	0.60
6	10	25	43	5	150	1	203	96	2.5	860	172	0.78	0.50
7	10	25	34	5	150	1	194	92	2.5	680	192	0.87	0.40
8	10	25	26	5	150	1	186	88	2.5	520	208	0.95	0.30
9	10	25	17	5	150	1	177	81	2.5	340	216	0.98	0.20
10	10	25	0	5	150	1	160	65	2.5	0	220	1.00	0.00

Table 85. Shear – Bending interaction simulation (C25/30, φ20 mm, design values, σcp=5.0 MPa)

No	Load Step 1	Step Mult.	Load Step 2	Step Mult.	Load Step 3	Step Mult.	∑ step	Final Step	σcp	Vrd	Mrd	$\dfrac{M_0}{M_{rd}}$	$\dfrac{V_0}{V_{rd}}$
	Axial force - N		Shear force - V		Moment - M		Analysis steps		MPa	kN/m	kNm/m		
1	10	50	89	5	0	1	99	99	5.0	1780	0	0.00	1.00
2	10	50	80	5	150	1	240	104	5.0	1600	56	0.25	0.90
3	10	50	71	5	150	1	231	109	5.0	1420	112	0.51	0.80
4	10	50	62	5	150	1	222	107	5.0	1240	140	0.64	0.70
5	10	50	53	5	150	1	213	104	5.0	1060	164	0.75	0.60
6	10	50	45	5	150	1	205	101	5.0	900	184	0.84	0.50
7	10	50	36	5	150	1	196	97	5.0	720	204	0.93	0.40
8	10	50	27	5	150	1	187	90	5.0	540	212	0.96	0.30
9	10	50	18	5	150	1	178	82	5.0	360	216	0.98	0.20
10	10	50	0	5	150	1	160	65	5.0	0	220	1.00	0.00

Table 86. Shear – Bending interaction simulation (C25/30, φ20 mm, design values, σcp=7.5 MPa)

No	Load Step 1	Step Mult.	Load Step 2	Step Mult.	Load Step 3	Step Mult.	∑ step	Final Step	σcp	Vrd	Mrd	$\dfrac{M_0}{M_{rd}}$	$\dfrac{V_0}{V_{rd}}$
	Axial force - N		Shear force - V		Moment - M		Analysis steps		MPa	kN/m	kNm/m		
1	10	75	86	5	0	1	96	96	7.5	1720	0	0.00	1.00
2	10	75	77	5	150	1	237	111	7.5	1540	96	0.44	0.90
3	10	75	69	5	150	1	229	108	7.5	1380	116	0.53	0.80
4	10	75	60	5	150	1	220	104	7.5	1200	136	0.62	0.70
5	10	75	52	5	150	1	212	104	7.5	1040	168	0.76	0.60
6	10	75	43	5	150	1	203	101	7.5	860	192	0.87	0.50
7	10	75	34	5	150	1	194	96	7.5	680	208	0.95	0.40
8	10	75	26	5	150	1	186	89	7.5	520	212	0.96	0.30
9	10	75	17	5	150	1	177	81	7.5	340	216	0.98	0.20
10	10	75	0	5	150	1	160	65	7.5	0	220	1.00	0.00

Table 87. Shear – Bending interaction simulation (C25/30, φ20 mm, design values, σcp=10.0 MPa)

No	Load Step 1	Step Mult.	Load Step 2	Step Mult.	Load Step 3	Step Mult.	∑ step	Final Step	σcp	Vrd	Mrd	$\dfrac{M_0}{M_{rd}}$	$\dfrac{V_0}{V_{rd}}$
	Axial force - N		Shear force - V		Moment - M		Analysis steps		MPa	kN/m	kNm/m		
1	10	100	82	5	0	1	92	92	10.0	1640	0	0.00	1.00
2	10	100	74	5	150	1	234	107	10.0	1480	92	0.42	0.90
3	10	100	66	5	150	1	226	101	10.0	1320	100	0.45	0.80
4	10	100	57	5	150	1	217	100	10.0	1140	132	0.60	0.70
5	10	100	49	5	150	1	209	100	10.0	980	164	0.75	0.60
6	10	100	41	5	150	1	201	99	10.0	820	192	0.87	0.50
7	10	100	33	5	150	1	193	94	10.0	660	204	0.93	0.40
8	10	100	25	5	150	1	185	88	10.0	500	212	0.96	0.30
9	10	100	16	5	150	1	176	80	10.0	320	216	0.98	0.20
10	10	100	0	5	150	1	160	65	10.0	0	220	1.00	0.00

Table 88. Shear – Bending interaction simulation (C40/50, φ24 mm, mean values, σcp=2.5 MPa)

No	Load Step 1	Step Mult.	Load Step 2	Step Mult.	Load Step 3	Step Mult.	Σ step	Final Step	σcp	Vrd	Mrd	$\frac{M_0}{M_{rd}}$	$\frac{V_0}{V_{rd}}$
	Axial force - N		Shear force - V		Moment - M		Analysis steps		MPa	kN/m	kNm/m		
1	10	25	154	5	0	1	164	164	2.5	3080	0	0.00	1.00
2	10	25	139	5	150	1	299	178	2.5	2780	116	0.23	0.90
3	10	25	123	5	150	1	283	181	2.5	2460	192	0.39	0.80
4	10	25	108	5	150	1	268	180	2.5	2160	248	0.50	0.70
5	10	25	92	5	150	1	252	180	2.5	1840	312	0.63	0.60
6	10	25	77	5	150	1	237	177	2.5	1540	360	0.73	0.50
7	10	25	62	5	150	1	222	171	2.5	1240	396	0.80	0.40
8	10	25	46	5	150	1	206	161	2.5	920	420	0.85	0.30
9	10	25	31	5	150	1	191	149	2.5	620	432	0.87	0.20
10	10	25	0	5	150	1	160	134	2.5	0	496	1.00	0.00

Table 89. Shear – Bending interaction simulation (C40/50, φ24 mm, mean values, σcp=5.0 MPa)

No	Load Step 1	Step Mult.	Load Step 2	Step Mult.	Load Step 3	Step Mult.	Σ step	Final Step	σcp	Vrd	Mrd	$\frac{M_0}{M_{rd}}$	$\frac{V_0}{V_{rd}}$
	Axial force - N		Shear force - V		Moment - M		Analysis steps		MPa	kN/m	kNm/m		
1	10	50	173	5	0	1	183	183	5.0	3460	0	0.00	1.00
2	10	50	156	5	150	1	316	192	5.0	3120	104	0.21	0.90
3	10	50	138	5	150	1	298	196	5.0	2760	192	0.39	0.80
4	10	50	121	5	150	1	281	197	5.0	2420	264	0.53	0.70
5	10	50	104	5	150	1	264	190	5.0	2080	304	0.61	0.60
6	10	50	87	5	150	1	247	187	5.0	1740	360	0.73	0.50
7	10	50	69	5	150	1	229	179	5.0	1380	400	0.81	0.40
8	10	50	52	5	150	1	212	168	5.0	1040	424	0.85	0.30
9	10	50	35	5	150	1	195	156	5.0	700	444	0.90	0.20
10	10	50	0	5	150	1	160	134	5.0	0	496	1.00	0.00

Table 90. Shear – Bending interaction simulation (C40/50, φ24 mm, mean values, σcp=7.5 MPa)

No	Load Step 1	Step Mult.	Load Step 2	Step Mult.	Load Step 3	Step Mult.	Σ step	Final Step	σcp	Vrd	Mrd	$\frac{M_0}{M_{rd}}$	$\frac{V_0}{V_{rd}}$
	Axial force - N		Shear force - V		Moment - M		Analysis steps		MPa	kN/m	kNm/m		
1	10	75	187	5	0	1	197	197	7.5	3740	0	0.00	1.00
2	10	75	168	5	150	1	328	209	7.5	3360	124	0.25	0.90
3	10	75	150	5	150	1	310	206	7.5	3000	184	0.37	0.80
4	10	75	131	5	150	1	291	204	7.5	2620	252	0.51	0.70
5	10	75	112	5	150	1	272	201	7.5	2240	316	0.64	0.60
6	10	75	94	5	150	1	254	197	7.5	1880	372	0.75	0.50
7	10	75	75	5	150	1	235	186	7.5	1500	404	0.81	0.40
8	10	75	56	5	150	1	216	172	7.5	1120	424	0.85	0.30
9	10	75	37	5	150	1	197	164	7.5	740	468	0.94	0.20
10	10	75	0	5	150	1	160	134	7.5	0	496	1.00	0.00

Table 91. Shear – Bending interaction simulation (C40/50, φ24 mm, mean values, σcp=10.0 MPa)

| No	Load Step 1	Step Mult.	Load Step 2	Step Mult.	Load Step 3	Step Mult.	Σ step	Final Step	σcp	Vrd	Mrd	$\frac{M_0}{M_{rd}}$	$\frac{V_0}{V_{rd}}$
	Axial force - N		Shear force - V		Moment - M		Analysis steps		MPa	kN/m	kNm/m		
1	10	100	200	5	0	1	210	210	10.0	4000	0	0.00	1.00
2	10	100	180	5	150	1	340	220	10.0	3600	120	0.24	0.90
3	10	100	160	5	150	1	320	218	10.0	3200	192	0.39	0.80
4	10	100	140	5	150	1	300	217	10.0	2800	268	0.54	0.70
5	10	100	120	5	150	1	280	211	10.0	2400	324	0.65	0.60
6	10	100	100	5	150	1	260	204	10.0	2000	376	0.76	0.50
7	10	100	80	5	150	1	240	191	10.0	1600	404	0.81	0.40
8	10	100	60	5	150	1	220	177	10.0	1200	428	0.86	0.30
9	10	100	40	5	150	1	200	164	10.0	800	456	0.92	0.20
10	10	100	0	5	150	1	160	134	10.0	0	496	1.00	0.00

Table 92. Shear – Bending interaction simulation (C40/50, ϕ20 mm, mean values, σcp=2.5 MPa)

| No	Load Step 1	Step Mult.	Load Step 2	Step Mult.	Load Step 3	Step Mult.	Σ step	Final Step	σ$_{cp}$	V$_{rd}$	M$_{rd}$	$\dfrac{M_0}{M_{rd}}$	$\dfrac{V_0}{V_{rd}}$
	Axial force - N		Shear force - V		Moment - M		Analysis steps		MPa	kN/m	kNm/m		
1	10	25	121	5	0	1	131	131	2.5	2420	0	0.00	1.00
2	10	25	109	5	150	1	269	144	2.5	2180	100	0.27	0.90
3	10	25	97	5	150	1	257	145	2.5	1940	152	0.42	0.80
4	10	25	85	5	150	1	245	145	2.5	1700	200	0.55	0.70
5	10	25	73	5	150	1	233	142	2.5	1460	236	0.65	0.60
6	10	25	61	5	150	1	221	141	2.5	1220	280	0.77	0.50
7	10	25	48	5	150	1	208	135	2.5	960	308	0.85	0.40
8	10	25	36	5	150	1	196	126	2.5	720	320	0.88	0.30
9	10	25	24	5	150	1	184	120	2.5	480	344	0.95	0.20
10	10	25	0	5	150	1	160	101	2.5	0	364	1.00	0.00

Table 93. Shear – Bending interaction simulation (C40/50, ϕ20 mm, mean values, σcp=5.0 MPa)

No	Load Step 1	Step Mult.	Load Step 2	Step Mult.	Load Step 3	Step Mult.	Σ step	Final Step	σ$_{cp}$	V$_{rd}$	M$_{rd}$	$\dfrac{M_0}{M_{rd}}$	$\dfrac{V_0}{V_{rd}}$
	Axial force - N		Shear force - V		Moment - M		Analysis steps		MPa	kN/m	kNm/m		
1	10	50	138	5	0	1	148	148	5.0	2760	0	0.00	1.00
2	10	50	124	5	150	1	284	158	5.0	2480	96	0.26	0.90
3	10	50	110	5	150	1	270	158	5.0	2200	152	0.42	0.80
4	10	50	97	5	150	1	257	158	5.0	1940	204	0.56	0.70
5	10	50	83	5	150	1	243	155	5.0	1660	248	0.68	0.60
6	10	50	69	5	150	1	229	150	5.0	1380	284	0.78	0.50
7	10	50	55	5	150	1	215	143	5.0	1100	312	0.86	0.40
8	10	50	41	5	150	1	201	132	5.0	820	324	0.89	0.30
9	10	50	28	5	150	1	188	122	5.0	560	336	0.92	0.20
10	10	50	0	5	150	1	160	101	5.0	0	364	1.00	0.00

Table 94. Shear – Bending interaction simulation (C40/50, ϕ20 mm, mean values, σcp=7.5 MPa)

No	Load Step 1	Step Mult.	Load Step 2	Step Mult.	Load Step 3	Step Mult.	Σ step	Final Step	σ$_{cp}$	V$_{rd}$	M$_{rd}$	$\dfrac{M_0}{M_{rd}}$	$\dfrac{V_0}{V_{rd}}$
	Axial force - N		Shear force - V		Moment - M		Analysis steps		MPa	kN/m	kNm/m		
1	10	75	152	5	0	1	162	162	7.5	3040	0	0.00	1.00
2	10	75	137	5	150	1	297	171	7.5	2740	96	0.26	0.90
3	10	75	122	5	150	1	282	171	7.5	2440	156	0.43	0.80
4	10	75	106	5	150	1	266	169	7.5	2120	212	0.58	0.70
5	10	75	91	5	150	1	251	165	7.5	1820	256	0.70	0.60
6	10	75	76	5	150	1	236	159	7.5	1520	292	0.80	0.50
7	10	75	61	5	150	1	221	149	7.5	1220	312	0.86	0.40
8	10	75	46	5	150	1	206	137	7.5	920	324	0.89	0.30
9	10	75	30	5	150	1	190	125	7.5	600	340	0.93	0.20
10	10	75	0	5	150	1	160	101	7.5	0	364	1.00	0.00

Table 95. Shear – Bending interaction simulation (C40/50, ϕ20 mm, mean values, σcp=10.0 MPa)

| No	Load Step 1	Step Mult.	Load Step 2	Step Mult.	Load Step 3	Step Mult.	Σ step	Final Step	σ$_{cp}$	V$_{rd}$	M$_{rd}$	$\dfrac{M_0}{M_{rd}}$	$\dfrac{V_0}{V_{rd}}$
	Axial force - N		Shear force - V		Moment - M		Analysis steps		MPa	kN/m	kNm/m		
1	10	100	165	5	0	1	175	175	10.0	3300	0	0.00	1.00
2	10	100	149	5	150	1	309	184	10.0	2980	100	0.27	0.90
3	10	100	132	5	150	1	292	182	10.0	2640	160	0.44	0.80
4	10	100	116	5	150	1	276	178	10.0	2320	208	0.57	0.70
5	10	100	99	5	150	1	259	173	10.0	1980	256	0.70	0.60
6	10	100	83	5	150	1	243	165	10.0	1660	288	0.79	0.50
7	10	100	66	5	150	1	226	154	10.0	1320	312	0.86	0.40
8	10	100	50	5	150	1	210	141	10.0	1000	324	0.89	0.30
9	10	100	33	5	150	1	193	130	10.0	660	348	0.96	0.20
10	10	100	0	5	150	1	160	101	10.0	0	364	1.00	0.00

Graph 87. Shear – Bending interaction comparison for reinforcement ratio (C25/30, mean values, σ_{cp}=2.5 MPa)
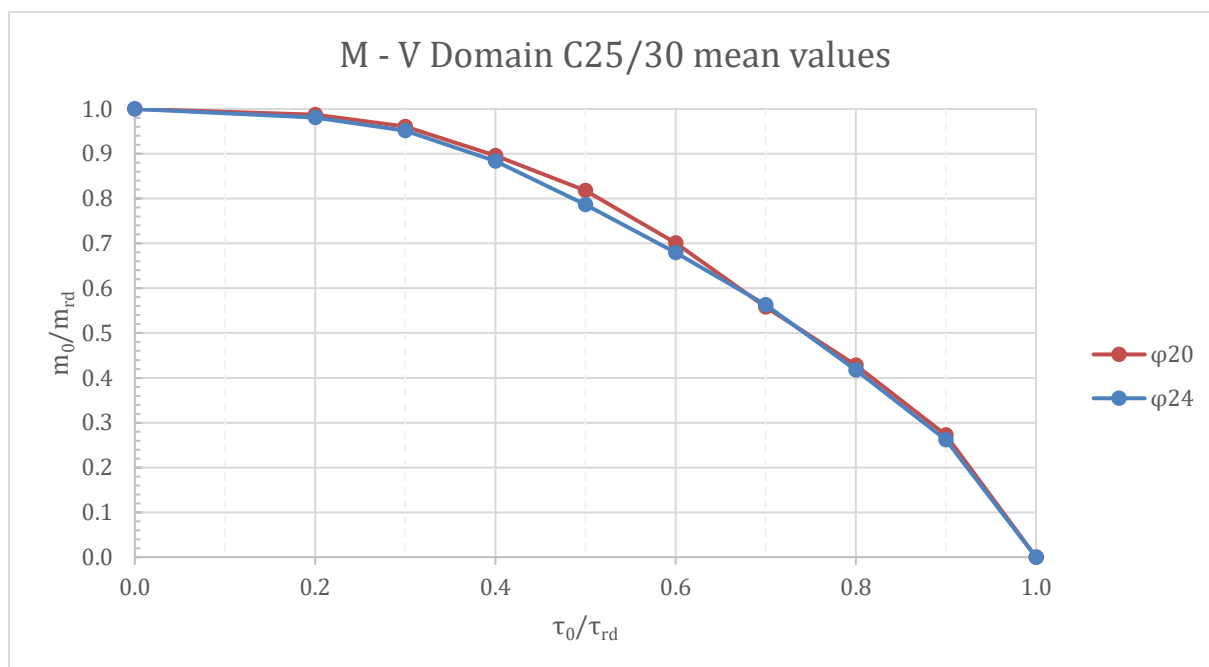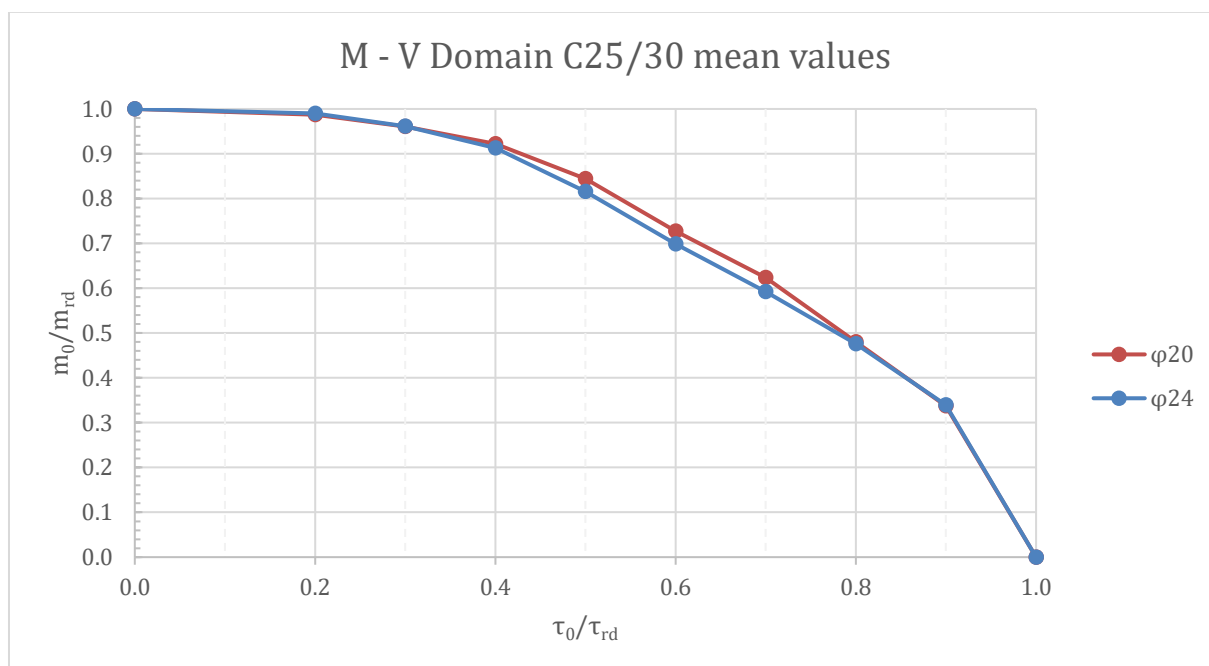

Graph 88. Shear – Bending interaction comparison for reinforcement ratio (C25/30, mean values, σ_{cp}=5.0 MPa)
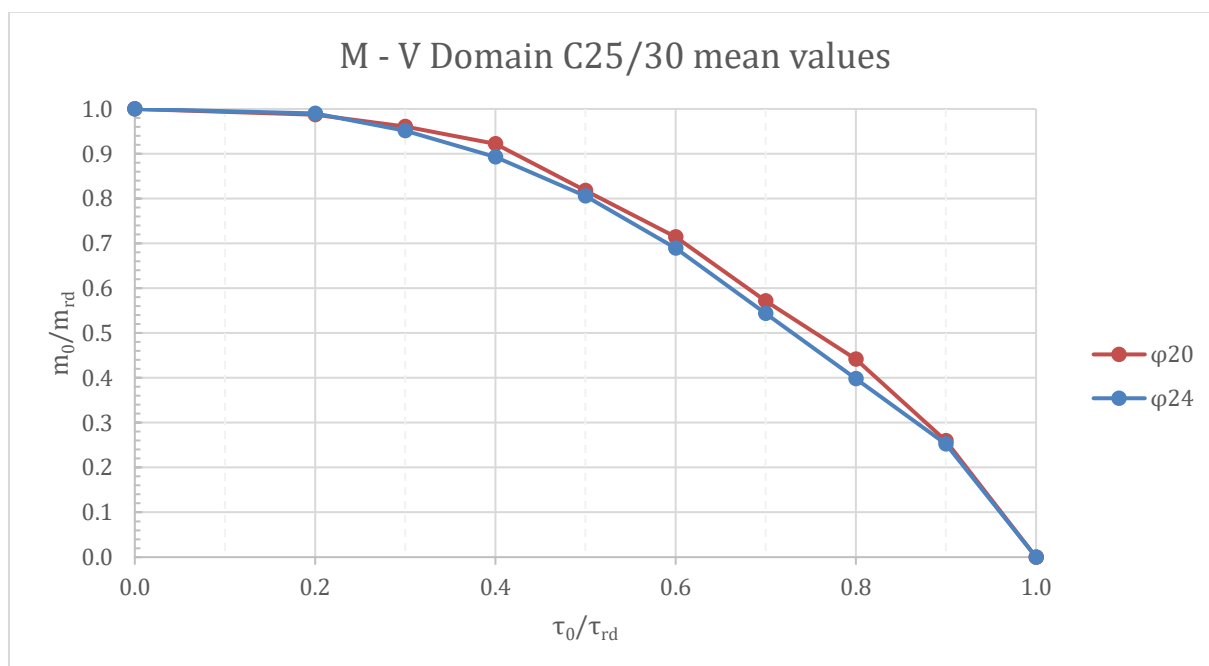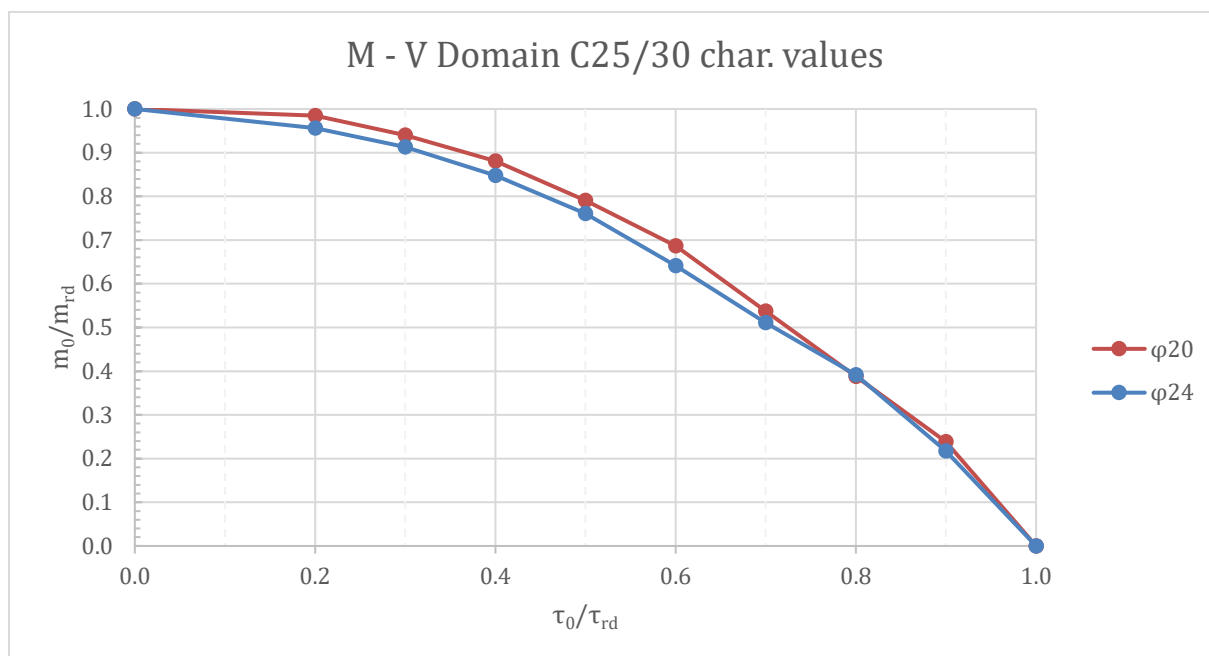
Graph 89. Shear – Bending interaction comparison for reinforcement ratio (C25/30, mean values, σ_{cp}=7.5 MPa)
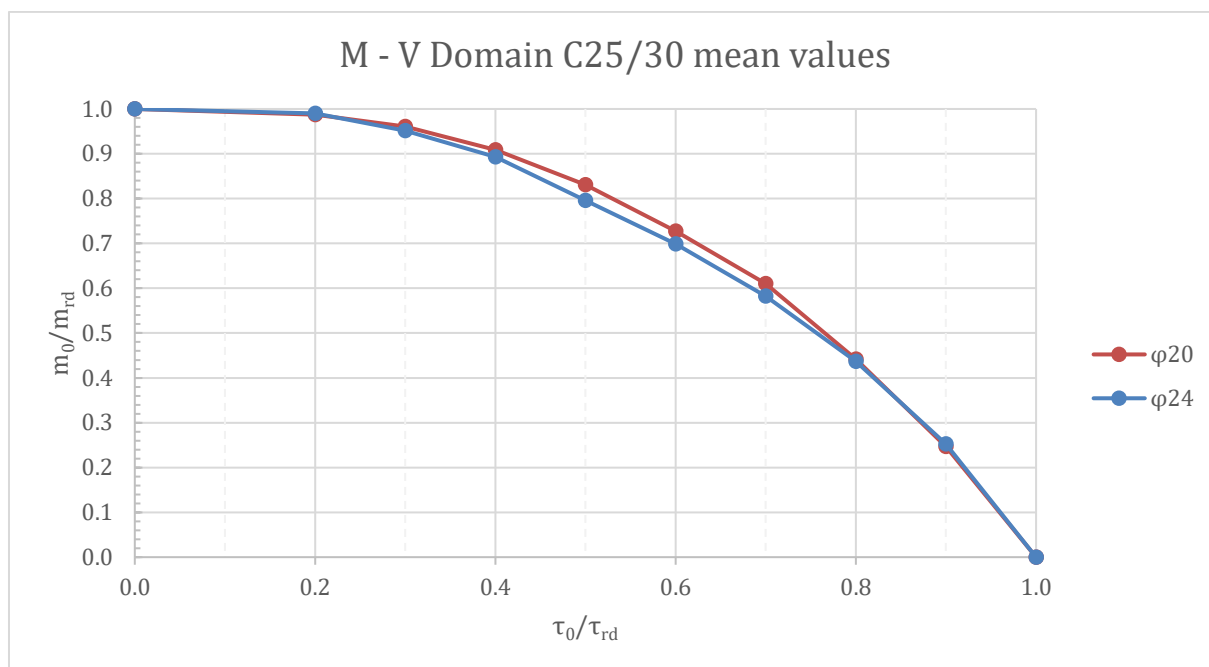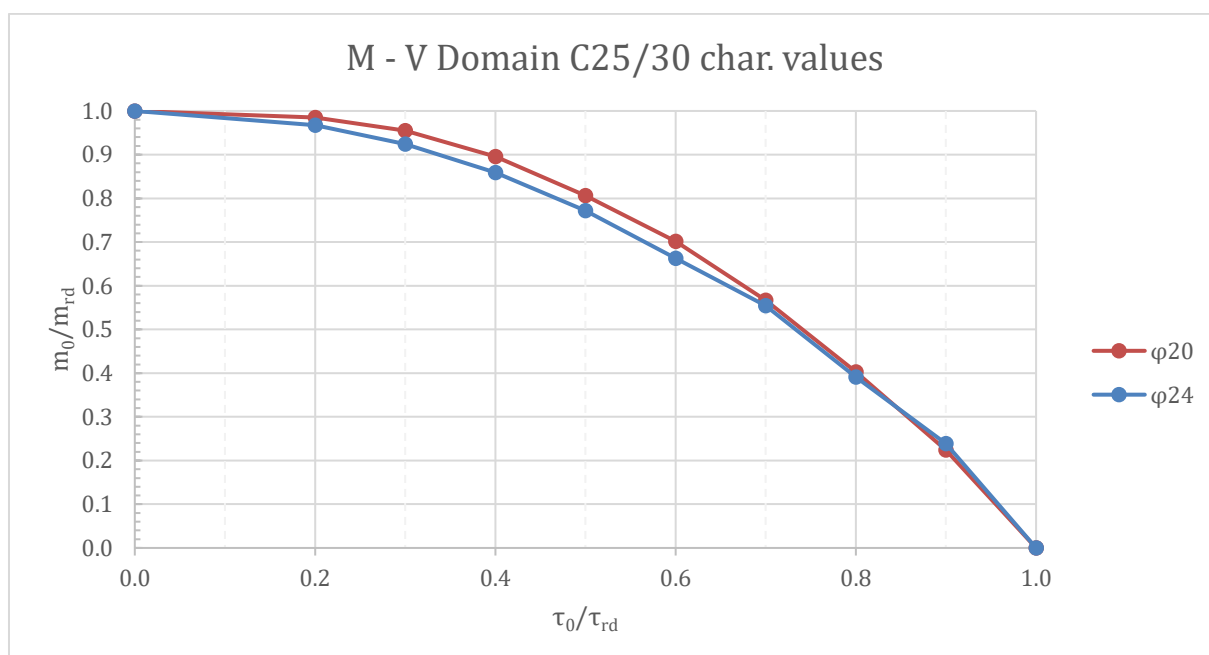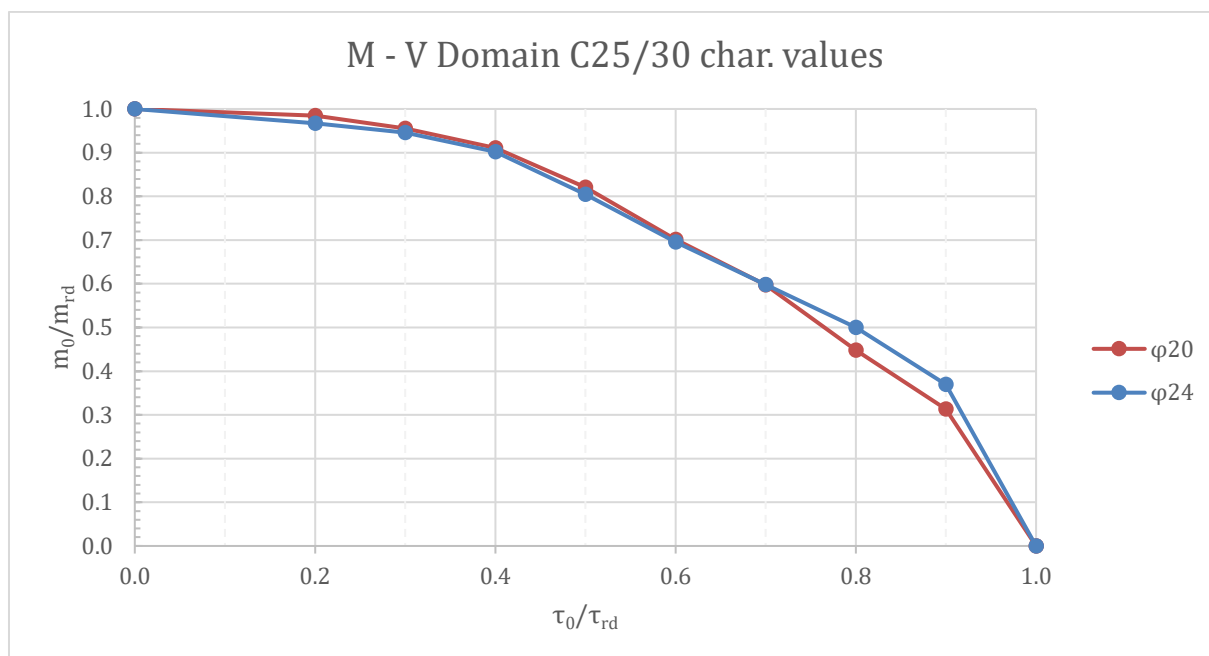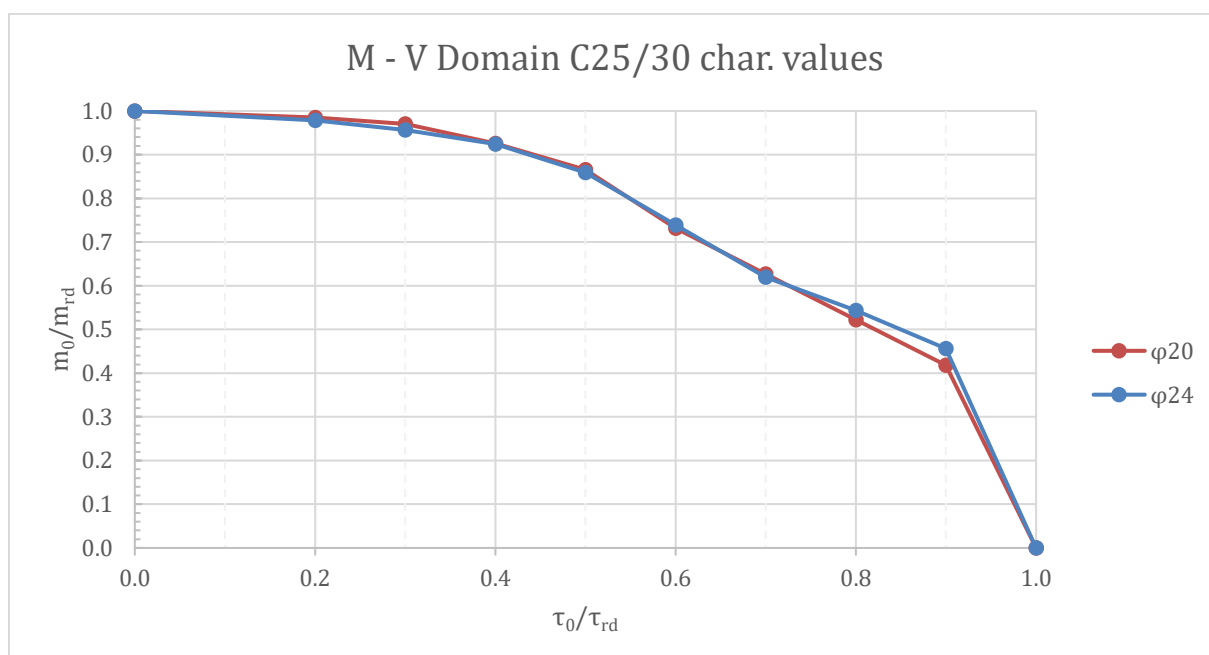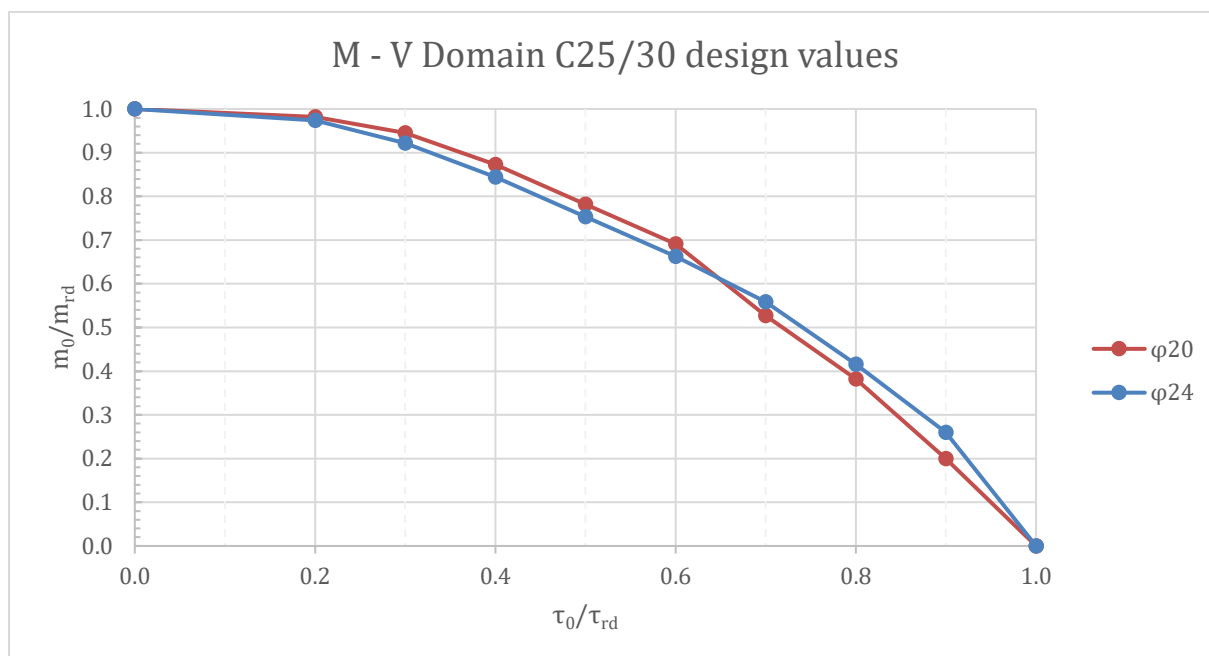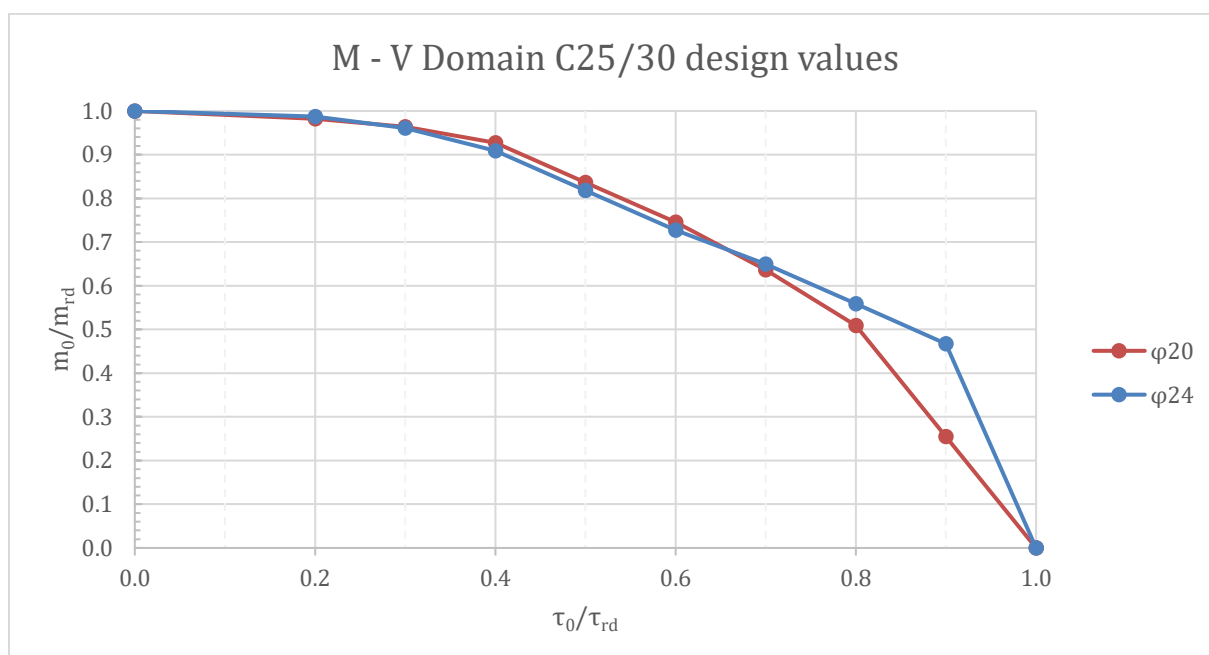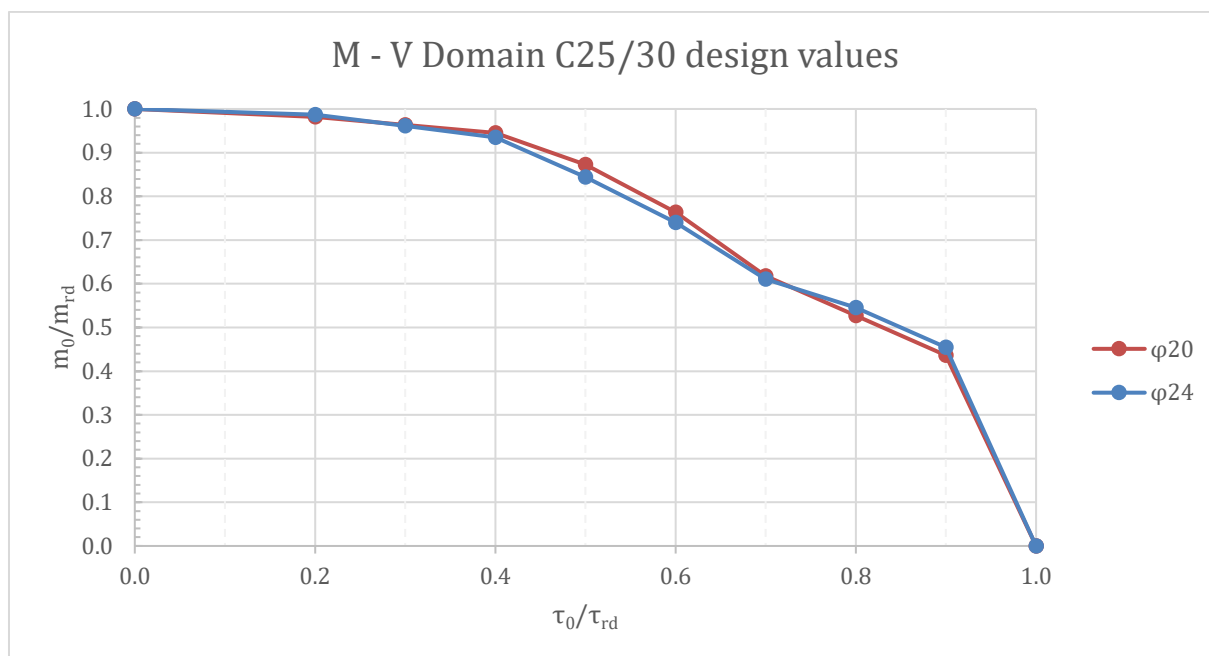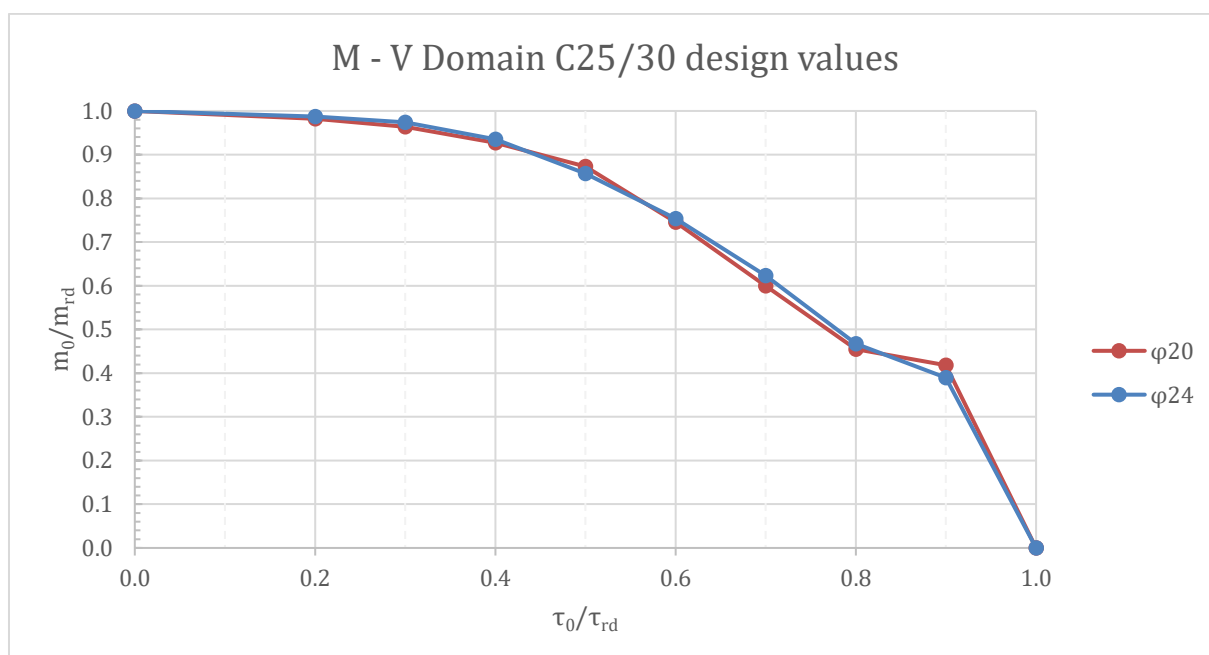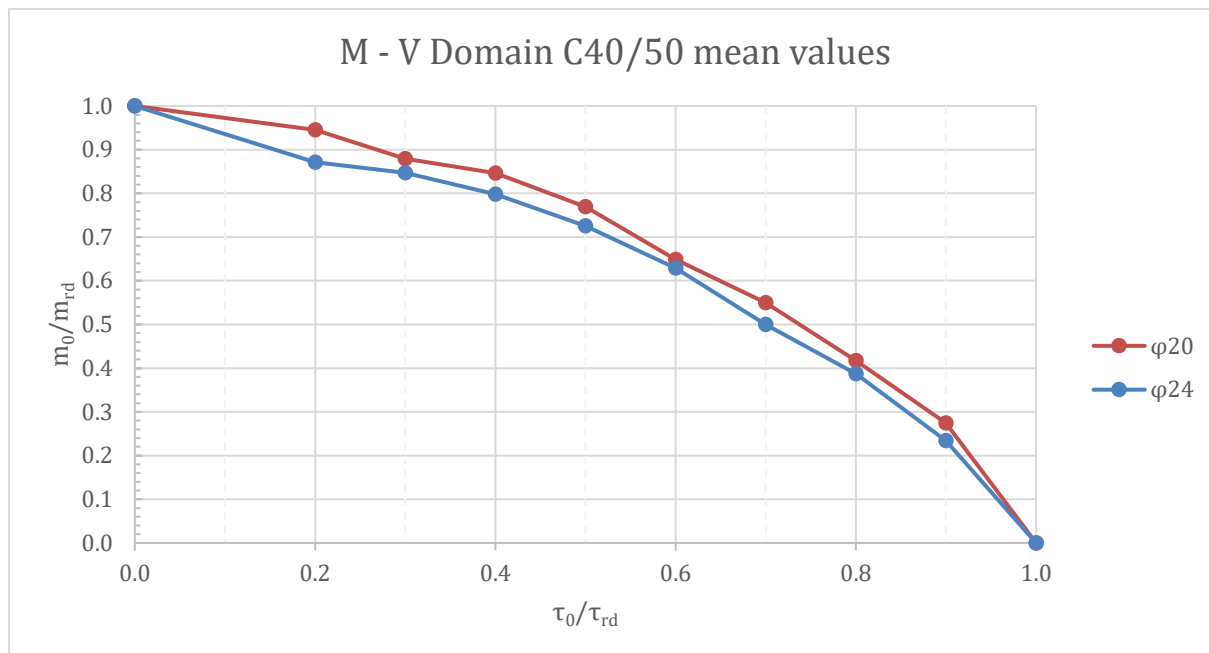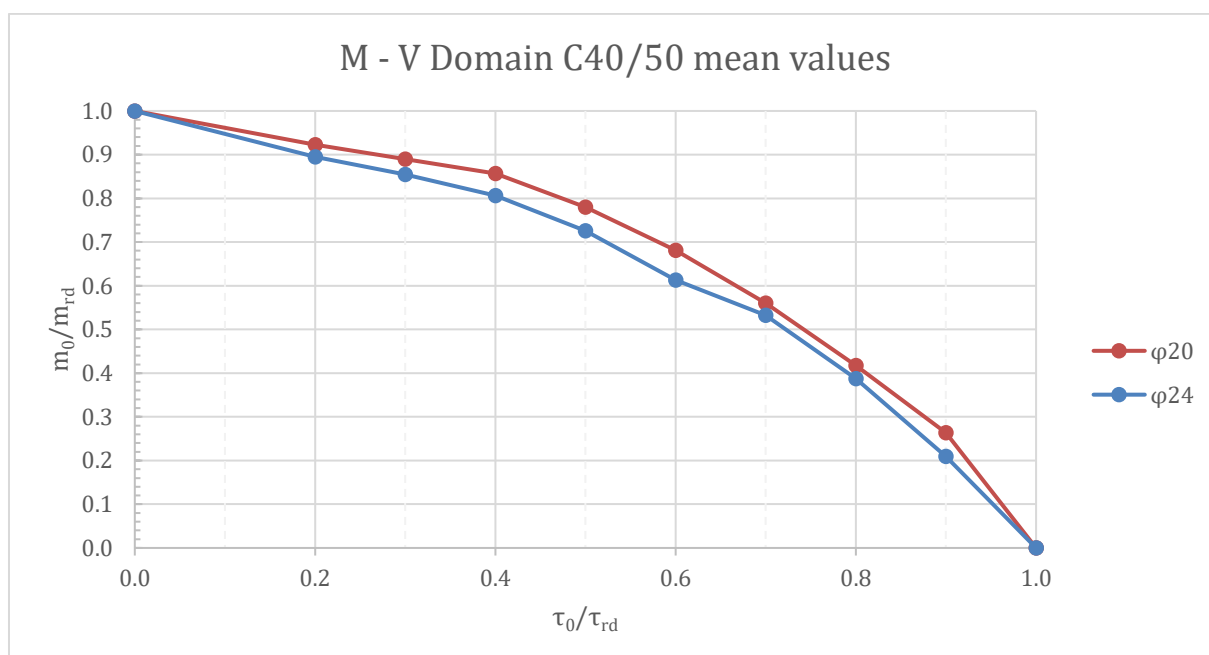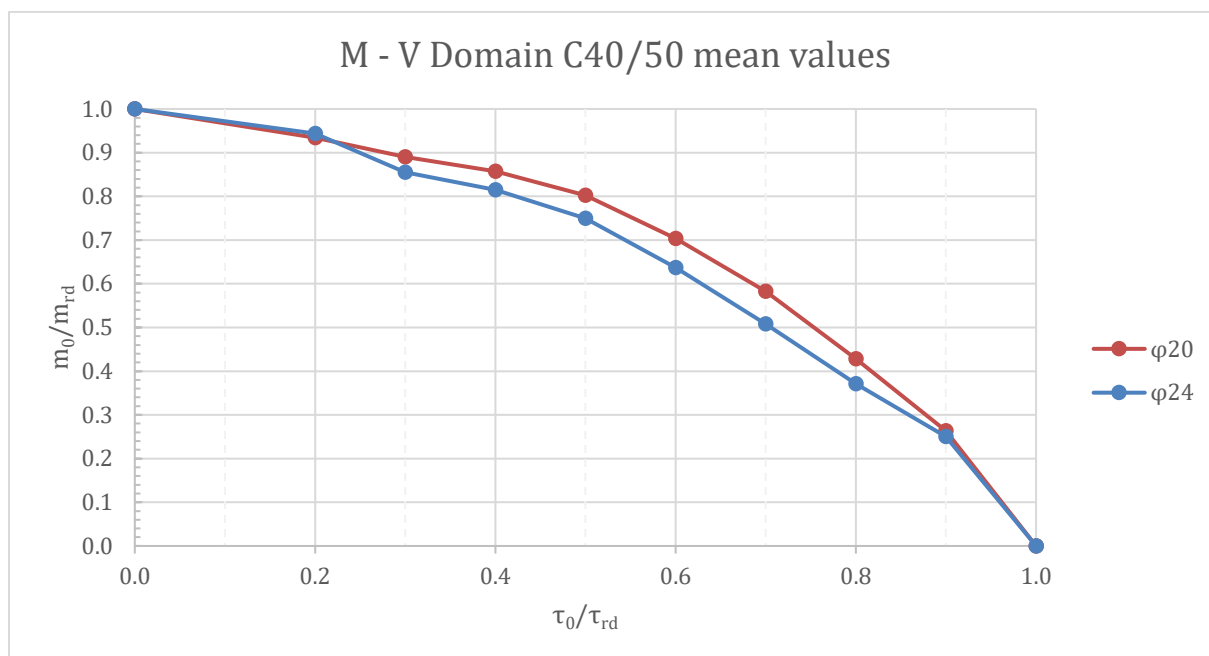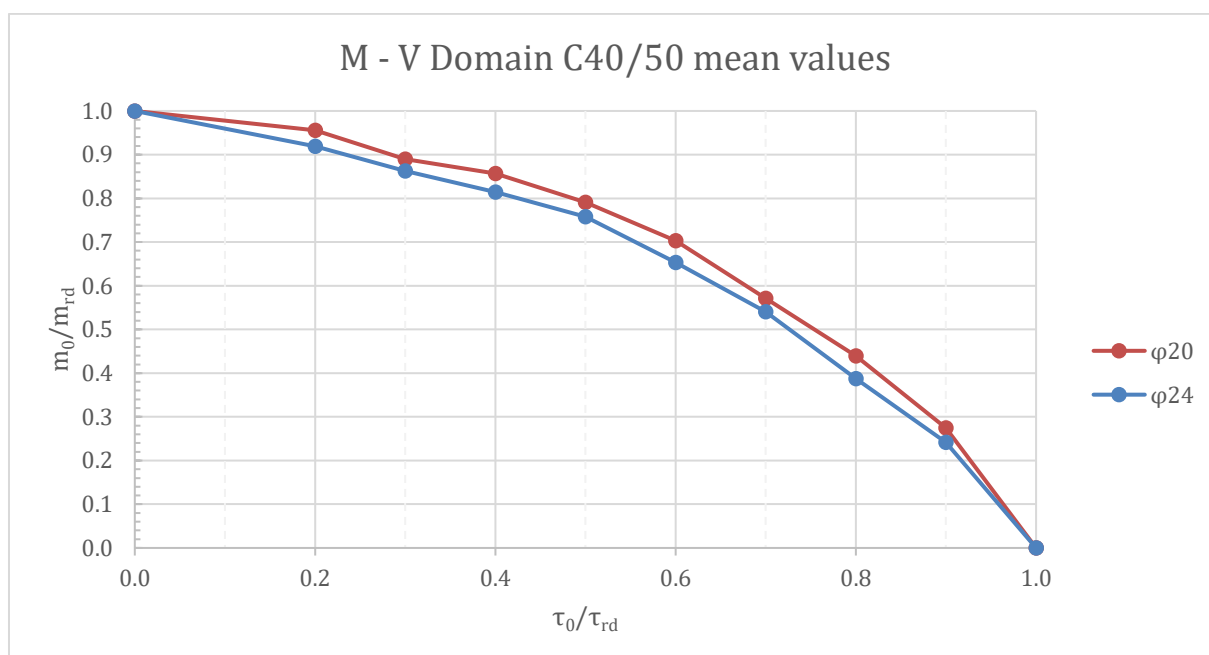

Graph 90. Shear – Bending interaction comparison for reinforcement ratio (C25/30, mean values, σ_{cp}=10.0 MPa)
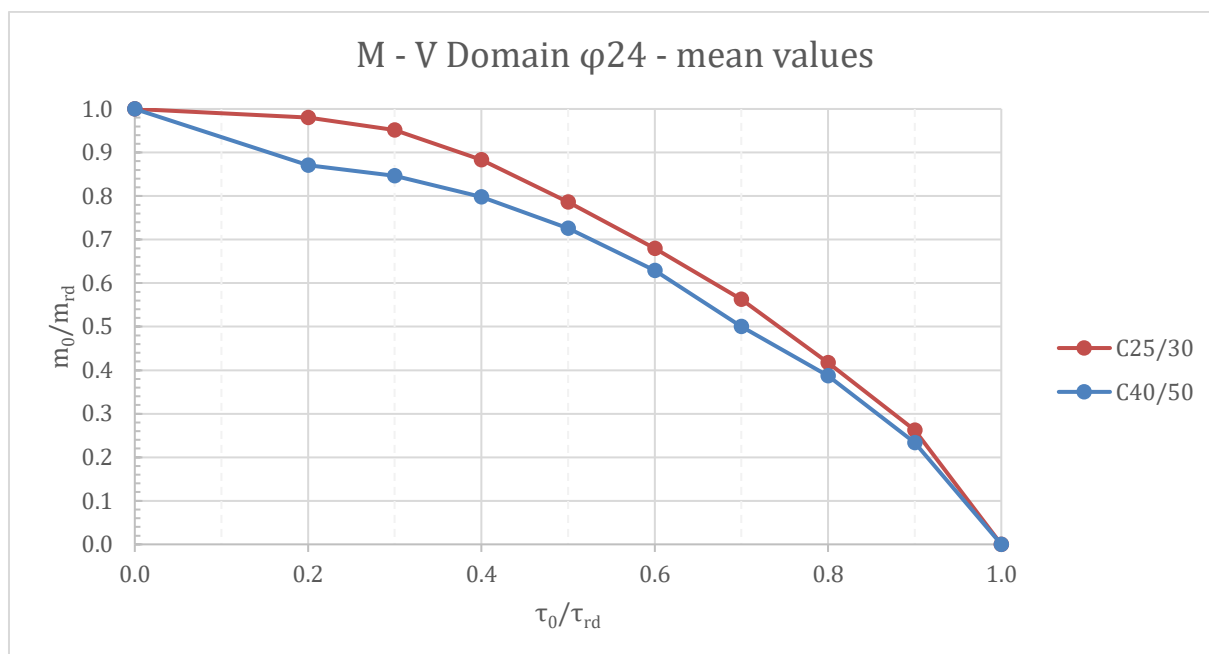
Graph 91. Shear – Bending interaction comparison for reinforcement ratio (C25/30, char. values, σ$_{cp}$=2.5 MPa)

Graph 92. Shear – Bending interaction comparison for reinforcement ratio (C25/30, char. values, σ$_{cp}$=5.0 MPa)

Graph 93. Shear – Bending interaction comparison for reinforcement ratio (C25/30, char. values, σcp=7.5 MPa)

Graph 94. Shear – Bending interaction comparison for reinforcement ratio (C25/30, char. values, σcp=10.0 MPa)

Graph 95. Shear – Bending interaction comparison for reinforcement ratio (C25/30, design values, σ_{cp}=2.5 MPa)

Graph 96. Shear – Bending interaction comparison for reinforcement ratio (C25/30, design values, σ_{cp}=5.0 MPa)

Graph 97. Shear – Bending interaction comparison for reinforcement ratio (C25/30, design values, σ_{cp}=7.5 MPa)
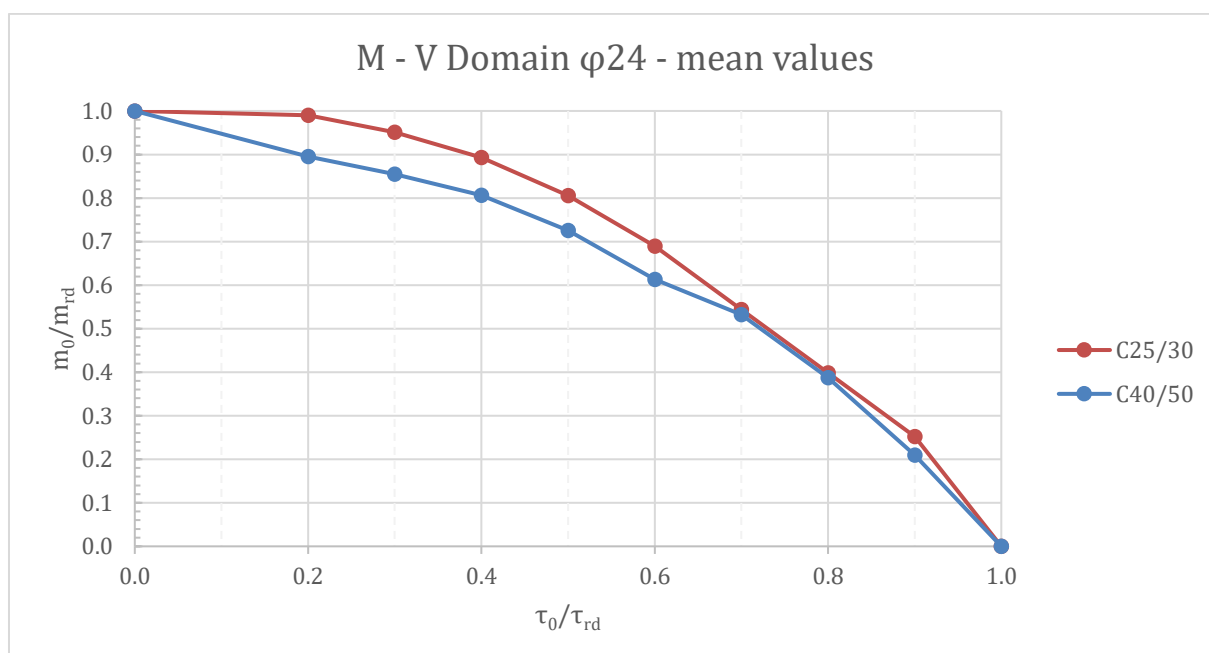

Graph 98. Shear – Bending interaction comparison for reinforcement ratio (C25/30, design values, σ_{cp}=10 MPa)

Graph 99. Shear – Bending interaction comparison for reinforcement ratio (C40/50, mean values, σ_{cp}=2.5 MPa)


M - V Domain C40/50 mean values

- φ20
- φ24

Y-axis: m_0/m_{rd}
X-axis: τ_0/τ_{rd}

Graph 100. Shear – Bending interaction comparison for reinforcement ratio (C40/50, mean values, σ_{cp}=5.0 MPa)

M - V Domain C40/50 mean values

- φ20
- φ24

Y-axis: m_0/m_{rd}
X-axis: τ_0/τ_{rd}

Graph 101. Shear – Bending interaction comparison for reinforcement ratio (C40/50, mean values, σ_{cp}=7.5 MPa)

M - V Domain C40/50 mean values

Axis labels: m_0/m_{rd} (vertical), τ_0/τ_{rd} (horizontal)

Legend: φ20, φ24

Graph 102. Shear – Bending interaction comparison for reinforcement ratio (C40/50, mean values, σ_{cp}=10 MPa)

M - V Domain C40/50 mean values

Axis labels: m_0/m_{rd} (vertical), τ_0/τ_{rd} (horizontal)

Legend: φ20, φ24

129

Graph 103. Shear – Bending interaction comparison for concrete strength ($\varphi 24$, mean values, σ_{cp}=2.5 MPa)

Graph 104. Shear – Bending interaction comparison for concrete strength ($\varphi 24$, mean values, σ_{cp}=5.0 MPa)

Graph 105. Shear – Bending interaction comparison for concrete strength ($\varphi24$, mean values, σ_{cp}=7.5 MPa)
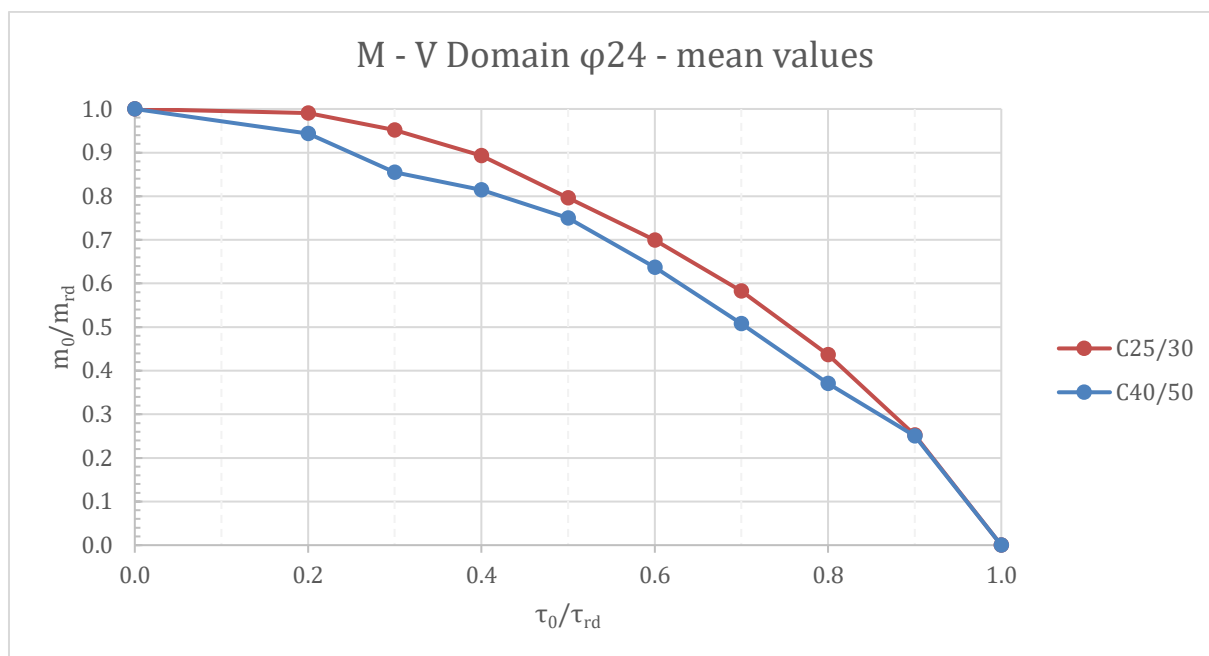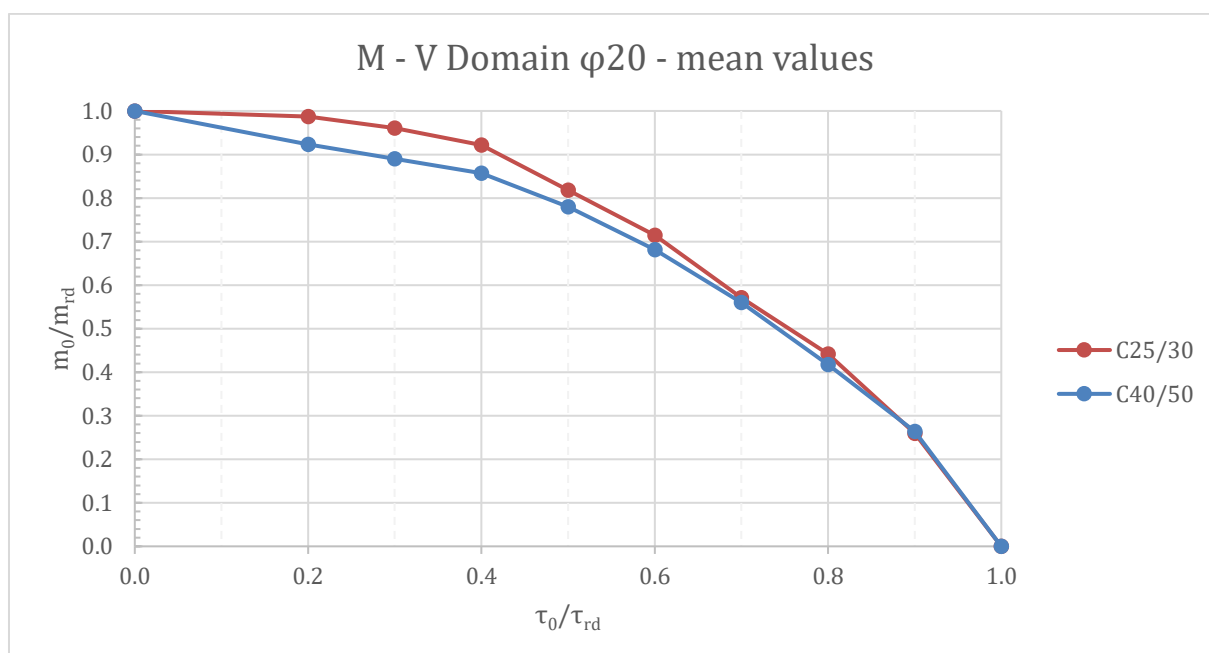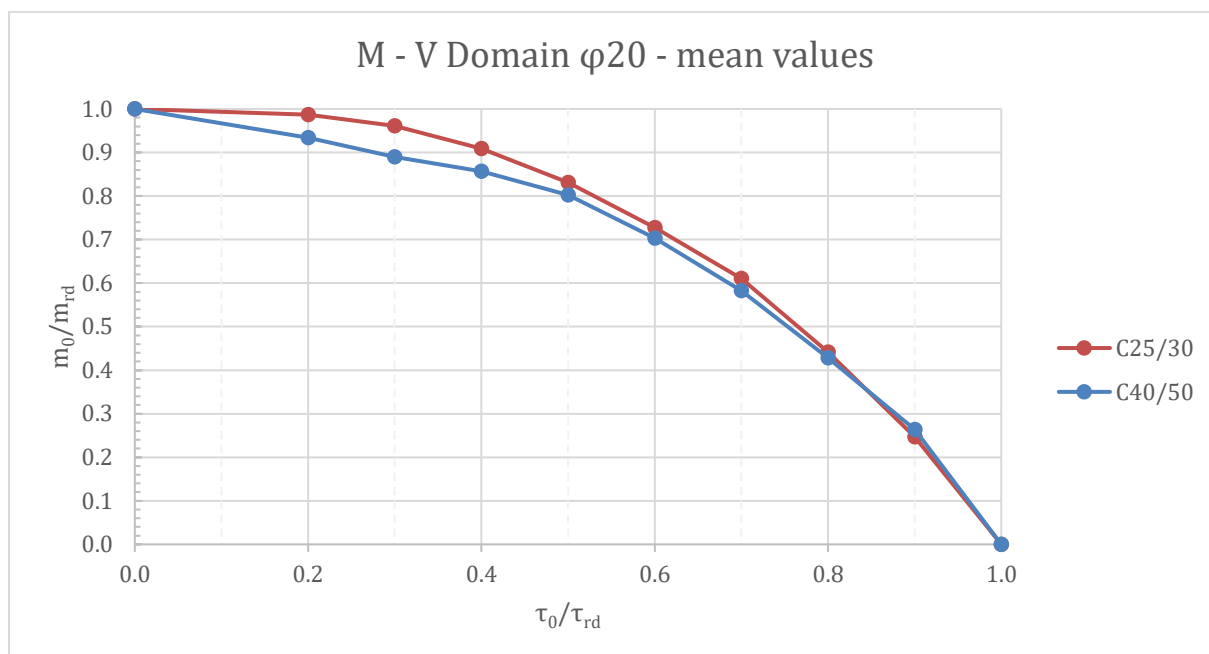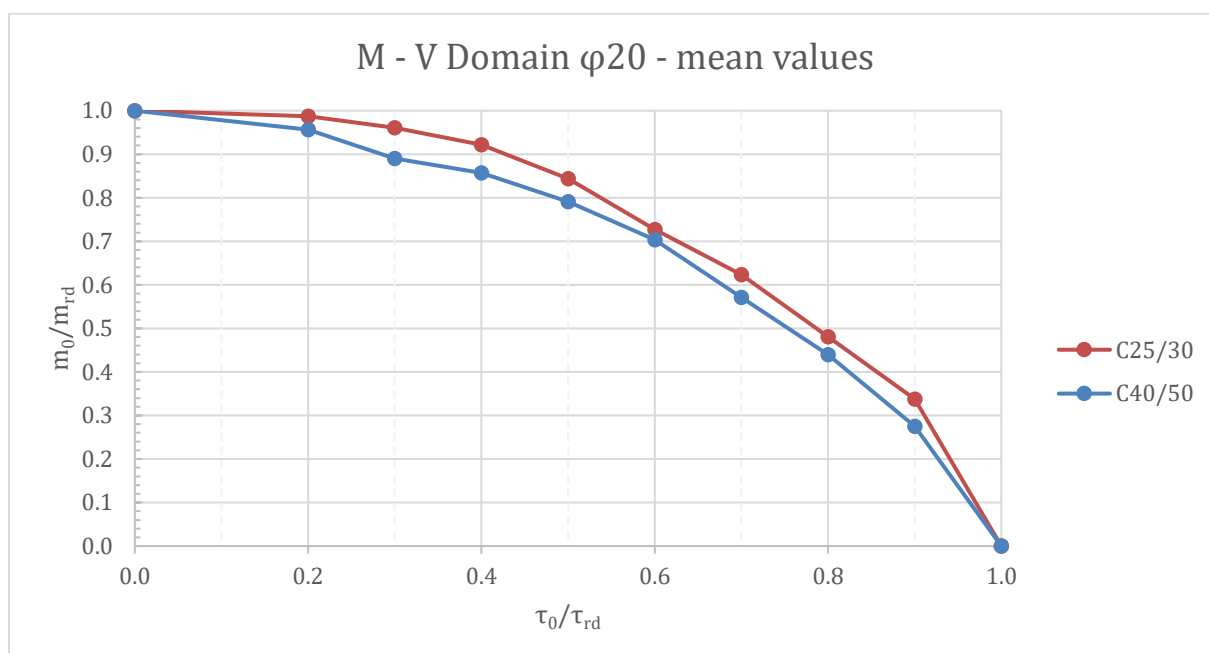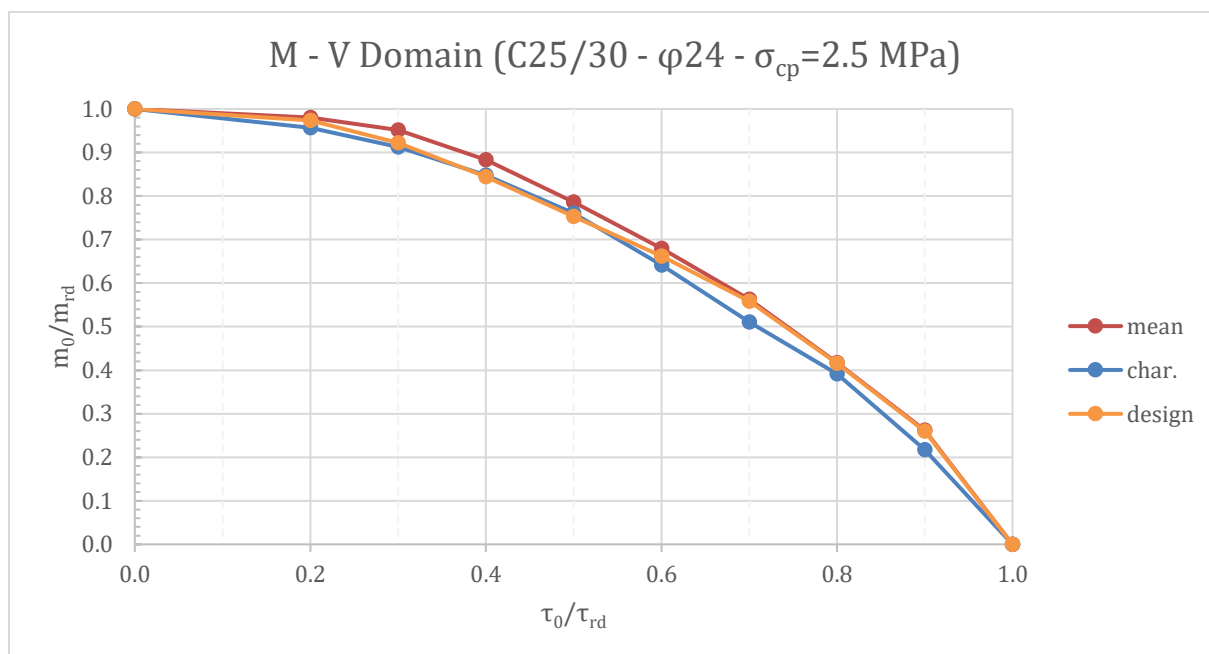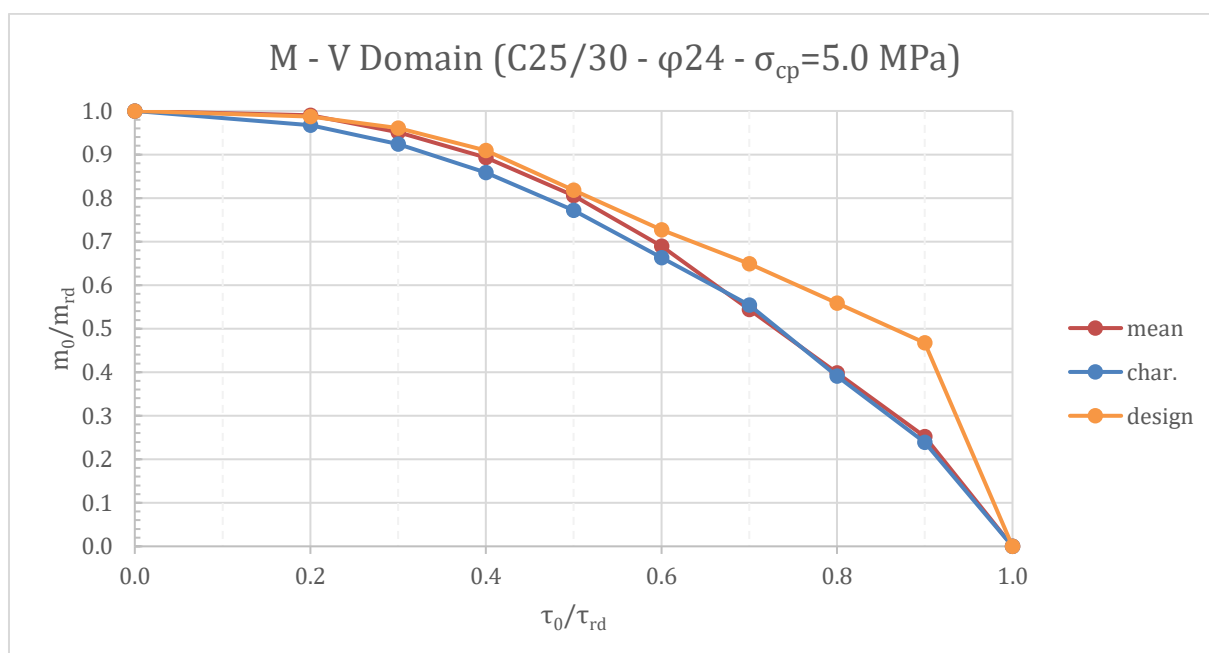

Graph 106. Shear – Bending interaction comparison for concrete strength ($\varphi24$, mean values, σ_{cp}=10 MPa)
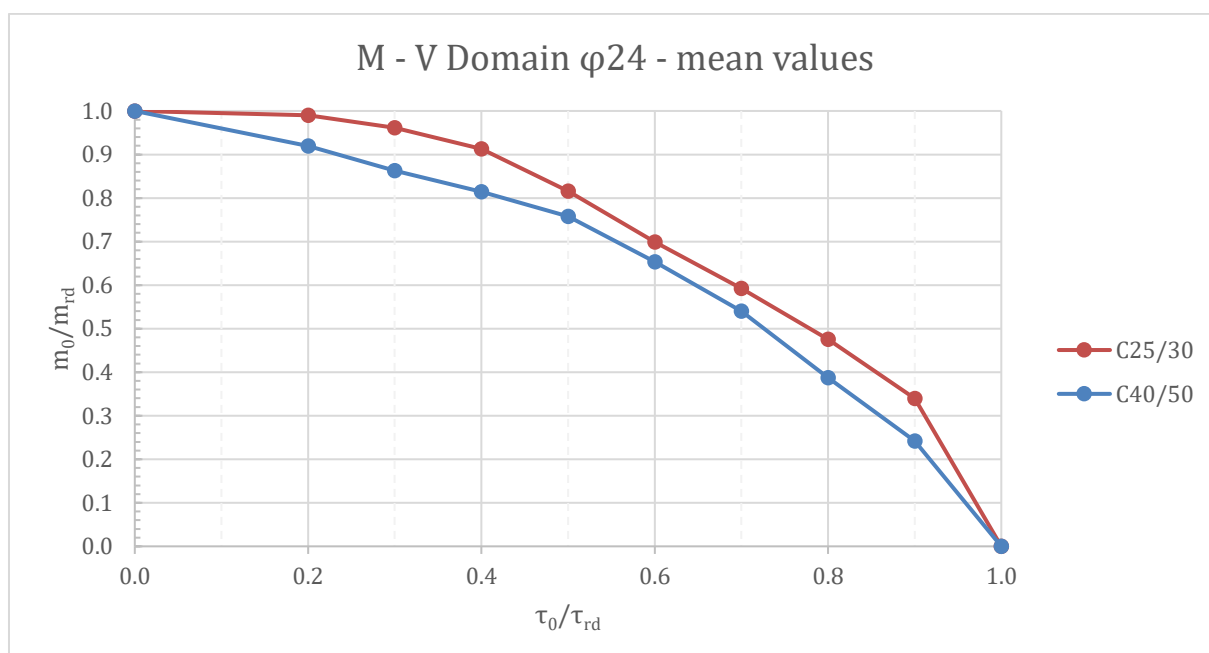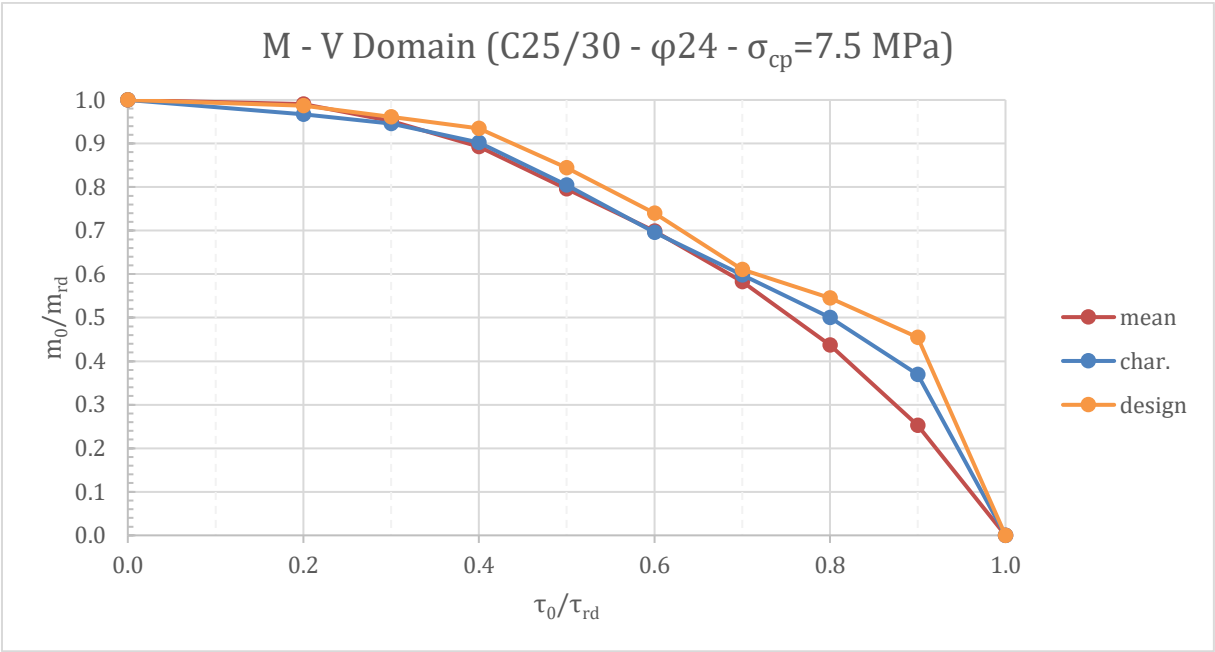
Graph 107. Shear – Bending interaction comparison for concrete strength ($\varphi20$, mean values, σ_{cp}=2.5 MPa)

M - V Domain $\varphi20$ - mean values

- C25/30
- C40/50

y-axis: m_0/m_{rd}
x-axis: τ_0/τ_{rd}
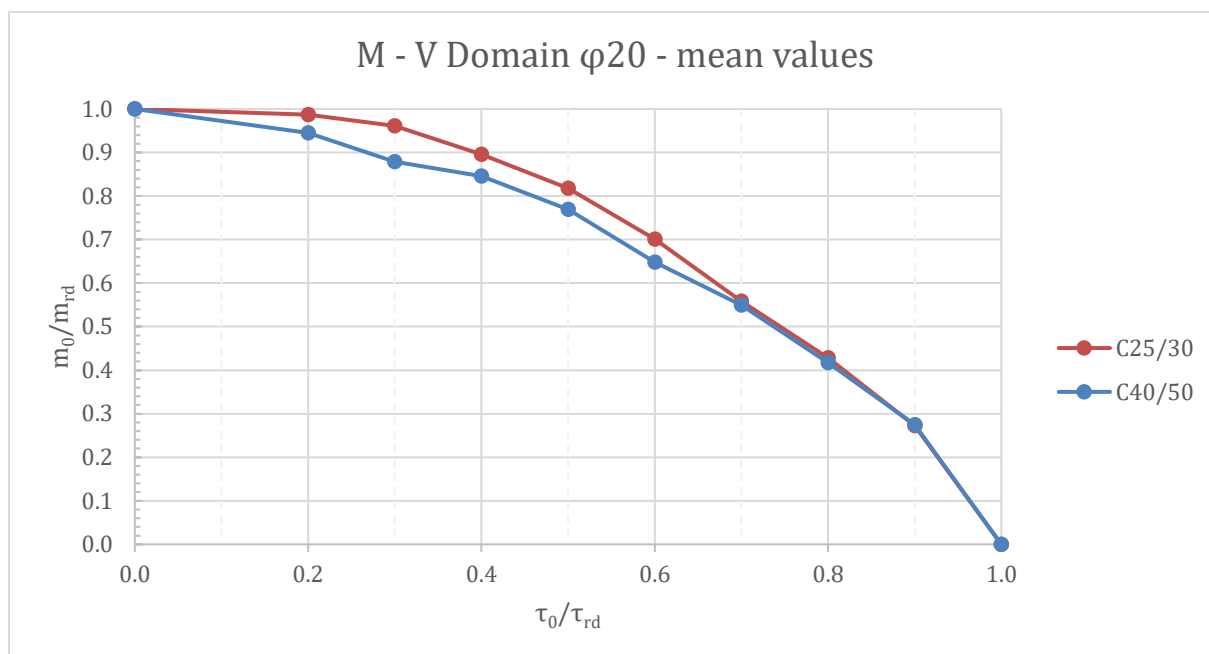
Graph 108. Shear – Bending interaction comparison for concrete strength ($\varphi20$, mean values, σ_{cp}=5.0 MPa)

M - V Domain $\varphi20$ - mean values

- C25/30
- C40/50

y-axis: m_0/m_{rd}
x-axis: τ_0/τ_{rd}

132

Graph 109. Shear – Bending interaction comparison for concrete strength (φ20, mean values, σ$_{cp}$=7.5 MPa)

Graph 110. Shear – Bending interaction comparison for concrete strength (φ20, mean values, σ$_{cp}$=10 MPa)

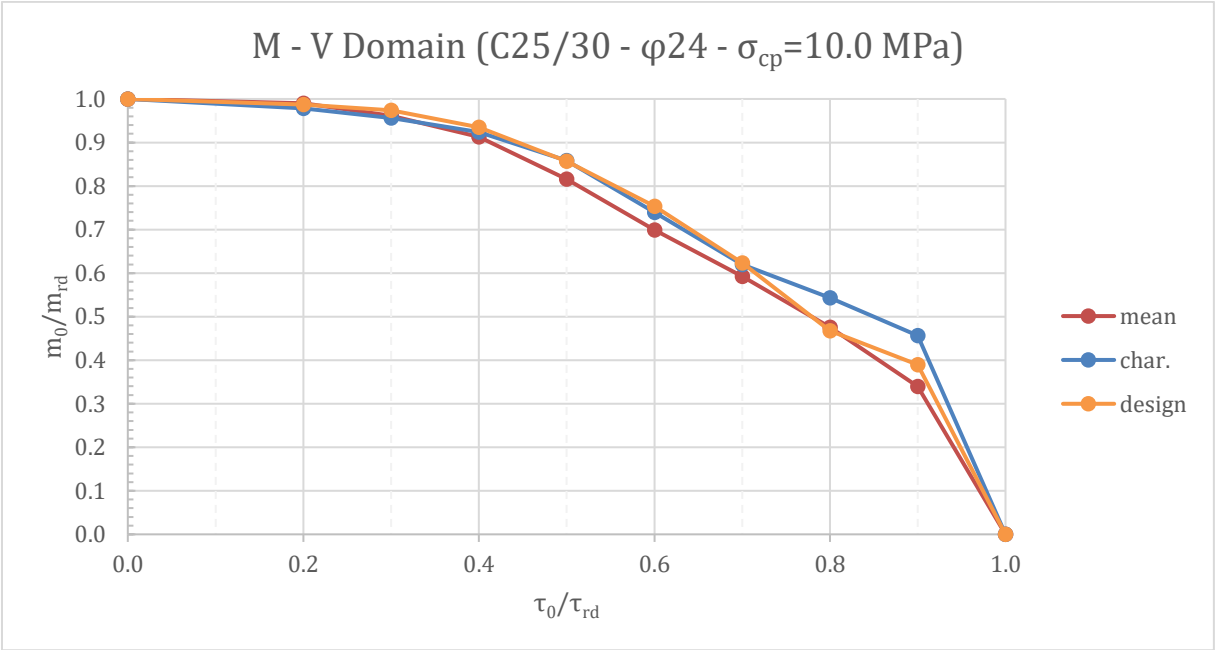*Graph 111. Shear – Bending interaction comparison for safety factor (C25/30, φ24, σ$_{cp}$=2.5 MPa)*

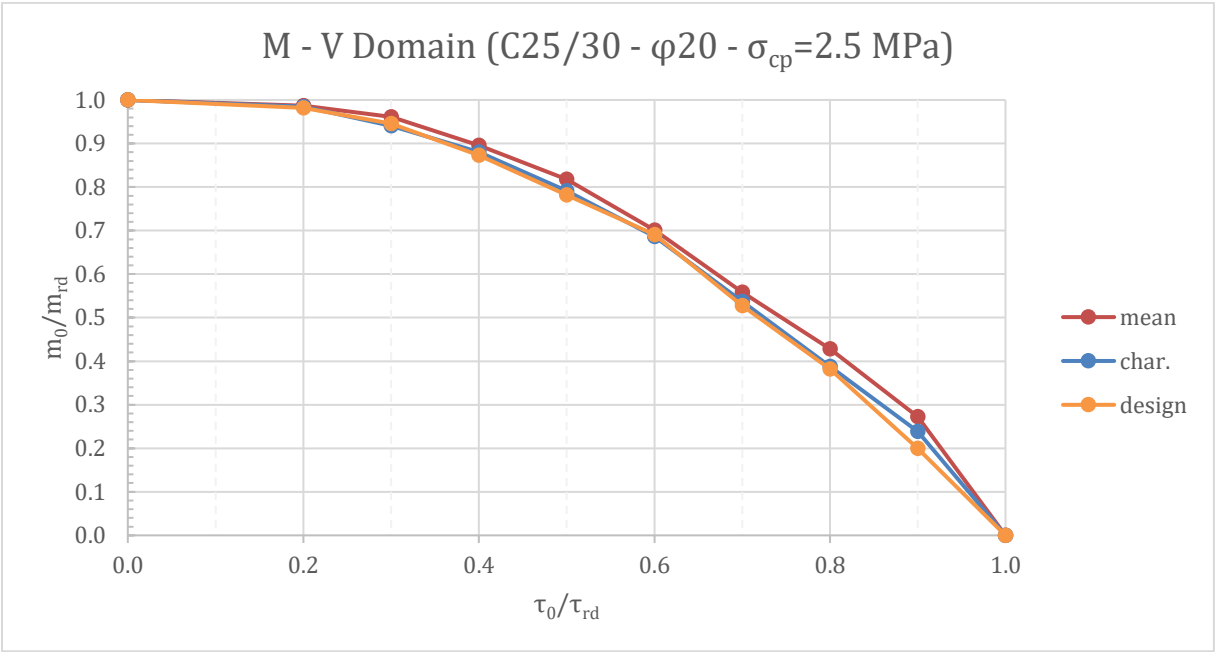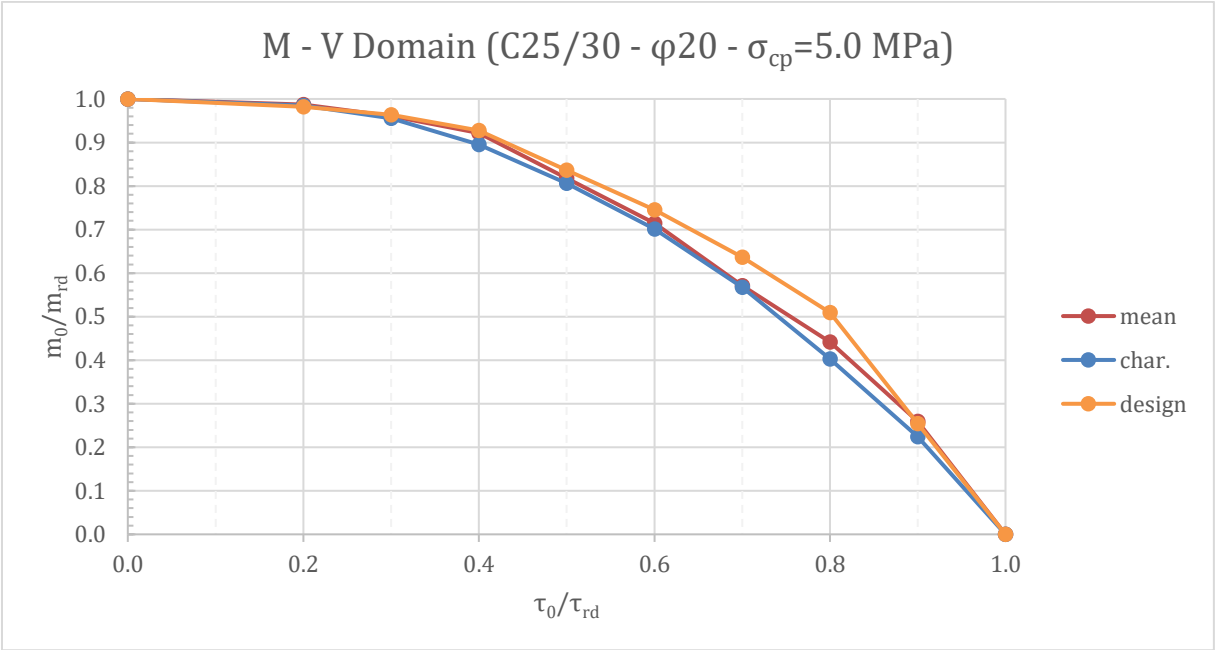*Graph 112. Shear – Bending interaction comparison for safety factor (C25/30, φ24, σ$_{cp}$=5.0 MPa)*

Graph 113. Shear – Bending interaction comparison for safety factor (C25/30, φ24, σ$_{cp}$=7.5 MPa)

M - V Domain (C25/30 - φ24 - σ$_{cp}$=7.5 MPa)

mean
char.
design

Graph 114. Shear – Bending interaction comparison for safety factor (C25/30, φ24, σ$_{cp}$=10 MPa)

M - V Domain (C25/30 - φ24 - σ$_{cp}$=10.0 MPa)

mean
char.
design

Graph 115. Shear – Bending interaction comparison for safety factor (C25/30, φ20, σ$_{cp}$=2.5 MPa)

M - V Domain (C25/30 - φ20 - σ$_{cp}$=2.5 MPa)

y-axis: m_0/m_{rd}
x-axis: τ_0/τ_{rd}

legend: mean, char., design

Graph 116. Shear – Bending interaction comparison for safety factor (C25/30, φ20, σ$_{cp}$=5.0 MPa)

M - V Domain (C25/30 - φ20 - σ$_{cp}$=5.0 MPa)

y-axis: m_0/m_{rd}
x-axis: τ_0/τ_{rd}

legend: mean, char., design

Graph 117. Shear – Bending interaction comparison for safety factor (C25/30, φ20, σ_{cp}=7.5 MPa)

M - V Domain (C25/30 - φ20 - σ_{cp}=7.5 MPa)

mean
char.
design
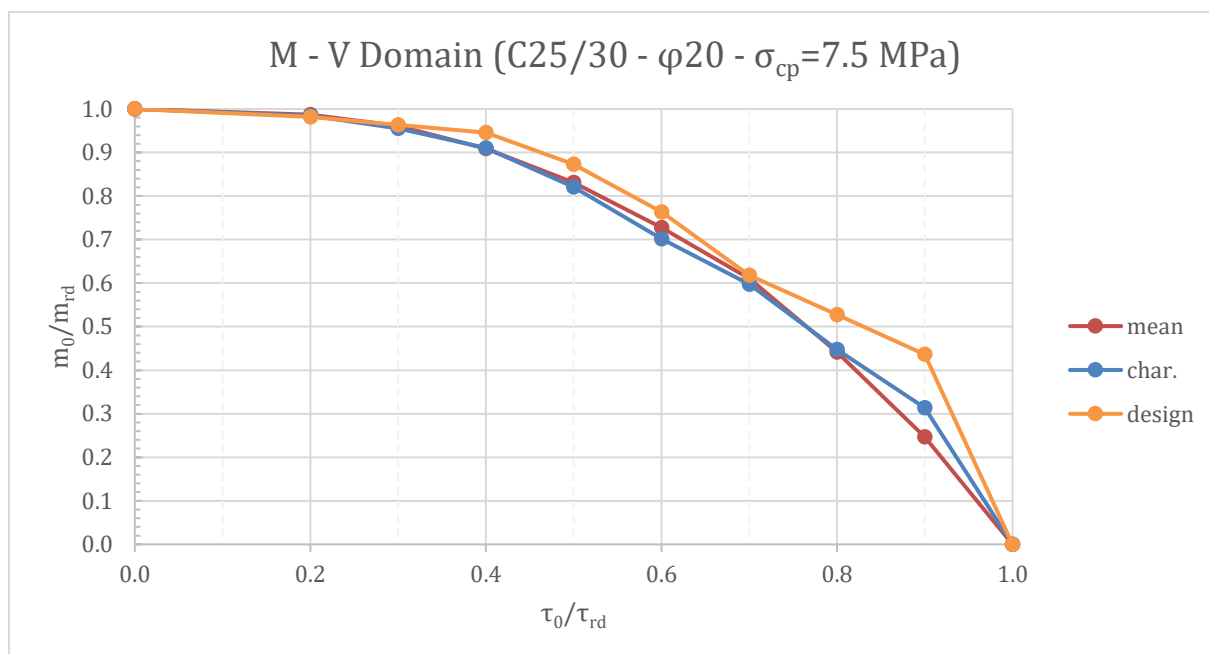
Graph 118. Shear – Bending interaction comparison for safety factor (C25/30, φ20, σ_{cp}=10.0 MPa)

M - V Domain (C25/30 - φ20 - σ_{cp}=10.0 MPa)

mean
char.
design
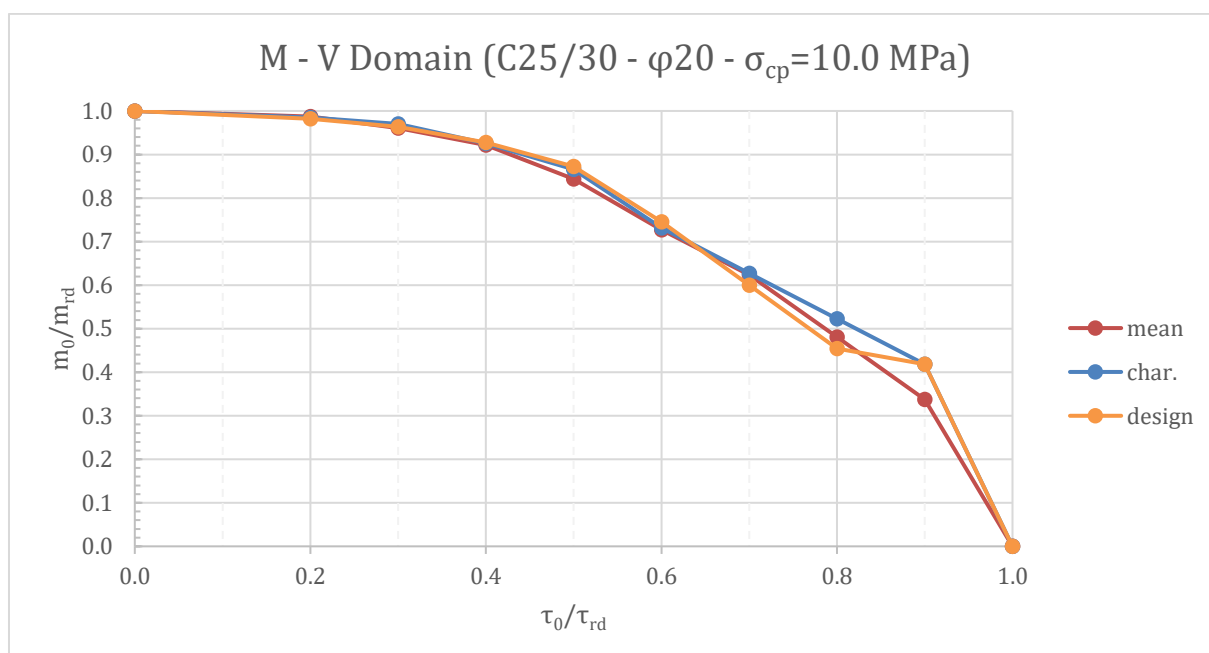
8. References

Červenka, V. and Papež, J. 2020. *ATENA Science – Program documentation (Manual).* s.l. : Červenka Consulting, 2020.

Consulting, Červenka. 2023. ATENA – Advanced tool for engineering nonlinear analysis. [Online] 2023. https://www.cervenka.cz.

Eurocode 2, CEN (European Committee for Standardization). 2004. *Eurocode 2: Design of concrete structures – Part 1-1: General rules and rules for buildings.* Brussels : CEN, 2004.

Fantili, A. 2023. *Theory and design of reinforced and prestressed concrete structures [Course material].* Torino : Politecnico di Torino, Department of Structural, Geotechnical and Building Engineering (DISEG), 2023.

fib, Fédération Internationale du Béton. 2020. *fib Model Code 2020: Draft for public discussion.* Istanbul : fib, 2020.

Giordano, L., & Gino, D. 2024. *Design and construction of bridges [Course material].* Torino : Politecnico di Torino, Department of Structural, Geotechnical and Building Engineering (DISEG), 2024.

Menn, Christian. 1990. *Prestressed Concrete Bridges.* Basel : Birkhäuser, 1990.

Recupero, A. & Granata, M.F. 2016. Interaction between longitudinal shear and transverse bending in prestressed concrete box girders. *Engineering Structures.* 2016.